Evaluating the Effects of Tunnel Construction on Buildings

Twana Kamal Haji

Department of Civil Engineering
University of Nottingham

Thesis submitted to the University of Nottingham for the degree of
Doctor of Philosophy

Faculty of Engineering November 2017

I would like to dedicate this thesis to my loving parents ...
my Father, *who sacrificed his soul for the freedom of all humanity*
my Mother, *whom I owe my life*

List of publications

Published articles

Haji, T.K., Marshall, A.M., and Tizani, W. (2018). A cantilever approach to estimate bending stiffness of buildings affected by tunnelling. *Tunnelling and Underground Space Technology*, 71:47–61.

Submitted articles

Haji, T.K., Marshall, A.M., and Franza, A. (2017). Mixed empirical-numerical method for investigating tunnelling effects on structures. *Tunnelling and Underground Space Technology*, under review.

Acknowledgements

Firstly, I would like to take this opportunity to give thanks to all those who have made a contribution to the accomplishment of my challenging PhD journey.

I would like to express my sincere gratitude to my beloved father *Kamal Haji* who was an ideal example of fatherhood and a great example of a loyal person who continuously stood against darkness.

I would like to sincerely thank my supportive supervisor, Associate Professor Alec Marshall, for his help, encouragement, and guidance during my study.

I am also very appreciative to Mr. Kosrat Rasool Ali for his continuous support. My special thanks also go to Darbaz Kosrat and Lava Jameel for their encouragement.

I am indebted to my good friends Younis Alshkane, Itai Elkayam and Andrea Franza for the excellent suggestions they had given me during my study. I am also very appreciative to my previous lecturers Dr. Salahaddin Abdul-Rahman and Dr. Ahmed Hidayat for their advice.

My friends have been a great source of encouragement, especially Ran Yuan, Yang Lu, Shu Liu, Hawkar H. Ibrahim, Kamaran S. Ismail, Zirak Allaf and Amged Abdelatif. I have made many friends in Nottingham with whom I had enjoyable experiences.

Finally, my special thanks go out to my family: my mother, my sister and her husband, my brother (Tola) and his wife, my brother (Dana), and my beloved sons (Tawa) and (Tana), for their continuous love and support throughout my studies. This challenge would not have been accomplished without them.

Abstract

New tunnels are continually constructed beneath the surface of large and developed cities due to the lack of surface space. These new tunnels will undoubtedly interact with existing surface and subsurface assets, such as building foundations, pipelines and other buried structures. There will be a two-way interaction whereby the tunnel construction affects the existing structure by inducing displacements in the underlying soil, and the structure influences tunnelling induced displacements via its weight and stiffness. The design of tunnels should include the consideration of this soil–structure interaction to avoid significant damage or failure to the existing structures due to the effect of the newly constructed tunnel.

The research presented in this thesis focuses on tunnel–building interaction, and more specifically on buildings with shallow foundations. Previously, numerical methods have been used to study specific scenarios or to obtain design charts for use by geotechnical engineers. The proposed design charts have various limitations. For instance, they are suggested for specific types of soils, the 3D nature of buildings is disregarded to a great extent, and most importantly, several main parameters that influence the behaviour of a building when affected by tunnelling have not been accurately considered. In this research, the 3D behaviour of buildings is investigated with a focus on the main parameters that affect the deformation of a building in reality. These parameters are determined based on mathematical relationships of the stiffness of a structural member. Furthermore, computationally efficient methods are proposed to estimate building bending stiffness that can be readily used by engineers.

The focus of this work is the effect of tunnelling on concrete framed buildings. The research deals with three main areas: [i] the estimation of the bending stiffness of a building's superstructure and foundation, [ii] the analysis of tunnel–soil–building interaction using realistic ground displacements achieved from the field or experimental studies, and [iii] the behaviour of a 3D building (weightless and weighted) in a soil–building system during the construction of a tunnel. Finite element analysis (ABAQUS 3D) is used to investigate these problems.

In research area [i], the building superstructure and the foundation are treated separately. Approaches are proposed in which the building response to tunnelling is related to the bending

of a beam and empirical-type relationships are developed to predict building bending stiffness. These approaches are somewhat unconventional, but it is shown that they capture the real 3D response of buildings and foundations to tunnelling induced ground displacements more accurately than previously proposed methods. The approaches are relevant to scenarios where the building is perpendicular to the tunnel axis. Additionally, two cases of tunnel–building relative position are considered: (1) a case where a tunnel is constructed outside the building plan area (i.e. the tunnel axis and the nearest edge of the building to the tunnel do not overlap by more than half of the tunnel cross-section), which is called the 'cantilever approach,' and (2) a scenario where the tunnel is located under the building centreline, which is called the 'fixed–ended approach.' It should be noted that a detailed understanding of how structural elements of a building contribute to the stiffness of the entire building system is missing in the literature.

The results of research area [i] show that the contribution of the building storeys to the global building bending stiffness is not uniform; the lower storeys have a larger contribution than the upper ones. Furthermore, buildings are mainly represented by 2D beams or frames in the current methods of building stiffness estimation. The proposed methods of this thesis (cantilever and fixed–ended methods) present accurate estimations of the true bending stiffness of 3D buildings subjected to tunnelling induced ground movements. In addition, the length of the building subjected to deflections, the length that is not affected by deformations, and the cross sectional flexural rigidity play the main role in the estimation of bending stiffness. These parameters are strongly interconnected, and should be considered together in the analysis of tunnel–building interaction. The results of this research show that the bending stiffness of a building decreases dramatically as the length affected by ground displacements increases. In contrast, the length of the building that is unaffected provides resistance to the building against rotation, which in turn increases the bending stiffness. This is because the unaffected length determines the boundary condition of the building, which is an important parameter in determining the bending stiffness.

Research area [ii] aims to provide a method to overcome issues arising when using numerical analyses to investigate tunnelling and its impact on structures, since ground displacements predicted with conventional numerical methods are generally wider and shallower than those observed in practice. A two-stage numerical technique is proposed to estimate the effect of building stiffness on ground displacements due to tunnelling. In the first stage, greenfield (no existence of structures) soil displacements are applied to the soil model and the nodal reaction forces are recorded. In the second stage, the effect of tunnelling on a structure is evaluated by applying the recorded nodal reactions to an undeformed mesh.

Results show that by using this technique, the role of the soil constitutive model is removed from the process of evaluating tunnelling induced ground displacements; it is only used in the evaluation of the soil–structure interaction. A realistic prediction of the structural stiffness effect can therefore be achieved due to the application of realistic ground displacements.

For research area [iii], the response of weightless and weighted 3D buildings to tunnelling in a global soil–building system is considered. For the weightless case, the degree of stiffness contribution of the foundation and the superstructure to the bending resistance of the building is investigated. Buildings in the literature are assumed to act as a single entity when affected by tunnelling. Results of this research show that the effect of the foundation stiffness has the most significant contribution to the global building resistance to soil deformations while the contribution of the superstructure stiffness is less significant. Using insights from these results as well as those of research area [i], an equivalent beam method is proposed to model 3D buildings as 2D beams in plane strain analyses. The equivalent beam considers the effect of parameters influencing bending stiffness of a member, and the non-uniformity of stiffness contribution of building storeys to the global building bending stiffness. For the weighted buildings, a study is presented about the approach used to design a building, and the assumptions made in the analysis and design stages prior to the construction of a tunnel. The design parameters most affected by the tunnel construction are determined and examined numerically. It is explained that there is a strong relationship between the weight and bending stiffness of a building.

Table of contents

List of figures

List of tables

List of Symbols

Roman Symbols

α^* relative axial stiffness

α^*_{mod} modified relative axial stiffness

α_{Kus} a coefficient to calculate C_{Kus}

α_{vor}, n_{vor} modified Gaussian parameters

$\bar{y}_{sl}$ distance from the neutral axis of a slab to the neutral axis of the building

Δ deflection

Δ_b beam deflection

δ_s soil deflection

$\varepsilon_{bt,max}$ maximum bending tensile strain induced in a beam

$\varepsilon_{st,max}$ maximum shear strain induced in a beam

γ_s soil unit weight, N/m^3

ρ^* relative bending stiffness

ρ^*_{mod} modified relative bending stiffness

σ_T tunnel support pressure

σ_{sur} surcharge weight on soil surface

$\varepsilon_{hc,bldg}$ maximum horizontal compressive strains induced in a building

$\varepsilon_{ht,bldg}$ maximum horizontal tensile strains induced in a building

A_{sl} cross sectional area of a slab

b_p plate width in plate load test

B_{bldg} building width parallel to the tunnel direction

b_{fb} cross sectional width of floor beams

b_{sb} cross sectional width of supporting beams

B_{sl} clear width of a slab

c_u undrained shear strength of soil

$C_{bc,b,eq}$ a coefficient to determine the boundary condition of the equivalent beam

$C_{bc,cant}$ a coefficient to estimate the degree of end fixity of a loaded floor

$C_{bc,fnd}$ a coefficient to estimate the boundary condition of a foundation

$C_{bf,cant}$ a coefficient to convert analytical bending stiffness of a floor to its actual bending stiffness

C_{cf} a coefficient to calculate C_{Kus}

$C_{K,reduct}$ a coefficient to consider the reduction of building bending stiffness caused by multi panels (in x-direction) affected by tunnelling

C_{Kus} a parameter to estimate the degree of stiffness contribution of upper storeys to the first storey

E material elastic modulus

EA axial rigidity of a member

EA_{col} axial rigidity of a column

EI flexural rigidity of a member

F_K a factor depending on applied force and boundary condition of a member

h_b cross sectional height of a beam

h_{fb} cross sectional height of floor beams

h_{sb} cross sectional height of supporting beams

I cross sectional moment of inertia

i horizontal distance from tunnel centreline to the inflexion point of the surface settlement trough

I_{bldg} cross sectional moment of inertia of a building

I_{fl} moment of inertia of floor cross section

I_{sl} cross sectional moment of inertia of a slab

K stiffness of a member

K_a axial stiffness of a member

K_b bending stiffness of a member

k_s modulus of subgrade reaction

K_t trough width parameter

$K_{b,bldg}$ building bending stiffness

$K_{b,fl,cant,eq,fix}$ equivalent bending stiffness of a floor

$K_{c,col}$ the stiffness of columns used for calculating coefficients

$K_{c,Lfl}$ the stiffness of the loaded floor used for calculating coefficients

$K_{c,sb}$ the stiffness of the supporting beam used for calculating coefficients

$K_{c,Sfl}$ the stiffness of the supporting floor used for calculating coefficients

$k_{s,p}$ modulus of subgrade reaction of a testing plate

$k_{s,rec}$ modulus of subgrade reaction of a rectangular footing

$k_{s,sq}$ modulus of subgrade reaction of a square footing

L length of a member

L_b length of a beam

L_f foundation length

L_{bldg} building length (perpendicular to the tunnel direction)

L_{col} length of a column

$L_{ds,t}$ length of the total displaced soil equal to settlement trough width

L_{ds} length of the displaced soil equal to half of the settlement trough width

$L_{f,ld}$ loaded (deformed) part of a foundation

$L_{f,sp}$ supporting part of a foundation

L_{inf} influenced length of a building by tunnelling

L_{sl} clear length of a slab

$M^{\varepsilon_{hc}}$ axial modification factor for compressive strains

$M^{\varepsilon_{ht}}$ axial modification factor for tensile strains

$M^{DR_{hog}}$ bending modification factor for hogging

$M^{DR_{sag}}$ bending modification factor for sagging

$N_{tun,c}$ tunnel failure stability ratio

N_{tun} tunnel stability ratio

P applied force to a member

q_s soil pressure, subgrade reaction

$S_h(x)$ horizontal ground displacements due to tunnelling

$S_v(x)$ ground vertical settlement

$S_{v,max}$ maximum ground settlement occurring at the tunnel centreline

t_{sl} slab thickness

$V_{ls,surf}$ ground surface volume loss in the greenfield condition

V_{lt} tunnel volume loss

V_s volume of the surface settlement trough per unit length

y_b deflection of a beam on elastic foundation

z_t tunnel depth

Chapter 1

Introduction

1.1 Background

The increase of population in developed countries has resulted in the utilisation of the surface land within cities by a great extent. In addition to the horizontal expansion of urban areas, many high-rise buildings are constructed that require raft foundations. Population increase has also led to the rise of traffic volume and additional quantities of water and waste water. In order to reduce surface traffic volume and to accommodate infrastructure development needs, tunnels have been constructed beneath structures.

All engineering structures must interact with the ground in some way. When the stress conditions in the underlying soil change due to the construction of underground structures, or when the system is subjected to external forces such as earthquakes, the response and behaviour of both the soil and the structure will be interconnected. This interrelationship between the structure and the ground is termed soil structure interaction.

Tunnelling in the ground produces soil stress relief in its vicinity due to the tendency of the soil to move towards the tunnel cavity. This in turn creates ground displacements that can influence surface and subsurface structures such as buildings, water tanks, roads, and buried pipelines. Among the surface structures, there are high-rise concrete framed buildings supported by raft foundations. These high-rise buildings in developed cities are usually constructed in clusters or very close to each other due to the lack of space. The foundations of these buildings as well as the superstructures may experience damage since the new tunnel has to pass beneath them.

The interaction between a newly constructed tunnel and an existing building is due to the induced ground movements resulting from the tendency of the soil to move towards the tunnel. This movement of the soil is also affected by the existence of the structure which

makes the interaction a two-way relationship (Potts and Addenbrooke, 1997). The following section explains the specific interaction problem considered in this research.

1.2 Problem Statement

The issue of the interaction between newly constructed tunnels and existing structures is continuously growing and becoming more essential. It has attracted the attention of many researchers, and numerous papers have been published utilising different experimental, analytical and numerical methods (Franzius et al., 2006; Giardina et al., 2015; Goh and Mair, 2014; Potts and Addenbrooke, 1997). It can be said that this interaction is a complicated problem and several complex parameters are involved in the analysis process.

The main parameters of the tunnel–building interaction are ground displacements and the building configuration. With regard to the ground displacements, both the displacement values and the settlement trough width have a significant effect on the interaction. Regarding the building, the type of the building, its stiffness, its weight and its location with respect to the tunnel are crucial. Some analysis methods estimate greenfield displacements induced by tunnelling and then apply the estimated values to the structures; it is assumed that the structure is flexible enough to follow the greenfield movements (Rankin, 1988). Other methods include the effect of the building, treating it as a beam or a frame (Giardina et al., 2015; Potts and Addenbrooke, 1997). Some researchers have included detailed structural models in their analyses (Mirhabibi and Soroush, 2013; Mroueh and Shahrour, 2003), however, the behaviour of the building is still not clear in the soil–structure system.

The ambiguity of the building behaviour in the soil-structure system is mainly related to the stiffness of the building and the relation between its stiffness and its weight. The stiffness of the building is estimated based on a simple beam or a frame; the 3D nature of the structure is not taken into account. Moreover, the role of the building stiffness in the soil–structure interaction is not investigated based on the parameters influencing the stiffness of a member; for instance, the length of a building located in the soil area that is influenced by tunnelling, the part located in the unaffected soil zone, and the boundary condition of the building in the soil–building system are not adequately included. Apart from this, the whole building is considered as a single entity, and the role of the foundation and individual storeys in the global building system is not taken into consideration.

It is worth noting that previously, numerical methods have been used to study specific scenarios or to obtain design charts for use by geotechnical engineers. The proposed design charts are subjected to the above limitations. In this research, the 3D behaviour of buildings

is examined in detail with a focus on the main parameters that affect the deformation of a building in reality. These parameters are specified based on mathematical equations of the deflection of a structural member. Furthermore, computationally efficient approaches are suggested to estimate building bending stiffness. The suggested methods can be readily used by engineers. It should be mentioned that these approaches are somewhat unconventional, but it is shown that they accurately capture the real 3D response of buildings and foundations to tunnelling induced ground displacements. Based on comparisons of the proposed methods with the currently available approaches to estimate building bending stiffness, it is also illustrated that the proposed approaches lead to more accurate estimation of building stiffness than previously proposed methods.

1.3 Scope of Research

The aim of this research is to determine, using finite element analyses, the realistic behaviour of 3D concrete framed buildings in the global soil–building system when a new tunnel is constructed. The determination of the realistic building behaviour considers the role of the building stiffness, weight, and relative position in a tunnel–building interaction problem. The research also aims to develop a method to quantify the bending stiffness of a global 3D concrete framed building in a soil–building domain depending on the properties of soil, building and relative tunnel–building position.

The objectives of the project can be summarised as below:

1. Development of methods to quantify the bending stiffness of the building superstructure and foundation
2. Development of an equivalent beam method to represent a 3D building by a 2D beam in the numerical analyses
3. Development of a mixed empirical–numerical method to quantify the effect of building stiffness on tunnelling induced ground movements
4. Investigation of the contribution of foundation and superstructure stiffness to the global building stiffness during the construction of a new tunnel
5. Study of the relation between the stiffness and weight of a building when subjected to tunnelling

1.4 Original Contributions of Research

The original contributions presented within this thesis are briefly presented here.

The role of building stiffness in tunnel–soil–building interaction has been shown to be influential in the literature; however the effect of building stiffness has not been investigated based on all the influential parameters. The investigations of building response to tunnelling in this work consider the main influential parameters that determine building stiffness. These parameters are obtained from mathematical expressions of beam deflections.

In the existing methods to estimate the stiffness of buildings or which represent buildings as an equivalent beam, it is assumed that the whole building behaves together as a single body without consideration of the contribution of different structural parts to the global building behaviour. The results presented in this thesis, which are related to concrete framed buildings with raft foundations, show that the foundation has the main contribution to the global building resistance against deformations; the role of the superstructure is less significant. Furthermore, the stiffness contribution of building storeys to the global building stiffness decreases with the increase of their distance from the foundation.

The majority of previous work aimed to utilise numerical methods to investigate specific scenarios or to propose design charts. Their limitations include disregarding the 3D nature of buildings, focusing on specific soil types, and overlooking some parameters that affect the response of buildings to tunnelling. This work presents methods to estimate the true bending behaviour of 3D buildings (foundation and superstructure); the mentioned limitations are eliminated in the proposed methods.

The relation between the stiffness and the weight of a building is not clear in the literature. There are methods that neglect the effect of building stiffness in the tunnel–building interaction problem, while there are others that significantly overestimate the stiffness effect. The outcomes presented within this thesis show that the weight and the stiffness of a building are greatly interconnected. The stiffness comes from the design stage of the building which depends on the outcomes of the analysis stage in which the loads applied to the building are calculated. Therefore, considering both the weight and the real stiffness of buildings is necessary to predict the true building behaviour in tunnel–soil–building interaction analyses.

The thesis also presents an efficient mixed empirical–numerical method to estimate building effects on ground displacements due to tunnelling. The method allows the estimation of the building effect on the soil layer above the tunnel crown in an elastic analysis. Any form of greenfield displacement profile can be used as an input to the method, including both vertical and horizontal displacements, which can be applied either together or separately.

The method overcomes several issues related to the use of conventional numerical analysis methods, which generally give unrealistically wide settlement troughs and large horizontal displacements.

1.5 Thesis Structure

The thesis is organised as follows:
Chapter 1 is an introduction to the thesis, containing: a succinct description of tunnelling effects on buildings, the problem definition, aims and objectives, and the thesis layout.
Chapter 2 presents a brief review of buildings, building structural members, and foundations.
Chapter 3 contains a review of tunnels, tunnelling techniques, numerical simulation of tunnels, methods of predicting ground movements due to tunnelling, and tunnel–soil–building interaction.
Chapter 4 explains the finite element software ABAQUS (used in this research), the type of elements chosen for the analyses of this work, and general material properties.
Chapter 5 proposes two methods to estimate the bending stiffness of a building's superstructure depending on the location of the tunnel in relation to the building: a cantilever method for the case where the tunnel is located outside the building plan area, and a fixed–ended case where the tunnel is located under the building centreline.
Chapter 6 uses the methods developed in Chapter 5 (a cantilever and a fixed–ended method) to estimate the bending stiffness of a raft foundation depending on the location of the tunnel in relation to the foundation.
Chapter 7 proposes a mixed empirical–numerical method to numerically analyse tunnel–building interaction and to quantify the effect of building stiffness on ground displacements.
Chapter 8 presents the effects of framed buildings on tunnelling induced ground movements. The chapter contains the investigation of the effect of a weightless building on ground movements, the study of the effect of building weight on ground displacements, and the development of an equivalent beam method to represent a 3D building in a soil–building domain.
Chapter 9 contains the conclusions and recommendations for further research.

Since this research is related to both tunnelling and buildings, Chapters 2 and 3 present a review about buildings, tunnelling, and tunnelling effects on structures. It should be noted that Chapter 2 contains a detailed discussion of the deflection of a beam explaining the parameters that have the main role in the beam deflection. This is because, in this research, the concept of the beam deflection is the basis of investigating the behaviour of a 3D building

affected by tunnelling. After explaining the use of ABAQUS and the material properties used in this thesis in Chapter 4, the superstructure of buildings is studied numerically in Chapter 5 based on the definition of the beam bending stiffness given in Chapter 2. The behaviour of the building is related to the deflection of a cantilever beam when the tunnel is not located under the building, and to a fixed–ended beam when the tunnel is under the building centreline. These two approaches (cantilever and fixed–ended) are also used in Chapter 6 to investigate the deformation of raft foundations when influenced by tunnelling. In Chapters 5 and 6, the tunnel is not simulated directly. The effect of tunnelling induced ground movements are replaced by forces applied to the structure.

Chapter 7 shows that the conventional numerical analysis of tunnelling results in wide and shallow settlement troughs. Since this shallowness does not agree with field measurements and experimental data, a mixed empirical–numerical method is proposed to estimate tunnel–building interaction, which overcomes the problems arising from conventional numerical analyses of tunnelling. The proposed mixed empirical–numerical method is then used in a section of Chapter 8 to investigate the 3D behaviour of buildings in a global soil–building system. Chapter 8 also includes the investigation of the effect of building weight on tunnel–building interaction using a conventional numerical method since the proposed mixed empirical–numerical method is only related to elastic analyses. It is worth noting that the main parameters that influence the deformation of a building during tunnelling are also investigated in Chapter 8 in a global soil–building system. Finally, the conclusions and recommendations for further research are presented in Chapter 9.

Chapter 2

Buildings and Foundation

2.1 Introduction

The main focus of this chapter is on reinforced concrete buildings since they are the structures relevant to the scope of this research. Reinforced concrete is a widely used construction material for buildings, bridges, dams and other types of structures. The properties of reinforced concrete depend on the properties of the constituent materials (concrete components, steel, admixtures) as well as the construction techniques (Li, 2011). A reinforced concrete framed building is made of reinforced concrete and generally consists of beams, slabs, columns, and a foundation. In some systems such as flat plates or flat slabs, beams are not included. These members are connected rigidly to each other by casting them monolithically such that they act as one unit. In between columns, partition walls are placed which are mainly non-structural elements in a framed building. Figure 2.1 displays a typical framed building showing the structural members of slabs, beams, columns and the foundation.

The behaviour of a building depends on the behaviour of its interconnected structural parts. For this reason, understanding structural parts is necessary to understand the global building behaviour. This chapter briefly presents general information about the structural behaviour of buildings relevant to the purpose of this research. The definition and the function of the superstructure members are first presented in which the analysis and design processes of the structural members are also discussed. Since buildings have been modelled as beams to a great extent in soil-structure interaction problems, and bending stiffness has been an essential parameter in quantifying soil-structure interaction, specific attention is given to the bending behaviour of beams to understand the actual parameters relevant to stiffness. This information supports some of the analyses in Chapters 5 and 6 about building stiffness estimation methods.

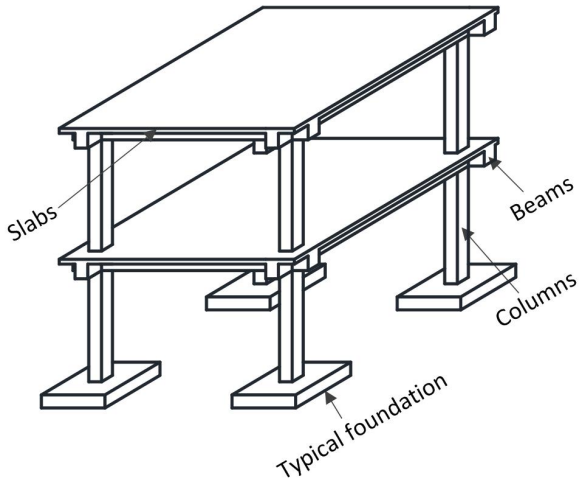

Fig. 2.1 Illustration of a 3D framed building

This section is then followed by an explanation about building foundations. Note that this research only focuses on the behaviour of raft foundations; different types of building foundations are briefly defined to provide some context. Modulus of subgrade reaction and shallow foundation design methods are briefly discussed. The modulus of subgrade reaction is not directly relevant to the scope of this research but its explanation may help in understanding the global behaviour of raft foundations and how they are dealt with practically. This section is relevant to the work presented in Chapters 6 and 8.

This chapter also presents a brief explanation about the stiffness of buildings, which is an important concept throughout the thesis.

2.2 Superstructure Members

Generally, the superstructure structural members include slabs, beams, columns and walls. The following sections present a brief explanation about the analysis and design stages of structural members, and an introduction to the main structural parts of a building.

2.2.1 Analysis and design of structural members

Prior to the construction of any building, structural members go through two vitally important stages: analysis and design. Detailed procedures and methods of these two stages can be found in reinforced concrete analysis and design books (e.g. Arya, 2009), and building construction codes (e.g. ACI-Building-Code, 2011). In the analysis process, the possible

loads, moments and torques that may be imposed to the building are calculated. Based on these calculated loads, the building is analysed to determine the induced shear forces as well as bending and torsional moments in the structural parts. This can be done using different analysis methods, such as finite element analyses. In this stage, preliminary values of material and geometrical properties of each building part may need to be assumed. After that, the design stage starts which depends on the determined internal forces of the building structural members computed in the analysis stage. A section is given to each structural member and the required dimensions and material properties in addition to the amount of steel reinforcement are calculated based on the applied forces.

Strength and stiffness are two essential parameters for every structural member. The stages of analysis and design are vitally important to understand how strength and stiffness of a member work together with the applied loads. To achieve appropriate strength and stiffness, the building should be analysed and designed based on limit states (Arya, 2009). When a building or a building member is not able to perform its intended function, it is assumed that it has reached a limit state (Wight and MacGregor, 2009). There are two categories of limit states: ultimate and serviceability (Arya, 2009). In the ultimate limit state, the building or its members should not experience failure when subjected to design loads (shear force, bending and torsional moments). Prevention of the loss of equilibrium, avoidance of the rupture of structural members and progressive collapse should be satisfied in the ultimate limit state (Wight and MacGregor, 2009). In the serviceability limit state, the structure should not lose its functionality because of vibration, excessive deflection or the occurrence of wide cracks (Bhatt et al., 2006).

The strength and stiffness given to a member during the design stage is based on the applied loads. It is worth noting that the investigation of a member's stiffness without considering applied loads may not represent reality unless the applied load on that member is negligible compared to its stiffness. Furthermore, it should be noted that understanding the stages of analysis and design of each building is crucial when assessing the potential damage caused by a newly constructed tunnel.

2.2.2 Slabs

Slabs are flat and horizontal structural elements that have small thickness in comparison to their spans. They form floors, roofs, stair cases and foundations in buildings and usually carry uniformly distributed loads perpendicular to the slab plane (Arya, 2009; Bhatt et al., 2006).

Structural slabs supported at two sides or having a length-to-width ratio of greater than or equal to 2 (or smaller than 0.5) act as beams and are called one-way slabs. Slabs supported on all sides or having length-to-width ratios smaller than 2 act as plates and are called two-way slabs. Bending in one-way slabs happens in one direction perpendicular to the supported edges whereas it occurs in both directions in two-way slabs (McCormac and Brown, 2014).

2.2.3 Beams

Beams are flexural structural members that have small cross sections compared with their spans and are supported at one or both ends. They withstand external loads generally acting at right angles to their longitudinal axis. The applied external loads create internal shear forces and bending or torsional moments in the beam (Ghoneim and El-Mihilmy, 2008).

Bending moments are created in a beam by the applied vertical loads that do not have eccentricity with respect to the beam longitudinal centreline. When a load with an eccentricity is applied to the beam, torsional moments in addition to bending moments are created. This happens in a building when the slabs on both sides of the beam are of different spans, if it is a curved beam, or an edge beam where there is a slab only on one side of the beam (McCormac and Brown, 2014).

From a geotechnical perspective, when analysing soil-structure interaction problems, buildings have often been represented as beams (Franzius et al., 2006; Pickhaver et al., 2010; Potts and Addenbrooke, 1997). In the majority of the cases where buildings were modelled as beams, the weight of the structure was excluded from the analysis and the focus was mainly on the bending and axial stiffness of the building (mostly the bending stiffness). However, building stiffness has not been estimated based on all relevant parameters. Therefore, a detailed explanation of beam bending stiffness is presented in this section with a discussion about all the parameters that have an effect on bending stiffness.

By definition, stiffness is the resistance of a member against deformation, or it is the structure's ability to resist changes in shape (Beer et al., 2012; Gere and Goodno, 2009; Young and Budynas, 2002). Bending stiffness is the resistance of a structure or a structural member against bending deformation, axial stiffness is the resistance against axial deformation, and torsional stiffness is the resistance against twisting. Practically, stiffness is the reaction force required to create a unit displacement along a direction while all other displacements are constrained. This can be rephrased as the ratio of the load applied to a member to the created deformation in that member, as expressed by Equation 2.1 (Baumgart, 2000).

$$\mathrm{K} = \frac{P}{\Delta} \tag{2.1}$$

where K is the stiffness, P is the force applied to a member and Δ is the deflection produced by the applied force.

Mathematically, bending stiffness of a beam loaded with a simple force can be derived from its deflection equation, i.e. Equation 2.2, where y is the deflection, x is the distance along the beam, $\frac{d^2y}{dx^2}$ is the curvature, $M(x)$ is the moment at any point along the member, and EI is the flexural rigidity of the beam cross section. The essential parameters on which the stiffness of a beam depend are the material elastic modulus, E, the cross sectional moment of inertia, I, and the applied moment, M, to the beam, which is based on the applied force, P, beam length, L and the boundary condition. The equation of the elastic curve and the maximum deflection of simple beams can be found in various books of mechanics of materials. The analytical equation of a beam's bending stiffness can be expressed by Equation 2.3.

$$\frac{d^2y}{dx^2} = \frac{M(x)}{EI} \tag{2.2}$$

$$K_b = F_K \times \frac{EI}{L^3} \tag{2.3}$$

where K_b is the bending stiffness, and F_K is a factor that depends on the boundary condition of the beam and the applied force. This form of equation is based on concentrated forces, P, or equivalent total forces when having distributed loads, $w = \frac{P}{L}$ for a rectangular distributed load and $w = \frac{2P}{L}$ for a triangular distributed load. In addition, Δ represents the maximum value of the deflection along the beam. Figure 2.2 displays the value of F_K for several types of beams.

The product of material elastic modulus and cross sectional moment of inertia, EI, is called flexural rigidity of a cross section. This parameter has a proportional effect on the bending stiffness of a beam. The effect of EI is opposite to that of the length since the length is inversely proportional and raised to the power 3, hence it has a considerable effect on the value of bending stiffness. For the same flexural rigidity, a beam with a short span has a considerably greater bending stiffness than a beam with a long span.

In addition, the boundary condition of the beam plays an important role in the resistance of that member against deformation. A simply supported beam, as shown in Figure 2.2a, has a significantly smaller bending stiffness than that of a beam with a fixed boundary at both ends, as shown in Figure 2.2c. As the beam boundaries approach a fixed condition, the

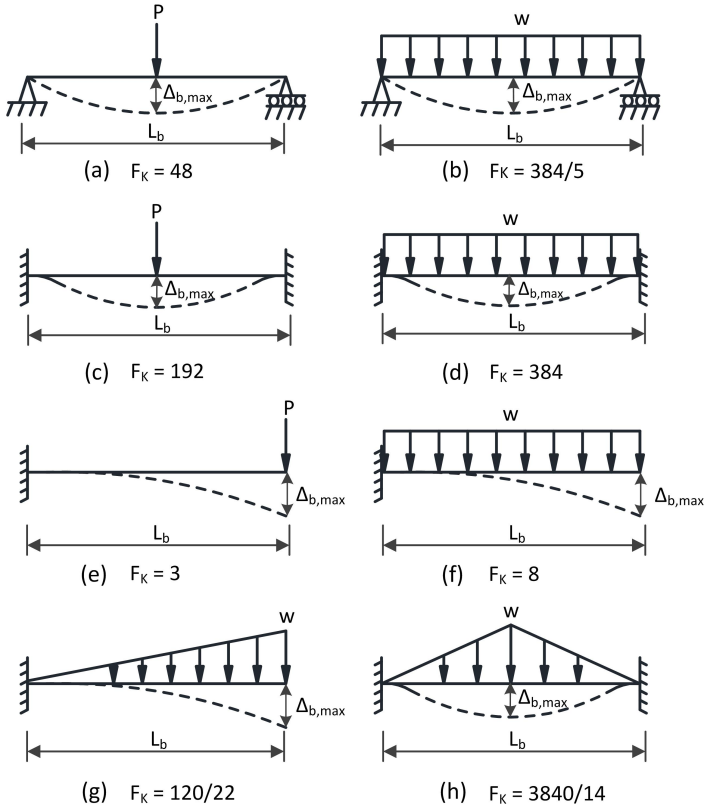

Fig. 2.2 Values of F_K (in Equation 2.3) for different types of beams under maximum deflection

rotation of the beam (at the supports) becomes more restricted, which in turn leads to the reduction of the deflection and the increase of bending stiffness. A beam with a high value of flexural rigidity and a short span that is allowed to rotate at its boundaries will have a small bending stiffness (which will depend on the degree of the rotation allowance by the boundaries).

Another important parameter of the beam bending stiffness is the type of the applied force. The equation for moment in a beam depends on the boundary conditions and the applied forces. For similar boundary conditions, bending stiffness increases as the load type approaches a uniform distribution. For instance, a beam fixed at both ends and loaded with a concentrated force at the middle, as shown in Figure 2.2c, has a smaller bending stiffness than that of the same beam loaded with a triangular shaped distributed force, as shown in Figure 2.2h. When the beam is subjected to a uniformly distributed load, as shown in Figure 2.2d, the bending stiffness will become greater than that of the other mentioned cases.

2.2.4 Columns

Columns are generally vertical members mainly designed to resist axial compressive forces, but which are sometimes also subjected to bending moments (Hibbeler, 2012). Columns support the floors and the roof, and transfer their weight to the subsoil. Columns are essential members in a framed building, and many structural failures have been related to the failure of columns (Ghoneim and El-Mihilmy, 2008).

Columns are designed either as short or long (slender) columns. Compressive behaviour is dominant in short columns which makes them axially strong. As the column length increases, bending deformations are produced due to the creation of secondary moments. If these secondary moments are of significant magnitude that decrease the axial capacity of the column, the column is categorised as a long or a slender member (McCormac and Brown, 2014; Wight and MacGregor, 2009). The load capacity of a column is inversely proportional to the slenderness ratio. The slenderness ratio is a function of the column dimensions (the height and the cross sectional geometry), radius of gyration and the end restraint conditions (Arya, 2009; Ghoneim and El-Mihilmy, 2008).

Axial stiffness is an essential parameter in columns because they are mainly subjected to axial forces. The axial stiffness is (Gere, 2004):

$$K_a = \frac{(EA)_{col}}{L_{col}} \tag{2.4}$$

where K_a is the axial stiffness, $(EA)_{col}$ is the axial rigidity of the column, A is the cross sectional area and L_{col} is the column length.

2.3 Building Foundations

Generally, a foundation is defined as the part of a structure which carries the superstructure and transfers the structural load to the underlying soil. The foundation should be designed to avoid over-stressing the soil which can cause damage to the structure due to excessive settlement or soil shear failure (Das, 2010). There are various kinds of foundations divided into two main groups: shallow and deep foundations, with different design methods. A brief explanation of foundation types and design methods are presented in the following sections.

2.3.1 Shallow foundations

Foundations that support structures at a shallow depth below the surface are called shallow foundations. There are different views about the definition of shallow foundations. Some authors have defined a shallow foundation as one having a depth equal to or less than its width (Bowles, 1997; Kimmerling, 2002) while others have defined it as having an embedment depth of less than or equal to 3 to 4 times its width (Das, 2010). Shallow foundations include spread footings, strap footings, combined footings and raft foundations (Murthy, 2007). Each type of shallow foundation is briefly explained below.

A **spread footing** is simply an enlargement of the base of a column or a wall to distribute the structural load over a wider area (Das, 2010; Murthy, 2007). A spread footing may support a single column (single or pad footing) or a wall (strip footing), and can be square, rectangular or circular. Figure 2.3a is an example of a pad footing.

Spread footings are mainly designed for downward compressive forces, P, which are distributed over a soil area and create a bearing pressure at the bottom of the foundation. The force tends to be applied to the centroid of the footing in order to obtain a more uniform pressure (Figure 2.3b) and an even settlement at the base of the foundation (Coduto, 2001). For a footing subjected to an eccentric force in which the applied force does not act at the foundation centroid, the pressure at the base of the footing will not be uniform, as shown in Figure 2.3c, and the allowable ground bearing pressure will be a function of the eccentricity.

It can be said that in reality, the soil pressure beneath a footing is not uniform; it is dependent on the footing rigidity and the underlying soil (Bowles, 1997). For example, when the footing rests on a loose sand, the grains close to the edges will displace laterally while the

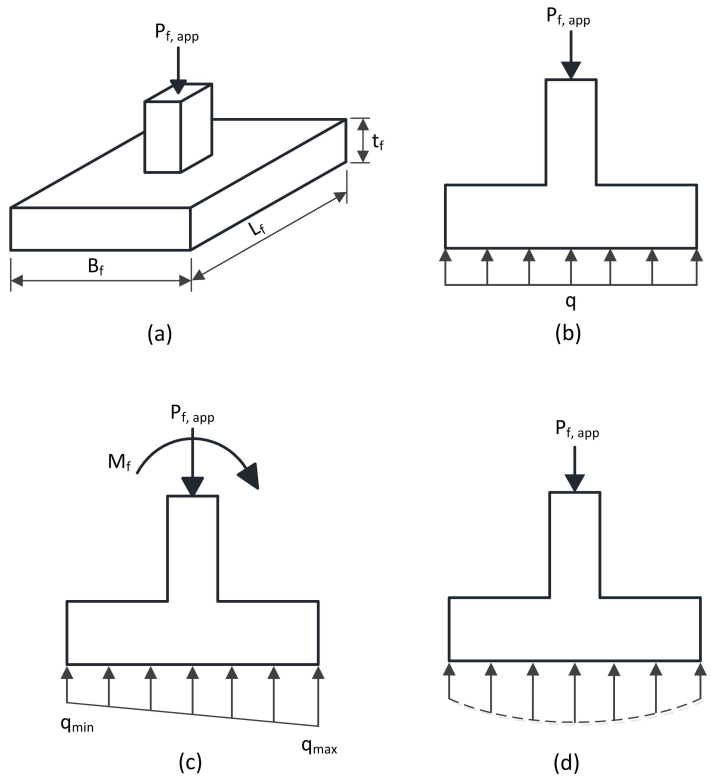

Fig. 2.3 Single footing: (a) typical pad footing, (b) uniform soil pressure, (c) non-uniform soil pressure, and (d) non-linear real soil pressure

soil under the footing centre is approximately confined. This produces a larger soil pressure under the middle of the footing compared to the edges, as shown in Figure 2.3d.

A **strap (cantilever) footing** is a rigid beam that connects an eccentrically loaded column footing to an interior column footing, as shown in Figure 2.4a. A strap footing can be an alternative for a combined footing if the allowable bearing capacity of the soil is great and the span between the columns is large (Das, 2010). The function of a strap footing is to transfer the moment created by the eccentricity in a footing to another interior footing in a way that a uniform soil pressure is obtained at the base of both footings (Bowles, 1997).

A **combined footing** is a type of foundation that supports two or more neighbouring columns on the same line, as shown in Figure 2.4b. Combined footings are used when columns cannot be placed at the centroids of spread footings due to the unavailability of an authorised land, or when the spread footings are so large that they are significantly close to each other. When the permitted land is not available for the expansion of a spread footing, eccentricity will happen which leads to a non-uniform soil pressure (Bowles, 1997; Das,

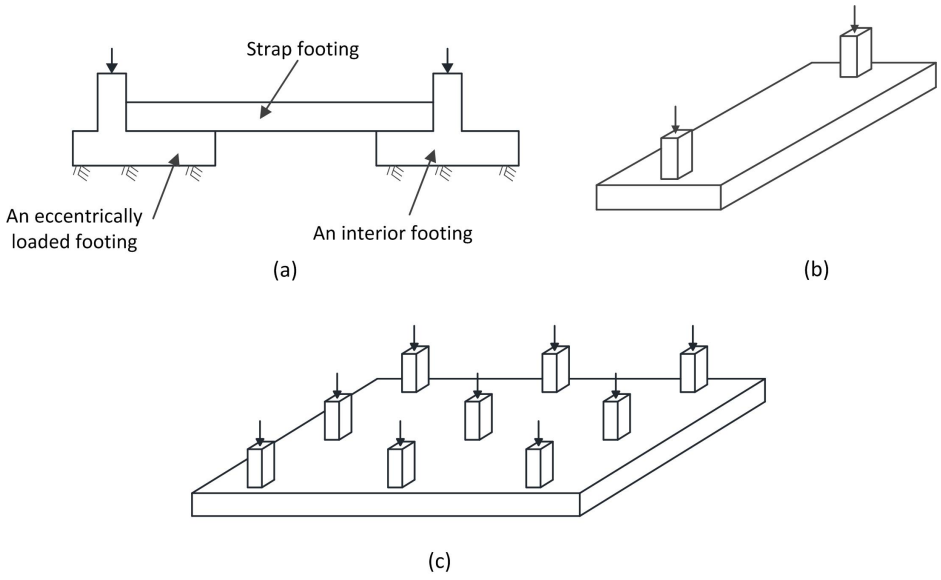

Fig. 2.4 Typical types of (a) strap, (b) combined and (c) mat footings

2010; Murthy, 2007). For the design of combined footings, rigid, flexible or numerical design methods can be used which are explained later in Section 2.3.3.

A **mat foundation** is a large footing that supports several columns in different rows, as shown in Figure 2.4c. Mat foundations are used when columns are subjected to such great loads that they need significantly large spread footings, when the soil conditions are considerably poor, or when the foundation is below the ground water level to provide a waterproof barrier (Bowles, 1997; Coduto, 2001).

There are different types of mat foundations including those with uniform thickness, flat plates thickened under the columns and flat plates with pedestals. In addition, mat foundations may be supported by piles in highly compressive soils to reduce building settlement. These foundations are called piled mats and they are a combination of shallow and deep foundations (Bowles, 1997; Coduto, 2001; Das, 2010). Mat foundations can be designed by rigid, flexible or numerical methods (Section 2.3.3).

2.3.2 Modulus of subgrade reaction

Modulus of subgrade reaction can be defined as the relationship between the applied pressure to a soil and the created deflection, expressed by the Winkler Equation (Equation 2.5) (Bowles, 1997). It is worth mentioning that k_s in Equation 2.5 is assumed to be independent of the

value of q_s, and has a uniform value at every point on the soil surface under the foundation (Murthy, 2007).

$$k_s = \frac{q_s}{\delta_s} \tag{2.5}$$

where k_s is the modulus of subgrade reaction, q_s is the soil pressure (or the subgrade reaction) and δ_s is the soil deflection.

The modulus of subgrade reaction can be estimated either experimentally or empirically. Amongst the experimental methods, the plate load test is a popular method which was proposed by Terzaghi (1955) to estimate the modulus of subgrade reaction based on a 305 mm square rigid plate placed on a soil medium. The test is performed by applying a specific load on the plate and measuring the soil deflection at each load increment to obtain the stress-deflection curve. The value of the modulus of subgrade reaction of the plate can be converted to that of the real foundation using Equations 2.6 and 2.7 for square and rectangular foundations, respectively.

$$k_{s,sq} = k_{s,p} \times \left(\frac{B_f + b_p}{2B_f} \right)^2 \tag{2.6}$$

$$k_{s,rec} = k_{s,p} \times \frac{1 + \frac{B_f}{L_f}}{1.5} \tag{2.7}$$

where $k_{s,sq}$ and $k_{s,rec}$ are moduli of subgrade reaction of square and rectangular foundations, respectively, $k_{s,p}$ is the modulus of subgrade reaction of the plate, B_f and L_f are the width and the length of the foundation, respectively, and $b_p = 0.305$ m is the width of the test plate.

The modulus of subgrade reaction is significantly affected by the size, shape and embedded depth of the plate. Das (2010) stated that square plates are occasionally used nowadays. Instead, a circular plate of 25 mm thickness with a diameter from 150 mm to 762 mm is used. Bowles (1997) explained that achieving a reasonable value of k_s with a big plate is very difficult due to the requirement of a large reaction force. In addition, for even small plates of about 450 mm to 750 mm diameter, k_s is difficult to be defined since the plate will not be stiff enough to behave rigidly. Furthermore, the assumptions of: (1) the soil in the influenced zone below the test plate is comparable to the soil layers in deeper zones below the foundation, and (2) relying on the short term settlement while clayey soils have long term (consolidation) settlement make the results more unreliable (Coduto, 2001; Murthy, 2007).

In addition to the mentioned method, the consolidation test (for an elastic soil acting as a spring), California Bearing Ratio (CBR) and Triaxial tests can also be used to estimate the modulus of subgrade reaction (Dutta and Roy, 2002; Huang, 2004; Naeini et al., 2014).

Different empirical methods for the estimation of the soil subgrade reaction have been proposed in the literature. After Winkler (1867) proposed Equation 2.5 to estimate the modulus of subgrade reaction, Biot (1937) elucidated that foundations are rarely dealt with based on the modulus of the subgrade reaction, k_s, achieved from stress-deflection curves. Instead, it should be investigated based on the two elastic parameters of Young's modulus, E_s, and the Poisson's ratio, ν_s. For the soil-foundation interaction problem, he analysed two models of Winkler and elastic continuum in order to evaluate k_s based on the elastic parameters of E_s and ν_s. Vesic (1961) analysed two similar models to Biot (1937) and defined a correlation for estimating the value of k_s by equating the maximum deflection of the analysed beam in both models.

Vlasov and Leont'ev (1966) proposed a two parameter model to eliminate the Winkler problem of having a uniform load on the foundation. Their estimation of the modulus of subgrade reaction was dependent on an elastic medium where the horizontal stresses were negligible. Bowles (1997) stated that since the value of E_s may not be easily available, other approximations can be done for the calculation of k_s. This is because the stiffness of the foundation is significantly higher than that of the soil and some reasonable approximations to the value of k_s will not have a considerable effect on the foundation bending moment and the calculated soil pressure.

2.3.3 Shallow foundation design methods

There are different design methods for combined and mat foundations: rigid, flexible and numerical methods. Each method is briefly explained below.

In **rigid foundation design methods**, it is assumed that the foundation is so rigid that it can span any underlying soil non-uniformities. Additionally, the foundation base pressure is presumed to be uniform or linearly variable, as shown in Figure 2.5a. It is worth mentioning that differential settlements are very small in rigid foundations but the induced bending moment and shear forces are high (Gupta, 1997).

This design method is easy to apply and hand calculations can be used without the aid of computer programs. However, there are some drawbacks related to this method. For instance, there are several approximations in the method: columns should be in a uniform pattern and the mat should be very rigid (Bowles, 1997; Ghoneim and El-Mihilmy, 2008).

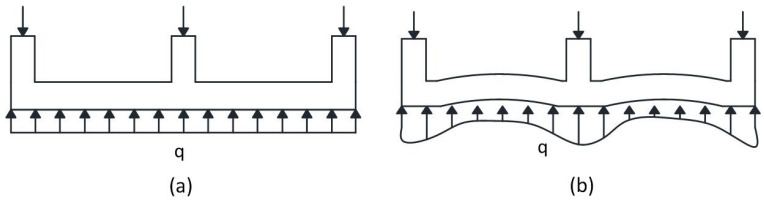

Fig. 2.5 Soil pressure distribution under (a) rigid and (b) flexible footings

The assumptions of infinite rigidity of the footing and uniform or linear variation of the soil pressure under the footing lead to unreliable computations of shear, moment and deformations in the mat foundation. In reality, the soil pressure is larger under the columns and smaller in the other zones, as shown in Figure 2.5b (Coduto, 2001).

The **flexible foundation design methods** assume that the soil consists of an infinite number of elastic springs. This is sometimes called the Winkler foundation as it is the classical Winkler solution (Bowles, 1997). The elastic constant of the springs is the elastic property of the soil which is called the coefficient or modulus of subgrade reaction, k_s. This method deals with both beams and plates on elastic foundations. Beam theory is used for foundations having one way deformations, while plate theory is used for foundations with a two-way response.

In the approach of beams on an elastic foundation, it is assumed that a beam is supported by an elastic foundation along its complete length. When the beam is subjected to an external load, the reaction forces of the foundation will be proportional at every section to the deflection of the beam at that section. Based on these conditions, the soil reaction per unit length of the beam can be expressed by $k_s y_b$, where y_b is the deflection of the beam (Timoshenko, 1940). In the case of having a plate on an elastic foundation, the deformations along the width of the footing should also be considered. A plate or a slab can be defined as a structure expanding in two dimensions. They can be rectangular or circular in shape. Rao (2011) presented three cases (based on the ratio of the foundation length, L_f, to width, B_f) to be considered in the analysis of a footing. If $L_f/B_f > 5$, the footing behaves as a beam. If $L_f/B_f < 3$, the footing acts as a plate. If $3 < L_f/B_f < 5$, the footing can be analysed as either a plate or a beam. Timoshenko and Woinowsky-Krieger (1959) outlined three types of plate analysis: thin plates with small deflections, thin plates with large deflections, and thick plates. Thin plates can be analysed as 2D problems while thick plates should be analysed as a 3D problem.

The classical solution of a Winkler foundation assumes that the closely spaced springs of the foundation are completely independent of each other and there is no continuity in the

foundation due to the lack of interaction between the springs, as shown in Figure 2.6a. Based on this, if a beam is subjected to an external load distributed over a specific length, the soil beyond the loaded zone will not be influenced (Rao, 2011). However, this approach has been broadly used in practical cases and has shown good agreement with real measurements for cases where there is a beam with an infinite length, such as railway tracks (Selvadurai, 1979; Timoshenko, 1940).

The basic differential equation of the Winkler's solution is expressed by Equation 2.8 (Bowles, 1997).

$$(EI)_f \cdot \frac{d^4 y_b}{dx^4} = q_{app} = -k_s B_f y_b \tag{2.8}$$

where $(EI)_f$ is the flexural rigidity of the foundation cross section.

In addition, an essential parameter, λL_f (Equation 2.9), is introduced during the solution of Equation 2.8 which can be used to decide whether a foundation should be analysed as rigid or flexible. Bowles (1997) proposed that the foundation is better to be analysed by the flexible approach if $\lambda L_f > \pi$, and by the rigid approach if $\lambda L_f < \frac{\pi}{4}$ where bending of the foundation is not considerably influenced by k_s. Furthermore, ACI-Committee-336 (2002) suggested that for a continuous footing, the rigid method can be used if the average of two adjacent spans in a continuous strip is less than $1.75/\lambda$, and the adjacent loads and column spacings are not different from each other by more than 20%.

$$\lambda = \sqrt[4]{\frac{k_s B_f}{4(EI)_f}} \quad OR \quad \lambda L_f = \sqrt[4]{\frac{k_s B_f L_f^4}{4(EI)_f}} \tag{2.9}$$

Researchers have proposed methods to add some interaction between the springs of the Winkler's foundation. Some researchers proposed two-parameter solutions to solve beams on elastic foundations. For example, Filonenko–Borodich (Rao, 2011) connected the tops of the springs by an elastic membrane subjected to a tension force to add shear interaction among adjacent points in the foundation, as shown in Figure 2.6b. Hetenyi (1946) and Hetenyi (1950) added an interaction among the independent springs by connecting their top ends with a beam in the 2D case and a plate in the 3D case (Figure 2.6b), with the assumption that the beam or plate is only subjected to bending deformations. Pasternak (1954) introduced shear interaction between the springs by adding a beam or a plate comprising incompressible vertical elements deforming only by transverse shear. Furthermore, Pasternak suggested another foundation model consisting of two spring layers connected by a shear layer, as shown in Figure 2.6c (Rao, 2011).

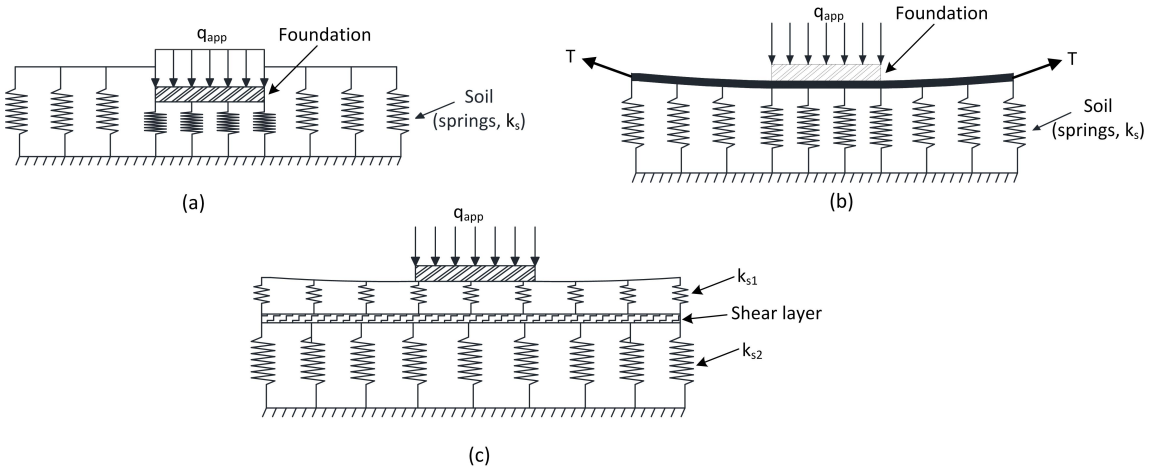

Fig. 2.6 Foundation types: (a) Winkler, (b) two-parameter and (c) Pasternak's models

The aforementioned two parameter models were based on adding shear interaction between the independent springs of a Winkler foundation. On the other hand, other researchers proposed two parameter foundation models based on the theory of an elastic-continuum. Reissner (1958) solved partial-differential equations of compatibility, constitutive relations and equilibrium to develop a simplified approach for the description of soil behaviour. His solution was based on two assumptions: the in-plane stresses are negligible throughout the foundation, and horizontal displacements at the upper and lower foundation surfaces are zero. The simplified method of Reissner (1958) was later extended by Horvath (1983) to consider the linear variation of E_s with depth.

Foundations can also be analysed using **numerical methods**. Since an analytical solution is not always achievable for all types of footings, numerical analyses become appropriate. There are analytical solutions for only a few cases of thick plates (Timoshenko and Woinowsky-Krieger, 1959). Furthermore, apart from circular plates subjected to axisymmetric external loading, the derivation of analytical solutions is not always possible for the other plate cases (Wang et al., 2005).

2.3.4 Piled foundations

Piles are structural members generally categorised as deep foundations. Their function is the conveyance of structural loads to lower soil layers (Bowles, 1997). Piles are mainly designed for axial loads, though they may be subjected to other types of forces such as uplift or lateral loads.

Piles can be classified in different ways. A classification method is based on the material type of the pile, such as timber, concrete, steel and composite (Prakash and Sharma, 1990). Another categorisation relates to the type of interaction between the soil and the pile, such as large displacement piles (solid sections), small displacement piles (rolled steel sections, bottom-opened tubes, hollow sections), and replacement piles created by drilling or other excavation methods (British-Standard, 1986; Tomlinson, 1994). Piles can also be categorised based on the way loads are transferred to the soil. This class includes end-bearing piles which transfer load through soft and weak soil layers to their ends which rest on a stiff/strong soil stratum, friction piles which transmit load to different layers of soil through the shear resistance along the shaft, and combined piles that are combinations between end-bearing and friction piles (Prakash and Sharma, 1990).

2.4 Stiffness of Buildings

In structural engineering, the stiffness of structural members are generally very significant. For the flexural members (i.e. beams and slabs), the bending stiffness should be sufficient to keep the deflection within an allowable range, even if the member has enough capacity to resist the applied forces. Excessive deflections can cause damage to nonstructural elements like partitions, doors and windows (Wight and MacGregor, 2009). It is worth mentioning that sufficient lateral stiffness should be provided to tall buildings to guarantee the safety of the building in both ultimate and serviceability limit states. Sudden collapse of the building should also be prevented in the ultimate limit state. Furthermore, nonstructural components like elevators and doors should work properly in addition to preventing load redistribution to non-bearing partitions (Smith and Coull, 1991). It should be mentioned that this type of stiffness (lateral) is not considered in the work of this thesis.

In soil–structure interaction, the focus is mainly on the bending stiffness of the building. Sometimes, axial stiffness of buildings is also considered however its importance is significantly less than that of the bending stiffness (Mair, 2013). The proposed methods in geotechnics to deal with the axial and bending stiffness of a building are presented later in Chapter 3.

2.5 Summary

This chapter briefly presented the type and function of the superstructure members in addition to the analysis and design stages of structural members which are important to comprehend

the global building behaviour. It is worth noting that the bending behaviour of beams was discussed in detail since the estimation of building stiffness in soil-structure problems is largely related to the behaviour of beams. A short explanation of foundation types and their design methods was also provided.

Chapter 3

Tunnelling and Tunnel-Soil-Building Interaction

3.1 Introduction

This chapter provides a review of tunnels and some consequences that arise from tunnelling. It covers the topics of tunnelling, tunnelling induced ground movements and their effects on existing buildings.

3.2 Tunnels

Tunnels are constructed for various reasons. Some essential factors include steep grades in mountainous areas, wide rivers, and developed cities with a lack of surface space. Tunnelling in urban areas poses many challenges because of the potential to adversely affect existing subsurface and surface structures (Kolymbas, 2005).

Over-excavation of soil and stress relief during tunnelling are possible causes that may lead to soil failure if sufficient support is not provided during the tunnelling process. In urban areas, the possibility of soil collapse is generally eliminated. The main focus is on controlling ground movements resulting from tunnelling. Analyses in this research consider the effect of tunnelling induced ground movements on existing structures, but a brief explanation of tunnel stability is also presented in Section 3.4 to outline how stability problems are generally treated.

Tunnelling in an area where there are no surface and subsurface structures is referred to as greenfield tunnelling. Figure 3.1 shows a general description of surface greenfield

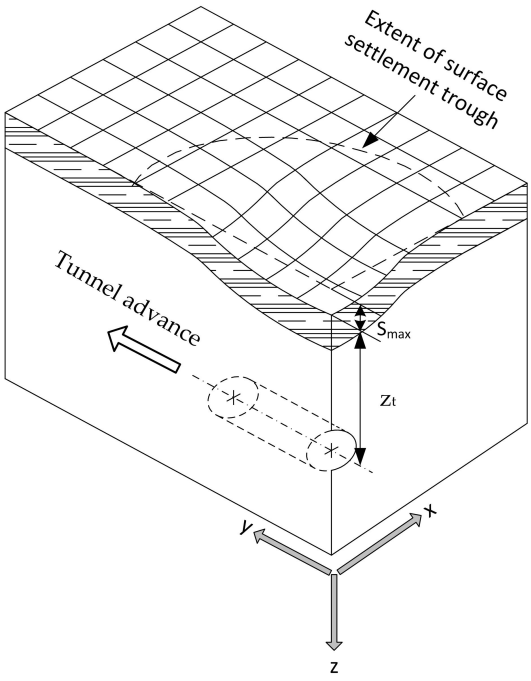

Fig. 3.1 Ground displacements created by tunnelling (after Attewell et al., 1986)

displacements due to tunnelling. It should be noted that tunnel construction is a 3D problem; however, engineers usually simplify it by considering 2D cross sections equivalent to transverse and longitudinal settlement troughs defined with respect to the axes of the tunnel (x- and y-directions, respectively in Figure 3.1) (Marshall, 2009).

3.3 Tunnel Excavation Techniques

Generally, a tunnel is first excavated for a specific length, then a support for the opening is provided and later, the excavated earth is removed. These steps can be performed using several tunnelling methods classified under two categories: the conventional (incremental) method and the continuous (TBM) method (mechanised) (Kolymbas, 2005). The selection of the excavation system depends on several parameters. In addition to financial and technical factors, the soil type, ground morphology, geology, hydrology and hydrogeology, soil physical and mechanical properties, its homogeneity, stress conditions and the section geometry play an important role in choosing the appropriate tunnelling technique (Lunardi, 2008).

Tunnel excavation by the conventional method includes blasting and mechanical excavation. More excavation choices are available with the mechanised methods, such as full face

rock cutters (TBM), shielded with single or double shield, simple shields, blade shields, compressed air shields, mixshields and earth pressure balanced (EPB) (Lunardi, 2008). Shields are steel tubes usually having circular cross sections (Kolymbas, 2005). Additionally, they can have either open or closed faces. Open face shields are used to excavate self-supporting soils; the tunnel face is not supported during excavation. For unstable ground conditions, the closed shield method is utilised which provides support for the tunnel face during excavation (Augarde, 1997). Support of the tunnel face can be provided by different methods, including slurry shields, earth pressure balance (EPB), and mix-shield multi-purpose (Lunardi, 2008). Nowadays, the utilisation of TBM for the tunnel construction is popular amongst geotechnical engineers since it leads to a significant reduction of the soil disturbance due to tunnelling which in turn provides more safety for existing buildings (Mroueh and Shahrour, 2008).

The tunnelling process produces different types of ground deformations. The soil around the tunnel face tends to move towards the tunnel opening due to stress relief. Radial relaxation of the soil surrounding the tunnel can also lead to ground deformations (Selby, 1999). In addition, the outer diameter of the lining is normally smaller than the outer diameter of the shield which creates a gap between the excavated soil and the lining, increasing the possibility of the creation of surface settlements. This gap should be filled with a material like mortar (Kolymbas, 2005). Other causes of ground settlements include soil over-cutting, lining deflection and soil consolidation (Mair and Taylor, 1997).

3.4 Tunnel Stability

An important point to be considered in tunnelling is the tunnel stability during construction. The stability becomes more essential when some tunnel areas are uncovered and need to be protected by lining. Figure 3.2a demonstrates an idealised cross section of a typical tunnel, and Figure 3.2b displays the tunnel heading. There are several factors affecting the stability of tunnels, such as the tunnel size, the progress rate of the excavation, the unsupported excavation length (L_{exc}, Figure 3.2b), the cover to diameter ratio of the tunnel (C_t/D_t, Figure 3.2b), the type of the soil, the existence of water pressure, the construction method and permeability of the soil (Mair and Taylor, 1997).

Tunnel stability can be evaluated based on undrained or drained conditions. Broms and Bennermark (1967) stated that the short–term stability of tunnels in clays was mostly controlled by the undrained shear strength, c_u. They proposed the concept of stability ratio, N_{tun}, to evaluate the undrained stability of a tunnel:

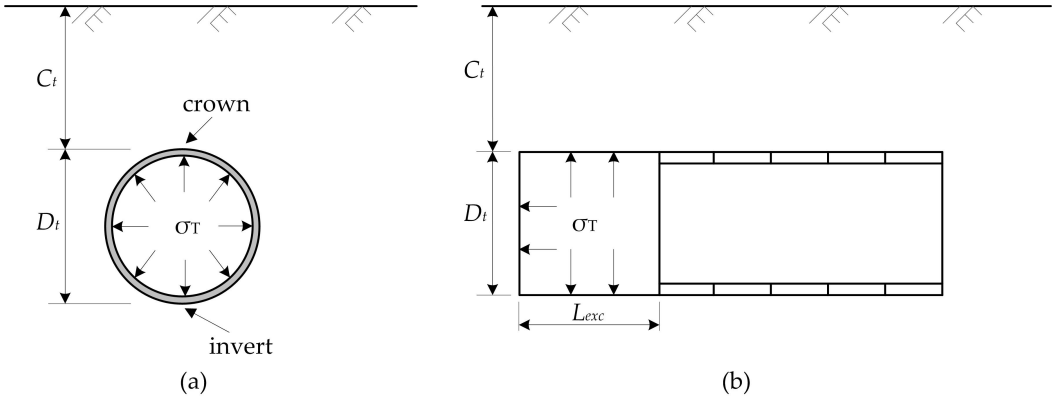

Fig. 3.2 (a) Idealised cross-section of a typical tunnel, (b) tunnel heading (after Mair and Taylor, 1997)

$$N_{tun} = \frac{\gamma_s z_t}{c_u} \tag{3.1}$$

where γ_s is the soil unit weight, z_t is the depth from the ground surface to the tunnel axis, and c_u is the undrained shear strength of soil before excavation. In order to include the effect of internal tunnel pressure and surcharge, Broms and Bennermark (1967) expressed the equation of undrained tunnel stability ratio as:

$$N_{tun} = \frac{\sigma_{sur} + \gamma_s z_t - \sigma_T}{c_u} \tag{3.2}$$

where σ_{sur} is the surface surcharge weight and σ_T is the support pressure of the tunnel.

High values of stability ratio lead to low stability of the tunnel. According to the stability equation, soils with low undrained shear strength, low tunnel support pressure and/or large surcharge weights need more attention as they result in large values of stability ratio. Based on laboratory tests and field observations, Broms and Bennermark (1967) found that the failure stability ratio, $N_{tun,c}$, was 6.0 (from Equation 3.2), which was also confirmed by Peck (1969). Based on centrifuge test results, Mair (1979) and Kimura and Mair (1981) presented some influential factors affecting $N_{tun,c}$, such as the unsupported length of excavation (L_{exc}, Figure 3.2) and cover to diameter ratio of the tunnel (C_t/D_t, Figure 3.2). Kimura and Mair (1981) defined a load factor, LF, as the ratio of the tunnel stability to the failure stability:

$$LF = \frac{N_{tun}}{N_{tun,c}} \tag{3.3}$$

Failure happens when the load factor is equal to one.

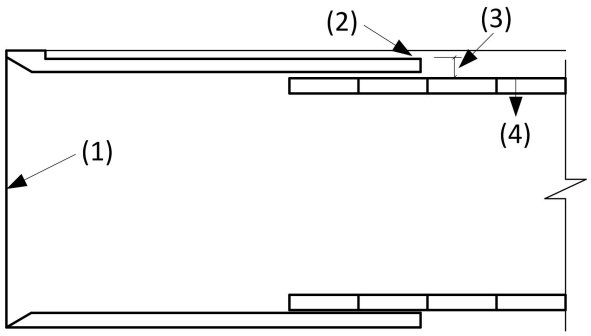

Fig. 3.3 Main components of ground movements associated with shield tunnelling (Mair and Taylor, 1997)

With regard to drained stability, Atkinson and Potts (1977) suggested an equation to estimate the collapse pressure of tunnels in granular soils. Their derivation was based on kinematic upper and lower bound plasticity solutions assuming perfectly plastic behaviour. Using a lower bound solution with the assumptions of no surcharge load and a non-weightless soil, they provided equations to obtain the required pressure to maintain tunnel stability (σ_T). They also presented equations for the case of a weightless soil having a surcharge weight (σ_{sur}).

3.5 Volume loss

During the construction of a tunnel, the soil in the surrounding area tends to move towards the tunnel cavity. This soil movement creates a ground loss. Different reasons for the occurrence of the ground loss are mentioned in the literature. Mair and Taylor (1997) listed 5 main reasons for the occurrence of ground movements due to shield tunnelling, 4 of which are shown in Figure 3.3. The sources are (1) face loss due to stress relief, (2) over-excavation of the tunnel cross section due to machine yawing which leads to radial soil movements, (3) the existence of a gap between the shield tail and the lining which leads to radial soil movements, (4) lining deflection due to ground load development, and (5) the occurrence of soil consolidation due to the change in pore water pressure.

The term volume loss or ground loss is used to quantify the amount of extra-excavation of the tunnel cross section. In undrained clays (short term), the displaced soil volume is assumed constant; the amount of ground loss that occurs at the tunnel (V_{lt}) is the same as that occurs in the soil (V_{ls}). However, the value of V_{lt} is different from that of V_{ls} in sands due to the occurrence of contraction or dilation of the soil during tunnelling (Marshall et al., 2012;

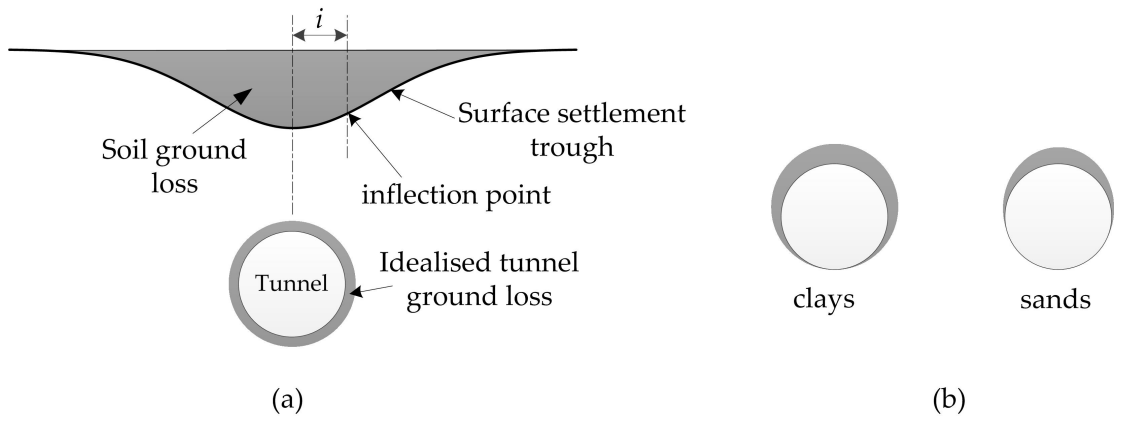

Fig. 3.4 (a) Typical soil and tunnel volume losses (after Franza, 2016), (b) distribution of tunnel volume loss in clays (Loganathan and Poulos, 1998) and sands (Zhou, 2014)

Vorster et al., 2005). Figure 3.4a shows the tunnel and soil ground losses. In plane-strain conditions, the soil volume loss (V_{ls}) is the ratio of the area of the settlement trough (V_s, soil volume per unit length) to the original tunnel area (A_t):

$$V_{ls} = \frac{V_s}{A_t} \quad (\%) \tag{3.4}$$

The tunnel volume loss (V_{lt}) is the ratio of the volume of the over-excavated soil per unit length (ΔV) to the original tunnel area:

$$V_{lt} = \frac{\Delta V}{A_t} \quad (\%) \tag{3.5}$$

In numerical and analytical solutions for tunnelling induced ground movements, different scenarios have been used to distribute V_{lt} over the tunnel cross section. Early researchers assumed a uniform contraction of the tunnel to produce ground displacements (Sagaseta, 1987). Some researchers only depended on the produced ground loss at the soil surface, disregarding the deformation shape of the tunnel (Franzius et al., 2006; Potts and Addenbrooke, 1997). These modelling methods did not simulate the actual distribution of the tunnel volume loss. Centrifuge modelling showed that there were little induced ground displacements at the tunnel invert (Mair, 1979). Loganathan and Poulos (1998) explained that in clays, the tunnel contracts according to an approximately oval shape shown in Figure 3.4b. Loganathan et al. (2001) confirmed that the shape of the tunnel face was elliptical and the lateral ground displacement into the tunnel opening was not uniform. They demonstrated that a downward movement of soil occurred at the sides of the tunnel as a result of the weight of soil at the

tunnel crown. This led to the reduction of upward soil displacements below the tunnel. This type of volume loss distribution was also used by other researchers in the field of numerical analyses (Cheng et al., 2007). With regard to sands, centrifuge experiments have shown that the ground loss is mainly concentrated at the tunnel crown, as shown in Figure 3.4b (Marshall, 2009; Zhou, 2014).

Mair and Taylor (1997) reviewed the settlement data provided in the literature for bored tunnelling, and presented the following approximate estimates of volume losses in different situations:

1. In stiff clays such as London clay, the magnitude of volume loss was generally between 1% and 2% when open face tunnelling was used.

2. Sprayed concrete lined (SCL) tunnelling in stiff clays generally resulted in volume losses between 0.5% and 1.5%.

3. Earth pressure balance (EPB) or slurry shields provided a high degree of settlement control, leading to volume losses of 0.5% in sands and 1% to 2% in soft clays

3.6 Greenfield Ground Displacements due to Tunnelling

An accurate prediction of ground movements due to tunnelling is crucial to assess the effects of tunnelling on structures. Different methods have been proposed to estimate tunnelling induced ground displacements. The methods consist of empirical and analytical relations, experimental tests, and numerical analyses. Explanation of different prediction methods is presented in the following sections.

Empirical relations are popular with engineers to predict tunnelling induced ground movements. Section 3.6.1 presents available empirical methods and also explains terms used in the field of tunnelling induced ground displacements. Chapter 7 of this thesis adopts a semi-analytical method fitted to centrifuge data to create ground displacements. Sections 3.6.2 and 3.6.4 present a review of the analytical and experimental methods, respectively, to predict ground deformations. Additionally, numerical methods, which are used in Chapters 7 and 8, are explained in Section 3.6.3. A discussion of some features of the mentioned methods for estimating ground displacements is also presented within this chapter.

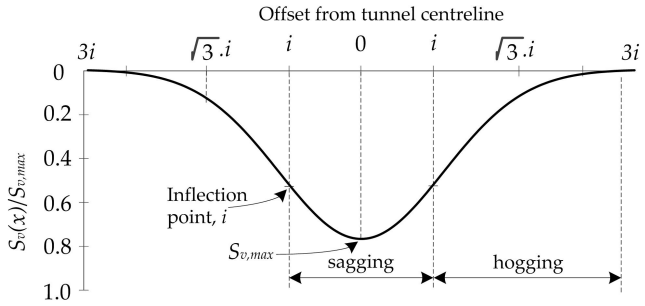

Fig. 3.5 Gaussian settlement trough

3.6.1 Empirical relations

Transverse vertical settlements

Peck (1969) and Schmidt (1969) were the first to propose the Gaussian distribution curve described by Equation 3.6 to approximate the transverse ground settlement due to tunnelling. Figure 3.5 shows a typical settlement trough described by a normal (Gaussian) distribution curve. The Gaussian equation does not have any theoretical basis; the suitability of the curve to predict settlements has been supported by case studies, centrifuge modelling and numerical analyses (Farrell, 2010). Loganathan and Poulos (1998) stated that the main reasons for the utilisation of the Gaussian curve are its simplicity and good ability to fit to settlement profiles created by tunnelling.

$$S_v(x) = S_{v,max} \cdot \exp\left(-\frac{x^2}{2i^2}\right) \tag{3.6}$$

where $S_v(x)$ is the vertical settlement, $S_{v,max}$ is the maximum ground settlement occurring at the tunnel centreline, x is the horizontal offset from the tunnel centreline, and i is the horizontal distance from the tunnel centreline to the inflexion point of the surface settlement trough. The volume of the surface settlement trough per unit length, V_s, is determined by integrating Equation 3.6. Additionally, the first derivative of Equation 3.6 gives the slope of the Gaussian curve, and the second derivative gives the curvature (Marshall, 2009).

Celestino et al. (2000) noticed that the Gaussian curve did not fit the ground settlement when having large volume losses. They stated that the displacement results given by Gaussian curve were lower than the real displacement values. To achieve a better fit, they proposed a three parameter relationship by utilising yield-density curves. Furthermore, Jacobsz et al. (2004) found that settlement troughs achieved from centrifuge tests were narrower than Gaussian settlement troughs.

Vorster et al. (2005) suggested a modified description of the Gaussian curve (Equation 3.7) and added a parameter, α_{vor}, to make sure that parameter i remains as the distance to the inflexion point. The addition of α_{vor} allows the inflection point to vary in the vertical direction. The surface volume of the modified Gaussian curve is obtained from the integration of Equation 3.7 (Marshall, 2009).

$$S_v(x) = \frac{n_{vor}}{(n_{vor}-1)+\exp(\alpha_{vor}(\frac{x}{i})^2)} \cdot S_{v,max} \tag{3.7}$$

$$n_{vor} = e^{\alpha_{vor}} \frac{2\alpha_{vor}-1}{2\alpha_{vor}+1} + 1 \tag{3.8}$$

where n_{vor} is the shape function parameter that controls the profile width.

Transverse horizontal displacements

It should be mentioned that tunnelling induced vertical movements are of larger magnitude than horizontal and generally pose more potential for damage to structures (Marshall, 2009). However, it is observed from specific cases that horizontal movements may cause an increase to the damage level of structures (Franza, 2016).

O'reilly and New (1982) presented a relationship (Equation 3.9) to estimate horizontal ground displacements related to the construction of tunnels in undrained clay. They assumed that the volume loss was constant, the direction of the soil displacement vectors was towards a point on the axis of the tunnel and the trough width did not change with depth.

$$S_h(x) = \frac{x}{z_t - z} \cdot S_v(x) \tag{3.9}$$

where $S_h(x)$ is horizontal ground displacements.

Attewell and Yeates (1984) provided an equation to estimate horizontal displacements based on the assumption of displacement vectors pointing to the tunnel axis in cohesive soils, and orienting towards a point below the tunnel axis in granular soils. Based on the assumption of displacement vectors directing towards the centreline of the tunnel, Taylor (1995b) also suggested an equation to compute horizontal displacements. Grant and Taylor (2000) reported that the equation proposed by Taylor (1995b) resulted in predictions that agreed with centrifuge test results in clay.

Longitudinal ground settlements

The 3D deformation field shown in Figure 3.1 is formed by the longitudinal and the transverse troughs together. Attewell and Woodman (1982) explained that a cumulative probability function can be assigned to the transverse settlement trough along the tunnel centreline in order to obtain ground settlements in the longitudinal direction. They assumed that the vertical settlement above the tunnel head reaches 50% of the maximum ground settlement. The proposed relationships to describe longitudinal displacements using Gaussian equation are expressed by:

$$S_v(x,y) = \frac{S_{v,max}}{2}\exp\left(-\frac{(x-x_t)^2}{2i^2}\right)\left(\text{erf}\left[\frac{(y-y_i)}{\sqrt{2}i}\right] - \text{erf}\left[\frac{(y-y_f)}{\sqrt{2}i}\right]\right) \tag{3.10}$$

$$S_l(x,y) = \frac{i\cdot S_{v,max}}{\sqrt{2\pi}z_t}\exp\left(-\frac{(x-x_t)^2}{2i^2}\right)\left(\exp\left[-\frac{(y-y_i)^2}{2i^2}\right] - \exp\left[-\frac{(y-y_f)^2}{2i^2}\right]\right) \tag{3.11}$$

where $S_v(x,y)$ and $S_l(x,y)$ are the vertical and longitudinal ground displacements, and erf is the error function given by Equation 3.12.

$$\text{erf}(z) = \frac{2}{\pi}\int_0^z e^{-t^2}dt \tag{3.12}$$

Variation of trough width

As explained before, the trough width is usually described by i which is the distance of the inflection point on the transverse settlement curve to the tunnel centreline, as shown in Figure 3.5. Researchers proposed different equations to estimate i. Based on centrifuge data for dry sands, Atkinson and Potts (1977) proposed an equation to relate i to the tunnel diameter (D_t) and the soil cover above the tunnel crown (C_t). Clough and Schmidt (1981) and Mair et al. (1982) connected the trough width to two parameters of tunnel diameter and depth in order to estimate i in soft clays. Additionally, depending on 19 case studies of tunnelling in clay, O'reilly and New (1982) plotted i against z_t and obtained a linear relation to calculate i. It is worth noting that O'reilly and New (1982) introduced the trough width parameter, K_t, to estimate i as: $i = K_t z_t$. They stated that K_t could change between 0.4 and 0.7 for stiff and soft clay, and $K_t = 0.5$ was convenient for most design purposes. Additionally, they suggested a value of 0.2–0.3 for sands above the water table. Mair and Taylor (1997) recommended a value of $K_t = 0.5$ for clays and 0.25–0.45 for coarse grained soils.

Mair et al. (1993) reported that the subsurface settlement due to tunnelling can be described by the Gaussian curve in the same way as the surface settlement. The subsurface settlement trough becomes progressively narrow with depth. Jacobsz (2002) and Farrell (2010) also agreed with that the trough width generally becomes linearly narrower with depth. To take into account the narrowness of the trough width with depth, Mair et al. (1993) suggested calculating i as: $i = K_t(z_t - z)$. They also proposed an equation to estimate K_t based on reviewing field data and centrifuge test results for clay. It should be noted that Mair et al. (1993) disregarded the effect of the tunnel size in their work. This led to erroneous prediction of deformations close to the tunnel (Marshall, 2009). The effect of the tunnel size on the settlement trough width was considered by Moh et al. (1996). Sugiyama et al. (1999) also took into account the tunnel size as well as the cover to diameter ratio (C_t/D_t) in their proposed equations to estimate i.

Heath and West (1996) explained that although the Gaussian distribution curve is a good tool for the surface settlement prediction, it has limitations for the prediction of subsurface displacements due to the lack of a connection between the settlement trough width and the depth below the ground level. They stated that the binomial distribution can be used for the subsurface settlement prediction since its trough width has a connection with a source. If the volume loss and the trough width of the surface are known, the use of the binomial distribution allows the estimation of ground displacements at any level. Other researchers also proposed relationships to estimate the trough width parameter, such as Jacobsz (2002) (based on data from his centrifuge tests in sand) and Osman et al. (2006).

Apart from the effect of tunnel depth and diameter, the ground volume loss also seems to have an effect on the variation of i. Hergarden et al. (1996) showed that the increase of volume loss from 1% to 10% in their centrifuge tests led to a decrease in the trough width. Grant and Taylor (2000) drew a different conclusion and illustrated that the change of volume loss from 2% to 20% did not have an effect on the predicted trough width. Centrifuge test results of Jacobsz (2002) and Vorster (2005) supported the finding of Hergarden et al. (1996) and observed a reduction of trough width with an increase in the volume loss.

Marshall et al. (2012) investigated parameters that had effects on the settlement trough in sands. They used data from centrifuge tests, and the focus of their work was on studying the effect of geometric and tunnelling-related parameters on the shape of the settlement trough. They explained that the key parameters (tunnelling and geometric) influencing the shape of the settlement trough were the relative depth ($z_t - z$), the cover-to-diameter ratio (C_t/D_t) and the tunnel volume loss (V_{lt}). Marshall et al. (2012) also illustrated that the decrease of the settlement trough width in sands was faster than that in clays due to the occurrence of

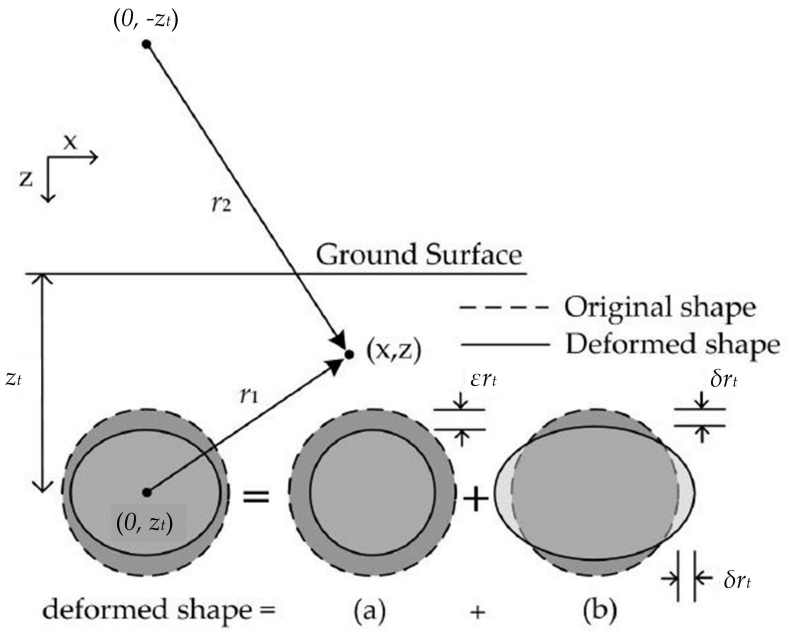

Fig. 3.6 Ground loss and ovalisation mechanism by Verruijt and Booker (1996), (Marshall, 2009)

chimney-like displacement mechanism in sands. Furthermore, the volume loss was found to have an influence on the trough width in sand. The results showed that higher volume loss values produced smaller trough width and greater settlements.

3.6.2 Closed–form analytical relations

By assuming linear elastic behaviour, an approximate solution for undrained soil deformations due to ground loss was suggested by Sagaseta (1987). The soil was assumed to be incompressible ($\nu_s = 0.5$), isotropic and homogeneous. Verruijt and Booker (1996) expanded the proposed method of Sagaseta (1987) by including the influence of ovalisation mechanism and considering compressible soils with Poisson's ratio of less than 0.5. The deformations and the ovalisation mechanism are illustrated in Figure 3.6.

For the cause of neutralising the surface shear stresses, an image solution was added at a location achieved by reflecting the considered point about the ground surface. The displacement descriptions for both components of $S_h(x)$ and $S_v(x)$ for the singular points and their images are as follows.

$$S_h(x) = -\varepsilon r_t^2 \left(\frac{x}{r_1^2} + \frac{x}{r_2^2}\right) + \delta r_t^2 \left(\frac{x\left(x^2 - k_1 z_1^2\right)}{r_1^4}\right)\left(\frac{x\left(x^2 - k_1 z_2^2\right)}{r_2^4}\right) \tag{3.13}$$

$$S_v(x) = -\varepsilon r_t^2 \left(\frac{z_1}{r_1^2} + \frac{z_2}{r_2^2}\right) + \delta r_t^2 \left(\frac{z_1\left(k_1 x^2 - z_1^2\right)}{r_1^4}\right)\left(\frac{z_2\left(k_1 x^2 - z_2^2\right)}{r_2^4}\right) \tag{3.14}$$

where $z_1 = z - z_t$, $z_2 = z + z_t$, $k_1 = \nu_s/(1-\nu_s)$, r_t is the tunnel radius, ε and δ are two parameters demonstrating the tunnel surface relative movement; ε is for the case of the uniform radial displacement, and δ is for the ovalisation case. The solution of the Boussinesq problem was finally added to the suggested solution in order to cancel out the normal stresses and to neutralise the stress distribution (Equations 3.15 and 3.16).

$$S_h(x) = -\frac{2\varepsilon r_t^2 x}{m_1}\left(\frac{1}{r_2^2} - \frac{2m_1 z z_2}{r_2^4}\right) - \frac{4\delta r_t^2 x z_t}{m_1+1}\left(\frac{z_2}{r_2^4} + \frac{m_1 z\left(x^2 - 3z_2^2\right)}{r_2^6}\right) \tag{3.15}$$

$$\begin{aligned} S_v(x) = {} & \frac{2\varepsilon r_t^2}{m_1}\left(\frac{(m_1+1)z_2}{r_2^2} - \frac{m_1 z\left(x^2 - z_2^2\right)}{r_2^4}\right) \\ & - 2\delta r_t^2 z_t \left(\frac{\left(x^2 - z_2^2\right)}{r_2^4} + \frac{m_1}{m_1+1}\frac{2z z_2\left(3x^2 - z_2^2\right)}{r_2^6}\right) \end{aligned} \tag{3.16}$$

where $m_1 = 1/(1-2\nu_s)$.

Loganathan and Poulos (1998) explained that in addition to obtaining unrealistic settlement values in granular soils, the empirical methods had essential limitations, such as the unsuitability of these methods for various construction techniques and ground conditions, and the lack of information they could give about horizontal and subsurface movements. Furthermore, they found that the method proposed by Verruijt and Booker (1996) resulted in a wider settlement trough and larger horizontal displacements than the observed values. For this reason, Loganathan and Poulos (1998) proposed a closed form solution to predict ground deformations by introducing the gap parameter presented by Lee et al. (1992) into the solution of Verruijt and Booker (1996). They considered tunnelling methods and tunnel configuration to define an equivalent undrained ground loss, ε_0. Additionally, Gonzalez and Sagaseta (2001) added a compressibility parameter, α, to the elastic solution of Verruijt and Booker (1996) to take into consideration the effect of soil dilation.

Bobet (2001) expanded the elastic solution of Einstein and Schwartz (1979) to predict ground deformations of a shallow tunnel in a saturated ground. The soil was assumed homogeneous and isotropic, and the tunnel boundary deformed uniformly without considering the ovalization of the tunnel. Osman et al. (2006) proposed an analytical approach to predict soil movements due to tunnelling in undrained soils. The deformation mechanism of the proposed method followed the Gaussian distribution approach and vertical ground surface movements were represented by the Gaussian curve, but the soil outside the boundaries of the deformation mechanism was considered to be rigid. Based on kinematic approach, Puzrin et al. (2012) proposed an approximate solution for the estimation of tunnelling induced ground deformations for undrained anisotropic elastic soil.

Franza and Marshall (2015a) introduced a new definition to the compressibility parameter, α, used in the solution of Gonzalez and Sagaseta (2001) by giving a physical meaning to the volume loss due to tunnelling. Using data from two centrifuge tests of $C_t/D_t = 1.3$ and 2.4, they assumed that the analytical surface volume loss is equal to experimental surface volume loss ($V_{ls,exp} = V_{ls,an}$).

Franza and Marshall (2015b) proposed a semi–analytical solution to predict vertical and horizontal displacements created by tunnelling in sand. The suggested formula was a modification of the elastic solution proposed by Verruijt and Booker (1996) for incompressible soils. The method took into account the change of ground volume loss with depth due to contraction and dilation of sands when affected by tunnelling. Based on the results of a centrifuge test in dense sand for a cover to diameter ratio (C_t/D_t) of 2.4, they introduced a parameter, ζ (Equation 3.19), to consider the volume loss change in sandy soils. The semi-analytical solution for horizontal (S_h) and vertical (S_v) displacements proposed by Franza and Marshall (2015b) is given by:

$$S_v = -2\varepsilon R_t^2 \zeta \left[\frac{z_1}{2r_1^2}\left(1-\frac{x^2-z_1^2}{r_1^2}\right) - \frac{z_2}{2r_2^2}\left(1+\frac{x^2-z_2^2}{r_2^2}\right) + \frac{1}{2r_2^4}\left(2(z+z_t)(x^2-z_2^2)+4z_t z z_2 \frac{3x^2-z_2^2}{r_2^2}\right)\right] \tag{3.17}$$

$$S_h = -2\varepsilon R_t^2 \zeta \left[\frac{x}{2r_1^2}\left(1-\frac{x^2-z_1^2}{r_1^2}\right) + \frac{x}{2r_2^2}\left(1-\frac{x^2-z_2^2}{r_2^2}\right) - \frac{4xz}{2r_2^4}\left(z_2 - \frac{z_t\left(x^2-3z_2^2\right)}{r_2^2}\right)\right] \tag{3.18}$$

$$\zeta = c_A \exp\left\{-\left[c_1\left(\frac{z}{z_t}\right)^2 + c_2\left(\frac{x}{z_t}\right)^2\right]\right\} + \quad c_B \exp\left\{-\left[c_3\left(\frac{z}{z_t} - c_4\right)^2 + c_3\left(\frac{x}{z_t}\right)^2\right]\right\} \tag{3.19}$$

where $\varepsilon = V_{lt}/(2 \times 100)$ is the tunnel convergence parameter, V_{lt} is the tunnel volume loss expressed in percentage, and ζ is the corrective term whose coefficients, c_i, depend linearly on V_{lt}.

These equations illustrate the effects of tunnel volume loss on soil deformation patterns. However, the coefficients of ζ in Franza and Marshall (2015b) were calibrated on the outcomes of a single centrifuge test (obtained from Marshall et al. 2012). Therefore, the solution has limited applicability.

The semi-analytical approach presented in Franza and Marshall (2015b) was extended in this research based on a wider set of centrifuge data, including the effects of cover to diameter ratio, C_t/D_t, and soil relative density, I_d. The extended form of the method is used in Chapter 7 to predict tunnelling induced ground movements in the numerical simulations used to propose a method to estimate tunnelling effects on buildings. It should be mentioned that the expansion of the method was done by the authors of Franza and Marshall (2015b). The detail of the modified method is given below.

Because the ground movement distribution may be narrower or wider than the elastic deformation pattern, depending on C_t/D_t and I_d, the expression for the corrective term ζ was modified with two additional coefficients (c_5 and c_6) to allow for more adaptable curve-fitting. Furthermore, to improve the curve-fitting of horizontal movements, two different corrective terms, ζ_v and ζ_h, displayed in Equation 3.20, were implemented in the vertical and horizontal directions, respectively. The adopted coefficients are listed in Table 3.1.

$$\begin{aligned}
\zeta_v = {} & c_{A,v} \exp\left\{-\left[c_{1,v}\left(\frac{z}{z_t}\right)^2 + c_{2,v}\left(\frac{x}{z_t}\right)^2 + c_{6,v}\left(\frac{x}{z_t}\right)^4\right]\right\} \\
& + c_{B,v} \exp\left\{-\left[c_{3,v}\left(\frac{z}{z_t} - c_{4,v}\right)^2 + c_{5,v}\left(\frac{x}{z_t}\right)^2\right]\right\} \\
\zeta_h = {} & c_{A,h} \exp\left\{-\left[c_{1,h}\left(\frac{z}{z_t}\right)^2 + c_{2,h}\left(\frac{x}{z_t}\right)^2 + c_{6,h}\left(\frac{x}{z_t}\right)^4\right]\right\} \\
& + c_{B,h} \exp\left\{-\left[c_{3,h}\left(\frac{z}{z_t} - c_{4,h}\right)^2 + c_{5,h}\left(\frac{x}{z_t}\right)^2\right]\right\}
\end{aligned} \tag{3.20}$$

$$\begin{aligned} C_A &= m_{a,i} \times V_{lt} + q_{a,i} \\ C_B &= m_{b,i} \times V_{lt} + q_{b,i} \\ c_i &= m_i \times V_{lt} + q_i \end{aligned} \tag{3.21}$$

$$\begin{aligned} C_{Ax} &= m_{ax,i} \times V_{lt} + q_{ax,i} \\ C_{Bx} &= m_{bx,i} \times V_{lt} + q_{bx,i} \\ c_{ix} &= m_{ix} \times V_{lt} + q_{ix} \end{aligned} \tag{3.22}$$

3.6.3 Numerical methods

As tunnelling has a great effect on the ground and nearby structures, a good and a detailed analysis is necessary to fully understand the influences induced by the tunnel construction on both the soil and structures. Li and Zhu (2007) explained that a good prediction of ground displacements due to tunnelling can be obtained using numerical analyses since various factors influencing ground movements can be investigated in detail. Furthermore, special cases of tunnelling and ground type can be modelled using numerical methods (Vafaeian and Mirmiran, 2003).

The majority of researchers have dealt with tunnelling as a 2D problem while it is a 3D problem and is time-dependent (Eberhardt, 2001; Finno and Clough, 1985). The reason for the wide utilisation of 2D modelling is the simplicity of plane–strain simulations compared to 3D, saving time and storage, and requiring less cost (Potts et al., 2001). Yeo et al. (2009) reported that two dimensional analysis of tunnelling does not adequately consider what happens in the vicinity of the tunnel head. Dasari et al. (1996) investigated tunnelling problems with both 2D and 3D analyses and concluded that optimum conditions due to tunnelling could not be achieved by the utilisation of 2D analyses. Gioda and Swoboda (1999) stated that 3D analysis could predict surface settlements due to tunnelling in a more accurate way than 2D analyses. This is because non-uniform distribution of the stress across the tunnel and the deformation influence of the excavation face were better accounted for in 3D modelling. Yahya and Abdullah (2014) cited that the patterns of stress and displacements are significantly different between 2D and 3D numerical modelling. Reaching a plane strain condition in tunnelling needs a specific distance from the tunnel head which is based on the amount of induced plasticity in the vicinity of the tunnel head.

Swoboda (1979) suggested the progressive softening method for modelling NATM tunnelling as a 2D problem. The stiffness of the soil within the tunnel heading is reduced according to a reduction factor, β, to create ground loss and allow the surrounding soil to

move towards the tunnel. The lining is activated when the reduction of the soil stiffness reaches the desired point.

Panet and Guenot (1982) proposed the convergence–confinement, or simply λ method for 2D tunnel numerical simulations. A force vector which is equivalent to the in situ soil stresses is applied to the tunnel boundary, then these forces are reduced by a reduction factor, λ, to create the soil ground loss. When the reduced tunnel pressure reaches the desired point, the lining is introduced.

Rowe et al. (1983) proposed the gap method to simulate tunnels as a 2D problem. In this method, a gap is predefined in the finite element mesh assumed to be the total ground loss created by tunnelling. The invert of the tunnel is rested on the underlying soil and a gap is prescribed at the crown. The final shape of the tunnel is defined by a lining. The tunnel boundary is allowed to displace until the void is closed and the soil reaches the lining position, then the lining is activated.

Addenbrooke et al. (1997) described the volume loss control method to simulate 2D tunnel construction. In this method, a volume loss is prescribed and tunnel excavation is modelled over a number of steps. Similar to the convergence–confinement method, the in situ stresses within the tunnel boundary are applied in reverse direction to the tunnel perimeter, and then reduced incrementally until the prescribed volume loss is obtained. This is done by calculating the soil volume moving into the tunnel, and dividing it by the original volume of the tunnel per unit length (cross-sectional area). The volume loss control method can also be applied in the 3D simulation of the tunnel construction (Franzius, 2003).

Katzenbach and Breth (1981) described a step by step method to model 3D tunnelling. The tunnel construction is simulated by removing the face elements consecutively and then, installing the lining step by step behind the tunnel face. There is a distance between the tunnel face and the installed lining which is called the excavation length.

In addition to different modelling techniques, the numerical simulation of the tunnel construction can be either force control or displacement control modelling. Force control modelling is a method of analysis which is performed by applying forces to the element nodes (Abdullah and Taha, 2013). In this method, free deformation is allowed to happen in the desired elements by releasing the equilibrium conditions of the specified elements (Eng, 2003). This method solves a non-linear equation system in order to estimate the nodal displacement vector depending on a known load vector (Zheng et al., 2005). On the other hand, displacement control modelling is a method of analysis in which displacements are applied to the element nodes. In this method, the application of displacements develops

stresses in the elements which consecutively leads to the creation of nodal forces (Borst et al., 2012).

It can be said that the choice of either methods, force or displacement control, depends on the situation being analysed. For example, force control modelling must be used to deal with creep problems, whereas in most of the other problems, displacement control modelling is a better choice (Borst et al., 2012). Regarding soil deformations due to tunnelling, Cheng et al. (2004) stated that the force control method resulted in a wide surface settlement with far field ground displacements. They also explained that displacement control modelling could overcome the problems occurring during simulations using force control modelling, i.e. the prediction of unrealistic profiles of surface and subsurface settlements.

Several authors in the literature followed the mentioned proposed numerical approaches to model the tunnel construction. Azevedo et al. (2002) perform a 2D elasoplastic finite element analysis of tunnelling process in residual soils using an approach similar to convergence–confinement method. Mroueh and Shahrour (2008) also used the convergence–confinement method to propose a simplified technique for the excavation of tunnels in a 3D finite element analysis using two release parameters: α_{dec} to account for the partial stress release, and L_{dec} to consider the length of the unlined zone of the tunnel. Galli et al. (2004) and Yeo et al. (2009) used the 3D step-by-step method to model the tunnel construction and lining installation. Cheng et al. (2007) used a displacement control method to simulate tunnel construction. They assumed that the tunnel volume loss was not distributed uniformly around the tunnel; the maximum settlement occurred at the tunnel crown while no movements occurred at the invert. The direction of the tunnel boundary displacements was controlled by a variable called β. β specified the location of the convergence point and moved between the original tunnel centre ($\beta = 1.0$ for deep tunnels) and the invert ($\beta = 0$ for shallow tunnels).

Shafiqu et al. (2008) used the elastoplastic-viscoplastic bounding surface model to analyse shield tunnelling process using a method similar to the gap approach. The analysis was done in four stages. In the first stage, outward elliptically distributed radial pressure was incrementally applied to the tunnel perimeter to cause heaving to the ground (created by the movement of the shield). The second stage included the simulation of the influence of tail void closure in which the pressure on the tunnel boundary was unloaded. The inward movement of the node at the tunnel crown was an indicator to know if the displacement amount reached the theoretical magnitude of the tail gap. When they were equal, the gap was assumed closed and in the third stage, the installation of lining started by activating lining elements. After that, the remained excavation forces from unrelieved soil stresses within the

tunnel elements were incrementally applied. The final stage consisted of the dissipation of remained excess pore water pressure.

Giardina et al. (2015) modelled tunnelling numerically to reproduce the centrifuge experimental set up. They used the convergence–confinement method and applied a pressure to the tunnel boundary to maintain the system in equilibrium before the start of the tunnel construction. Then the applied pressure was gradually reduced to zero. After that, they applied an inward pressure to the tunnel perimeter to reproduce the volume losses created in the centrifuge tests.

3.6.4 Experimental methods

Besides having numerous analytical and numerical methods with powerful computer packages, researchers prefer to verify their results and support their new ideas by experimental methods. Furthermore, non-linearity in soil is a complicated behaviour and is related to its stress history in addition to its current situation. The degree of this complexity increases to a greater extent when soil interaction with structures is also included. The limitations of the previously mentioned methods will require the examination of physical soil models.

The ideal solution to predict the soil's behaviour is to deal with full-scale samples or to monitor the real behaviour of the soil during the construction process. This choice is very restrained and difficult to be performed due to several obstacles. Marshall (2009) listed some of the barriers like high cost of site monitoring, limited number of available projects to monitor, uncertainty in the quality of the achieved data, difficulties in controlling site conditions and obtaining a non-representative picture of soil and structure behaviour because of the results being from limited locations.

An optimal solution can be chosen instead of the ideal one which is testing small-scale samples. In this choice, the real sample is scaled to a small sample in a way that the particles can interact well with each other and the sample mass behaves in a close way to the real non-scaled mass in terms of strength and stiffness. To perform the optimal solution, the centrifuge testing machine is used which consists of the centrifuge strong box made of steel, the model tunnel made of a hollow brass cylinder sealed entirely within a latex membrane, a system to control the tunnel volume, the soil, and different devices to measure displacements.

When a sample is scaled down by a factor, N, stress conditions will also be reduced by N times leading to erroneous results of the small-scale sample. In order to overcome such a problem, the acceleration of the model is increased using a centrifuge so that the gravity (g) is boosted N times (Ng). Nevertheless, Taylor (1995a) and Farrell (2010) outlined some issues

with centrifuge modelling. For instance, there are considerable scaling errors in centrifuge due to the non-uniformity of the acceleration field, and it is difficult to represent sufficient prototype detail in a small-scale model.

The principle of centrifuge is that after the dimensions of a sample are reduced by a factor, N, the sample will undergo an acceleration which is N times larger than the earth's gravity, g (Marshall, 2009). The model is rotated on the beam centrifuge at an angular velocity, ω, with a centrifugal acceleration of $a = \omega^2 r$ about the rotation axis, where r is the distance from the centrifuge rotation point to the point of interest (Farrell, 2010). The scale factor, N, is computed by Equation 3.23.

$$N = \frac{\omega^2 r}{g} \tag{3.23}$$

Some scaling rules for centrifuge modelling were presented by Taylor (1995a), as shown in Table 3.2.

The distance between soil depths inside the model and the centrifuge rotation centre is not constant. This produces non-linear stress variations throughout the model and results in an underestimation of stresses in the upper section of the model, and an overestimation of stresses close to the bottom. To decrease these errors, an effective radius, R_e, can be computed using Equation 3.24 (Taylor, 1995a). The effective radius is measured from the central axis of the model to one–third depth. This shows the place where the exact stress agreement between the model and the prototype is obtained, which is at two-thirds model depth.

$$R_e = R_t + \frac{h_m}{3} \tag{3.24}$$

where R_t is the radius to the top of the model and h_m is the height of the model.

3.6.5 Features of empirical, analytical and numerical methods

The simplicity of empirical methods is an advantage of the method. They have few parameters which make the calculation of displacements easy, and they can give an approximation of ground displacements for comparison with other methods and obtaining a general idea about displacement patterns. However, there are various drawbacks of the method. Maraš-Dragojević (2012) explained that empirical methods are good when the parameters are achieved from well–known tunnelling conditions, or when settlement data of a completed tunnel is available. Azevedo et al. (2002) explained that significant assumptions should be

made when using empirical methods which need good experience in tunnel construction. Celestino et al. (2000) reported that in some cases, building damage obtained from Gaussian settlements was significantly lower than that of the measured cases. They also stated that the linear increase of the maximum building distortion with the maximum settlement does not reflect the reality. Based on physical evidence, the increase of distortions is significantly faster than that of the maximum settlement. Fattah et al. (2012) clarified that empirical methods have limited applicability to various soil types. Dasari et al. (1996) explained that empirical methods are limited to specific types of soil and are not able to model the interaction between the soil and the tunnel lining. Furthermore, horizontal displacements are not predicted directly in empirical methods (Yahya and Abdullah, 2014).

Analytical and closed-form methods can address more parameters than empirical methods. Nevertheless, there are still several assumptions and simplifications in the currently available analytical solutions that prevent their use for complex geometric ground conditions (Fattah et al., 2012). Additionally, there are limited number of available solutions, and also applied to specific soil conditions (Yahya and Abdullah, 2014).

Numerical analyses are powerful tools to investigate different parameters in predicting ground displacements due to tunnelling, however there are some drawbacks of the method. Mair (1993) stated that the surface settlement trough predicted by finite element analysis was very wide and shallow compared to settlements obtained from field and empirical methods. This wideness/shallowness of the settlement trough predicted numerically was also mentioned by other authors, such as Augarde (1997); Franzius et al. (2005, 2006); Jurecic et al. (2013); Mair et al. (1982). Moreover, an in–depth understanding of the method is required to avoid misleading results, and sometimes it is difficult to validate the obtained results (Yahya and Abdullah, 2014).

The lateral earth pressure coefficient (K_0) has an important role in the numerical prediction of ground displacements due to tunnelling. Möller (2006) stated that ground surface displacements and structural forces induced in linings are considerably affected by the value of K_0. Based on the finite element simulations performed by different researchers, ground displacements predicted numerically adopting high values of K_0 result in significantly wide and shallow settlement troughs (Franzius et al., 2005). Addenbrooke et al. (1997) and Potts and Addenbrooke (1997) did a suite of 2D numerical analyses of tunnelling with $K_0 = 1.5$. They reported that the numerically predicted ground settlements were too wide and shallow. Zymnis et al. (2013) cited that it was possible for the maximum ground settlement not to occur above the tunnel centreline when using high values of K_0. Addenbrooke (1996) simulated tunnelling in London Clay with two values of K_0: 0.5 and 1.5. He explained that

displacement results from $K_0 = 0.5$ led to deeper and narrower settlement trough, and are also closer to the field data. Gunn (1993) simulated tunnelling in London clay using $K_0 = 1$. He compared the numerical results of ground displacements due to tunnelling with the Gaussian fit and found that the numerical displacements were significantly wider. Möller (2006) said that this wideness could have been due to the use of elastic soil models. In addition, he modelled different values of $K_0 = 0.5$, 1.0, 1.25, 1.5 and 2.0, and observed an overwhelming impact of K_0 value on the maximum ground settlement. For $K_0 = 0.5$, a settlement of 23 mm was observed. This value decreased with the increase of K_0 until reached 3 mm for $K_0 = 1.25$. After that, the increase of K_0 caused heave to the ground.

Some researchers stated that the poor prediction of ground displacements by numerical methods could be due to analysing the tunnelling process as a 2D problem. Lee and Ng (2002) stated that the three dimensional analyses of tunnelling improved the shape of the surface settlement curve compared to the 2D analyses. However, it was explained by Guedes and Pereira (2000) that for K_0 values of 0.5 and 1, both 2D and 3D numerical analyses of tunnel construction gave very similar settlement shapes. In a comparison of numerical simulations to measurements made for Mrazovke Exploratory Gallery in Prague, Dolezalová (2002) explained that among different K_0 values used in her analyses (0.5, 1 and 2), only the results of $K_0 = 0.5$ were in agreement to the shape of the surface settlement trough. Furthermore, she observed no difference between the results of 2D and 3D simulations of the tunnel construction. Franzius et al. (2005) also reported that there was no significant difference between the results of 2D and 3D numerical analyses.

The material model and use of isotropic properties have also been investigated numerically by different researchers. It can be said that the most influential factor causing the wideness/shallowness of the settlement trough is the soil constitutive model used in the numerical analysis. Developing a constitutive model for soil is complicated as its behaviour is non-linear and can exhibit anisotropy and time-dependency during loading (Ti et al., 2009). It should be mentioned that sophisticated soil material models have been developed that better-predict tunnelling induced ground movements in specific cases, but soil parameters that are not conventionally measured have to be obtained for these models. This adds a degree of difficulty to the analyses since some of these parameters are difficult or impossible to determine using standard tests (Oettl et al., 1998). With the aid of 2D finite element analyses, Oettl et al. (1998) investigated the prediction of tunnelling induced ground movements using different constitutive models, namely: linear elastic relations, Mohr-Coulomb, Drucker–Prager (compressive and tensile) and an elastic–plastic cap model. They clarified

that it was difficult to achieve similar settlement results to the field data. However, the cap model predicted ground displacements better than the other material models.

Gunn (1993) and Addenbrooke et al. (1997) reported that there was not a significant improvement of the displacement prediction results in their numerical analyses by modelling soil anisotropy. Franzius et al. (2005) modelled tunnel construction in London Clay with including soil anisotropy. They stated that for realistic values of soil parameters, the inclusion of soil anisotropy did not improve the settlement profile. Although, a different conclusion was drawn by Simpson et al. (1996) in which soil anisotropy showed an effect on improving the prediction of surface settlements for overconsolidated clays. Wongsaroj et al. (2007) also mentioned that considering soil stiffness anisotropy showed an effect on the long–term ground response for a soil with a high value of K_0.

3.6.6 Summary

This section presented the literature relating to the prediction of tunnelling induced ground movements. Different prediction methods were explained, and some features of the empirical, analytical and numerical methods were shown. This research mainly uses numerical analyses to predict tunnelling induced ground movements. During the review of the literature, the wide and shallow settlement trough predicted numerically was recognised as the main issue related to the numerical prediction of ground displacements due to tunnelling. Chapter 7 proposes an elastic method to solve the problem of the shallowness of the settlement trough. The semi-analytical method that is used to predict ground movements due to tunnelling in some simulations of Chapter 7 was also explained in Section 3.6.2.

3.7 Tunnelling Effects on Buildings

As explained in the previous sections, when a tunnel is constructed, a zone of soil will be affected by tunnelling and ground displacements will be induced. Similarly, when a structure is built on or under the ground, a zone of soil will be affected due to the weight and the stiffness of the structure. When these two influence zones intersect, tunnel–soil–building interaction will occur. The behaviour of this zone will be different from the scenario where the tunnel or the structure is not present (Bloodworth, 2002).

Some researchers have assumed that surface structures have no effect on ground displacements due to tunnelling, i.e. structures were considered to follow greenfield deformations (Bloodworth, 2002; Franzius, 2003). However, research has shown that there is an effect of

building stiffness and self-weight on tunnelling induced ground movements (Franzius, 2003; Mair and Taylor, 1997; Potts and Addenbrooke, 1997). Mair and Taylor (1997) provided data from several cases to show that building stiffness caused a significant reduction in the measured deflection ratio and horizontal strains induced in buildings compared to greenfield ground movements. Based on case studies, Franzius (2003) reported that building stiffness could significantly reduce building deformation.

Potts (2003) stated that investigating tunnelling effects on structures using conventional analysis methods (closed form and simple methods of analysis) is very difficult or may be impossible, while it can be modelled in a numerical analysis relatively easily.

In the following section, an extensive review of numerical investigations of tunnel–building interaction is presented. The assessment of building damage caused by tunnelling is not the aim of this research, but an explanation of building damage estimation is presented in order to provide some context to why evaluating tunnelling effects on structures is important.

3.7.1 A review of tunnel–soil–building interaction

Several studies have considered the interaction between a newly constructed tunnel and existing buildings. Numerical analyses have been used as a tool to investigate this interaction. Furthermore, different methods to model the soil, building and the interaction between them have been proposed. Buildings have been modelled as 2D beams, 2D frames, 3D shells (elastic equivalent 3D beams without modelling the actual building parts) and 3D buildings (modelled with actual structural members of foundation, columns, beams and slabs). Some researchers have considered weightless buildings while others have included the weight of the building.

Potts and Addenbrooke (1997) used 2D finite element (FE) analyses to investigate the tunnel–building interaction. The purpose of their work was to quantify the modification of the ground surface movements due to the effect of a structure's bending and axial stiffness in London Clay. They considered several influential parameters of both the soil and the structure, such as material elastic modulus, building length and cross sectional moment of inertia. The soil was modelled as a non–linear elastic, perfectly plastic material with Mohr–Coulomb failure criterion, and the building as an equivalent weightless elastic beam.

Using results from their 2D numerical analyses, Potts and Addenbrooke (1997) proposed a method to estimate a structure's effect on tunnelling induced ground displacements. The method was based on the relative stiffness of a building compared to the underlying soil,

known as the 'relative stiffness approach'. They proposed two relationships (Equations 3.25 and 3.26) to estimate the relative bending and axial stiffness of the soil and the structure.

$$\rho^* = \frac{E_b I_b}{E_s \left(L_{bldg}/2\right)^4} \tag{3.25}$$

$$\alpha^* = \frac{E_b A_b}{E_s (L_{bldg}/2)} \tag{3.26}$$

where ρ^* is the relative bending stiffness, α^* is the relative axial stiffness, E_b and E_s are the elastic moduli of the equivalent beam and the soil, respectively, I_b is the cross sectional moment of inertia of the equivalent beam, A_b is the cross-sectional area, and L_{bldg} is the length of the building perpendicular to the tunnel direction. For their plane strain problem, α^* is dimensionless but ρ^* has dimensions of m^{-1}.

Potts and Addenbrooke (1997) calculated the moment of inertia of the structure from that of each slab by employing the parallel axis theorem, with the centreline located at the mid-height of the building (as shown by Equation 3.27). The footing was represented as a slab having the same dimensions and properties of the other building slabs. This means that a building of m storeys has $m+1$ slabs. An equivalent beam was then used to represent the building, which was designed such that it had a similar bending or axial stiffness as the building. Building damage parameters were proposed, referred to as the sagging and hogging deflection ratios (DR_{sag}, DR_{hog}), and compressive and tensile horizontal strains induced in the building (ε_{hc} and ε_{ht}), as shown in Figure 3.7. Subscripts $bldg$ and gf refer to $building$ and $greenfield$, respectively. The inflection point, i, of the settlement trough separates the zones of sagging and hogging. Strains were obtained directly from the output of the FE analyses at the neutral axis of the beam in order to eliminate bending effects.

$$I_{bldg} = \sum_{i=1}^{m+1} \left(I_{sl,i} + A_{sl,i} \cdot \bar{y}_{sl,i}^2\right) \tag{3.27}$$

where A_{sl} is the cross sectional area of slabs and $\bar{y}_{sl,i}$ is the distance from the neutral axis of the i^{th} slab to the neutral axis of the building.

Potts and Addenbrooke (1997) suggested the following modification factors to relate the deflection ratios (Equation 3.28) and maximum horizontal strains (Equation 3.29) to the corresponding finite element greenfield situations.

$$M^{DR_{sag}} = \frac{DR_{sag,bldg}}{DR_{sag,gf}} \; ; \; M^{DR_{hog}} = \frac{DR_{hog,bldg}}{DR_{hog,gf}} \tag{3.28}$$

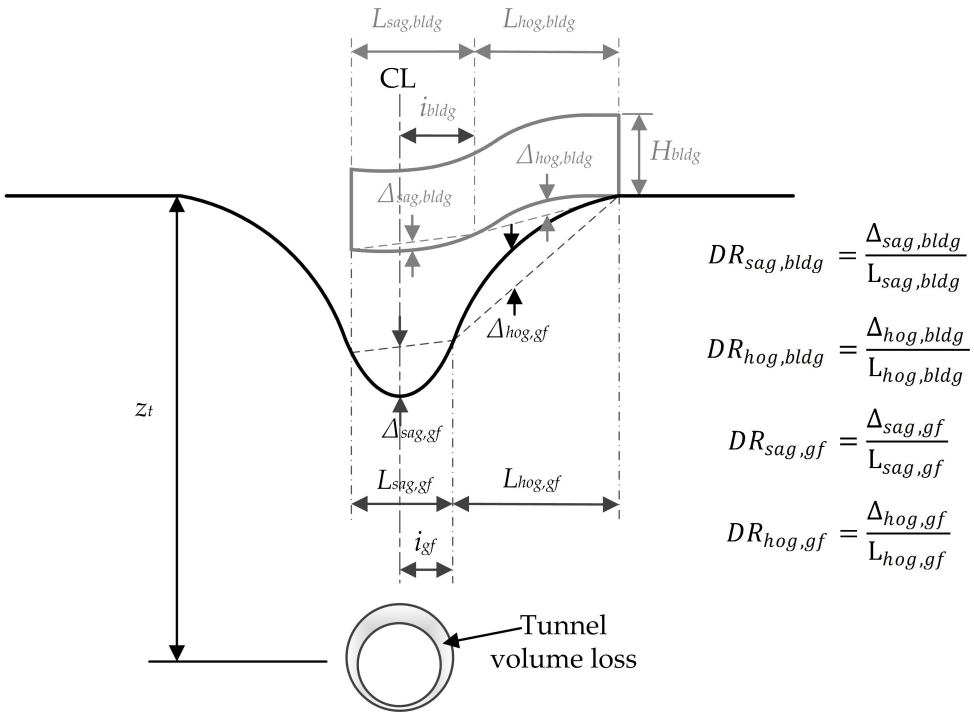

Fig. 3.7 Transverse geometry of the interaction problem and deflection ratio parameters

$$M^{\varepsilon_{hc}} = \frac{\varepsilon_{hc,bldg}}{\varepsilon_{hc,gf}} \; ; \; M^{\varepsilon_{ht}} = \frac{\varepsilon_{ht,bldg}}{\varepsilon_{ht,gf}} \tag{3.29}$$

where ε_h is maximum horizontal strains and the subscripts c and t denote compressive and tensile, respectively. The greenfield values are related to that portion of the greenfield settlement curve lying beneath the building.

Potts and Addenbrooke (1997) showed a significant reduction of ground surface displacements due to the influence of building bending stiffness. Moreover, they proposed design curves to consider bending and axial stiffness of the building in the analysis of tunnel building interaction.

Selby (1999) modelled one and two storey masonry-walled buildings influenced by tunnelling induced ground movements using 2D plane strain, linear elastic analyses. The buildings consisted of reinforced concrete ground-bearing slabs, cavity brickwork walls and light-weight steel sheeted roofs. He applied tunnelling induced ground surface movements to a finite element numerical model using Gaussian equations to estimate tunnelling effects on structures. His numerical results showed considerable modifications to the ground surface displacements due to the stiffness effect of the existing weightless structures.

Burd et al. (2000) simulated the soil and the building using 3D finite element analyses. The building was masonry and only its façades were created in the numerical model. The roof and the floors were not created; they assumed that the weight and the stiffness of a masonry building mainly comes from the façades. They mentioned that the portion of the building located in the sagging zone of the displaced soil area seemed to show more stiffness than that located in the hogging area. Therefore, the degree of damage to the building was higher in the hogging zone. This behaviour of the building in the sagging area was also explained by Burland and Wroth (1974). Burd et al. (2000) showed that the weight of the building increased surface ground displacements, and the building stiffness tended to decrease differential settlements. Similarly, Liu et al. (2000) investigated tunnelling effects on masonry buildings using 2D finite element analyses and drew conclusions similar to those of Burd et al. (2000). Liu et al. (2000) changed the relative position of the building and the tunnel, and varied the weight of the building in their analyses. They stated that the building weight played an important role in controlling the settlement occurring under the building. Furthermore, they concluded that for a specific building weight, the stiffness changed the settlement trough under the building, and the increase of the stiffness resulted in the increase of trough flatness. In addition, considerable tilt occurred to the building when it was located in the hogging area, whereas when the building located partially above the tunnel, it increased ground settlements under the corner close to the tunnel.

Miliziano et al. (2002) performed 2D analyses to study the effect of tunnelling on masonry buildings. To take into consideration the spacing between the structural members of the houses, they assigned a reduced equivalent stiffness to the masonry in their 2D models. Their results showed that the increase of building stiffness or the decrease of soil stiffness led to a reduction in the building deformations.

Mroueh and Shahrour (2003) modelled a 3D concrete framed building consisting of beams and columns to quantify the tunnel–building interaction. The building centreline coincided with the centreline of the tunnel. They suggested that the weight of buildings should be included in the numerical analysis of tunnel–building interaction because neglecting it would reduce the induced plasticity close to the building foundation and around the tunnel. They also explained that the stiffness of the building needed to be accounted for in the analysis; neglecting the structural stiffness led to considerable overestimation of internal forces induced in the structural members.

Franzius et al. (2004) analysed 2D elastic beams modelled previously by Potts and Addenbrooke (1997) and included the effect of building weight. They showed that the inclusion of the weight did not have a significant effect on the results compared with the case

of weightless buildings. It is worth mentioning that the calculation method of the equivalent building stiffness using the approach of Potts and Addenbrooke (1997) leads to a significant overestimation of the equivalent beam stiffness (Mirhabibi and Soroush, 2013; Potts and Addenbrooke, 1997). The application of a realistic building load to an equivalent beam with a considerably high bending stiffness will not have a significant impact on the analysis results.

Franzius et al. (2006) extended the relationships proposed by Potts and Addenbrooke (1997) to 3D to include the effect of the building width as well as more directly consider the effect of tunnel depth. Franzius et al. (2006) used the same principles as Potts and Addenbrooke (1997) for estimating building stiffness, and modelled the building as a 3D solid body consisting of shell elements. It is worth noting that the building was not modelled as a realistic structure with structural members. They suggested the following expressions for calculating bending and axial modification factors:

$$\rho^*_{mod} = \frac{E_b I_b}{E_s z_t L^2_{bldg} B_{bldg}} \tag{3.30}$$

$$\alpha^*_{mod} = \frac{E_b A_b}{E_s L_{bldg} B_{bldg}} \tag{3.31}$$

where ρ^*_{mod} is the modified relative bending stiffness, α^*_{mod} is the modified relative axial stiffness, z_t is the tunnel depth and B_{bldg} is the building width parallel to the tunnel direction. It was shown that explicitly including the tunnel depth in the relationship for ρ^*_{mod} provided a more realistic representation of bending response (building stiffness relative to soil stiffness increases with the decrease of the tunnel depth); this was not the case for the axial response described by α^*_{mod}. Moreover, the significance of considering the effect of structural stiffness on ground displacements was also confirmed in the work of Franzius et al. (2006).

Dimmock and Mair (2008) demonstrated the analysis of two- to three–storey masonry buildings at Moodkee Street and Keetons Estate in London. They obtained data from references within the low–rise building area and compared with equivalent greenfield data to find out the effect of building stiffness on tunnelling induced ground movements. Similar to the findings of Burd et al. (2000), Dimmock and Mair (2008) clarified that the behaviour of the buildings was nearly flexible in the hogging zone while it was semi–flexible in the sagging zone. Furthermore, the relative axial stiffness of the buildings was high since the horizontal strains induced at the base of the façades were insignificant. The authors used the method of Potts and Addenbrooke (1997) in their analysis, and mentioned that the stiffness

of the buildings was overestimated. They suggested reducing the estimated stiffness of a building based on the existence of openings (doors and windows).

Giardina et al. (2009) modelled a tunnel construction in Amsterdam on which there was a historic building supported by pile foundations. The analysis was two dimensional and two building locations were considered: inside the sagging zone, and inside the hogging zone. The authors showed that a building located in the hogging zone would experience more damage from tunnelling induced ground movements compared to the same building in the sagging zone. In addition, the amount of openings in the building were found to have an important role in tunnel–building interaction.

Giardina et al. (2010) performed 3D finite element analyses similar to the modelling of Giardina et al. (2009). They created building façades using shell elements. The roof and the floor were not modelled since they were relatively flexible. They confirmed the importance of 3D modelling of tunnel–building interaction to understand the effects of tunnel advancement on the building. Moreover, the relative tunnel–building distance was also determined as an influential parameter governing the settlement trough type.

Pickhaver et al. (2010) proposed an equivalent beam method to investigate tunnelling effects on masonry buildings. The building was modelled as an equivalent beam in 3D finite element analyses. They used Timoshenko beam theory to develop their proposed equivalent beam formulation. Furthermore, an equivalent inplane flexural and shear stiffness (denoted by EI^*_{in} and GA^*, respectively) were given to the equivalent beam. The stiffness was calculated based on the strip method in which the building façades were divided into horizontal strips to calculate I^*_{in}, and vertical strips to compute A^* (some strips were solid and others contained openings due to windows and doors).

The effective height of each strip, h^*_j, was calculated as a_j/L_j where a_j is the strip area excluding the openings, and L_j is the strip length. The equivalent cross sectional moment of inertia of the strip was calculated as: $I_j = t_j \left(h^*_j\right)^3 /12 + t_j h^*_j \left(b_j\right)^2$, where t_j is the wall thickness and b_j is the distance between the centroid of each strip to the neutral axis. The moment of inertia of the whole façade was then calculated as $I^*_{in} = \sum I_j$. The area of the façade to resist shear, A^*, was calculated from the vertical strips as: $A^* = L_{bldg} \cdot \sum L^*_i / A_i$, where L^*_i is the strip width and A_i is the total area of the strip cross section. For a length to height ratio of a façade (L_{bldg}/H_{bldg}) smaller than 3, they suggested reducing the values of I^*_{in} and A^* by a factor, $k = (L_{bldg}/H_{bldg})/3$, to avoid overestimating the stiffness of the façade.

Pickhaver et al. (2010) stated that a good match of the equivalent beam results with those of the modelled masonry façades in the sagging zone was obtained, but in the hogging zone, the masonry façades behaved more flexibly relative to the equivalent beam. This was because

of the development of cracks at the top of the masonry façades. The crack development was not considered in the equivalent beam which led to the overestimation of its stiffness in the hogging area. For this reason, they stated that a reduced stiffness should be used for the hogging zone in order to obtain better results.

Based on centrifuge experiment data, Farrell (2010) proposed the partitioned approach to define the relative bending stiffness separately for sagging and hogging zones:

$$\rho^*_{sag,par} = \frac{EI_{bldg}}{E_s L^3_{bldg,sag} B_{bldg}} \tag{3.32}$$

$$\rho^*_{hog,par} = \frac{EI_{bldg}}{E_s L^3_{bldg,hog} B_{bldg}} \tag{3.33}$$

where $\rho^*_{sag,par}$ and $\rho^*_{hog,par}$ are relative bending stiffness for sagging and hogging zones, respectively; subscript *par* refers to partitioned.

Son and Cording (2010) numerically investigated the building response to ground displacements due to excavations, and took into account the occurrence of cracks in the building, the effect of structural type and soil stiffness. They explained that generally, a significant part of urban areas is constructed with brick–bearing buildings (i.e. bearing walls are constructed with bricks) ranging from 50 to 100 years old. Apart from age, the quality of the construction, the utilisation of older building codes, and repair works may also have affected the functionality of the existing buildings. They concluded that using elastic analyses for the building considerably underestimated the building damage. The stiffness of a building decreased significantly with the occurrence of severe cracks. Therefore, the development of cracks and postcrack behaviour of the building should be considered in the analysis to achieve a better prediction of the excavation effects on buildings. Furthermore, for the same magnitude of induced ground movements, a structure on a soft soil showed a stiffer response to the excavation compared to the same structure on a stiff soil.

Maleki et al. (2011) used the same modelling method as Franzius et al. (2006) to make a comparison between 2D and 3D modelling of a building when estimating displacements due to tunnelling. The outcomes of the 2D and 3D models were stated to be very similar.

Goh and Mair (2011a) investigated deep excavation–masonry building interaction and modelled the building as an elastic beam with bending and axial stiffness. Similar to Farrell (2010), they separated the building into sagging and hogging parts based on a case study on the response of the Singapore Art Museum to excavation-induced displacements. It was observed that building bending stiffness had an effect on ground displacements. The part of

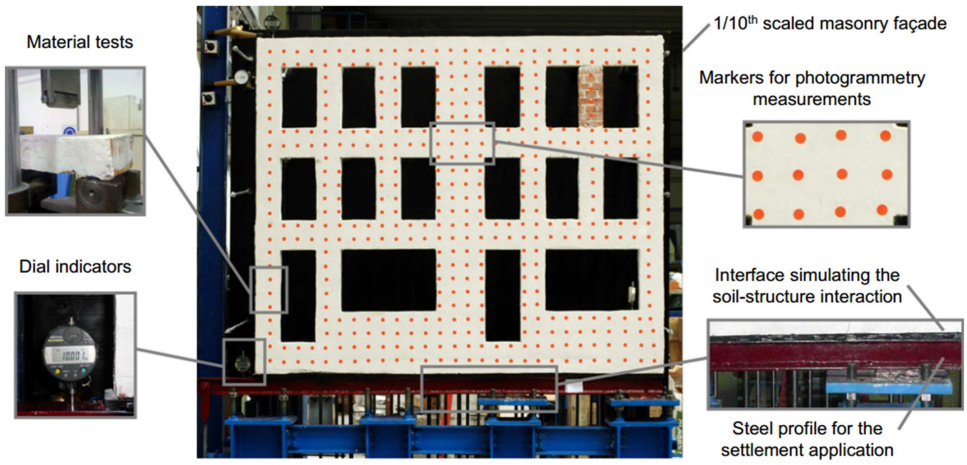

Fig. 3.8 Main features of the experimental test of a masonry façade (Giardina et al., 2012)

the building located in the sagging zone of the surface settlement curve behaved semi-rigidly while the part located in the hogging zone was fully flexible. They suggested Equations 3.34 and 3.35 to estimate the value of relative bending stiffness, ρ, in the sagging and hogging zones, respectively.

$$\rho_{sag} = \frac{(EI)_{bldg}}{E_s \cdot L^3_{bldg,sag}} \tag{3.34}$$

$$\rho_{hog} = \frac{(EI)_{bldg}}{E_s \cdot L^3_{bldg,hog}} \tag{3.35}$$

Giardina et al. (2012) modelled a building façade experimentally to evaluate the interaction between a newly constructed tunnel and existing masonry buildings. They created a $1/10^{th}$ scaled façade of a masonry building using scaled bricks and thin joints of mortar. A vertical load was applied to the façade to reproduce the prototype stress field. The base of the façade was then connected to a flexible steel profile and a known settlement trough was applied to the façade. Furthermore, the interaction between the building and the soil was achieved by introducing a rubber layer between the façade and the steel profile. The insertion of the rubber layer was used to replicate the stiffness of the interface. The tested model was then monitored, and dial gauges were used to measure deformations of specific points on the façade. Figure 3.8 shows their modelled masonry façade.

Giardina et al. (2012) found that the interface between the soil and the building played an important role in the response of the building, and reduced the applied vertical settlements.

Stress redistributions also occurred based on the façade–interface relative stiffness. The influence of doors and windows was also studied which caused stress concentrations at their corners, and had a significant effect on the development of cracks.

Farrell and Mair (2012) and Farrell et al. (2014) performed centrifuge tests to evaluate building response to tunnelling considering elastic and non-elastic building behaviour with different geometry and stiffness. The elastic buildings were represented by aluminium beams of variable thickness with a rough interface between the soil and the beams. The non-elastic buildings in which crack development was allowed were created using "micro concrete and masonry with cement based mortar." Masonry buildings were made using $1/12^{th}$ scaled model bricks and mortar. The ductility of the mortar was reduced by adding plaster of Paris. Another group of masonry buildings were modelled using $1/50^{th}$ scaled model bricks with an elastic mortar to obtain a low bending and axial stiffness for the simulated beam.

Farrell and Mair (2012) and Farrell et al. (2014) showed that the interactive relationship between the soil and the building is remarkably non-linear. There was a significant load redistribution in the rigid buildings which caused appreciable embedding of the structure into the soil. Additionally, the induced horizontal strains in the building were negligible, even for the very flexible beams. The occurrence of the building load redistribution was also confirmed in the works of Farrell et al. (2012) and Farrell et al. (2014) based on centrifuge data and the case study of two buildings affected by tunnelling in Italy. Rigid buildings tended to embed into the soil whereas flexible buildings followed greenfield deformations.

Rampello et al. (2012) studied tunnel–building interaction numerically using 2D and 3D analyses. The building was modelled as an equivalent solid body embedded into the soil. It was given an equivalent stiffness and weight. The results showed that there was an increase in ground settlements due to the weight of the building, and less building distortions due to the stiffness.

Mair (2013) used the proposed method of Goh and Mair (2011a) to develop design curves to take into consideration the stiffness effect of a building in tunnel-building interaction analysis. The proposed design curves were independent of tunnel-building eccentricity whereas the previously adopted methods varied with eccentricity. Furthermore, the results showed the creation of very small horizontal strains in the building.

Kappen et al. (2013) studied how the position of a masonry building with respect to the tunnel axis affects the interaction between them, using 3D finite element analyses. The floors were not modelled due to having negligible stiffness. The walls were created using shell elements, and building loads were applied to them. The advancement of the tunnel head was simulated by simultaneously deactivating soil elements within the tunnel and activating lining

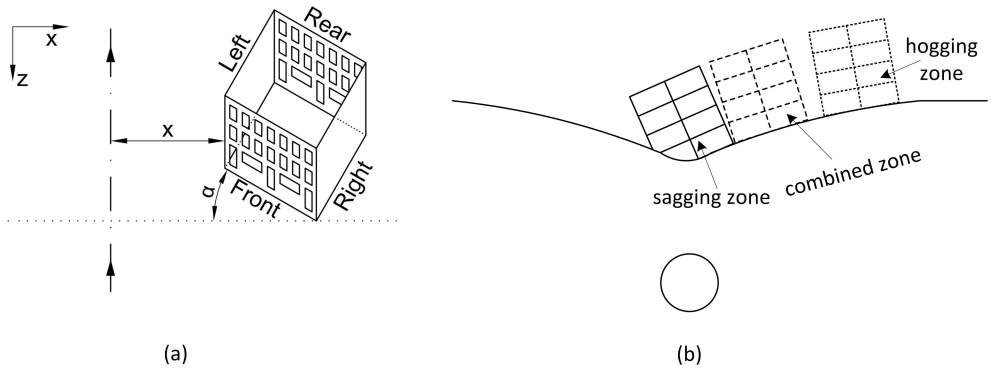

Fig. 3.9 (a) Building alignment angle, (b) tunnel–building relative position (Kappen et al., 2013)

elements. The alignment of the building axis with the tunnel axis was examined for angles from $\alpha = 0$ to 180° with increments of 22.5° (see Figure 3.9a). Additionally, three building positions were tested: in the sagging zone, combined (sagging and hogging), and hogging zones, as shown in Figure 3.9b. They evaluated building damage based on the induced crack width. It was concluded that for buildings located in the sagging zone, the rotation of the building axis from 0 to 135° would increase the level of damage to the building, while for the other two cases, low alignment angles caused larger damage compared to the damage occurring in the case of high rotation angles.

Mirhabibi and Soroush (2013) assessed the effect of 2D and 3D building modelling on ground movements due to twin tunnelling. They modelled a concrete framed building consisting of slabs, beams and columns with and without exterior and interior walls. They explained that building stiffness did not have a significant effect on tunnel–building interaction especially for the open-framed building.

Zhang et al. (2014) developed a systematic approach to evaluate the safety of buildings adjacent to a constructed tunnel. They analysed a concrete framed building with single footings and explained that the presence of the building could lead to an increase in the soil surface settlement especially in the vicinity of the building foundation.

Losacco et al. (2014) made an uncoupled evaluation of the tunnelling effects on existing masonry buildings. In their analysis, they simplified the 3D masonry building to a simple solid part called the equivalent solid which had the same shape as the building part located under the ground. Each façade of the building was replaced by an equivalent solid, and the equivalent properties were calculated from an iterative numerical process based on the 3D building. At first, a set of 3D analyses of the whole 3D building was simulated. Ground

displacements calculated empirically using the Gaussian function were applied to the base of the buildings. The initial properties of the building were calculated using the strip approach proposed by Pickhaver et al. (2010). After that, the equivalent solid for each façade was modelled, the same Gaussian displacements as the 3D building case were applied to the base of the embedded equivalent solid and its properties changed iteratively until the same behaviour as that of the 3D building was obtained. Losacco et al. (2014) stated that a generally good agreement between the results of the whole 3D building with the equivalent solid model was obtained.

Goh and Mair (2014) modelled the building as a 2D frame consisting of beams and columns to estimate building response to excavation–induced soil movements. They proposed a method to estimate bending stiffness of a 2D frame by using the column stiffening factor (C_{col}) proposed by Meyerhof (1953) to increase the flexural rigidity of an entire beam line in a rigidly connected frame:

$$C_{col} = 1 + \frac{L_{sag,hog}^2}{L_{bay}^2} \left(\frac{K_{c,LC} + K_{c,UC}}{K_{c,LC} + K_{c,UC} + K_{c,b}} \right) \tag{3.36}$$

where $L_{sag,hog}$ is the length of the beam line in sagging or hogging, L_{bay} is the span length of each beam bay, $K_{c,LC}$ and $K_{c,UC}$ are the average stiffness ($= (EI)_{col}/L_{col}$) of the lower (LC) and upper (UC) columns, respectively, L_{col} is the column height, and $K_{c,b} = ((EI)_b/L_{bay})$ is the average stiffness of the beam line. The bending stiffness of the frame is then estimated by $EI_{frame} = \sum((EI)_b * C_{col})_{i^{th}\ floor}$

Giardina et al. (2014a) numerically modelled the centrifuge tests performed by Farrell (2010) in which buildings were represented by aluminium plates resting on dry fine sand. Their aim was to investigate how the stiffness and the weight of a building interacts when affected by tunnelling. They used a no–tension interface between the soil and the building, and explained that a gap formed during tunnel excavation. They concluded that the increase of weight led to the decrease of the gap between the soil and the building. Additionally, including the weight in the analyses caused the building to undergo larger deformations and to try to follow greenfield vertical movements. Furthermore, Giardina et al. (2015) studied the interaction between tunnel construction in sand and surface structures based on 2D numerical simulations and included centrifuge test results from Farrell (2010). They concluded that the effect of building stiffness on tunnelling induced deformations depends on the building weight. They added the effect of building weight to the equations proposed by Farrell (2010) to estimate relative bending stiffness in the sagging and hogging zones (Equations 3.32 and 3.33), as shown in Equations 3.37 and 3.38.

$$\rho^*_{norm,sag} = \frac{\rho^*_{sag,par}}{\frac{\sigma}{\sigma_1}} \tag{3.37}$$

$$\rho^*_{norm,hog} = \frac{\rho^*_{hog,par}}{\frac{\sigma}{\sigma_1}} \tag{3.38}$$

where $\rho^*_{norm,sag}$ and $\rho^*_{norm,hog}$ are normalised relative bending stiffness for sagging and hogging zones, respectively, σ is the total bearing pressure acting on the foundation, and σ_1 is the bearing pressure of each building storey.

Fargnoli et al. (2015) numerically investigated the interaction between existing buildings and the construction of the new Milan (Italy) metro-line 5. The whole building was modelled as a 3D building consisting of foundation, beams, columns and floors in some analyses, and the buried part of the building was modelled in other analyses. Furthermore, the building was simplified as a 2D plate for further investigations, and the approach of Franzius et al. (2006) was used to calculate the equivalent building properties. Fargnoli et al. (2015) concluded that the stiffness and the weight of the building had an effect on the settlement trough. The weight of the building increased the volume loss and ground settlements. Additionally, the portion of the structure located above the ground did not show a significant contribution to the total building stiffness. The results of the models including the entire building and the buried building part were very similar, indicating that the stiffness effect of the building on ground displacements mainly came from the foundation. Moreover, they showed that the simplified plate model of the building using the approach of Franzius et al. (2006) showed a large stiffness of the plate and led to unrealistic results of predicted ground displacements.

Son (2015) numerically investigated tunnelling effects on buildings in loose and dense sands, and soft and stiff clays, respectively, using 2D discrete element analyses. Two types of building were modelled: brick–bearing buildings and brick–infilled framed buildings. "Tunnel, structure, ground, and construction conditions together" were found to be the most influential parameters affecting the building response to tunnel construction. It was explained that buildings constructed on a loose sand or soft clays experienced less damage compared to those built on a dense sand or stiff clay. In addition, the brick–bearing building underwent relatively more damage than the brick–infilled building. This was because the building frame in the brick–infilled structure provided a good confinement to the brick walls and reduced crack propagation.

Bilotta et al. (2017) investigated the effect of tunnelling under a historic church on Line 6 of the Naples Underground using Plaxis 3D. The building was modelled as a flexible plate

subjected to a uniformly distributed load. Their numerical modelling included the investigation of different parameters affecting the soil–structure interaction, such as: excavation span, tunnelling technique and tunnel–building relative distance. The relative tunnel–church distance was recognised as a critical problem in the stage of the tunnel preliminary design. Furthermore, they observed a negligible effect of the structural stiffness on the maximum ground displacement.

3.7.2 Estimating building damage

Ground movements in urban areas can cause significant damage to existing buildings. The assessment of damage level to surrounding buildings is of great importance when constructing a new tunnel. Damage risk assessment plays an important role in the planning, design and construction of new tunnels in urban areas (Mair et al., 1996).

Burland and Wroth (1974) proposed an approach to evaluate the potential damage to buildings due to settlements. They assumed that the damage to a building is mainly recognised through the cladding and finishes. Buildings usually lose serviceability before the collapse of structural members which indicates that the evaluation of finishes and cladding is satisfactory for the assessment of building damage. They also explained that most building damage appearing as cracks resulted from induced tensile strains. Since their aim related to visible damage (not collapse), the concept of critical tensile strain, $\varepsilon_{t,crit}$, could be used to indicate the loss of the tensile strength and visible crack development.

Burland and Wroth (1974) defined some terms related to the deformation of foundations, as shown in Figure 3.10. Vertical settlement, S_v, is the vertical movement of a point. Differential settlement, ΔS_v, is the settlement of a point relative to another point. Rotation, θ, is the change in gradient of the straight line defined by two reference points embedded in the structure. Angular strain, α, produces sagging or upward concavity when it is positive while hogging or downward concavity is described by a negative value. Tilt, ω, is the rigid body rotation of the whole superstructure or a well-defined part of it. Angular distortion, β, describes the rotation of the straight line joining two reference points relative to the tilt. Deflection ratio, Δ/L, is the ratio of relative settlement and the corresponding length, and is equal to Δ_{max}/L_{AD} in Figure 3.10b.

Burland and Wroth (1974) assumed the building as a uniform, weightless, elastic beam of unit thickness in order to apply the concept of critical strain to evaluate the development of initial cracks. They explained that bending and shear cracks are likely to happen together in a beam, but they are dealt with separately to understand the performance of the beam.

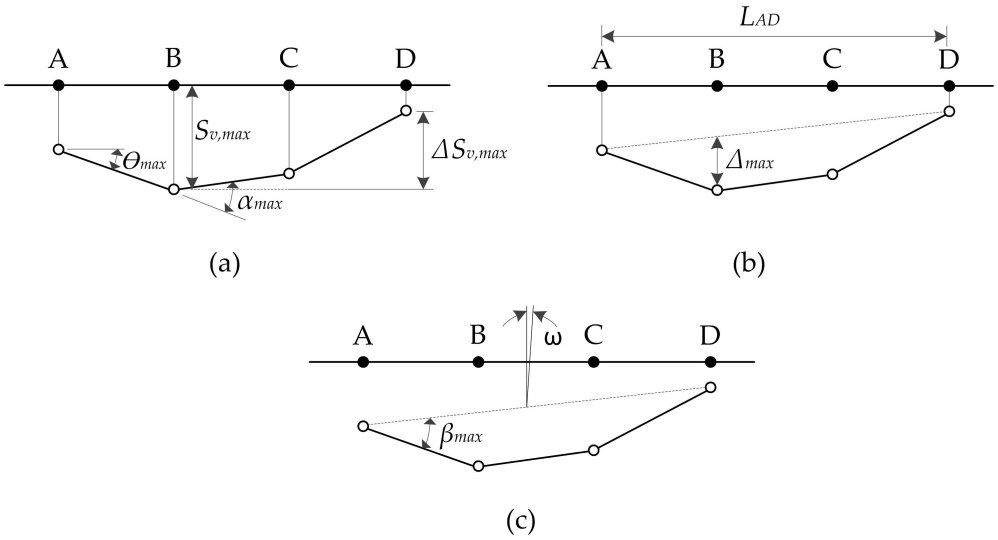

Fig. 3.10 Suggested definitions of foundation deformations (Burland, 1995)

Bending cracks occur due to the creation of direct tensile strains, and shear cracks develop due to the induction of diagonal tensile strains. The deflection equation (bending and shear) of a beam loaded at the centre is given by Timoshenko (1940):

$$\Delta_b = \frac{PL_b^3}{(EI)_b}\left(1+\frac{18(EI)_b}{L_b^2 h_b G_b}\right) \tag{3.39}$$

where Δ_b is the beam deflection, L_b is the length, h_b is the cross sectional height, and G_b is the shear modulus.

For a beam having a Poisson's ratio of $\nu_b = 0.3$, with its neutral axis located at the mid–height of the cross section, Equation 3.39 can be re-written in terms of maximum bending and shear strains, as in Equations 3.40 and 3.41, respectively (Burland and Wroth, 1974).

$$\frac{\Delta_b}{L_b} = \left(0.167\frac{L_b}{h_b}+0.65\frac{h_b}{L_b}\right)\varepsilon_{bt,max} \tag{3.40}$$

$$\frac{\Delta_b}{L_b} = \left(1+0.25\frac{L_b^2}{h_b^2}\right)\varepsilon_{st,max} \tag{3.41}$$

where Δ_b/L_b is the deflection ratio, $\varepsilon_{bt,max}$ and $\varepsilon_{st,max}$ are maximum bending and shear strains. Since foundations play an important role in restraining deformations, Burland and Wroth

(1974) stated that it would be more realistic to consider the neutral axis at the lower extreme fibre of the beam. Then the limiting Δ_b/L_b can be written as:

$$\frac{\Delta_b}{L_b} = \left(0.083\frac{L_b}{h_b} + 1.3\frac{h_b}{L_b}\right)\varepsilon_{bt,max} \tag{3.42}$$

$$\frac{\Delta_b}{L_b} = \left(1 + 0.064\frac{L_b^2}{h_b^2}\right)\varepsilon_{st,max} \tag{3.43}$$

Burland et al. (1976) clarified that the quantification of building damage was very complicated due to dependence on "subjective criteria." Furthermore, the function of the building was also important to specify the quantity of damage. An allowable damage for a specific type of building may be unsatisfactory for another. Based on the visible damage, Burland et al. (1976) proposed a "five–point classification table" to evaluate the risk of damage to buildings due to movements. They used the severity measure to categorise the potential damage to a building; the measure was based on the "ease of repair" as well as the width of the developed cracks in the building. It started from 1 indicating very slight damage to 5 signifying severe damage. Negligible damage was also mentioned, but not given a category in their table. The width of the cracks were chosen depending on the opinion of engineers who had previously observed building performance and dealt with the reaction of building occupants. Table 3.3 shows the classifications proposed by Burland et al. (1976).

It is worth noting that Burland et al. (1976) explained that the location of the damaged part in the building should be taken into consideration. Additionally, crack width is not a direct measurement of damage; it only represents one aspect of damage.

Boscardin and Cording (1989) made further investigation about the limiting tensile strains based on case histories, and linked it directly to the building damage categories. The classification of damage based on Boscardin and Cording (1989) is presented in Table 3.4.

Boscardin and Cording (1989) presented Equation 3.44 to calculate the angular distortion, β (which is a measure of shear strain), and linked it with the deflection ratio to take into account the effect of vertical differential settlements on the degree of building damage. Furthermore, they suggested to calculate the total tensile strain from the greater of the combination of the maximum bending strain and the average horizontal strain, and the combination of the maximum diagonal strain and the average of the horizontal strain (the higher value of ε_{total} between $\varepsilon_{total} = \varepsilon_h + \varepsilon_{bt}$ and $\varepsilon_{total} = \varepsilon_h + \varepsilon_{st}$). On the other hand, Geddes (1991) presented a discussion about building response to settlements, and concluded that horizontal strains calculated based on the approach of Boscardin and Cording (1989)

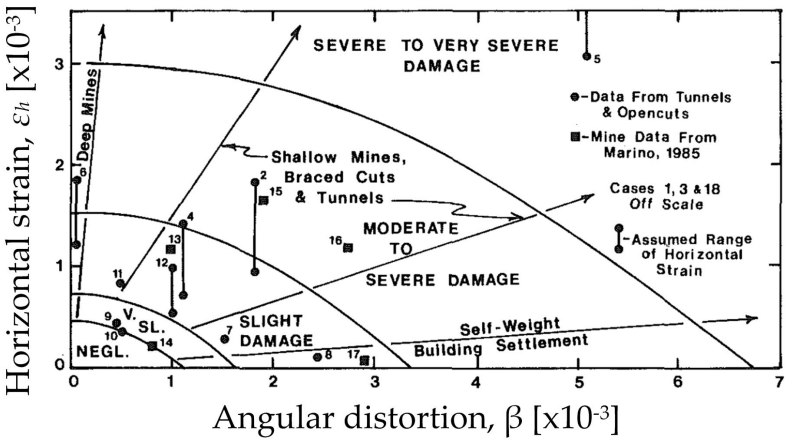

Fig. 3.11 Relationship of damage to angular distortion and horizontal strains for $L_b/h_b = 1$, (Boscardin and Cording, 1989)

were significantly overestimated. In addition to Table 3.4, Boscardin and Cording (1989) also presented Figure 3.11 to link the building damage to the horizontal strains and the angular distortion (β).

$$\beta = 3\frac{\Delta_b}{L_b}\left(\frac{1+4\frac{E_b}{G_b}\left(\frac{h_b}{L_b}\right)^2}{1+6\frac{E_b}{G_b}\left(\frac{h_b}{L_b}\right)^2}\right) \tag{3.44}$$

Burland (1995) proposed a three-stage process to evaluate the risk of damage to buildings: preliminary assessment, second stage assessment and the detailed evaluation.

In the preliminary assessment, the building is assumed to be non–existent, and greenfield deformations under the virtual building are predicted. If the maximum vertical displacement does not exceed 10 mm, and the maximum slope is smaller than 1/500, the damage is considered as negligible and further calculations are not required.

The second stage assessment is performed when the maximum vertical displacement and the maximum slope exceed the limits mentioned in the preliminary assessment. In this stage, the building is represented by an equivalent elastic beam subjected to greenfield displacements. It is worth noting that the building is assumed to follow the greenfield displacements; the effect of weight and stiffness are neglected. The damage is then categorised based on the available damage classification tables. Burland (1995) mentioned that the actual damage to the building is usually less than the predicted damage in the second stage assessment.

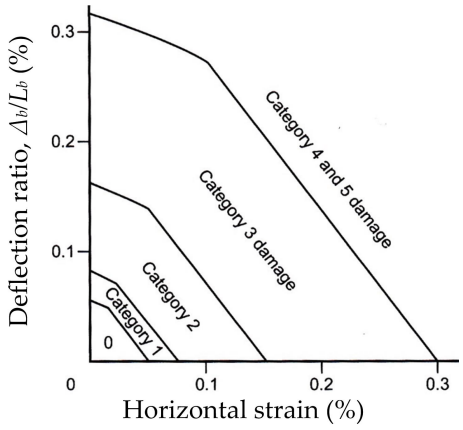

Fig. 3.12 Design chart developed by Burland (1995) for $L_b/h_b = 1$

If the damage category obtained in the second stage assessment is greater than or equal to 3, a detailed evaluation of tunnel–building interaction is required considering the method of tunnel construction, the type of the structure and the foundation, building orientation and previous building displacements. Burland (1995) stated that the damage category predicted in the detailed evaluation was usually lower than the category predicted in the second stage analysis. This was because of the high level of safety considered in the second stage analysis.

Burland (1995) also presented Figure 3.12 to estimate building damage graphically without calculating strains. The design chart depends on the percentage of Δ_b/L_b and horizontal strains.

Boone (1996) and Boone (2001) stated that considering a single parameter in the assessment of building damage would disregard the effect of many other important factors. Boone (1996) suggested including other parameters in the assessment of building damage using the following procedure. The settlement profile is divided into the sagging and hogging zones. Based on provided graphs and equations, the value of elongation strain (ε_{el}), direct lateral extension strain (ε_{le}), and bending strain (ε_M) are calculated to estimate the total tensile strain as: $\varepsilon_{t,total} = \varepsilon_M + \varepsilon_{el} + \varepsilon_{le}$. Then, shear strain (tan γ) is computed, and the maximum principal tensile strain (ε_{tp}) is taken as $0.5\varepsilon_{t,total}$. The values of $\varepsilon_{t,total}$, ε_{tp} and tan(γ) (the approximate shear strain) are compared separately to Table 3.5 to obtain the crack width. Finally, Table 3.3 is used to evaluate the degree of damage. Note that the term L/H in Table 3.5 is the length to height ratio of a wall or a building.

Following the work of Burland and Wroth (1974), Finno et al. (2005) suggested the use of $(EI)_b/(G_bA_v)$ instead of E_b/G_b (where $(EI)_b$ was assumed to be the bending stiffness of the beam and G_bA_v to be the total shear stiffness) to estimate the building damage based on the

beam-analogy approach. The building was modelled as a laminate beam in which bending deformations are restrained by the floors, and shear deformations by walls (both bearing and in–fill walls between the columns). The damage assessment procedure can be summarised as follows. Estimate ground movements and locate the influenced structure with respect to the settlement profile. If necessary, divide the settlement curve into sagging and hogging zones using the inflection and tangent points, and the end of the building. Calculate the slope for each deformation mode (m), and compute the rotation of the building as a rigid body (ω) by calculating the slope of the entire building. Calculate the additional shearing strain in each deformation mode from $\gamma_{add} = m - \omega$. Define the properties and geometry of the relevant sections in the building, and find suitable values of critical strain using Table 3.5. For each failure mode, calculate the limiting deflection ratio (Δ_b/L_b) using the computed bending and shear stiffness of the laminate beam. Finally, compare the deflection ratios obtained from the estimated settlement profile with the limiting deflection ratio; if the obtained deflection ratios are greater than the limiting one, the occurrence of cracking is possible.

Based on the state of strain at a point being independent of L_{bldg}/H_{bldg}, E_{bldg}/G_{bldg} and the location of the neutral axis, Son and Cording (2005) evaluated building damage using the crack width criterion. The damage categories were related to the maximum principal strain, ε_p, calculated by Equation 3.45.

$$\varepsilon_p = \varepsilon_l \cos\theta_{max}^2 + \beta \sin\theta_{max} \cos\theta_{max} \tag{3.45}$$

$$\tan(2\theta_{\max}) = \beta/\varepsilon_{\mathrm{l}} \tag{3.46}$$

where β is the angular distortion, ε_l is the lateral strain and θ_{max} is the direction of crack formation measured from the vertical plane.

Schuster et al. (2007) introduced a limit state, $g(x)$ (Equation 3.47), calculated based on the principal strain to evaluate the potential building damage.

$$g(x) = \varepsilon_{p,R} - \varepsilon_{p,L} \tag{3.47}$$

where $\varepsilon_{p,R}$ and $\varepsilon_{p,L}$ are the resisting and loading principal strains. It is worth noting that the loading principal strain represents the actual principal strain of a building, and the resisting principal strain represents the limiting principal strain specified depending on the building damage observations. The case where $g(x) < 0$ indicates the occurrence of a large and unacceptable damage to the building. Based on Son and Cording (2005), Schuster et al. (2007) suggested a limiting principal strain of 1.67×10^{-3}. Schuster et al. (2008) found

this limiting principal strain to be 1.19×10^{-3} using a trial–and–error process. In addition, Schuster et al. (2009) noted that the damage to buildings in the hogging part were generally greater than in the sagging part. This was also observed by various other researchers (Camós et al., 2014; Castaldo et al., 2013; Goh and Mair, 2011a).

Using results of physical modelling and numerical analyses, Cording et al. (2010) explained that the existence of a relatively stiff building modifies greenfield ground displacements, and reduces the structural distortions compared to a scenario where the building follows greenfield displacements. Additionally, the induced lateral strains decrease significantly depending on the type of foundation. Furthermore, shear stiffness of the building led to a reduction in the angular distortion, β.

Giardina et al. (2014b) proposed two models for the assessment of damage to masonry buildings using polynomial and piecewise linear functions. The possible damage caused to a building by tunnelling induced ground movements was related to the main parameters affecting the building response to displacements. The influential parameters included the geometry of the building and the existence of openings, the predicted settlement profile and the properties of the masonry and the soil–building interaction. A 2D finite element analysis was used to investigate the effect of various parameters, such as geometrical and material properties, loading, and boundary conditions. The 3D effect of the tunnel head construction and the torsional response of the building were studied using 3D finite element analyses.

Giardina et al. (2014b) defined a damage function, d, related to the deflection ratio (Δ/L), and a set of parameters collected in an array called x. The final response of the building was linearly dependent on the selected parameters for the sensitivity study when using the polynomial function while a "further opportunity to interpret the effect of each parameter variation on the initiation and progression of damage" was obtained using the piecewise function. The existence of openings in a building was found to increase the possibility of building damage to a great extent; it could increase the level of damage up to two categories based on the currently available methods of building damage assessment.

3.7.3 Summary

This section reviewed the research in the field of tunnel–building interaction. Different numerical methods have been used to quantify tunnel–structure interaction, and various modelling techniques were adopted to represent the building in the numerical analyses, including simple beams, frames and 3D structures. Researchers have shown that the stiffness and the weight of buildings can have an effect on the tunnel–building interaction.

Representing buildings as equivalent beams in numerical analyses generally led to an overestimation of the effect of building stiffness on tunnel–building interaction. The utilisation of 3D buildings resulted in a significant reduction of the stiffness effect. Furthermore, Fargnoli et al. (2015) noted that the foundation of the building, compared to the over ground portion, had the main contribution to the building stiffness.

Despite the amount of work done in this area, the behaviour of the building in the global tunnel–soil–building system is still not clear. This ambiguity mainly belongs to two important points that have been overlooked or over-simplified in previous studies: (1) the individual effect of building structural parts (e.g. foundation and individual storeys) in the global building system, and (2) the main parameters influencing building behaviour when affected by tunnelling, such as the boundary condition, the length of the building influenced by tunnelling, and the effect of the building length not influenced by tunnelling. These points will be studied in detail in this research.

The section also presented the methods used to assess building damage caused by tunnelling. It was shown that the deflection ratio and the induced horizontal strains in the building were important parameters to make building damage assessment. These parameters are achieved from the analysis of tunnel–building interaction. The subject of building damage assessment is not included in the aims of this thesis, however, the proposed methods in later chapters of this thesis can be helpful to estimate the parameters on which building damage assessment depends.

Table 3.1 The adopted coefficients for semi–analytical approach

I_d	0.3	0.3	0.9	0.9
C_t/D_t	2.4	4.4	2.4	4.4
m_a	-0.12	-0.02	-0.16	-0.15
q_a	2.21	2.18	1.46	1.89
m_b	0.11	0.34	0.20	0.03
q_b	0	0	0	0
m_1	0.13	0	0.11	0
q_1	1.07	1.49	1.38	1.11
m_2	0.15	0.07	0.14	0.14
q_2	-0.73	-0.75	0.05	-0.40
m_3	0.27	16.29	1.18	16.75
q_3	0	0	0	0
m_4	0	0	0	0
q_4	0.83	0.90	0.83	0.90
m_5	3.33	1.00	11.53	1.00
q_5	0	0	0	0
m_6	0	0	0	0
q_6	0.10	0.10	0.10	0.10
m_{ax}	-0.12	-0.02	-0.16	-0.15
q_{ax}	2.21	2.18	1.46	1.89
m_{bx}	0.11	0.16	0.20	0.03
q_{bx}	0	0	0	0
m_{1x}	0	0	0	0.48
q_{1x}	3.89	26.36	7.06	5.01
m_{2x}	-0.09	-0.79	-0.03	-0.36
q_{2x}	0.63	4.37	1.40	2.43
m_{3x}	0.27	16.29	1.18	16.75
q_{3x}	0	0	0	0
m_{4x}	0	0	0	0
q_{4x}	0.83	0.90	0.83	0.90
m_{5x}	3.33	1.00	11.53	1.00
q_{5x}	0	0	0	0
m_{6x}	0	0	0	0
q_{6x}	0.10	0.10	0.10	0.10

Table 3.2 Centrifuge scaling laws (Taylor, 1995a)

Parameter	**metric unit**	**model scale**	**prototype scale**
Gravity	m/S^2	N	1
Length	m	1	N
Area	m^2	1	N^2
Volume	m^3	1	N^3
Weight, Force	$N = kg \cdot m/s^2$	1	N^2
Density	kg/m^3	1	1
Stress and Pressure	$Pa = N/m^2$	1	1
Strain	$-$	1	1
Bending stiffness, EI	Nm^2	1	N^4
Axial stiffness, EA	N	1	N^2

Table 3.3 Classification of visible damage to walls (Burland et al., 1976)

Category of damage	**Degree of severity**	**Description of typical damage**	**Approximate crack width, mm**
0	Negligible	Negligible and hairline cracks of less than about 0.1 mm are classed as negligible.	< 0.1
1	Very slight	Fine cracks which can easily be treated during normal decoration. Perhaps isolated slight fracture in building. Cracks in external brickwork visible on close inspection.	≤ 1
2	Slight	Cracks easily filled. Redecoration probably required. Several slight fractures showing inside of building. Cracks are visible externally and some repainting may be required externally to ensure weather tightness. Doors and windows may stick slightly.	≤ 5
3	Moderate	The cracks require some opening up and can be patched by a mason. Recurrent cracks can be masked by suitable lining. Repainting of external brickwork and possibly a small amount of brickwork to be replaced. Doors and windows sticking. Service pipes may fracture, Weather tightness often impaired.	5 to 15, or number of cracks ≥ 3
4	Severe	Extensive repair work involving breaking–out and replacing sections of walls especially over doors and windows. Windows and door frames distorted, floor sloping noticeably. Walls leaning or bulging noticeably, some loss of bearing in beams. Service pipes disrupted.	15 to 25, but also depends on number of cracks
5	Very severe	This requires a major repair job involving partial or complete re-building. Beams lose bearing, walls lean badly a require shoring. Windows broken with distortion. Danger of instability.	Usually ≥ 25, but depends on number of cracks

Table 3.4 Building damage categories (Boscardin and Cording, 1989)

Category of damage	**Normal degree of severity**	**Limiting tensile strain**
0	negligible	0.000 – 0.050
1	very slight	0.050 – 0.075
2	slight	0.075 – 0.150
3	moderate	0.150 – 0.300
4 to 5	severe to very severe	> 0.300

Table 3.5 Critical Cracking Strain Data (Boone, 1996)

Test condition	**Mode of deformation**	**Critical strain** (%)
Brick buildings with L/H > 3	Tensile from flexure	0.050
Full scale frames with brick infill	Diagonal–tensile	0.081 – 0.137
Full scale frames with brick infill	Shear approximation	0.160 – 0.270
Hollow tile and clinker block, brickwork	Shear distortions	0.220 – 0.330
Hollow tile and clinker block, brickwork	Diagonal-tensile	0.110 – 0.160
Full scale brick walls with supporting concrete beams, 1.2 < L/H < 3.0	Tensile from flexure	0.038 – 0.060
Concrete beams supporting brick walls	Tensile from flexure	0.0350
Fiberboard or polywood on wood frame	Shear strain	0.600 – 1.660
Gypsum/fiberboard/plaster on wood frame	Shear strain	0.370 – 0.700
Structural clay tiles with cement-line	Shear strain	0.100
Clay brick with cement-lime mortar	Shear strain	0.100 – 0.200
Cement–line mortared concrete blocks	Shear strain	0.100
Core samples of brick and mortar	Tension	0.001 – 0.010
Full–scale brick walls in field test	Tension	0.020 – 0.030
Reevaluation of full-scale wall panel tests	Principle tensile	0.020 – 0.030

Chapter 4

Finite Element Analysis

4.1 Introduction

This chapter presents a general explanation about finite element analysis and the finite element software ABAQUS. The element types and the general procedures to create a model are briefly described. Material properties used in this research, the tunnel construction technique and the soil–building interface are also presented.

4.2 Numerical Methods

Numerical methods are techniques used to approximate engineering problems. An engineering problem can be defined as a mathematical model of a physical condition. A mathematical model of a physical condition consists of a set of differential equations showing different aspects of the physical situation in terms of variables (Moaveni, 1999; Reddy, 2006). The solution of the differential equations of some mathematical models are difficult to obtain by exact methods. An alternative to an exact method can be a numerical method to obtain an accurate yet approximate solution (Reddy, 2006). An exact solution of a problem describes the exact behaviour of a condition at all points while a numerical solution shows an approximation of a system at different points called nodes (Moaveni, 1999).

A numerical solution of a differential equation may contain initial and boundary conditions. Consider Equation 4.1 which is assumed to be a differential equation.

$$f''(x) = Cx \tag{4.1}$$

If a set of conditions are given to Equation 4.1 at the same value of x (i.e. $f(0) = 2$, $f'(0) = 1$), the system is called an initial value problem. When the conditions are given at different values of x (i.e. $f(0) = 2$, $f(1) = 1$), the system is called a boundary value problem (Davis, 1984).

Two common numerical methods that are used to solve differential equations in engineering are the finite difference and finite element analyses. These two methods are powerful techniques used in various fields and have a wide range of engineering applications, including geotechnical engineering. The finite difference is an older numerical method as compared to the finite element method. It uses a local Taylor expansion to approximate the derivatives of functions (Peiro and Sherwin, 2005). Furthermore, the finite difference method was the first numerical method utilised in the field of geomechanics. The method was used before the appearance of computers to reduce differential equations to a set of linear equations in order to obtain their solutions by a simple classical method (Bobet, 2010).

Moaveni (1999) explained that the finite difference method has some advantages such as being easy to understand and apply, and also less time consuming. However, it is most appropriate for the solution of relatively simple problems. When the geometry becomes complicated or the problem has complex boundary conditions, the solution becomes complicated. Furthermore, Potts et al. (2001) clarified that the applicability and accuracy of the finite element and finite difference methods in geotechnics are mostly dependent on the capability of the constitutive models (explained later in this chapter) to replicate the real behaviour of soil as well as the appropriateness of the imposed boundary conditions. A brief explanation of finite element analysis is presented in the following section.

4.3 Finite Element Analysis

The finite element method (FE) is a numerical approach utilised to obtain solutions to a great variety of engineering problems. The advancement of computers has led to considerable development of the finite element method (Bull, 1993). Moaveni (1999) presented a brief history about FE analysis and stated that the starting point of the modern FE method was in the early 1900s due to the utilisation of discrete equivalent elastic bars by some researchers to model elastic continua. Based on published papers, Courant (1943) was defined as the person who first developed the FE method. After Courant, the method was developed to a greater extent by Boeing in the 1950s when he, and some later investigators, modelled airplane wings using triangular stress elements. After 1960, the term finite element was made

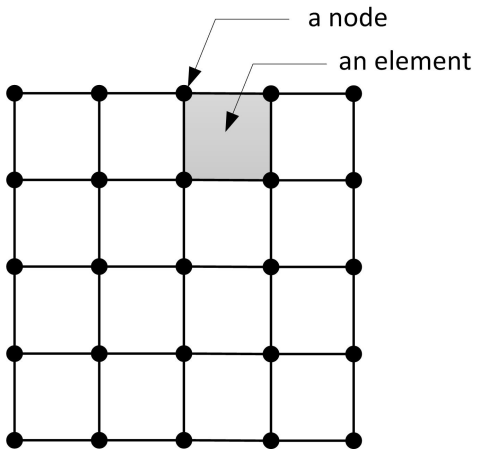

Fig. 4.1 Elements and nodes in FE method

popular by Clough, and this method was applied by other researchers to different fields of engineering.

According to Davies (2011), the utilisation of finite elements as a simple principle belongs to much older times than the 1900s. Additionally, he stated that the modern FE method was first used in structural engineering, and Hrennikoff (1941) and McHenry (1943) were the first who tried to develop the FE method for aircraft structural design.

Nghiem (2009) explained the general theory and principles of FE method. In this method, a member is modelled as a collection of finite tiny parts known as an element. Each element has a geometrical shape. The elements are affixed to each other through their nodes. These nodes have a number of degrees of freedom (DOF) based on the type of the model. In geotechnics, the degrees of freedom are usually displacements. The solution of the algorithmic equations in FE analysis leads to the determination of the degrees of freedom. Figure 4.1 shows typical nodes and elements in FE analysis.

Three principal steps of FE analysis are demonstrated in Roylance (2001): preprocessing, analysis and postprocessing. In the preprocessing step, a model is constructed for analysis in a way that its geometry is divided into elements connected at their nodes. The displacement of some of these nodes is known and the load of the others is predefined. The preparation of these models may require a significant amount of time. In the analysis step, the data prepared by the preprocessor is input to the FE code, and then, the code creates linear or nonlinear system and solves the equations. The system consists of three main parameters in the form of matrices called displacement, force and stiffness matrices, as in Equation 4.2.

$$K_{ij}u_{ij} = F_{ij} \tag{4.2}$$

where u_{ij} and F_{ij} are the nodal displacements and nodal applied forces, respectively, and K_{ij} is the stiffness matrix which is based on the type of problem being solved. After analysing the data and solving the algebraic equations, the postprocessing step starts in which the results are displayed.

An element in a finite element mesh (Figure 4.1) is treated as a separate part from the original object (before meshing). Algebraic equations are developed for each independent finite element, and then, the elements are returned to the original locations of the analysed object and all developed relationships are then assembled (Reddy, 2006).

There are three fundamental requirements for the solution of any static boundary value problem: equilibrium, compatibility and material behaviour. The equilibrium of the system should be satisfied; compatibility is satisfied through "the continuity of the displacement field in which no gaps or overlaps must occur in the problem domain during the deformation process;" the material behaviour relates strains to stresses, and is described by the constitutive equation $\sigma = D\varepsilon$ where σ is stresses, ε is strains and D is the constitutive matrix (Franzius, 2003).

There are different shapes, sizes, number and configurations of finite elements. The selection of the elements should be made carefully such that the meshed part represents the original part as closely as possible without adding extra computational effort to solve the problem. The geometry of the part and the required number of coordinates play an important role in the selection of the correct element type. One, two and three dimensional elements can be chosen based on the geometry, material properties and problem field variables. For example, deformation of a bar under axial loads can be modelled by one-dimensional elements, deformation of a plate can be simulated using two dimensional elements, and the advancement of tunnel head construction can be modelled by three-dimensional elements (Rao, 2004).

4.4 An Introduction to ABAQUS

SIMULIA (2012) is a detailed ABAQUS user's manual including comprehensive explanation about the software. The software is FE based and contains five programs: ABAQUS/Standard which is a general-purpose FE program, ABAQUS/Explicit which is an explicit dynamics FE program, ABAQUS/CFD which is related to fluid dynamics, ABAQUS/CAE which is an interactive environment and ABAQUS/Viewer which is a subset of ABAQUS/CAE. The simulations of this research depend on ABAQUS/Standard (using ABAQUS/CAE).

ABAQUS is extensively used in the academic field as it allows the creation and modelling of different types of materials and has the capability to simulate interactions between different elements and parts. The software offers different types of elements with various ways of meshing. Different material behaviour can be simulated with various constitutive laws. Additionally, new constitutive models can be added to the program via user subroutines. For instance, UMAT allows the addition of user constitutive models to the software, DISP can be used to define user-defined displacements, and DLOAD is used to introduce a load which is a function of time or position.

Moreover, the software performs a complete analysis through three stages: pre-processing or modelling which involves the creation of an input file, processing (FE analysis) which produces an output visual file, and post-processing in which reports, images and animations are generated. Furthermore, the program accepts input files (modelling) from CAD software, and monitoring is available to the processing stage.

In the following sections, various aspects of ABAQUS that are relevant to the modelling done in this project are discussed. These include: meshing techniques, element types, material properties, constitutive laws, interface and analysis details. It is worth noting that the information presented about meshing techniques, element types and interfaces in ABAQUS is from the ABAQUS user's manual (SIMULIA, 2012).

4.5 General Procedures to Create a Model in ABAQUS/CAE

Generally, there are 9 steps to create a model, run it and obtain results in ABAQUS/CAE. Each step is briefly explained below, and if necessary, more detail is provided in relevant sections.

1. Part

Parts are used to represent the geometry of objects in ABAQUS. The geometry of the object that is going to be analysed is either created in ABAQUS/CAE using part module, or imported from other applications. Figure 4.2a shows parts of a model.

2. Property

The property module is used to create a material and define its properties. Sections, in which the material and the cross sectional geometry (if necessary) are specified, are also defined in the property module. Each part should be assigned a section.

3. Assembly

Each part that is created in the part module is independent of the other parts in the model, and may have a different orientation. The assembly module is used to define the final geometry

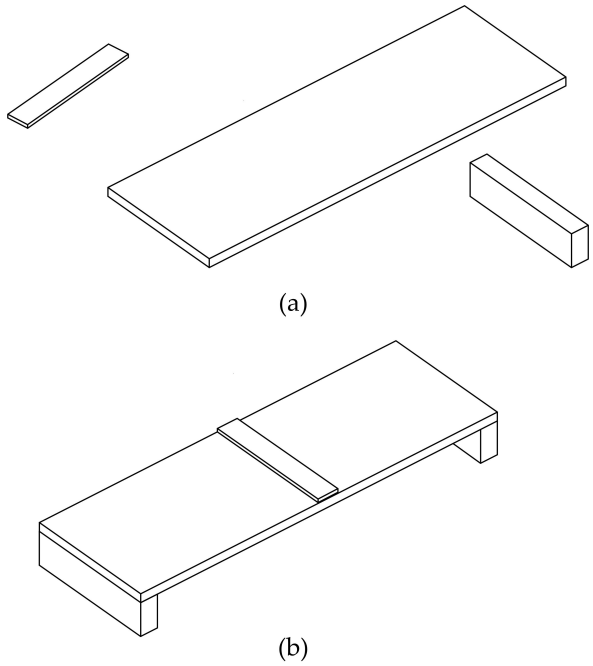

Fig. 4.2 (a) Parts, and (b) assembly in ABAQUS/CAE

of the global model by creating instances of a part, and then positioning them relative to each other. Each instance (i.e. inserted part to the assembly) can be copied as many times as required. Figure 4.2b shows an assembly of a model.

4. Steps

The step module is used to define the analysis steps of the model. Different steps are available in the step module, such as: Geostatic step to define geostatic stresses in a geotechnical analysis; Soils to analyse problems including coupled pore fluid diffusion and stress analysis; General, static analysis to apply loads to the model. It should be noted that there is a default (compulsory) initial step to define boundary and initial conditions to the model.

5. Interaction

The interaction module is used to define interaction between different parts of the model. This module provides different types of constraints (to constrain the degrees of freedom between parts or regions of a model, such as multi-point constraints, tie, embedded region, equation), and interactions (e.g. surface-to-surface contact, self-contact) in which interaction properties (e.g. contact, film condition) are defined. The detail relevant to this research is given in Section 4.9.

6. Load

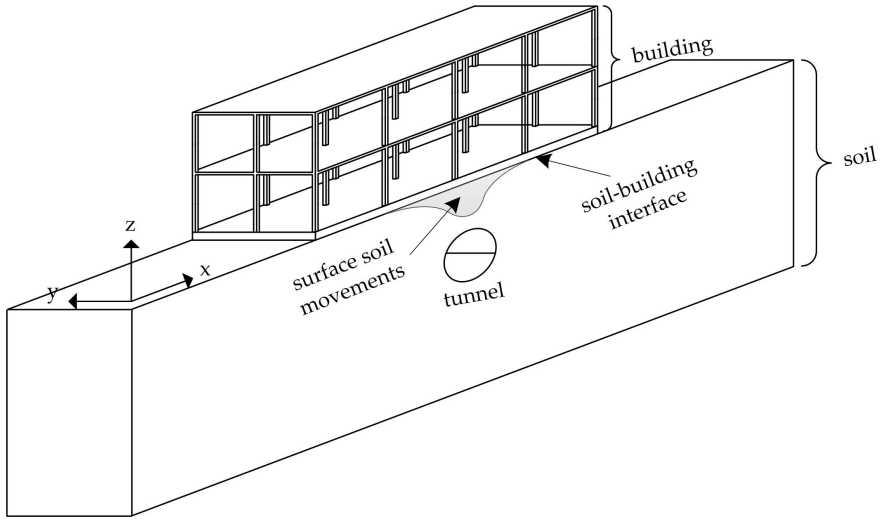

Fig. 4.3 A generic model of tunnel–soil–building interaction problem

The load module is used to to apply loads and to define boundary conditions. Initial conditions such as geostatic stresses, pore water pressure and saturation degree are also defined in the load module.

7. Mesh

The mesh module is utilised to mesh the model (either parts or assembly). The module contains features such as: mesh controls (the technique to mesh the model and specify element shapes), element types (to assign a particular element type to the model), and seeds (to specify the size and number of elements in the model). More information about this module is given in Section 4.6.

8. Job

The job module is used to create a job and to submit it for analysis. If the created model does not have any errors and is ready for analysis, it will start running to analyse the problem.

9. Visualization

After successfully completion of the job, the results become ready to view in the visualization module. The visualization module reads the output database generated by ABAQUS/CAE during the analysis.

Figure 4.3 shows a generic model of the tunnel–soil–building interaction problem considered in this project. The building and the soil are created as two separate parts. The final global model is created in assembly, and then an appropriate interface as well as boundary conditions are assigned to the model. The detail of the material properties, boundary conditions and the soil–building interface are presented in the following sections.

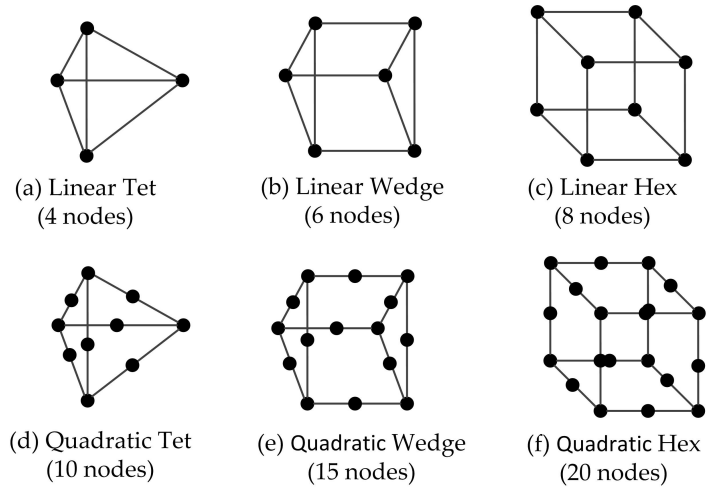

Fig. 4.4 Finite element shapes and node numbers

4.6 Meshing and Elements in ABAQUS

There are four meshing techniques in ABAQUS/CAE, as listed below:

- Free meshing
- Structured meshing
- Sweep meshing
- Bottom-up meshing

In addition, four shapes of elements are offered which are: Hex, Hex-dominated, Tet, and Wedge. Each element shape can be linear or quadratic. Figure 4.4 shows examples of the element shapes for linear and quadratic elements.

Free meshing is the most flexible technique which offers meshing without pre-defining patterns, and is available with Tet elements. **Sweep** meshing is used to create complicated meshes. It is available with all element shapes except Tet elements. **Structured** meshing technique is used to create structured meshes by predefining meshing regions. This technique is available with the Hex element shape. The most control over the created mesh can be obtained using the structured meshing technique. Partitioning the part is a good choice to obtain a meshable region with the structured technique. The final meshing technique is **bottom-up**, which is the most complicated technique and should be used carefully to mesh highly complex geometries.

ABAQUS provides a variety of element types for both standard and explicit analyses. Elements have different characteristics like family (i.e. 3D stress, continuum shell, heat transfer), number of nodes (Figure 4.4), degree of freedom per node (i.e. displacement, rotation) and integration (i.e. reduced and full integration). Linear elements have nodes only at their corners (Figure 4.4a,b,c) while quadratic elements have an extra node at the middle of each edge (Figure 4.4d,e,f). Elements also have unique names in ABAQUS. For instance, C3D8R stands for Continuum, 3D, 8-node, reduced integration elements; S4R stands for Shell, 4-node, reduced integration elements.

Examples of the commonly used element families are truss, beam, shell and solid continuum elements. Truss elements are used to model one dimensional bars that are subjected to axial forces (tensile or compressive), for example truss members. Beam elements are used to model members that have small cross sectional dimensions compared to their length. The 3D member is approximated to a 1D beam; only the longitudinal centreline is created and the cross sectional dimensions are assigned to the part via material cross section properties. These elements accept displacement and rotation degrees of freedom. Examples include beams and columns. Shell elements are used to model members that have a small thickness compared to their length and width. The 3D member is approximated as a 2D member. In conventional shell elements, the length and the width are created, and the thickness is given to the part via the material cross section properties; continuum shell elements allow the creation of the 3D part. Examples include slabs and raft foundations. Solid continuum elements are used to create 3D members, and are suitable for linear and non-linear analyses including contact and plasticity problems. They only accept displacement degrees of freedom; they do not allow rotation at the connections.

C3D8R solid elements were used throughout this research to model the soil and the structural parts. The accuracy of the results are checked in different stages by comparing the results with available data and exact solutions. The reason for choosing this type of element is that an acceptable accuracy with less time can be obtained. Furthermore, the problem of shear locking in the elements is eliminated. A very fine mesh is used to obtain accurate results and to avoid the occurrence of hourglassing in the elements. The problems of shear locking and hourglassing are discussed in Section 4.6.1.

ABAQUS uses numerical methods for any required integration over the element volume; for most elements, Gaussian quadrature is used. There are integration points within each element in which the material response is evaluated (i.e. the primary variables for the function that should be integrated are solved). This integration can be full or reduced depending on the number of integration points. For example, the element type C3D20 (continuum 3D, 20

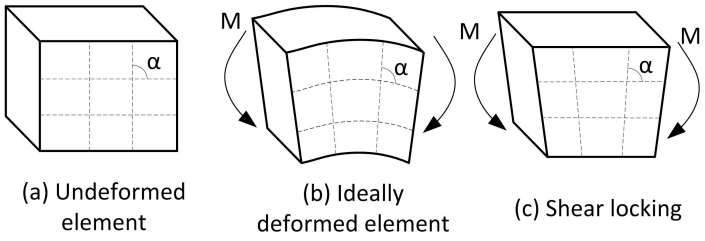

Fig. 4.5 Shear locking of an element (after Sun, 2006)

nodes) uses 27 integration points while for the reduced integration element (C3D20R), there are only 8 points. The choice of the integration method should be made carefully to avoid accuracy problems. For quadratic elements, the reduced integration in ABAQUS/standard generally leads to more accurate results than the full integration, but for linear elements, the accuracy depends on the nature of the problem. The required time and cost for the reduced integration is significantly less than that for the full integration. It should be noted that for the numerical analyses of this research, the choice of reduced integration was used.

4.6.1 Shear locking and hourglassing

Shear locking and hourglassing are two possible problems that may occur in FE analysis. They can lead to inaccurate numerical results if they are not taken into consideration before analysing the engineering problem.

Shear locking occurs when an element becomes overly stiff in bending because of the existence of several integration points. This problem is mainly caused by fully integrated elements. Figure 4.5a shows an undeformed element. When it is subjected to bending moments, it is supposed to deform as in Figure 4.5b in which horizontal dashed lines deform to curves, and α remains at a right angle. When shear locking occurs due to integration points, a deformation like that of Figure 4.5c happens in which the horizontal lines remain straight and the angle α does not remain 90°. This leads to the generation of shear deformations instead of bending deformations, and erroneous results are computed (Sun, 2006).

Linear elements with reduced integration may experience deformations without creating strains; this phenomenon is called Hourglassing which involves deformations with a zero-energy mode. It happens in elements having only one integration point. The element C3D8R has only one integration point while C3D8 has eight points. This reduction in integration points is useful in terms of tolerance to shape distortions. Fully integrated elements become less accurate when undergoing large deformations. However, the occurrence of hourglassing

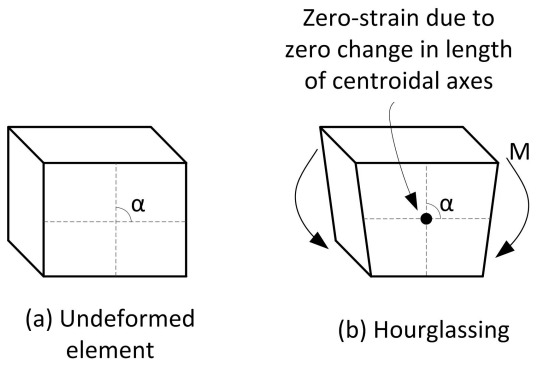

Fig. 4.6 Occurrence of hourglassing (after Sun, 2006)

should be avoided when using reduced integration. Coarse meshing can be a source of hourglassing. Although ABAQUS has default hourglassing control to reduce this problem, coarse meshing should still be avoided especially through the thickness of the model (z-direction in Figure 4.3). Single layer elements through the thickness may cause hourglassing even in quadratic elements. Figure 4.6 shows the occurrence of hourglassing in an element due to the applied moments. The element undergoes deformations, but the length of the centroidal axes does not change leading to zero-strains at the integration point. For the models of this project, the problem of hourglassing was avoided by having a fine mesh for each part, especially along the thickness of the model (z-direction in Figure 4.3).

4.7 Constitutive Models and ABAQUS Material Properties

Material models are mathematical expressions used to describe the stress-strain behaviour of materials. These models are vitally important in numerical analyses; the accuracy of results mostly depends on the appropriateness of the material model. It is worth noting that ABAQUS contains several constitutive models related to soil, such as: linear elastic model, and plastic models of Mohr-Coulomb and Drucker Prager. Other material models can be added to the program via user subroutines.

It is worth noting that in tunnelling, the elastic parameters are generally more influential on the response of soil than the strength parameters. This is because the tunnel construction does not cause significant plasticity to the soil; mainly a small region around the tunnel head experiences plastic deformations. Several researchers have reported that soil deformations due to tunnelling are not sufficiently large to cause plastic changes to the soil; a nonlinear

elastic model can provide a good prediction of tunnelling induced ground displacements (Cheng et al., 2007; Dasari, 1996; Giardina et al., 2015).

The results of this project mainly relate to the elastic properties. For the sections in which plastic behaviour is considered for soil, the elastic perfectly plastic model with Mohr-Coulomb failure criterion is used. It should be noted that the Mohr-Coulomb criterion is a simple model that has an extensive use in geotechnical engineering. The elastic parameters in the model are Young's modulus and Poisson's ratio. The failure criterion is defined by friction angle, ϕ, and cohesion, c; the flow rule is defined by the dilation angle, ψ (Ti et al., 2009). It can be said that the parameters of the friction angle and cohesion are usually more easily obtained compared to the properties of other soil material models (Alshkane, 2015).

For most analyses in this thesis, the elastic properties of the soil were: $E_s = 35$ MPa and $\nu_s = 0.25$. The value of the elastic modulus was changed in some sections to investigate the effect of elastic modulus. Furthermore, the soil was assumed to be a fine dry sand similar to Fraction E Leighton Buzzard silica sand, or simply, fraction E sand (Zhao, 2008). The Poisson's ratio of a similar sand was assigned a value of 0.25 in the work of Giardina et al. (2015). Moreover, values of Poisson's ratio in different sources range from 0.20 to 0.45 for medium to dense sand (Das, 2010; Gunaratne, 2006). Elastic modulus was assumed to be constant (throughout the depth) in this research, despite the fact that it increases with depth in cohesionless sands (Das, 2010). Giardina et al. (2015) used a linear relationship to increase the soil elastic modulus with depth, with a value of 25 MPa at the surface. Zhao (2008) presented values of secant Young's modulus for fraction E sand based on triaxial test results. The values of the elastic modulus for 0.01% axial strain were between 25 and 105 MPa. Representative values of E_s given in Das (2010) range from 10 MPa to 70 MPa for loose to dense sands. A representative value of 35 MPa was taken in this work to have a constant elastic modulus.

Regarding the strength parameters of the soil, a friction angle of 35° and a dilation angle of one third of the friction angle were assigned to the soil. Furthermore, a cohesion of 5 kPa was used in the analyses to avoid numerical convergence problems. The unit weight of the sand was 15.9 kN/m^3. The chosen value of the friction angle is based on the approximate values given in the literature for sand. Approximate values range from 30° to 40° from loose to dense sands (Bowles, 1997; Das, 2010). Additionally, $\phi = 35°$ was also used by Elkayam (2013) in his numerical verification of soil–structure interaction formulation (using FLAC^{3D}) for a soil composed of sand.

The dilation angle of cohesionless soils is usually small. Vermeer and Borst (1984) reported that for a very dense sand, the dilation angle reaches 15° while it is just a few

degrees for a loose sand. A dilation value of one third of the friction angle is 11.6° which is below the maximum dilation angle proposed by Vermeer and Borst (1984). Vermeer et al. (2002) also stated that the variation of angle of dilation did not have a significant effect on the results of their tunnel head stability analysis. Furthermore, a set of simulations were performed in this research in which the dilation angle of the soil varied from 0 to 23° with and without a beam of 1 m thickness. It was found that there was no effect of the angle of dilatation on the results. The details of the modelled soil and building used for this verification is presented in Chapter 7.

It should be noted that if numerical analyses are performed using the Mohr–Coulomb failure criterion with an associated plastic flow, the friction and the dilation angles will be the same. This may lead to an overestimation of volume changes in granular soils when plastic failure occurs. For this reason, non–associated plastic flow was proposed in which the dilation angle is smaller than the friction angle (Liu, 2016).

The true cohesion of a dry sand is theoretically zero. As it will be explained in the later sections in this chapter, numerical simulations of the tunnel construction adopted a displacement control process. A very small value of cohesion caused some numerical convergence problems; for this reason, a value of 5 kPa was chosen to eliminate such problems. It is worth noting that in a set of simulations done in this work, the value of cohesion was varied from 1 kPa to 5 kPa, but similar to the case of dilation angle, it showed no effect on the results.

On the other hand, the building was assumed to be a concrete framed building; more detail of the building geometry is presented in the relevant chapters. The concrete was assigned an elastic modulus between 20 and 60 GPa with a Poissoin's ratio of 0.15. The elastic modulus was changed in some sections to investigate its effect on the soil–structure analysis results. A value of 20 to 60 GPa for the elastic modulus yields a concrete compressive strength of about 18 to 163 MPa based on the relationship $E_c = 4700\sqrt{f_c^{'}}$ for normal concrete, where $f_c^{'}$ is the concrete compressive strength for a cylindrical sample (ACI-Building-Code, 2011). For the majority of the simulations, realistic values of 23 and 30 GPa were used (which lead to a compressive strength of 24 and 41 MPa, respectively).

Although values of concrete compressive strength greater than or equal to 41 MPa are high for reinforced concrete buildings constructed in the past, they were chosen to represent a reasonably stiff building so that a higher estimate of the building effect on ground displacements due to tunnelling could be obtained. It is worth mentioning that based on section 5.1.1 of ACI-Building-Code (2011), a concrete with a compressive strength of less than 17 MPa should not be used in the design and construction of reinforced concrete

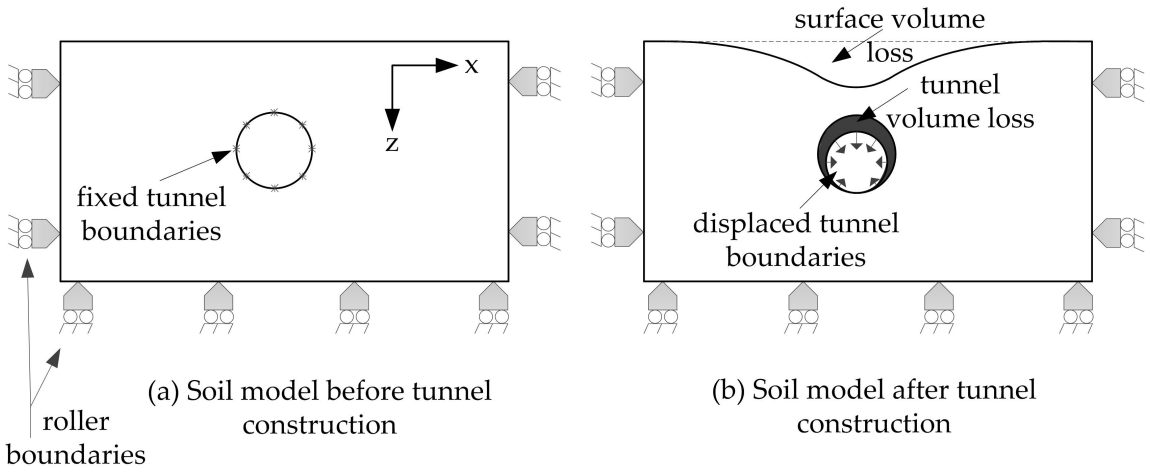

Fig. 4.7 Tunnel simulation using displacement control method

structures, however the minimum recommended value is 21 MPa which approximately gives an elastic modulus of 21.5 GPa.

4.8 Tunnel Construction

For tunnelling in an elastic-plastic medium, the tunnel excavation was simulated using the displacement control method described by Cheng et al. (2007) in which the tunnel volume loss was not distributed uniformly; the maximum displacement occurred at the crown while there were no displacements at the invert. The direction of the displacement vectors were oriented towards the centre of the converged tunnel. It should be noted that the tunnel simulation was included in Chapters 7 and 8. For tunnelling in an elastic medium, Chapter 7 contains the suggestion of a method to simulate tunnelling and to evaluate soil–structure interaction.

The modelled tunnel had a diameter of 4.65 m. Its depth was variable, and mentioned in the relevant chapters. The tunnel was excavated instantaneously along its length creating a plane strain problem in the greenfield situation. The boundaries of the model and the fineness of the mesh were chosen after analysing different scenarios to eliminate their effects on the analysis results. The size of the model is given in relevant chapters. As shown in Figure 4.7, roller boundaries were applied to the soil model. The movement perpendicular to each plane was fixed, and the other components were free.

Before starting the numerical excavation of the tunnel, initial soil stresses were calculated and given to the FE program. The total vertical stress of the soil, which was also the total

effective stress since the soil did not contain water, was calculated from: $\sigma_{s,v} = \gamma_s \times z$ where $\sigma_{s,v}$ is the soil vertical stress. The coefficient of lateral earth pressure, K_0, was given to the program to calculate the horizontal insitu stresses from: $\sigma_{s,h} = K_0 \times \sigma_{s,v}$ where $\sigma_{s,h}$ is the horizontal ground stresses. The coefficient of lateral earth pressure was assigned a value of 0.5 which was an assumed value for sands in centrifuge experiments (Elkayam, 2013; Zhou, 2014).

In the first step of the numerical tunnel construction, the nodes of the tunnel boundary were fixed in all directions (x,y and z) and initial soil stresses were defined, as shown in Figure 4.7a. The elements within the tunnel were removed prior to the tunnel construction. In the second step, the nodes around the perimeter of the tunnel were displaced by an amount calculated based on the predefined tunnel volume loss and assumed deformed shape. A typical deformed tunnel is shown in Figure 4.7b.

4.9 Soil–Building Interface

ABAQUS offers various types of contacts (interaction and constraints) to model the contact surface between two deformable bodies that are in touch at one or more points. Modelling the contact behaviour between two surfaces is complicated and requires care and knowledge of the user (SIMULIA, 2012). In this work, a tie constraint to model the soil–building interface was used in the analyses where the building weight was not included, and surface-to-surface contact was used in the analyses with weighted buildings.

A tie constraint firmly attaches two disconnected surfaces together for the duration of a simulation, and does not allow any relative slip or separation between them. This type of constraint is independent of the meshing type of the two bodies; it can be used to tie two surfaces with dissimilar meshes.

A surface to surface contact has a normal and a tangential response. The chosen normal behaviour has a hard contact. In the normal behaviour with a hard contact, separation between the surfaces will not happen unless the contact pressure between them becomes zero or negative. With regard to the tangential behaviour, it is a rough contact for some simulations and a frictionless contact for others. The tangential component allows sliding of surfaces relative to each other, with frictional shear stresses developing.

It is worth noting that none of these interfaces represent reality since separation is not allowed and relative movement between the surfaces is prevented in some cases. There are two main reasons for choosing these two interface types. A value of μ between 0 and 1 could have been used, but it is difficult to know what value best represents reality. Choosing the

upper and lower limits ensures that the behaviour of the contact interface falls between these two limits. Second, the foundation of the building is not sufficiently stiff to allow separation from the soil and to carry the applied building load without the aid of the underlying soil. It should be mentioned that a detailed explanation of the contacts can be found in SIMULIA (2012).

Chapter 5

Cantilever and Fixed–ended Approaches for Estimating Building Bending Stiffness

5.1 Introduction

Several researchers have investigated the effect of structural stiffness on tunnelling- or excavation-induced ground movements, such as Potts and Addenbrooke (1997), Franzius et al. (2006), Dimmock and Mair (2008), Goh and Mair (2014) and Giardina et al. (2015). The methods used to estimate the stiffness of the building vary. Lambe (1973) algebraically added the individual flexural rigidity of all floor slabs, $(EI)_{sl}$, to calculate the whole building stiffness: $(EI)_{bldg} = \sum(EI)_{sl}$. Potts and Addenbrooke (1997) and Franzius et al. (2006) proposed Equations 3.25 and 3.30, respectively, to estimate the relative bending stiffness of the building with respect to the underlying soil. Melis and Rodriguez Ortiz (2001) used a similar approach to Lambe (1973) and estimated the bending stiffness of a building by adding the cross sectional modulus of rigidity of all the floors, walls and the basement together: $K_{b,bldg} = \alpha(EI)_{bldg}$, where $(EI)_{bldg} = \sum[(EI)_{sl} + \sum(EI)_{walls} + \sum(EI)_{basement}]$ and α is a reduction factor to take into account the effect of openings. More detail about the previous work on the role of building stiffness in tunnel–building interaction was presented in Section 3.7.1.

The accurate evaluation of building bending stiffness in tunnel-building interaction analyses is clearly important. However, the real behaviour of three-dimensional (3D) buildings in response to applied displacements from the ground is disregarded to a great extent. Results

from the literature relating to numerical analyses of 3D buildings with structural members provide a good general appreciation of tunnelling effects on buildings, but a detailed understanding of how each panel or storey behaves and how they contribute to the stiffness of the entire building system is still missing. Furthermore, the available methods for building stiffness estimation are mainly based on representing the building as a 2D beam or frame and assuming it acts as a single entity, disregarding the effect of the stiffness contribution of each storey to the global building stiffness. This chapter proposes new methods for estimating the bending stiffness of 3D concrete framed buildings subjected to tunnelling induced ground movements. The methods are based on results obtained from rigorous FE analyses that are able to replicate the real behaviour of structures.

Two cases of tunnel locations are considered in this chapter. The first case (cantilever approach) considers a tunnel located under the building edge or outside the building plan area. The second case (fixed–ended approach) considers a tunnel with its centreline coinciding with the building centreline.

5.2 General Principles

When a tunnel is constructed under a building, the induced ground displacements will cause deformations to the building. Since the building has a stiffness, it will show a resistance against deformations. The focus of this research is on the resistance of the building against bending deformations. If it is assumed that the tunnel is constructed instantaneously along its length, and the effect of the tunnel head advancement is not considered, the building will deform only in the direction perpendicular to the tunnel axis. This means that the building does not deform in the direction parallel to the tunnel axis; this is called one way deformation.

A 2D finite element analysis is sufficient to predict such ground movements if the existence of the building is disregarded. When the presence of the building is simulated, a 3D finite element model is required since the behaviour of the building is three dimensional despite having 2D ground displacements. This is because a concrete framed building consists of different parts: foundation, columns, beams and slabs. This combination of parts does not produce 2D behaviour because of the varying response of the different parts (i.e. axial, flexural) and the space between the structural members. Therefore, this problem can be expressed as a 2D problem globally (considering the global deformation of the soil and the building), and a 3D problem locally for the building.

In this research, the simple definition of the beam bending stiffness is applied to estimate the bending stiffness of the building (i.e., Equation 2.3: $K_b = F_K((EI)_b/L_b^3)$, where K_b is

the beam bending stiffness, $(EI)_b$ is the flexural rigidity and L_b is the length). An analogy is made between the induced deformation of the building and that of a loaded beam. This analogy is fundamental to the proposed approaches as it allows relationships to be developed which relate accurate assessments of building deformation obtained from finite element analyses to those of a simple analytical expression for bending of a beam. All influential parameters included in Equation 2.3 are taken into consideration. A new definition of the beam cross section is introduced to calculate the cross sectional moment of inertia, I. Then, numerical simulations are performed to estimate the correct value of F_K (Equation 2.3). The simple beam–analogy problem is then expanded to cover the effect of the whole building in all directions.

It is worth noting that in this chapter, the building is treated as an independent entity with respect to the soil and the foundation; the method solely focuses on determining the bending stiffness of the building superstructure. A view of the building, including various geometric parameters, is shown in Figure 5.1a. Furthermore, the analysis considers the interaction between a newly constructed tunnel and an existing building that runs perpendicular to the tunnel. The elastic modulus of the structural parts was 30 GPa throughout the analyses of this chapter. It should also be noted that the element number (meshing) of numerical models ranged from 150,000 to 700,000 elements.

5.3 Terminology and Assumptions

Within this chapter, the structure is a reinforced concrete framed building. A panel refers to the combination of a slab, four beams and four columns with a length perpendicular and a width parallel to the tunnel centreline. The slab of each panel has a clear width of B_{sl} and a clear length of L_{sl}. The maximum size of the tested slabs in a panel was 7×8 m ($B_{sl} \times L_{sl}$) due to the need for a very fine mesh to achieve accurate results (based on comparison to analytical solutions). This maximum slab size represents a common panel size in buildings. Figure 5.1a shows an isometric view of a framed building.

Each storey consists of a group of panels at the same level; the ground-floor is referred to as the 1^{st} storey (Figure 5.1a). An individual floor in a panel is made up of a slab and two beams in the direction perpendicular to the tunnel (x-axis in Figure 5.1). The slab and the beams in a floor are considered as a single entity, rather than separate structural elements, as shown in Figure 5.2a.

The following assumptions are made in the analysis.

1. The behaviour of all structural members is elastic.

2. The building is weightless.
3. All joints in the building are rigidly connected.
4. The width of the column cross section (parallel to the tunnel axis) coincides with the width of the floor beam ($b_{col} = b_{fb}$), and its cross sectional height (perpendicular to the tunnel axis) coincides with the width of the supporting beam ($h_{col} = b_{sb}$) (Figure 5.2a).
5. The bay length does not vary along the building length in each direction (e.g. all bays in x-direction are of the same length, but not necessarily the same length as in the y-direction). Furthermore, all storeys are the same in terms of dimensions and material properties.
6. The stiffness of the loaded beam (Figure 5.2b,c) has no effect on the bending stiffness of the floor, and the stiffness of all partition walls (bearing and non-bearing) has no effect on the building bending stiffness. This is a common assumption in the structural design of buildings (Mirhabibi and Soroush, 2013).
7. Tunnelling induced ground displacements are transferred through columns to the loaded beam, which are then distributed uniformly over the floor cross section (the slab and two floor beams), Figure 5.2a,b.

5.4 A cantilever Approach

The cantilever method applies to the case where the plan area of the building does not cover more than half of the cross-section of the tunnel (or lies completely adjacent to the tunnel) (Figure 5.1b). The analogy is made between the building and a cantilever beam because, in the case where the tunnel is not located directly under the building and the soil displacements that occur along the tunnel axis (y-axis in Figure 5.1) are constant, the deformed shape of the building does not include a sagging zone and coincides well with the hogging shape of a cantilever beam loaded at its end. The methodology and the results of the analyses are presented in the following sections.

5.4.1 Methodology

The methodology considers the contribution of the various structural parts to the overall stiffness of the building using five stages. **Stage 1** compares the behaviour of a single floor in an edge panel (Figure 5.2a) to that of a cantilever beam fixed at one end and loaded at

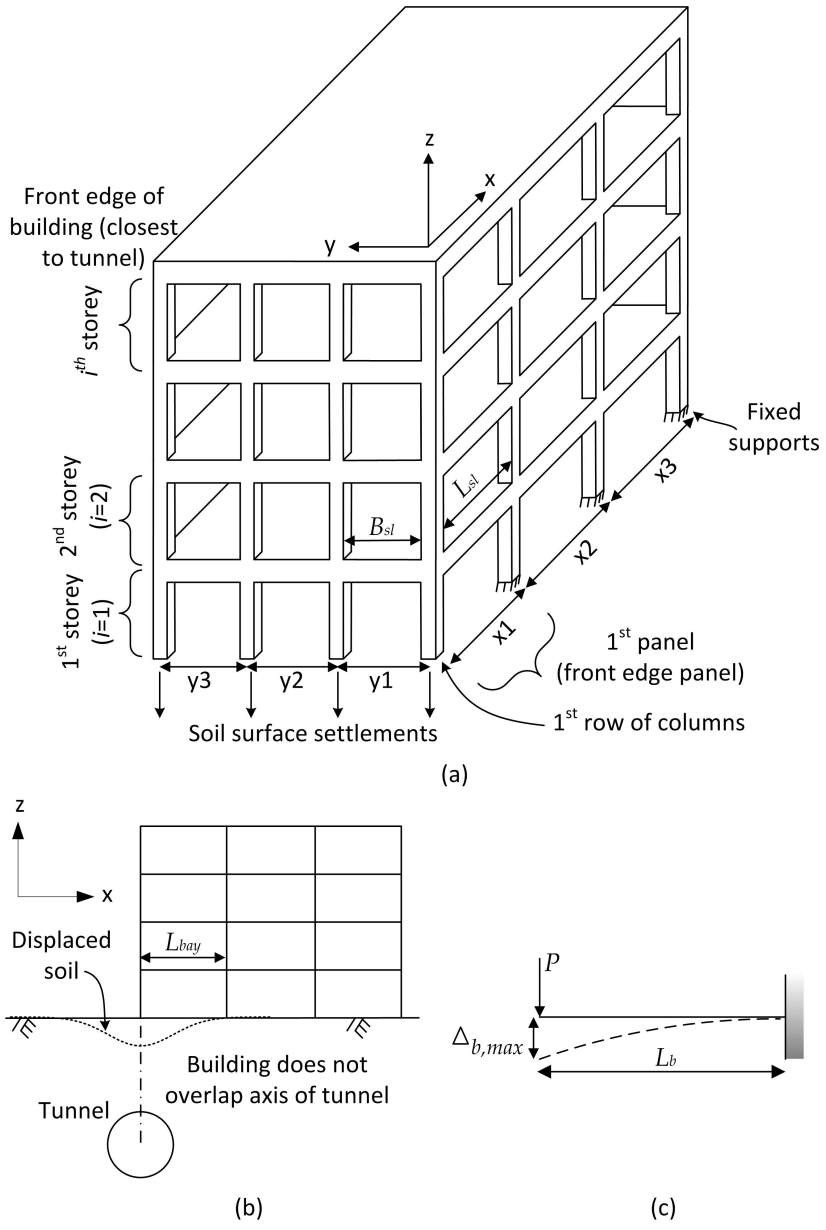

Fig. 5.1 (a) Isometric view of framed building, (b) 2D view of building and tunnel, and (c) cantilever beam

the other (Figure 5.1c). **Stage 2** determines the actual boundary condition of the cantilever floor (which was assumed to be fixed in stage 1) by adding more bays in the x-direction (Figure 5.2c). This step determines the value of F_K in Equation 2.3. **Stage 3** determines the effect of adding storeys (Figure 5.2d). **Stage 4** considers the effect of adding bays in the y-direction. In stages 1 to 4, the assumption was made that only the first panel of the building was affected by soil displacements; **stage 5** considers the case where multiple x-bays are affected (i.e. wider settlement trough).

Figure 5.3 demonstrates a flowchart of the methodology stages and coefficients introduced in each stage.

5.4.2 Stage 1: cantilever beam analysis of single floor

If only the row of edge columns (Figure 5.1a) is subjected to downwards displacement then edge floors will act as cantilever beams (Figure 5.1c). Equation 2.3 can be used for calculating the bending stiffness of a cantilever beam using $F_K = 3$. Numerical simulations in this stage investigate how floors behave when they are fixed at one end and loaded at the other in order to make a direct comparison with analytical results achieved using Equation 2.3.

Stiffness of beams was obtained numerically with a high degree of accuracy (less than 1% error). Figure 5.4 shows the ratio of analytically computed bending stiffness ($K_{b,b,an}$ from Equation 2.3) to the numerically obtained values ($K_{b,b,num}$) for two cantilever beams of different cross sectional dimensions. The figure illustrates that there is an excellent agreement between bending stiffness results of the analytical equation and the numerical simulation.

An edge floor can be represented by a cantilever beam if the transferred forces or displacements are distributed uniformly over its cross section, as shaded in Figure 5.2c (based on assumption 7 in Section 5.3). For this case, the moment of inertia of the floor cross section (I_{fl}) may be used in Equation 2.3. I_{fl} includes the moment of inertia of both floor beams and the slab as one rigid body, and is calculated using the parallel axis theorem. Several numerical simulations were done to consider different dimensions of the structural parts. The range of the dimensions are presented in Table 5.1, where t_{sl} is the slab thickness, and b_{fb}, b_{sb} are the cross sectional widths of the floor and supporting beams, respectively.

Table 5.1 Range of sizes of structural parts considered in stage 1 analyses

Parameter	L_{sl}	B_{sl}	t_{sl}	b_{fb} and b_{sb}	h_{fb} and h_{sb}
Range (m)	1 to 8	1 to 7	0.075 to 0.2	0.2 to 0.6	0.2 to 0.75

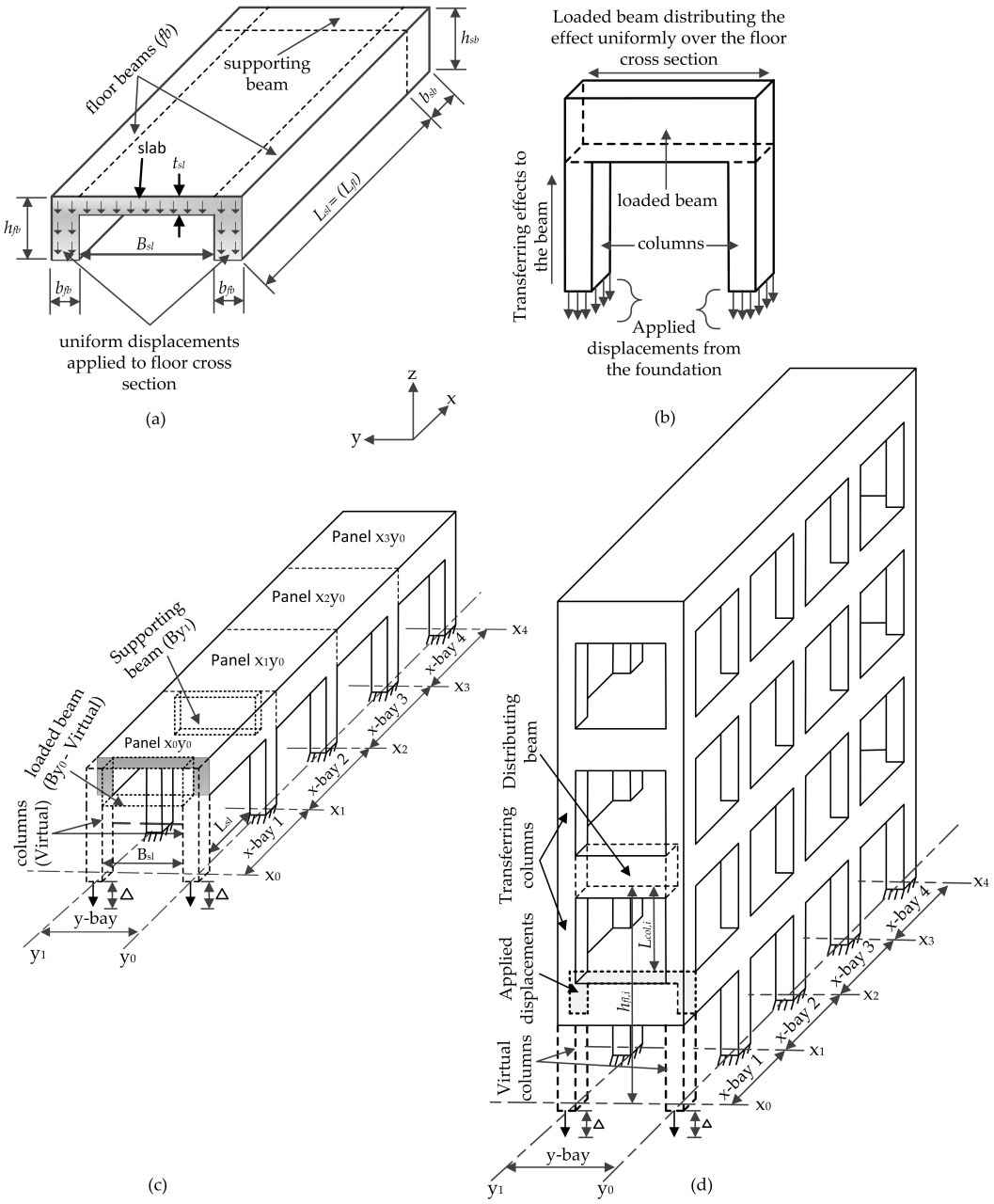

Fig. 5.2 (a) Typical floor subjected to displacements, (b) conveying displacement effects through columns to beams, (c) typical numerical model of a single storey, single y-bay building, (d) single y-bay, multi x-bay and multi storey building

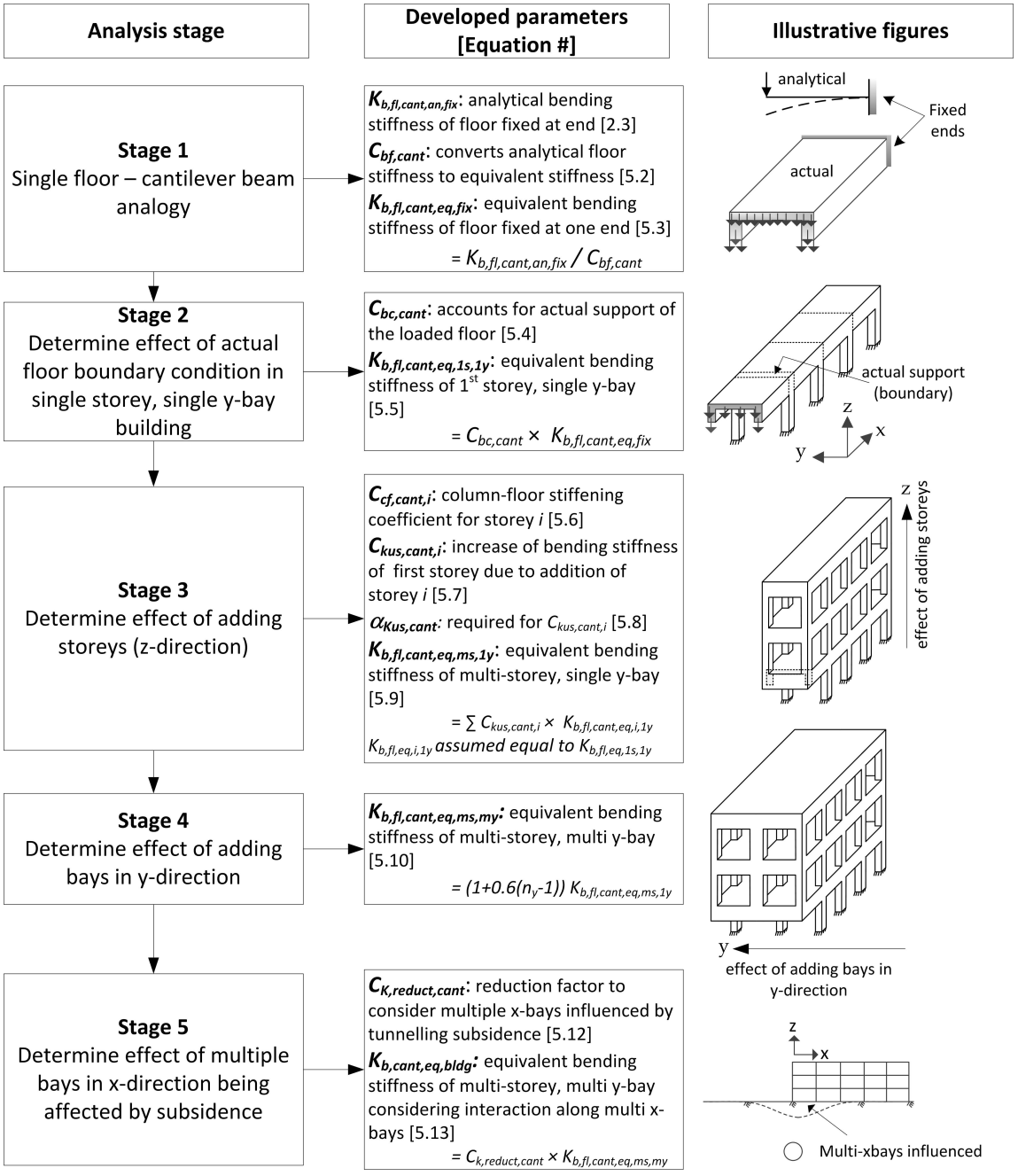

Fig. 5.3 Flow chart of the analysis stages of the cantilever approach

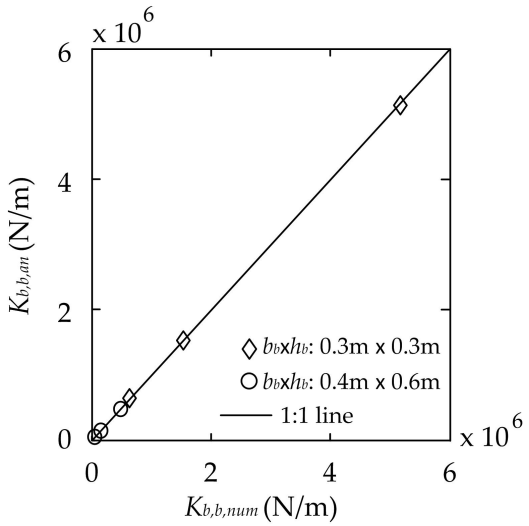

Fig. 5.4 Ratio of the analytical ($K_{b,b,an}$) to numerical ($K_{b,b,num}$) bending stiffness of beams

In this stage, the supporting beam shown in Figure 5.2c was not modelled. Instead, a fixed boundary was applied to that end of the floor (at the end of length L_{fl}, excluding b_{sb}). The applied distributed displacements to the floor cross section are also shown in Figure 5.2a. The sum of the nodal reaction forces were determined and divided by the applied displacement to obtain the numerically determined (subscript *num*) floor bending stiffness ($K_{b,fl,num,fix}$) for a fixed support (subscript fix):

$$K_{b,fl,num,fix} = \frac{\sum P_{nodes}}{\Delta_{applied}} \quad (N/m) \tag{5.1}$$

where $\sum P_{nodes}$ is the sum of the nodal reaction forces created by the applied displacements, and $\Delta_{applied}$ is the applied displacement. For the cantilever approach presented in this section, the subscript *cant* is added to bending stiffness notation: $K_{b,fl,cant,num,fix}$.

Figure 5.5a shows the ratio of floor bending stiffness calculated using Equation 2.3 ($K_{b,fl,cant,an,fix}$), where subscript *cant* indicates the cantilever approach, and *an* indicates an analytically determined value, to that determined from the numerical analysis ($K_{b,fl,cant,num,fix}$) at different values of L_{sl}/B_{sl}. In one set of simulations, the slab width (B_{sl}) and beam cross sections were constant and only the length of the slab (L_{sl}) was changed (variable L_{sl}). In the other set, L_{sl} and beam cross sections were constant and B_{sl} was varied (variable B_{sl}). Figure 5.5a demonstrates that the deflection of the edge floors subjected to displacements along their exterior edge is very close to that of a cantilever beam when $L_{sl}/B_{sl} > 1.25$

(difference of less than 10%). Therefore, Equation 2.3 can be used directly to compute its bending stiffness when $L_{sl}/B_{sl} > 1.25$.

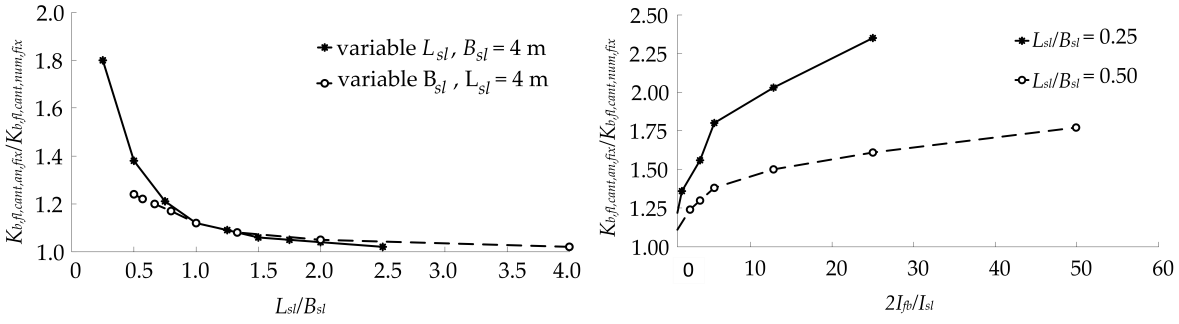

(a) (b)

Fig. 5.5 (a) Ratio of analytical to numerical floor bending stiffness for different L_{sl}/B_{sl} values, (b) effect of $2I_{fb}/I_{sl}$ on floor bending stiffness

The reason for the slight overestimation of the floor bending stiffness for $L_{sl}/B_{sl} > 1.25$ when using Equation 2.3 is related to the difference in the bending stiffness of the individual slab and beams in the floor system. In a monolithically cast beam-slab system, the interior and edge beam cross sections will be T- or L-shaped, as shown in Figure 5.6a (e.g. see McCormac and Brown, 2014; Wight and MacGregor, 2009). When B_{sl} is small compared to L_{sl}, a significant part of the slab acts as a beam (b_{eff}, as illustrated in Figure 5.6a), which produces a beam behaviour in the global floor. The size of b_{eff} depends on L_{sl}. The criteria of calculating the length of the slab that works with the beam can be found in different building codes (Bhatt et al., 2006). Furthermore, when L_{sl} is large, both floor members (the beams and the slab) are sufficiently flexible to deform together when they are affected by a load. Therefore, when the beam behaviour is dominant in the floor system, the floor bending stiffness can be calculated reasonably well using Equation 2.3.

For $L_{sl}/B_{sl} \leq 1.25$ (i.e. small L_{sl} or large B_{sl}), a smaller portion of the slab will act as a beam (small b_{eff}) and the remaining portion of the slab will be of considerable size in the floor system. In such cases, the bending stiffness of individual beams becomes considerably larger than that of the slab due to having a larger cross sectional height (greater moment of inertia). For this reason, the force required to displace the slab by a specific amount will be smaller than for the beams. This means that, regardless of how a uniform displacement is applied to the cross section of the floor in the numerical analysis, the corresponding forces will not be uniform over the floor cross-section; the slab will have smaller forces than the beams. In Equation 2.3, the slab and the beams in the floor system are assumed to show the same stiffness and deflect by the same amount. Therefore, the summation of P_{nodes} in the

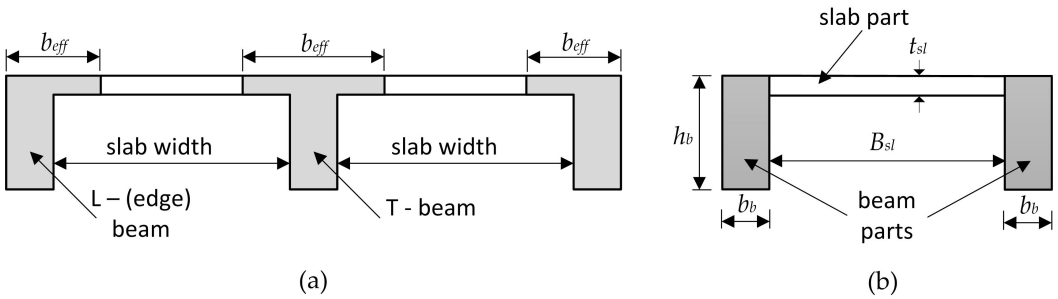

Fig. 5.6 (a) Effective beam width (b_{eff}) in edge or interior beams, (b) beam and slab parts for the calculation of the moment of inertia of floor cross section

numerical analysis leads to a lower value of bending stiffness of the floor system compared to that calculated using Equation 2.3.

It is worth mentioning that even for larger values of L_{sl}, an increase of B_{sl} still causes the mentioned problem but the magnitude of L_{sl} reduces the scale of difference in the bending stiffness between the numerical and analytical estimations. This is because the effect of L_{sl} in the computation of a member's bending stiffness is dominant (raised to the power 3). Larger values of L_{sl} result in smaller values of bending stiffness and, in turn, reduce the role of the flexural rigidity of the floor which is the main cause of the difference between the numerical and analytical computation of the bending stiffness.

The ratio of the bending stiffness of floor beams ($2K_{b,fb}$) to that of the slab ($K_{b,sl}$) in the floor system also has a considerable effect on the stiffness overestimation of floors with small lengths (L_{sl}). Simulations were conducted in which the length and the elastic modulus of the beams and slabs were kept the same. Therefore, the ratio of bending stiffness of beams to that of the slab can be taken as the ratio of the moments of inertia: $2I_{fb}/I_{sl}$, as plotted in Figure 5.5b for two specific cases of L_{sl}/B_{sl}.

Based on the numerical results of varying L_{sl}, B_{sl} and $2I_{fb}/I_{sl}$, a coefficient $C_{bf,cant}$ (Equation 5.2) can be used to modify the analytical floor bending stiffness calculated by Equation 2.3 to reasonably match the numerical model results of the bending stiffness of a cantilever floor when $L_{sl}/B_{sl} \leq 1.25$. This coefficient takes into account the effects of the moment of inertia of the slab and floor beams, and is approximately equal to $K_{b,fl,cant,an,fix}/K_{b,fl,cant,num,fix}$.

$$C_{bf,cant} = \left(\frac{6I_{fb}}{I_{sl}}\right)^{\frac{B_{sl}}{20L_{sl}}} \geq 1.0 \tag{5.2}$$

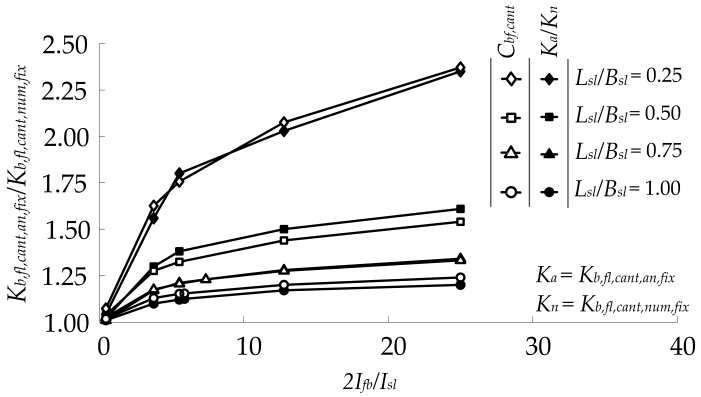

Fig. 5.7 Comparison of $K_{b,fl,cant,an,fix}/K_{b,fl,cant,num,fix}$ and $C_{bf,cant}$ for different values of L_{sl}/B_{sl}

where values of I_{fb} and I_{sl} are calculated independently of each other according to the cross-sectional areas shown in Figure 5.6b. The main factor causing the differences between numerical and analytical results is the bending stiffness of the beams, which is largely affected by L_{sl}. For this reason, in the expression of $C_{bf,cant}$, the term $(2I_{fb}/I_{sl})$ is factored by 3 and L_{sl} by 20. Figure 5.7 illustrates the good fit obtained by using $C_{bf,cant}$ (i.e. a good match with $K_{b,fl,cant,an,fix}/K_{b,fl,cant,num,fix}$).

To summarise, the analytically computed bending stiffness of the floor is satisfactory when $L_{sl}/B_{sl} > 1.25$; otherwise it should be divided by $C_{bf,cant}$ to obtain a good approximation of the numerical bending stiffness of the floor:

$$K_{b,fl,cant,eq,fix} = \frac{K_{b,fl,cant,an,fix}}{C_{bf,cant}} \tag{5.3}$$

where $K_{b,fl,cant,eq,fix}$ is the equivalent bending stiffness of the fixed support floor (subscript *eq* denotes an equivalent parameter based on a curve-fitting coefficient C).

5.4.3 Stage 2: evaluation of floor boundary condition

In stage 1, the simulations were performed on fixed-ended floors, however this case does not reflect the reality of framed buildings. To evaluate the effect of the real degree of end fixity of the loaded floor, numerical simulations were performed including additional (up to 6) panels in the x-direction. Figure 5.2c shows an illustrative numerical model of a single storey building with a single bay in the y-direction and multiple bays in the x-direction. The range of dimensions of the structural parts considered are presented in Table 5.2. It is worth

noting that column cross sectional dimensions depended on the cross sectional dimensions of the floor and supporting beams (i.e. $h_{col} = b_{sb}$ and $b_{col} = b_{fb}$).

Table 5.2 Range of sizes of structural parts considered in stage 2 analyses

Parameter	L_{sl}	B_{sl}	t_{sl}	b_{fb} and b_{sb}	h_{fb} and h_{sb}	L_{col}
Range (m)	3.5 to 8	2.5 to 7	0.075 to 0.175	0.15 to 0.4	0.25 to 0.6	1.75 to 4

Six scenarios were analysed; first considering only one x-panel and subsequently adding panels in the x-direction. The numerical simulations were conducted as follows: a fixed boundary was applied to the bottom of all columns except the virtual (displaced) columns (Figure 5.2c). First, only the loaded panel (x_0y_0 in Figure 5.2c, including the loaded floor, supporting beam and two columns at $x1$) was included in the analysis. A specific uniform displacement was applied to the cross section of the loaded floor and the nodal reaction forces were determined. The floor bending stiffness was then calculated based on Equation 5.1. One supporting panel (Figure 5.2c) was then added to the analysis and the same procedure was repeated to determine the floor bending stiffness of the loaded panel. This process was repeated until five supporting panels were added to the analysis. Note that in all simulations, the displacements were only applied to the cross section of the loaded floor.

Adding supporting panels provides an additional degree of end fixity to the loaded floor, which effectively specifies the value of F_K in Equation 2.3 for the loaded panel. The degree of end fixity here means how the supported end of the floor is constrained. The term is related to the connection of the loaded floor to the supporting beam and columns. If the connection does not allow the rotation of the member, the end is perfectly fixed; if some rotation is allowed, there will be a degree of end fixity which restricts the rotation of the member to some extent (between a hinge and fixed support).

The addition of a single supporting panel (panel x_1y_0 in Figure 5.2c) provides significant resistance against rotation to the supporting beam, and increases the degree of floor end fixity. The degree of end fixity of a loaded floor (connected to supporting panels) can be related to the bending stiffness of the fixed support scenario of that floor (from stage 1). It can be defined as the ratio of the bending stiffness of the loaded floor in a single storey, one y-bay numerical analysis ($K_{b,fl,cant,num,1s,1y}$) to that obtained for a fixed-ended loaded floor ($K_{b,fl,cant,fix}$ from stage 1). Figure 5.8a shows the variation of $K_{b,fl,cant,num,1s,1y}/K_{b,fl,cant,num,fix}$ with the number of supporting panels for three cases of b_{sb}/h_{sb}. The numerical results show that the addition of more than one supporting panel has a negligible effect on the change of bending stiffness.

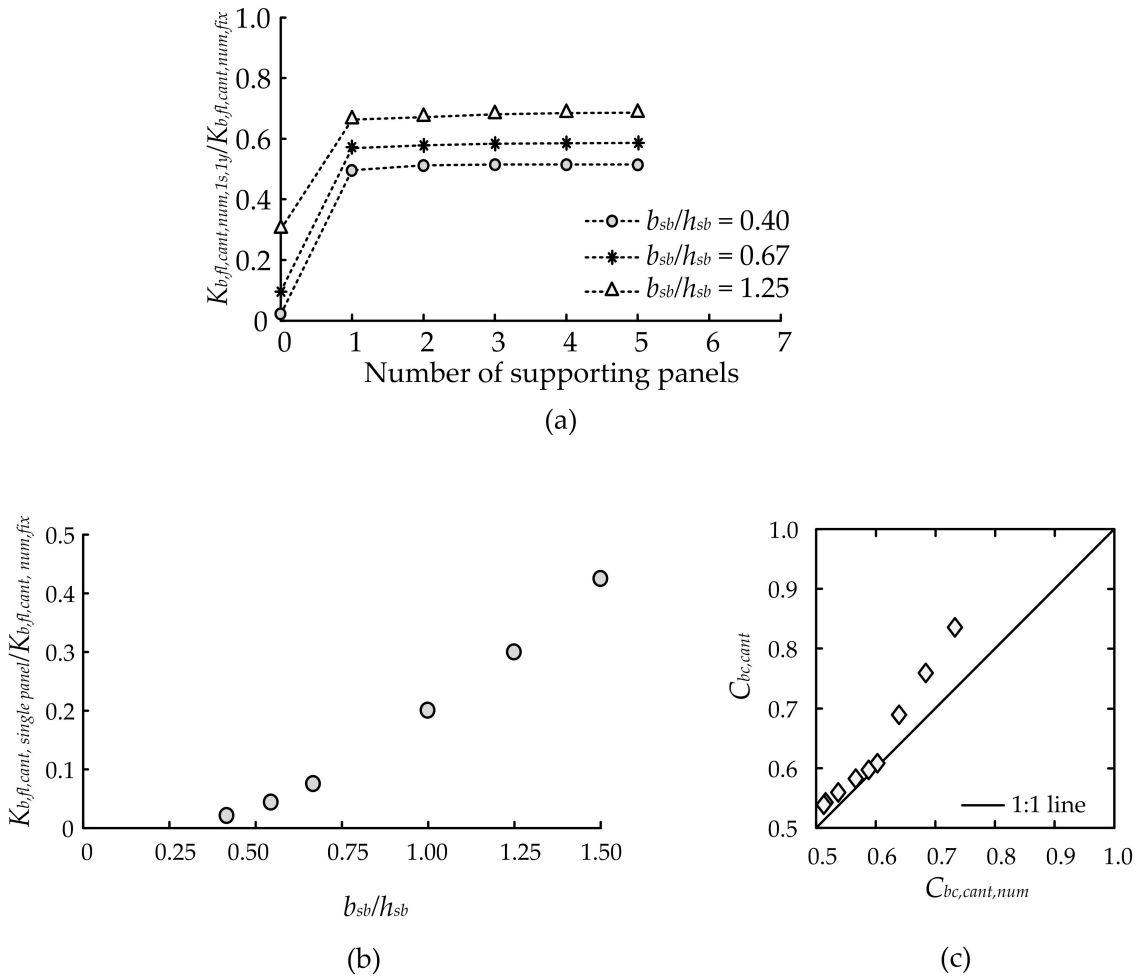

Fig. 5.8 (a) Effect of supporting floors on the end fixity of the loaded floor, (b) the ratio of $K_{b,fl,cant,single\ panel}/K_{b,fl,cant,num,fix}$, (c) comparison of proposed $C_{bc,cant}$ values (Equation 5.4) with numerical results

The bending stiffness of the floor for the loaded panel alone (without supporting panels) depends on the stiffness of the supporting beam and columns (x_1y_0 and x_1y_1 in Figure 5.2c). The ratio of b_{sb}/h_{sb} is also an influential parameter as it has a significant effect on the rotation of the loaded floor and provides its end fixity. Figure 5.8a illustrates that the bending stiffness of a single loaded panel is very small compared to the bending stiffness of its fixed-ended scenario (i.e from stage 1). Furthermore, the ratio of b_{sb}/h_{sb} is not an effective parameter for the floor bending stiffness when the loaded floor is connected to supporting panels.

Figure 5.8b presents the ratio of the bending stiffness of a floor in a single panel (without supporting panels), $K_{b,fl,cant,single\ panel}$, to that of a fixed floor, $K_{b,fl,cant,num,fix}$ ($K_{b,fl,cant,single\ panel}/K_{b,fl,cant,num,fix}$). It is shown that the bending stiffness of a single loaded panel could be of moderate value compared to the bending stiffness of its fixed-ended scenario (i.e. $K_{b,fl,cant,single\ panel}/K_{b,fl,cant,num,fix} \geq 0.1$) when there is a supporting beam with a considerable width (i.e. beams having $b_{sb}/h_{sb} \geq 1.0$). In terms of structural design of buildings, these ratios of b_{sb}/h_{sb} can be considered unrealistic. This is because beams are mainly designed to resist shear and bending moments which require greater cross sectional heights than widths; torsion problems are generally dealt with using reinforcement in the beam. In addition, there is no torque on the interior beams of equal spans in static load cases. Furthermore, a building with only a single panel is not realistic. Therefore, the floor bending stiffness of a single panel (with no supporting panels) was disregarded.

It is worth noting that the foundation rigidity is also an important factor affecting the bending stiffness of the superstructure but its effect is eliminated by assuming fixed boundaries at the bottom of the first storey columns. This assumption is one of the choices of the base column boundary condition in the structural analysis of framed buildings. Duggal (2009) explained that when small column bending moments due to lateral loads work in combination with large axial loads, and large foundations are provided, the boundary of the base columns can be assumed fixed. Furthermore, McCormac and Brown (2014) stated that fixed end base columns can be assumed for buildings with gravity loads applied to their floors or roofs.

The stiffness of the supporting beam, two supporting columns (x_1y_0 and x_1y_1 in Figure 5.2c) and the floor of the first supporting panel (panel x_1y_0 in Figure 5.2c) have the most significant effect on the degree of end fixity of the loaded floor. Based on these parameters, the following modification coefficient $C_{bc,cant}$ is proposed to estimate the degree of end fixity of the loaded floor:

$$C_{bc,cant} = \frac{K_{c,Sfl} + K_{c,sb} + 2K_{c,col}}{K_{c,Lfl} + K_{c,Sfl} + K_{c,sb} + 2K_{c,col}} < 1.0 \tag{5.4}$$

where $K_{c,Sfl} = (EI/L)_{fl}$ is the stiffness of the supporting floor, $K_{c,Lfl} = K_{c,Sfl}$ is the stiffness of the loaded floor, $K_{c,sb} = G_b J_{sb}/L_{sb}$ is the torsional stiffness of the supporting beam (subscript sb), $G_b = E_b/2(1+\nu_b)$ is the shear modulus of the beam material, $J_{sb} = (b_{sb}h_{sb}/12) \times (b_{sb}^2 + h_{sb}^2)$ is the polar moment of inertia, L_{sb} is the supporting beam length (equal to the slab width B_{sl}), $K_{c,col} = (EI)_{col}/L_{col}$ is the column stiffness, and L_{col} is the column height. Note that the K_c terms are stiffness parameters used for calculating coefficients, with units of Nm (as opposed to beam/building bending stiffness parameters, K_b, with units of N/m). The coefficient $C_{bc,cant}$ can be used to evaluate the bending stiffness of the loaded floor in the first storey of a single y-bay building using:

$$K_{b,fl,cant,eq,1s,1y} = C_{bc,cant} \times K_{b,fl,cant,eq,fix} \tag{5.5}$$

where $K_{b,fl,cant,eq,fix}$ is obtained from Equation 5.3. Figure 5.8c compares results of $C_{bc,cant}$ using Equation 5.4 with $C_{bc,cant,num} = K_{b,fl,cant,num,1s,1y} / K_{b,fl,cant,num,fix}$, an equivalent coefficient determined from numerical analyses. The results show that the equivalent values using Equation 5.4 give a satisfactory match to the numerical results.

5.4.4 Stage 3: effect of adding storeys

Numerical analyses were conducted to evaluate the stiffness effect of adding up to 10 storeys to the single y-bay building from stage 2, as shown in Figure 5.2d. The sizes of floors, beams and columns considered were the same as in stage 2 (Table 5.2). The area of applied displacements is consistent with stage 2, as indicated in Figure 5.2d. For a given number of x-bays (up to 10), numerical analyses were conducted sequentially by adding additional storeys. The first storey is used as a reference for which the bending stiffness is compared when additional storeys are added, thereby illustrating the additional bending stiffness each storey contributes.

Columns transfer foundation displacements to upper storeys, but they also convey the stiffness contribution of upper storeys to the foundation. The influence of a storey on the overall structural response is therefore proportional to the relative stiffness of columns compared to the connected floors. The ratio of column stiffness to that of the upper floor can be used as a parameter to quantify this effect. In this way, the column stiffness takes into account the distance between floors. When the global building system is considered, the influence of the distance from the foundation to the considered floor is also important. Based on these two factors, a column-floor stiffening effect coefficient $C_{cf,cant}$ is introduced:

$$C_{cf,cant,i} = \frac{2K_{c,col}}{2K_{c,col} + K_{c,Lfl}} \times \left(\frac{L_{col,i}}{h_{fl,i}}\right) \tag{5.6}$$

where subscript i indicates a measurement for the i^{th} floor, $L_{col,i}$ is column height, and $h_{fl,i}$ is the total height between the i^{th} floor and the foundation, as shown in Figure 5.2d.

The reason for calculating bending stiffness of the loaded floor in the first storey is because of the building bending behaviour when affected by tunnelling. The first storey is initially influenced by displacements from the ground, then the structural parts transfer this effect to the upper storeys. Based on the numerical results, the storey which was in direct-contact with the first storey (i.e. the 2^{nd} storey) had the greatest effect on the structural response of the building. This effect decreased gradually for higher storeys. There are different causes for the reduction of the stiffness contribution of upper storeys to the building global bending stiffness.

Columns are connected to the foundation and floors at specific locations; the areas between successive columns deform differently from the areas connected to the columns. This open space is not able to transfer the foundation deformations to the upper floors. If floors were continuously connected (e.g. reinforced concrete walls) then the maximum interaction effect between the foundation and the upper storeys would be achieved. It is for this reason that in each storey, the stiffness of the columns and of the upper storey has the dominant role in transferring the stiffness effect of the upper storey to the lower one.

It was found that the contribution of the stiffness of upper storeys to the global building bending stiffness diminishes after the second storey, as demonstrated in Figure 5.9, where Δ is the displacement measured at the top of the cross section of the edge floors, Δ_{max} is the applied displacement to the loaded floor (1^{st} storey) which is the maximum displacement among the storeys of the building, P is the created force due to the applied displacements, and P_{max} is the largest induced floor force among the floor forces of the building. To show the reduction of the stiffness contribution of upper storeys to the global building bending stiffness, the displacements created at each storey in an 11 storey building, with their corresponding forces, are plotted in Figure 5.9. It is shown that the trend of the displacements is approximately constant and most of the displacements from the first storey are transferred to the upper storeys, while the forces required to produce these displacements decrease remarkably due to the flexibility of the upper storeys.

Note that for force calculation, floor bending stiffness in each storey was achieved by taking away bending stiffness of a building with $(m-1)$ storeys from that of m storeys

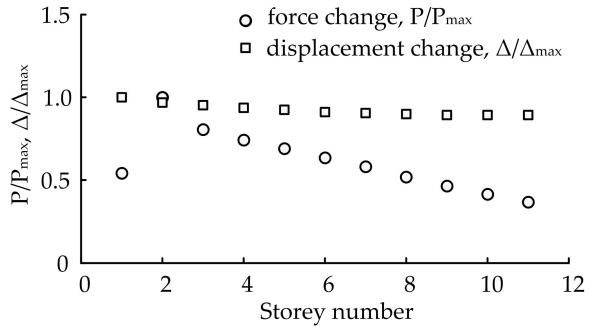

Fig. 5.9 Change of displacements and forces with storey number for an 11 storey building

($K_{b,m\ storeys} - K_{b,(m-1)\ storeys}$). In this way, bending stiffness of each floor was obtained and multiplied by the produced displacement to get the required force

Another essential factor causing the decreased bending stiffness of the upper storeys is that as the building height increases, the whole building becomes more flexible to lateral deflection. This is because the building acts as a cantilever beam constrained at its base (foundation). This leads to greater deformations at points further from the foundation.

A coefficient $C_{Kus,cant,i}$ is defined as the ratio of the increased bending stiffness of the superstructure due to the addition of the i^{th} upper storey (subscript *us*) to the bending stiffness of the first storey. Figure 5.10 illustrates how the addition of x-bays and storeys affects the value of $C_{Kus,cant}$. The number of x-bays is shown to have an effect on $C_{Kus,cant}$ up to approximately 8 (Figure 5.10a). Figure 5.10b plots the value of $C_{Kus,cant}$ obtained for each storey within a 7-storey building with 3, 6, and 9 x-bays. The data illustrate the decreasing trend of $C_{Kus,cant}$ with storey number as well as the increase of $C_{Kus,cant}$ with number of x-bays.

The numerical analyses indicated that $C_{Kus,cant}$ has a logarithmic relationship with $C_{cf,cant}$, as illustrated in Figure 5.11 for cases of high, intermediate, and low column stiffness relative to the loaded floor stiffness ($2K_{c,col}/K_{c,Lf} = 0.905$, 0.617, and 0.207, respectively) in a 6 storey building; the data can be reasonably well fitted with the following curve:

$$C_{Kus,cant,i} = \log_{10}(C_{cf,cant,i}) + \alpha_{Kus,cant} \quad \geq 0.0 \tag{5.7}$$

where $\alpha_{Kus,cant}$ accounts for the effect of the ratio of building length in the x-direction, $L_{x,bldg}$, to the storey height, L_{col}. Note that the effect of distance of each storey from the foundation is included in coefficient $C_{cf,cant}$ (Equation 5.6). Figure 5.12 illustrates the relationship between $\alpha_{Kus,cant,num}$, obtained from the numerical results, and the ratio $L_{x,bldg}/L_{col}$. The numerical data in Figure 5.12 was fitted using the following expression:

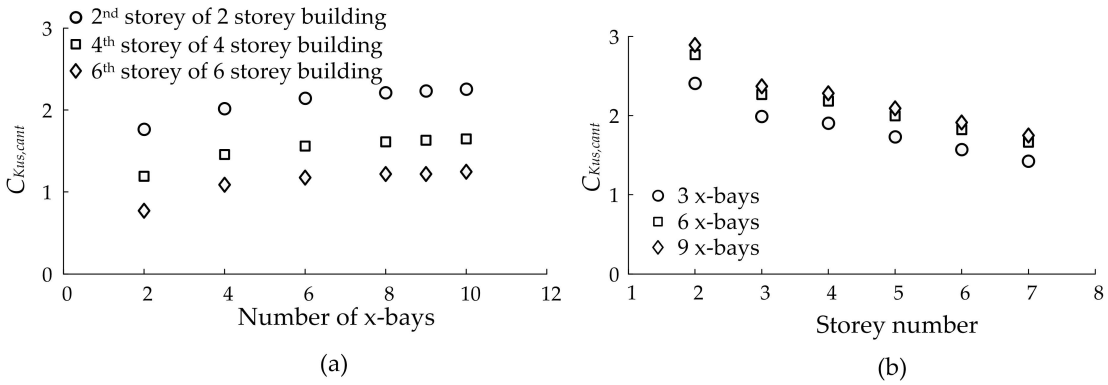

Fig. 5.10 (a) Effect of x-bays on $C_{Kus,cant}$ of uppermost floor, and (b) change of $C_{Kus,cant}$ with storey number for a 7-storey building.

$$\alpha_{Kus,cant} = 1.9\left(\frac{L_{x,bldg}}{L_{col}}\right)^{0.2} \tag{5.8}$$

The stiffness contribution of each storey is obtained by multiplying $C_{Kus,cant,i}$ by its floor bending stiffness, $K_{b,fl,cant,eq,i,1y}$ (note that, based on assumption [5] that floor parameters remain constant across all storeys, $K_{b,fl,cant,eq,i,1y} = K_{b,fl,cant,eq,1s,1y}$, which is calculated in stage 2 of the analysis). The bending stiffness of the entire multi-storey (subscript *ms*) single y-bay building ($K_{b,fl,cant,eq,ms,1y}$) is then obtained by summing the individual storey contributions:

$$K_{b,fl,cant,eq,ms,1y} = \sum_{i=1}^{m}\left(C_{Kus,cant,i} \times K_{b,fl,cant,eq,i,1y}\right) \tag{5.9}$$

where m is the total number of storeys. Figure 5.13 compares the bending stiffness of single y-bay buildings computed using the proposed method (using stages 1 to 3) with their equivalent numerical results. The figure includes 208 data points including buildings from 1 to 11 storeys.

5.4.5 Numerical verification of stages 1 to 3

To validate stages 1 to 3, a single y-bay, eleven-storey building made of concrete with an elastic modulus of 30 GPa was numerically modelled in a way that the virtual columns (Figure 5.2c) which were removed in the previous simulations were added to the model and the displacements were applied to their bases. Using this technique allows the transfer of

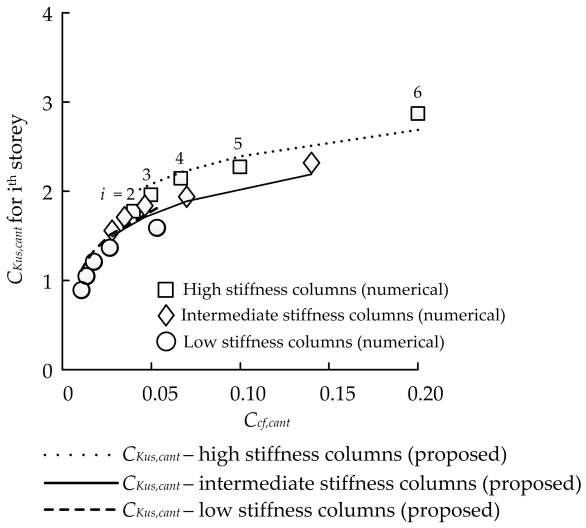

Fig. 5.11 Relationship between $C_{Kus,cant}$ and $C_{cf,cant}$ for a 6-storey building with varying column stiffness

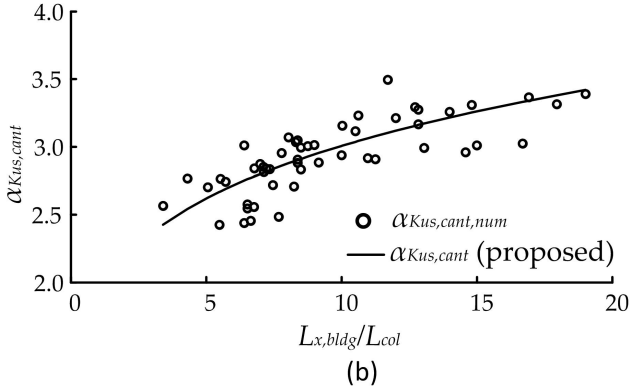

Fig. 5.12 Comparison between $\alpha_{Kus,cant}$ values obtained from curve fitting of numerical results, and proposed values calculated by Equation 5.8

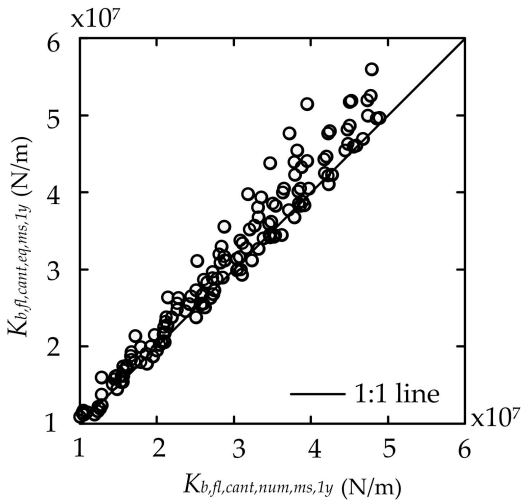

Fig. 5.13 Bending stiffness of single y-bay, multi-storey (up to 11 storeys) buildings: proposed method ($K_{b,fl,cant,eq,ms,1y}$) versus numerical results ($K_{b,fl,cant,num,ms,1y}$)

the displacements through the columns to floors, and eliminates the assumption of applying uniform displacements to the cross section of the first floor.

Column dimensions were 0.4×0.4×4 m (b_{col}, h_{col} and L_{col}, respectively), floor and supporting beam dimensions were 0.4×0.6 m (b_{fb} or b_{sb}, and h_{fb} or h_{sb}, respectively), and slab dimensions were 7×8×0.175 m (B_{sl}, L_{sl} and t_{sl}, respectively).

Figure 5.14a shows the $C_{Kus,cant}$ values for the numerical and the proposed methods. There is generally good agreement between the coefficients. It is shown that there is a small difference between the coefficients of the numerical and the proposed methods after storey 8. To show the effect of this difference, the ratio of the numerical to empirical bending stiffness of building storeys is presented in Figure 5.14b, which shows that the ratios of $K_{b,fl,cant,eq,ms,1y}/K_{b,fl,cant,num,ms,1y}$ are close to 1.0 and the stiffness difference between the two methods is negligible.

5.4.6 Stage 4: effect of adding y-bays in direction of tunnel

This section considers the effect of adding bays in the direction of the tunnel (y-direction) to the stiffness of the building. Figure 5.15a demonstrates the change of $C_{Kus,cant}$ for each storey of a 5-storey building as the number of y-bays is increased from 1 to 3, based on the numerical analyses. The value of $C_{Kus,cant}$ for the i^{th} floor was calculated from the numerical results as $(K_{fl,cant,i} - K_{fl,cant,(i-1)})/K_{fl,cant,1}$. Also included in Figure 5.15a are values obtained using the proposed method (Equation 5.7) for a single y-bay building.

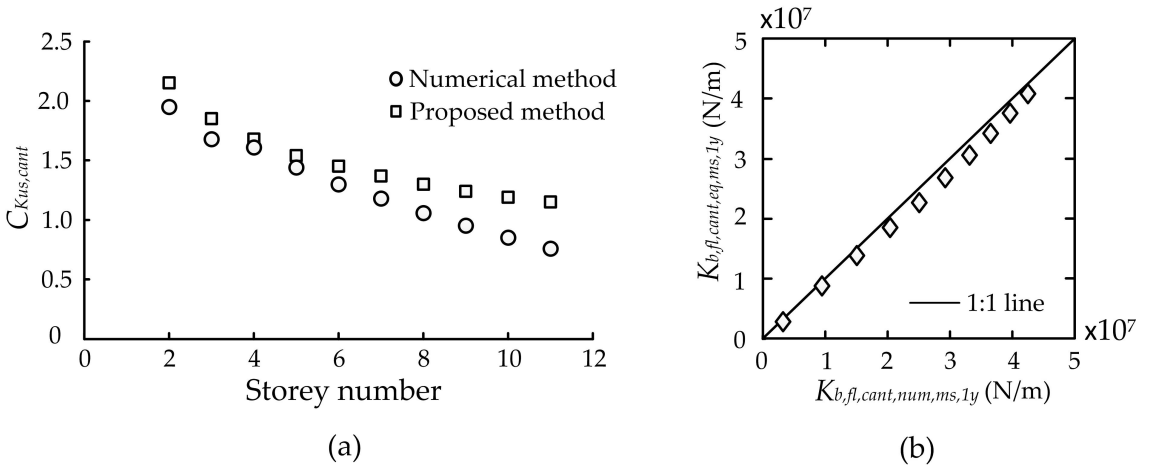

Fig. 5.14 (a) Comparison of $C_{Kus,cant}$ between numerical and the proposed methods, (b) comparison of bending stiffness values of the superstructure between the numerical and the proposed methods

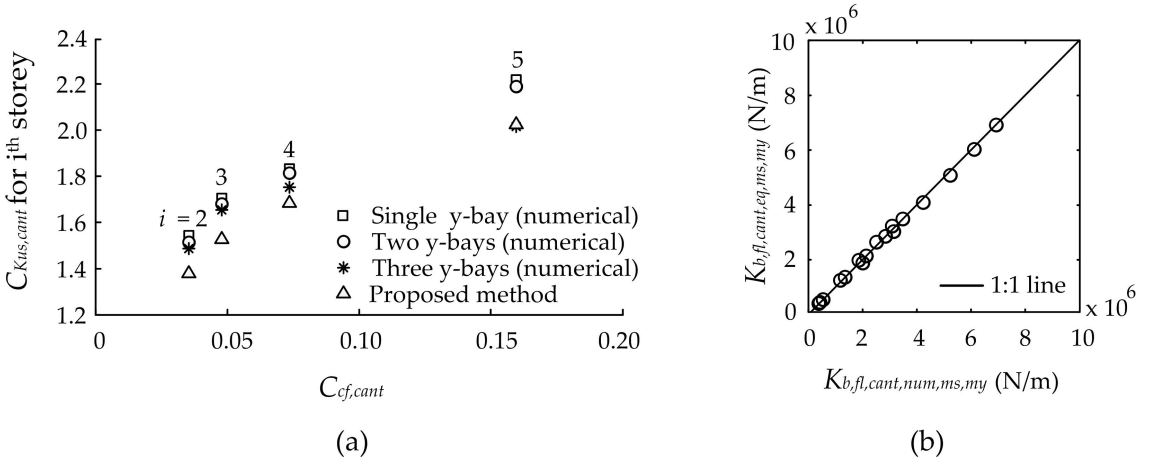

Fig. 5.15 (a) Comparison between numerical and proposed values of $C_{Kus,cant}$ considering buildings with different numbers of y-bays, (b) comparison of the numerical bending stiffness of multi y-bay buildings with their equivalent calculated values based on stages 1 to 4

The numerical results show that the addition of each y-bay increases the bending stiffness of the building superstructure by approximately 60% of the bending stiffness of a single y-bay building. For this reason, Equation 5.10 is proposed to estimate the bending stiffness of a multi-storey building with multiple y-bays (subscript *my*), $K_{b,fl,cant,eq,ms,my}$:

$$K_{b,fl,cant,eq,ms,my} = (1 + 0.6(n_y - 1)) \times K_{b,fl,cant,eq,ms,1y} \tag{5.10}$$

where n_y is the number of y-bays. An example calculation of building stiffness using the proposed method is provided in Appendix A. Figure 5.15b shows the comparison of the bending stiffness of multi y-bay buildings obtained from the numerical analyses, and calculated using the proposed method (stages 1 to 4). The buildings range from 2 to 3 y-bays, and 1 to 7 storeys.

5.4.7 Stage 5: considering multiple x-bays affected by ground displacements

The numerical simulations thus far only considered the case where one edge panel of the building was subjected to downward displacements (i.e. affected by tunnelling settlements). When more panels are affected, the bending stiffness of the building will decrease dramatically due to the increased deflected length of the building (bending stiffness is inversely proportional to the cube of affected length, as in Equation 2.3).

Figure 5.16 shows a tunnel constructed close to a building. If the building is located entirely inside the displaced soil zone, the bending stiffness of the superstructure will not have a significant contribution to the global building bending stiffness because the whole structure is subjected to rotation. This rotation does not allow the building to provide any resistance against the produced bending deformations. As explained in previous sections, the resistance of the building against bending deformations is achieved when a part of the building is located outside the displaced soil zone, providing a degree of end-fixity.

To consider the effect of the influenced length of the building, numerical simulations were performed to evaluate how bending stiffness of a storey decreases when more panels are affected by ground displacements. It was assumed that the building behaves like a cantilever beam subjected to multiple loads, as shown in Figure 5.17. Multi-storey buildings with 1 y-bay and 8 x-bays were numerically simulated. The number of affected panels considered was 1, 2, 3 and 4; the bases of columns in the unaffected zone were fixed. The displacement was modelled by applying forces at the locations of the affected columns; the applied forces

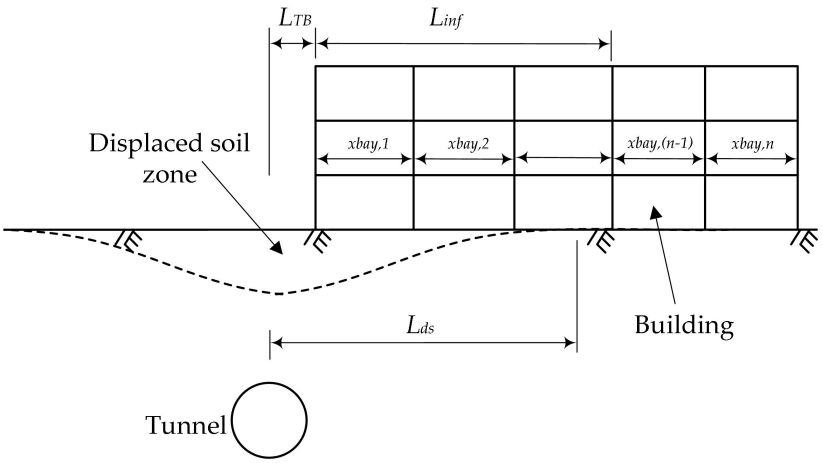

Fig. 5.16 Soil and building zones affected by tunnelling induced ground displacements

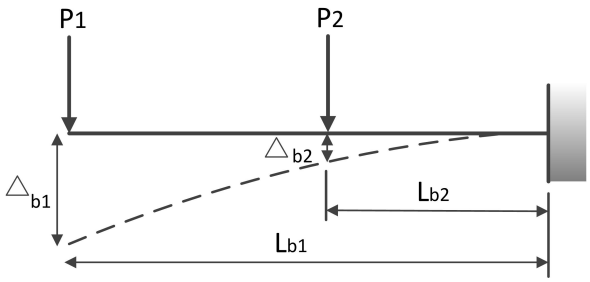

Fig. 5.17 A cantilever beam subjected to multiple loads

changed linearly from a maximum value above the tunnel centreline to zero at the columns in the unaffected zone.

The analytical bending stiffness of a beam subjected to multiple loads is significantly more complicated than for a single load. A simplified method for approximating bending stiffness of a building subjected to multiple loads is proposed using the following expression:

$$K_{b,multi\,load} = \frac{P_1 L_{b1} + P_2 L_{b2} + \ldots + P_n L_{bn}}{\Delta_{b1} L_{b1} + \Delta_{b2} L_{b2} + \ldots + \Delta_{bn} L_{bn}} \tag{5.11}$$

where P is a concentrated load, Δ_b is deflection at the location of P, L_b is the distance from P to the end of the affected zone (i.e. beginning of the assumed fixity), and subscripts $1, 2, \ldots n$ represent the column locations, starting from that nearest to the tunnel. Equation 16 is simply a weighted representation of bending stiffness considering the multiple locations of the loads and measured displacements and is used to obtain the general trend of bending stiffness reduction of a beam subjected to multiple loads in comparison to a beam subjected to a single

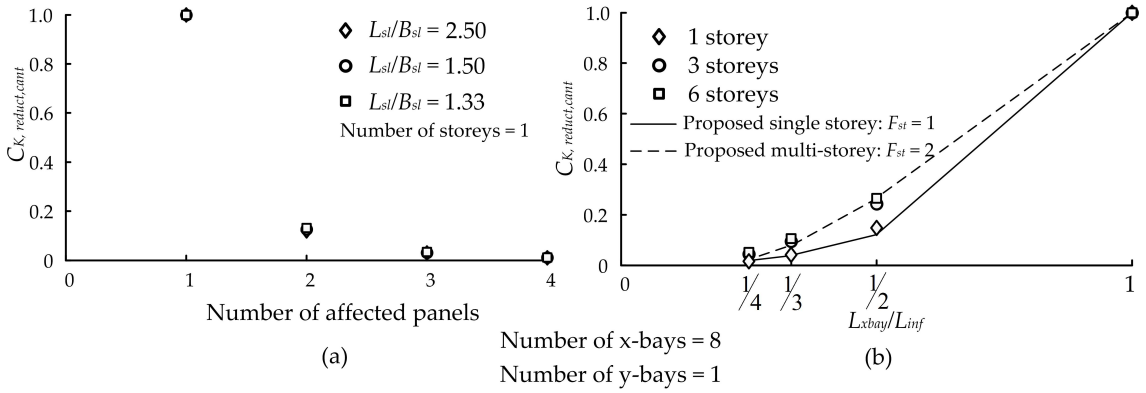

Fig. 5.18 (a) Reduction of building bending stiffness with number of panels located in displaced zone, (b) comparison between numerical and proposed values of $C_{K,reduct,cant}$

load. Note that Equation 5.11 is the same as Equation 5.1 when the beam is subjected to a single force.

A reduction factor, $C_{K,reduct,cant}$, is defined as the ratio of the bending stiffness of a building with multiple affected panels to its bending stiffness with one affected panel. This allows the conversion of the building bending stiffness calculated in Stages 1-4 (based on one affected panel) to one which considers the actual number of affected panels (based on an assumed settlement profile).

Figure 5.18a plots results for a single y-bay, 8 x-bay, 1 storey building when the number of affected panels is increased from one to four and illustrates that there is a dramatic reduction of the building bending stiffness when two or more panels are affected by ground displacements. The results also indicate that $C_{K,reduct,cant}$ is insensitive to panel size (L_{sl}/B_{sl}). Figure 5.18b shows results for the same building but with additional storeys added; a slight increase in the value of $C_{K,reduct,cant}$ is noted for multi-storey buildings. Based on these numerical results, $C_{K,reduct,cant}$ can be expressed as:

$$C_{K,reduct,cant} = F_{st} \times \frac{L_{xbay}^3}{L_{inf}^3} \tag{5.12}$$

where L_{xbay} is the length of one bay in the x-direction (Figure 5.16), L_{inf} is the length of the building located inside the affected zone (Figure 5.16), and F_{st} =1 and 2 for one-storey and multi-storey buildings, respectively. The value of L_{inf} can be calculated as $\left(L_{inf} = L_{ds} - L_{TB}\right) \leq L_{bldg}$, where L_{ds} is the length of the displaced zone and L_{TB} is the horizontal offset of the building edge to the tunnel centreline (see Figure 5.16). For practical purposes, L_{inf} should correspond to the location of a building column.

The final value of the building bending stiffness, $K_{b,cant,eq,bldg}$, can be calculated using:

$$K_{b,cant,eq,bldg} = C_{K,reduct,cant} \times K_{b,fl,cant,eq,ms,my} \tag{5.13}$$

where $C_{K,reduct,cant} = 1$ if tunnelling settlements only affect the first x-bay or calculated using Equation 5.12 otherwise.

5.4.8 Comparison with other methods

For comparison against the 2D analysis methods of Lambe (1973) and Goh and Mair (2014), a 2D based calculation of EI from the method proposed here is used. It is worth noting that the proposed method is based on 3D buildings where bending stiffness of the whole building is calculated rather than the cross sectional flexural rigidity. To show an approximate comparison with the available 2D methods, coefficient $C_{Kus,cant}$ is used to consider the contribution of the EI of each storey to the global EI_{bldg}. The procedure is as follows. The value of EI_{fl} was calculated for the cross section of each floor. It should be noted that I_{fl} was calculated using the parallel axis theorem, as explained in Section 5.4.2 (stage 1). The values of $C_{Kus,cant}$ based on the proposed method (stages 1 to 3) were then calculated for each storey (above the first storey) in the building. Finally, the increase of EI_{fl} of the first storey due to the effect of EI_{fl} of the upper storeys was computed to obtain the global EI_{bldg}.

For the approach of Lambe (1973), EI of all floor slabs was added together to achieve EI of the whole building. For Goh and Mair (2014), Equation 3.36 was used to compute the column stiffening factor (C_{col}) assuming $L^2_{sag,hog}/L^2_{bay} = 1$, indicating that only one bay of the frame was affected by ground displacements.

With regard to the 3D buildings, the proposed method was compared against the bending stiffness obtained using the approaches of Potts and Addenbrooke (1997) and Franzius et al. (2006) as well as results obtained from the numerical analyses conducted as part of this project (details of the numerical models were presented in stages 1 to 3). For both 2D and 3D cases, the comparison was made for a multi-storey (1 to 11) single y-bay building with the parameters given in Table 5.3.

Figure 5.19 shows that the approach used by Lambe (1973) results in the lowest values of EI_{bldg} because it disregards the effect of the interaction between the slabs through their connecting links. In the Lambe (1973) method, each slab in the building system is subjected to bending deformations independently, hence the moment of inertia of the building is a straightforward addition of the moment of inertia of each slab and does not consider the

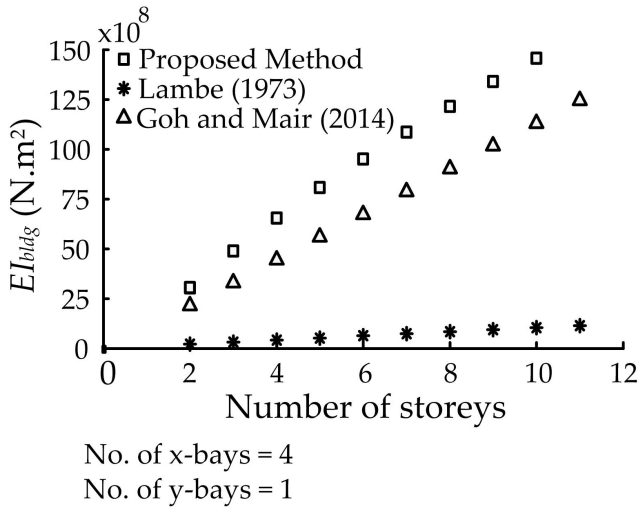

Fig. 5.19 Comparison of EI_{bldg} between the proposed method and approaches suggested by Lambe (1973) and Goh and Mair (2014)

effect of the distance between the slabs and the axis about which bending of the building occurs.

Table 5.3 Sizes of structural parts (1 to 11 storey building) considered in 2D and 3D comparative analyses

Parameter	L_{sl}	B_{sl}	t_{sl}	b_{fb} and b_{sb}	h_{fb} and h_{sb}	L_{col}
Dimension (m)	8.00	7.00	0.175	0.40	0.60	4.00

The trend of the EI_{bldg} curves of the proposed method and the method of Goh and Mair (2014) are similar but EI_{bldg} values of the proposed method are greater by approximately 27% (average). EI_{bldg} values and their trends will change for different frame geometries. For that reason, it is more logical to plot the column stiffening factor (C_{col}) and $C_{Kus,cant}$ to indicate their difference in estimating the value of EI_{bldg}. Figure 5.20 displays C_{col} of Goh and Mair (2014) and $C_{Kus,cant}$ of the proposed method with the numerically predicted coefficients for an 11 and 6 storey building. The stiffening factor proposed by Goh and Mair (2014) is constant and, similar to the approach of Lambe (1973), disregards the effect of the distance between the desired floor and the axis about which the building bends (i.e. the foundation level). For an 11 storey building, this leads to an underestimation of EI contribution of storeys close to the foundation and an overestimation of EI contribution of higher storeys to the global EI_{bldg}. Figure 5.20a shows that stiffening factors calculated

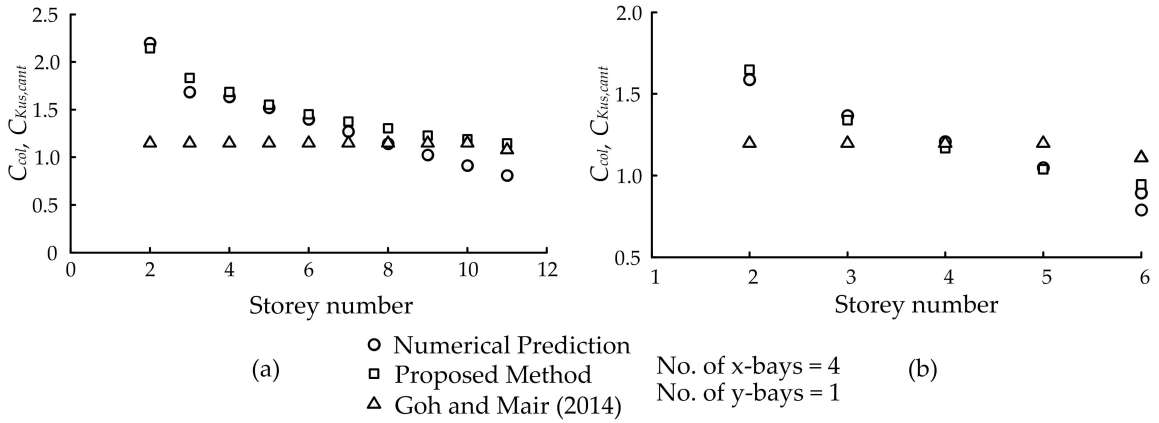

Fig. 5.20 Comparison of C_{col} and $C_{Kus,cant}$ between the proposed method, the approach suggested by Goh and Mair (2014) and numerically predicted values for (a) an 11 storey, and (b) a 6 storey building

based on the Goh and Mair (2014) approach were underestimated for storeys 1 to 7 while they were overestimated for storeys 9 to 11.

If a 6-storey building with less stiff columns is considered, for instance $K_{c,col} = 0.29 \times 10^7$ Nm and $K_{c,sb} = 2.25 \times 10^7$ Nm, the Goh and Mair (2014) method will lead to a similar value of EI_{bldg} to the numerical result because column stiffening factors in the Goh and Mair (2014) method will be reasonably large and constant for all storeys while these factors in the numerical analysis start from high initial values to low final values, as shown in Figure 5.20b. If the building were more than 6 storeys, the Goh and Mair (2014) method would start to overestimate EI_{bldg} because it disregards the reduction of the stiffening factor for the upper storeys.

On the other hand, the assumed influenced part of the building by tunnelling was only one bay. In case of having more than one bay affected by tunnelling, the magnitude of $L^2_{sag,hog}/L^2_{bay}$ in the method of Goh and Mair (2014) would increase and lead to a significant increase of the magnitude of EI_{bldg}. Furthermore, the value of bending stiffness calculated using the proposed method, and that obtained from the numerical analysis would reduce considerably. This would increase the difference between the calculated EI_{bldg} using the Goh and Mair (2014) method, and that of the proposed and numerical methods.

A comparison of bending stiffness of the mentioned 3D building (Table 5.19) between the numerical prediction and the method proposed in this chapter, Potts and Addenbrooke (1997) and Franzius et al. (2006) is presented in Figure 5.21a for five buildings of 2, 4, 6, 8 and 10 storeys. The bending stiffness values of the two latter methods were too large

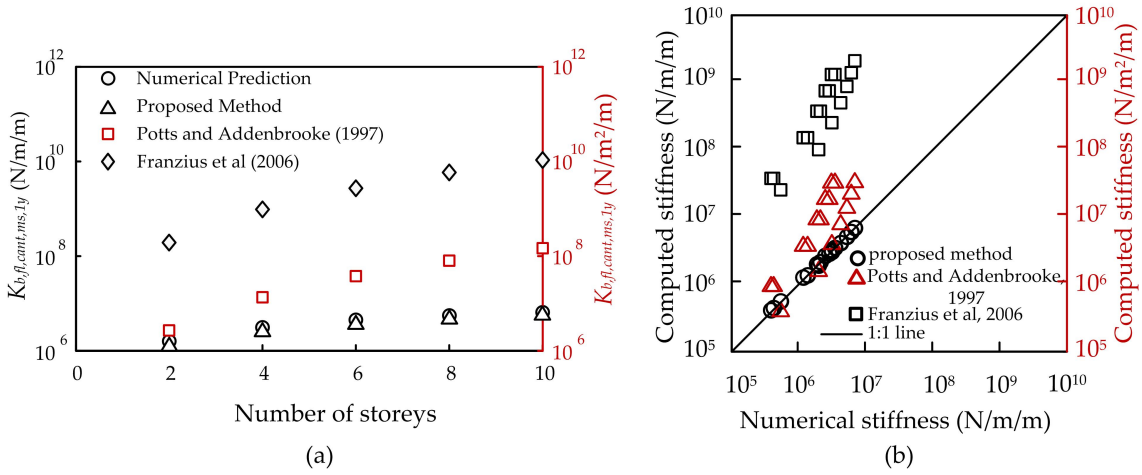

Fig. 5.21 (a) Comparison of a 3D building bending stiffness using different methods, (b) comparing computed building bending stiffness using different methods with the numerically achieved bending stiffness for buildings of multiple y-bays

to be plotted on a normal axis figure with the two former methods. For this reason, the y-axis of Figure 5.21a was chosen to be logarithmic. The building bending stiffness was calculated as $(EI)_{bldg}/(L_{bldg}/2)^4$ in the Potts and Addenbrooke (1997) approach, and as $(EI)_{bldg}/(B_{bldg}L_{bldg}^2)$ in the Franzius et al. (2006) method, where $L_{bldg} = 34$ m.

It should be noted that the stiffness unit of the Potts and Addenbrooke (1997) method is $\mathrm{N/m^2}$ which is different from that of the other methods. It is not very logical to compare two properties with different units, however what is presented here is only to give an idea to the reader about bending stiffness values achieved using different approaches. Furthermore, the building stiffness calculation proposed by Potts and Addenbrooke (1997) and Franzius et al. (2006) are not only related to the building but they are parts of relative stiffness equations to consider the soil-building relative stiffness (Equations 3.25 and 3.30).

The moment of inertia of the building in methods proposed by Potts and Addenbrooke (1997) and Franzius et al. (2006) were calculated using the parallel axis theorem which resulted in a large overestimation of the real building bending stiffness. In addition, the boundary condition and the length of the building subjected to ground deformations due to tunnelling are not taken into consideration in these methods. The bending stiffness for a considerably long building with a small part affected by ground deformations will be underestimated while the stiffness of a short building located entirely within the affected zone will be overestimated. This does not give a good representation of reality since building bending stiffness should decrease with the increase of its deformed (affected) length, and

should increase with the increase of the degree of its end fixity due to a better constriction of the building against rotation.

Figure 5.21b compares the bending stiffness of a range of multi y-bay buildings calculated by the proposed method of this work (based on stages 1 to 4), and the approaches of Potts and Addenbrooke (1997) and Franzius et al. (2006). There is a good agreement between the numerical results and those of the proposed method, while there is a general overestimation of the building stiffness using the approaches of Potts and Addenbrooke (1997) and Franzius et al. (2006).

5.5 A fixed–Ended Approach

A fixed–ended method applies to the case where the tunnel is located exactly under the centreline of the building plan area (Figure 5.22b). The similarity between a building and a beam is based on the fixed–ended beam analogy. This is because in such cases where the tunnel is located directly under the building centreline and the soil displacements that occur along the tunnel axis (y-axis in Figure 5.1) are constant, the building will deform symmetrically about its centreline. The deformation that occurs at the building centre is larger than that of its edges, and both sagging and hogging zones will be created in the deformed shape of the building. This shape of deformation is similar to that of a beam fixed at its ends and loaded at the midpoint. The methodology and the results of the analyses are presented in the following subsections. It should be mentioned that the assumptions made in Section 5.3 are also applied to the fixed–ended approach.

5.5.1 Methodology

The methodology of the fixed–ended approach is similar to that of the cantilever approach (Section 5.4) to take into account the contribution of the various structural parts to the overall stiffness of the building using five stages. **Stage 1** compares the behaviour of two connected floors in two middle panels (Figure 5.23a) to that of a beam fixed at both ends and loaded at the middle (Figure 5.22c). **Stage 2** determines the actual boundary condition of the loaded floors (which was assumed to be fixed in stage 1) by adding more bays in the x-direction (Figure 5.23c). This step determines the value of F_K in Equation 2.3. **Stage 3** determines the effect of adding storeys (Figure 5.23d). **Stage 4** considers the effect of adding bays in the y-direction. Similar to the cantilever approach, in stages 1 to 4, the assumption was made

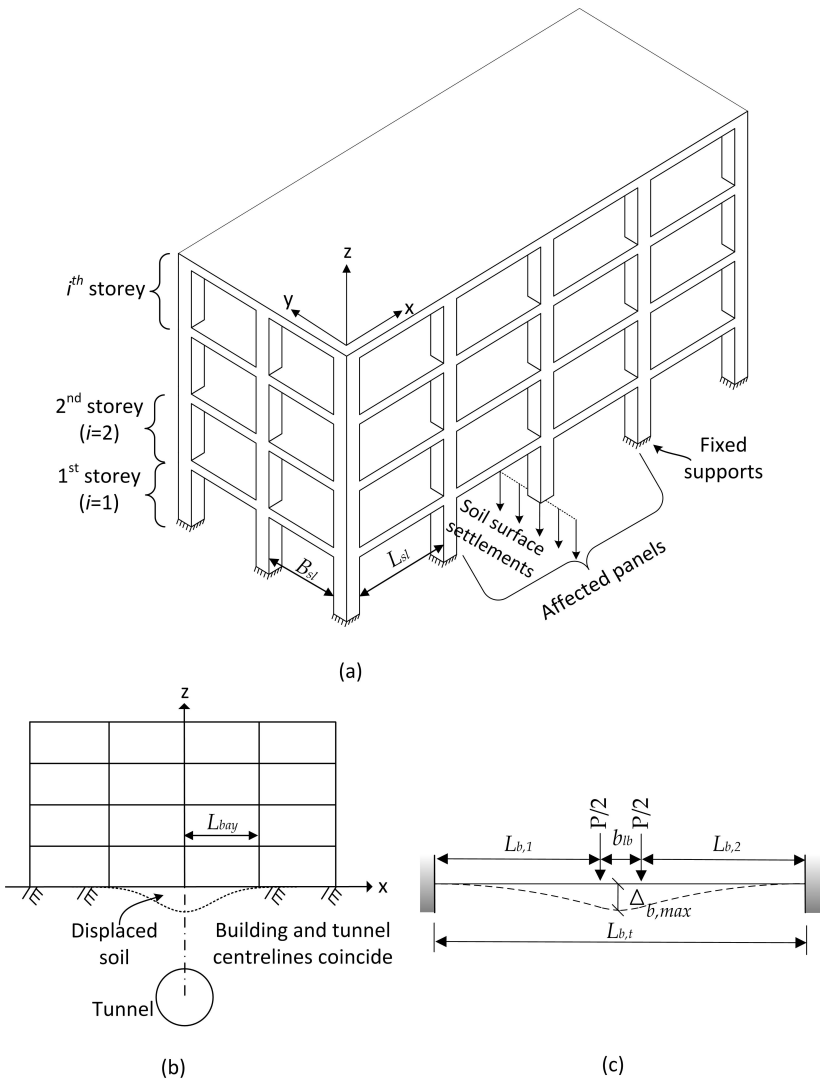

Fig. 5.22 (a) Isometric view of framed building, (b) 2D view of building and tunnel, and (c) fixed–ended beam

that only the two middle panels of the building were affected by soil displacements; **Stage 5** considers the case where multiple x-bays are affected.

Figure 5.24 demonstrates a flowchart of the methodology and coefficients introduced in each stage.

5.5.2 Stage 1: fixed–ended beam analysis for influenced floors

If only one interior row of columns (the middle row, Figure 5.23c,d) is subjected to downward displacements, the two floors connected to the affected columns will behave as a beam fixed at both ends (Figure 5.22c). If the fixed–ended beam shown in Figure 5.22c is subjected to only one concentrated force at the middle (instead of two closely located concentrated forces), its bending stiffness can be calculated using Equation 2.3 with $F_K = 192$.

If it is assumed that the loaded beam that connects the two loaded floors in the building system is a line on which the displacements are applied, the floors will act in the same way as a fixed-ended beam subjected to a single point load at the middle. Numerical simulations were conducted in this way to investigate how floors behave when they are fixed at both ends and loaded at the middle in order to make a direct comparison with analytical results achieved using Equation 2.3. Since the width of the loaded beam (b_{lb}) is relatively small compared to to the length of the two connected floors, the results obtained based on Equation 2.3 can be modified to estimate the bending stiffness of the floors subjected to two line loads located at each edge of the loaded beam.

Initially, the case where the fixed–ended beam is subjected to only one concentrated load at the middle is modified to estimate the bending stiffness of the loaded floors, then the more realistic case of Figure 5.22c (a fixed–ended beam subjected to two point loads) is adjusted. It is worth noting that the following sections completely depend on the case of the fixed–ended beam shown in Figure 5.22c.

Two interior connected floors can be represented by a fixed–ended beam if the transferred forces or displacements are distributed uniformly over their cross sections, as shaded in Figure 5.23c (based on the previously stated assumption [7]). For this case, the moment of inertia of the floor cross section (I_{fl}) may be used in Equation 2.3. I_{fl} includes the moment of inertia of both floor beams and the slab as one rigid body, and is calculated using the parallel axis theorem. Numerical simulations were conducted to consider a range of sizes of the structural parts, as shown in Table 5.4, where t_{sl} is the slab thickness, and b_{fb}, b_{sb}, b_{lb} are the cross sectional widths of the floor, supporting and loaded beams, respectively. Additionally, half of the model (Figure 5.23a) was numerically analysed due to symmetry.

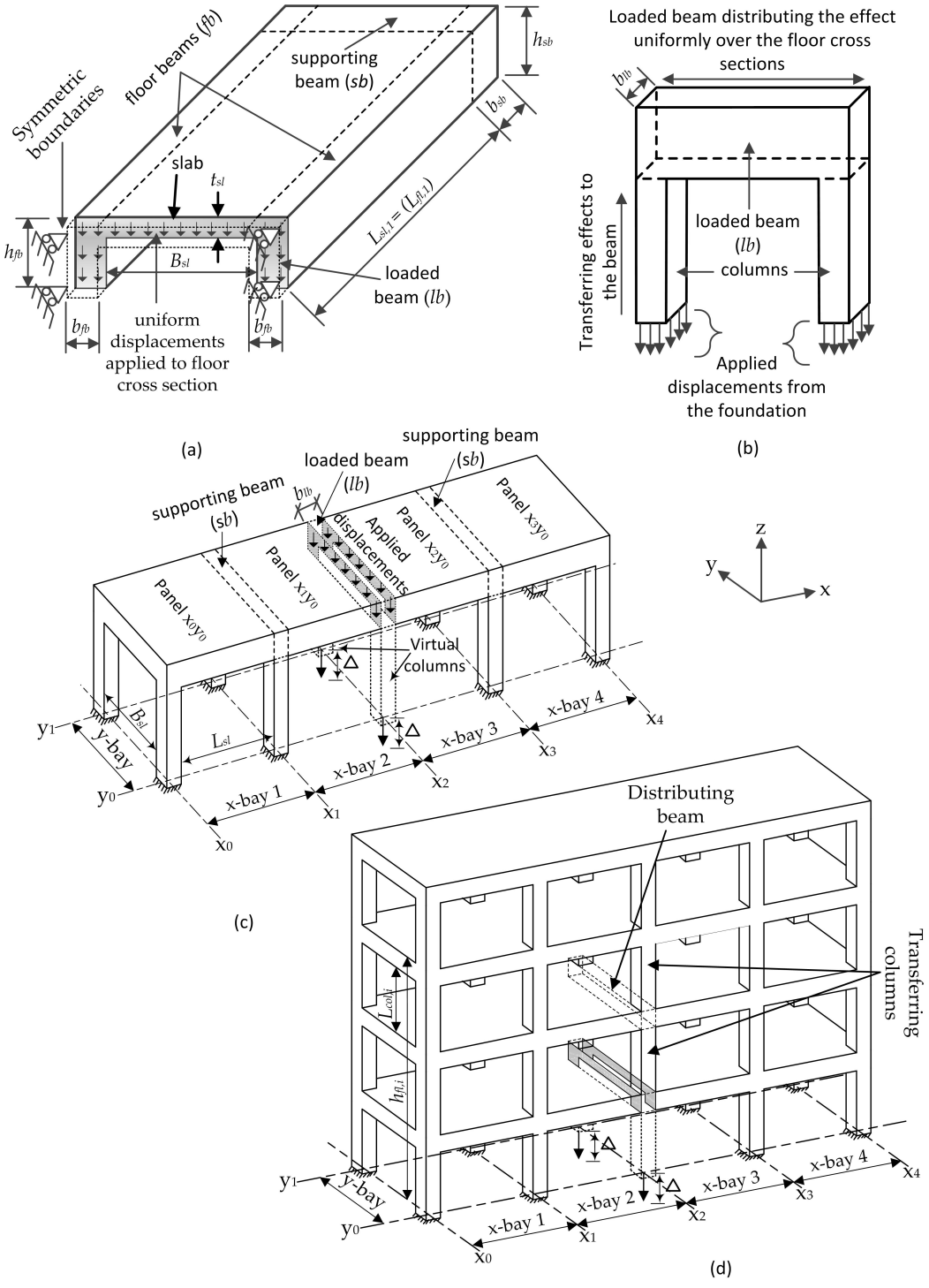

Fig. 5.23 (a) Typical floor subjected to displacements, (b) conveying displacement effects through columns to beams, (c) typical numerical model of a single storey, single y-bay building, (d) single y-bay, multi x-bay and multi storey building

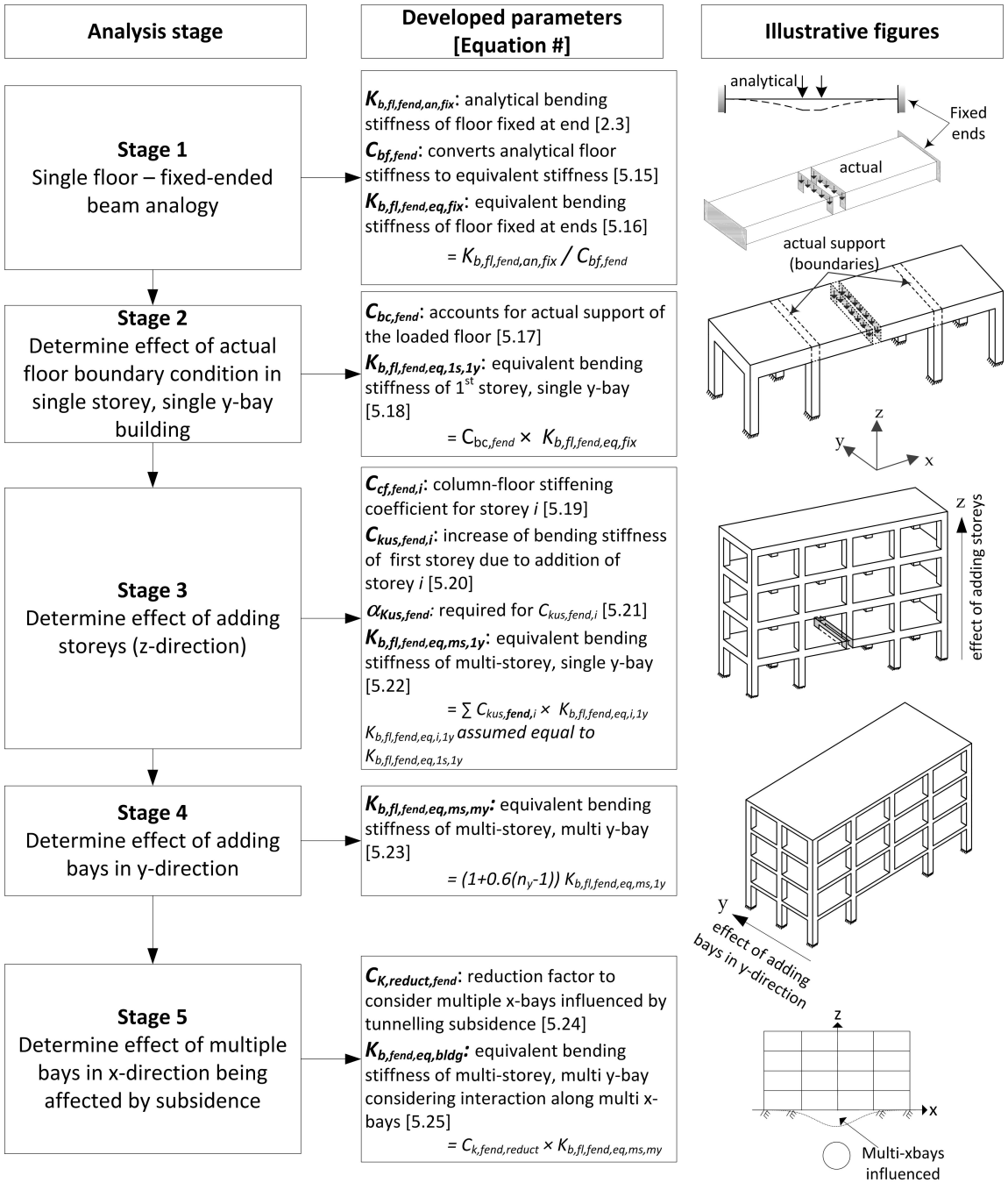

Fig. 5.24 Flow chart of the methodology of the fixed–ended approach

Table 5.4 Range of sizes of structural parts considered in stage 1 analyses

Parameter	L_{sl}	B_{sl}	t_{sl}	b_{fb} and $b_{sb} = b_{lb}$	h_{fb} and $h_{sb} = h_{lb}$
Range (m)	1.5 to 9	1.5 to 9	0.1 to 0.2	0.2 to 0.4	0.3 to 0.75

In this stage of analysis, the supporting beam shown in Figure 5.23a,c was not modelled. Instead, a fixed boundary was applied to the ends of the connected floors (at the end of length L_{fl}, excluding b_{sb}). The applied distributed displacements to the floor cross sections are also shown in Figure 5.23a. The sum of the nodal reaction forces were determined and divided by the applied displacement to obtain the numerically determined bending stiffness using Equation 5.1.

Fixed-ended beam subjected to one point load

In the case of a fixed–ended beam subjected to one point load at its centre, the symmetric boundary condition of the floor cross sections (Figure 5.23a) was applied directly to the cross section of the modelled floor indicating that the width of the loaded beam is zero. For using the analytical equation of computing bending stiffness (Equation 2.3), the total length of the deflected floors should be considered which is: $L_{fl,t} = L_{fl,1} + L_{fl,2} + b_{lb}$. The length of the floors are assumed equal ($L_{fl,1} = L_{fl,2}$), then $L_{fl,t} = 2 \times L_{fl} + b_{lb}$ where L_{fl} is the length of one floor and is equal to the length of the slab ($L_{fl} = L_{sl}$), and $b_{lb} = 0$.

Figure 5.25a shows the ratio of floor bending stiffness calculated using Equation 2.3 ($K_{b,fl,fend,an,fix}$, where subscript *an* indicates an analytically determined value, and $fend$ indicates fixed–ended) to that determined from the numerical analysis ($K_{b,fl,fend,num,fix}$) at different values of L_{sl}/B_{sl}. In one set of simulations, the slab width (B_{sl}) and beam cross sections were constant and only the length of the deflected floors ($L_{fl,t}$, by varying L_{sl} and/or b_{lb}) was changed (variable $L_{fl,t}$). In the other set, $L_{fl,t}$ and beam cross sections were constant and B_{sl} was varied (variable B_{sl}). Note that $b_{lb} = 0$ for the group of simulations shown in Figure 5.25.

Figure 5.25a demonstrates that the bending stiffness of the deflected floors calculated analytically based on Equation 2.3 is generally overestimated to some extent compared to the numerically obtained bending stiffness. It is also displayed that the overestimation increases as the ratio of L_{sl}/B_{sl} decreases.

The reason for the overestimation of the floor bending stiffness using Equation 2.3 is related to the difference in the bending stiffness of the individual slab and beams in the floor system ($2K_{b,fb}/K_{b,sl}$), and the length of the slab relative to its width (L_{sl}/B_{sl}). These factors

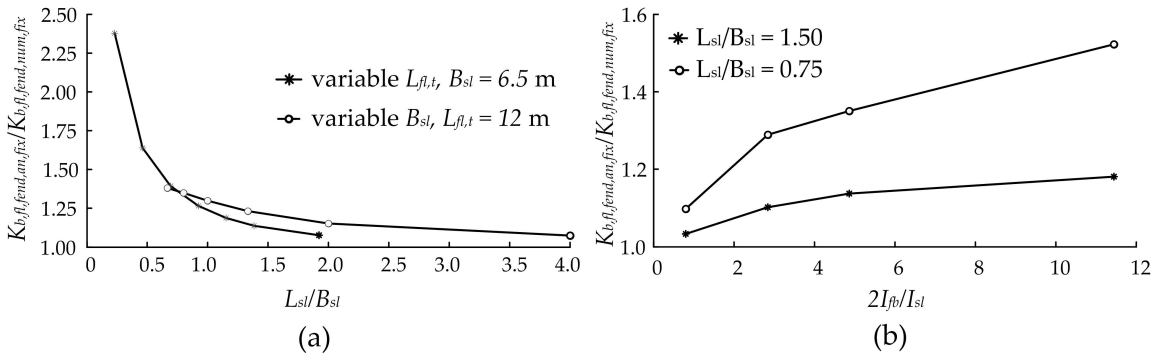

Fig. 5.25 (a) Ratio of analytical to numerical floor bending stiffness for different L_{sl}/B_{sl} values, (b) effect of $2I_{fb}/I_{sl}$ on floor bending stiffness

are explained in detail in Section 5.4.2. Similar to the cantilever approach, the length and the elastic modulus of the beams and slabs were kept the same in the simulations. Therefore, the ratio of bending stiffness of beams to that of the slab was taken as the ratio of the moments of inertia: $2I_{fb}/I_{sl}$, as plotted in Figure 5.25b for two specific cases of L_{sl}/B_{sl}.

Based on the numerical results of varying L_{sl}, B_{sl} and $2I_{fb}/I_{sl}$, a coefficient $C_{bf1,fend}$ (Equation 5.14) can be used to modify the analytical floor bending stiffness calculated by Equation 2.3 to reasonably match the numerical model results of the bending stiffness of a fixed–ended floor assuming the width of the loaded beam is zero. This coefficient takes into account the effect of L_{sl}, B_{sl} and the individual moment of inertia of the slab and floor beams, and is approximately equal to $K_{b,fl,fend,an,fix}/K_{b,fl,fend,num,fix}$.

$$C_{bf1,fend} = \left(\frac{24I_{fb}}{I_{sl}}\right)^{\left(\frac{B_{sl}}{18L_{sl}}\right)} \tag{5.14}$$

where values of I_{fb} and I_{sl} are calculated independently as explained in Section 5.4.2. The main factor causing the differences between the numerical and analytical results is the bending stiffness of the beams, which is largely affected by L_{sl}. For this reason, in the expression of $C_{bf1,fend}$, the term $(2I_{fb}/I_{sl})$ is factored by 12 and L_{sl} by 18. Figure 5.26 illustrates the good fit obtained by using $C_{bf1,fend}$ (i.e. a good match with $K_{b,fl,fend,an,fix}/K_{b,fl,fend,num,fix}$).

Fixed-ended beam with two point loads

As mentioned earlier, the width of the loaded beam (b_{lb}) is generally small compared to the total length of both deflected floors ($L_{fl,t}$), but it may still have some effect on the numerical estimation of floor bending stiffness. It is assumed that the moment of inertia of the floor and

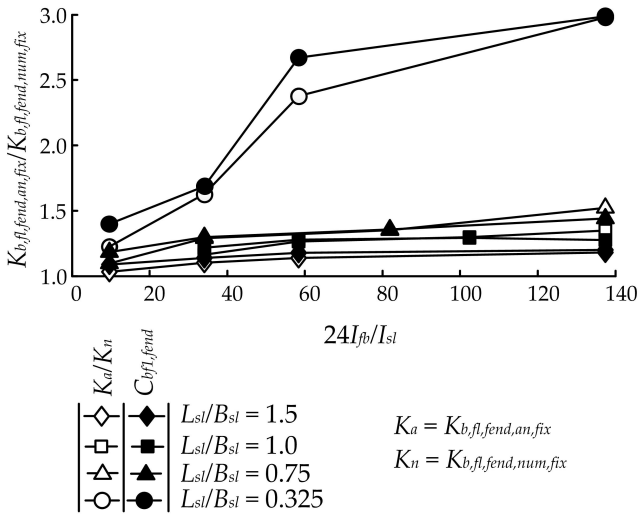

Fig. 5.26 Comparison of $K_{b,fl,fend,an,fix}/K_{b,fl,fend,num,fix}$ and $C_{bf1,fend}$ for different values of L_{sl}/B_{sl}

the cross section of the beams do not change due to the width of the loaded beam. Therefore, the part of Equation 5.14 related to the moment of inertia ($24I_{fb}/I_{sl}$) is kept constant, and the part related to the dimensions of the floors ($B_{sl}/18L_{sl}$) is modified to take into consideration the width of the loaded beam (b_{lb}) and the nature of the applied load.

When the deflected floors are subjected to two line loads, the deformation of the loaded floors becomes more restricted compared to the case where the floors were loaded at the middle. The application of two line loads divide the floors into three parts: two large parts with lengths of L_{sl} and a small part with a length of b_{lb}. The existence of two line loads results in a reduction in the difference between bending stiffness values obtained numerically, and those calculated from Equation 2.3. This reduction is due to the effect of b_{lb}/B_{sl} which is not captured by Equation 5.14 (coefficient $C_{bf1,fend}$).

Figure 5.27 shows how the ratio of $K_{b,fl,fend,an,fix}/K_{b,fl,fend,num,fix}$ varies with the change of b_{lb}/B_{sl}. To obtain a good fit to the numerical results, the term $18L_{sl}$ in Equation 5.14 should be replaced by $9L_{fl,t}$ ($L_{fl,t}$ here includes b_{lb}), and a term $(1 - b_{lb}/B_{sl})$ should be added. A new coefficient is introduced, $C_{bf,fend}$, which is approximately equal to $K_{b,fl,fend,an,fix}/K_{b,fl,fend,num,fix}$ for deflected floors subjected to two line loads, and is expressed by Equation 5.15. Equation 5.15 yields the same values as $C_{bf1,fend}$ when $b_{lb} = 0$. Figure 5.27 also exhibits the values of $C_{bf1,fend}$ and $C_{bf,fend}$. It is indicated that b_{lb}/B_{sl} has a significant effect on the results, and this effect is well-captured by Equation 5.15 ($C_{bf,fend}$).

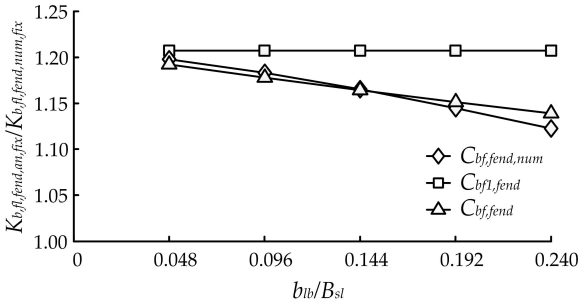

Fig. 5.27 Comparison of $K_{b,fl,fend,an,fix}/K_{b,fl,fend,num,fix}$ with $C_{bf,fend}$ and $C_{bf1,fend}$ for $L_{sl}/B_{sl} = 1.2$ and $24I_{fb}/I_{sl} = 58.5$

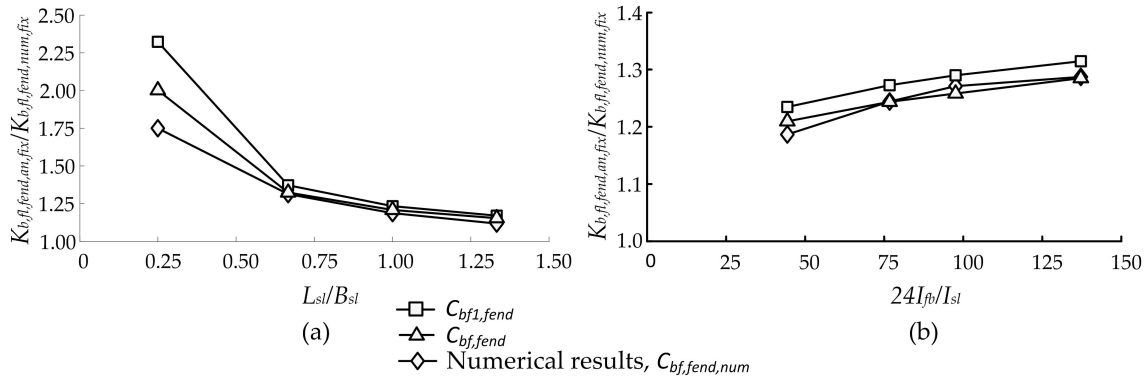

Fig. 5.28 Comparison of $K_{b,fl,fend,an,fix}/K_{b,fl,fend,num,fix}$ with $C_{bf,fend}$ and $C_{bf1,fend}$ for $b_{lb}/B_{sl} = 0.0667$: (a) $24I_{fb}/I_{sl} = 44.44$, (b) $L_{sl}/B_{sl} = 1.0$

$$C_{bf,fend} = \left(\frac{24I_{fb}}{I_{sl}}\right)^{\left(\frac{B_{sl}}{9L_{fl,t}} \times (1 - b_{lb}/B_{sl})\right)} \tag{5.15}$$

Figures 5.28a and b present a comparison of coefficients $C_{bf1,fend}$ and $C_{bf,fend}$ for a constant value of b_{lb}/B_{sl}. There is a better agreement of coefficient $C_{bf,fend}$ with the numerical values compared to that of coefficient $C_{bf1,fend}$.

To summarise, the coefficient $C_{bf,fend}$ is used in the calculation of floor bending stiffness in the rest of the calculations within the fixed–ended approach. The analytically computed bending stiffness of the floors is divided by $C_{bf,fend}$ to obtain a good approximation of the numerical bending stiffness of the floors:

$$K_{b,fl,fend,eq,fix} = \frac{K_{b,fl,fend,an,fix}}{C_{bf,fend}} \tag{5.16}$$

where $K_{b,fl,fend,eq,fix}$ is the equivalent bending stiffness of the fixed support floors (subscript *eq* denotes an equivalent parameter based on a curve-fitting coefficient *C*).

5.5.3 Stage 2: evaluation of floor boundary condition

In stage 1, the analyses were done on deflected floors fixed at their ends, however this case is not realistic in framed buildings. To estimate the effect of the real degree of end fixity of the deflected floors, numerical simulations were performed including additional panels (up to 6 from both boundaries) in the x-direction. Figure 5.23c shows an illustrative numerical model of a single storey building with a single bay in the y-direction and multiple bays in the x-direction. The range of dimensions of the structural parts considered are presented in Table 5.5. It is worth noting that column cross sectional dimensions depended on the cross sectional dimensions of the floor and supporting beams (i.e. $h_{col} = b_{sb}$ and $b_{col} = b_{fb}$).

Table 5.5 Range of sizes of structural parts considered in stage 2 analyses

Parameter	L_{sl}	B_{sl}	t_{sl}	b_{fb} and b_{sb}	h_{fb} and h_{sb}	L_{col}
Range (m)	3 to 8	2.5 to 8	0.1 to 0.2	0.2 to 0.4	0.4 to 0.65	2.8 to 4

Six scenarios were analysed; first considering only two deflected x-panels and subsequently adding panels in the x-direction from both sides. The numerical simulations were conducted as follows: a fixed boundary was applied to the bottom of all columns except the virtual (displaced) columns (Figure 5.23c). First, only the loaded panels (x_1y_0 and x_2y_0 in Figure 5.23c, including the loaded floors, supporting beams and columns at $x1$ and $x3$) was included in the analysis. Note that the numerical modelling only considered half of the model due to symmetry. Similar to the cantilever approach, a specific uniform displacement was applied to the cross sections of the loaded floors and the nodal reaction forces were determined. The floor bending stiffness was then calculated based on Equation 5.1. One supporting panel from each side of the loaded panels in the x-direction (Figure 5.23c) was then added to the analysis and the same procedure was repeated to determine the floor bending stiffness of the loaded panels. This process was repeated until five supporting panels on both sides in the x-direction were added to the analysis. Note that in all simulations, the displacements were only applied to the cross sections of the loaded floors.

Adding supporting panels provides an additional degree of end fixity to the loaded floors, which effectively specifies the value of F_K in Equation 2.3 for the loaded panels. The addition of a single supporting panel from each side in the x-direction (panels x_0y_0 and x_3y_0

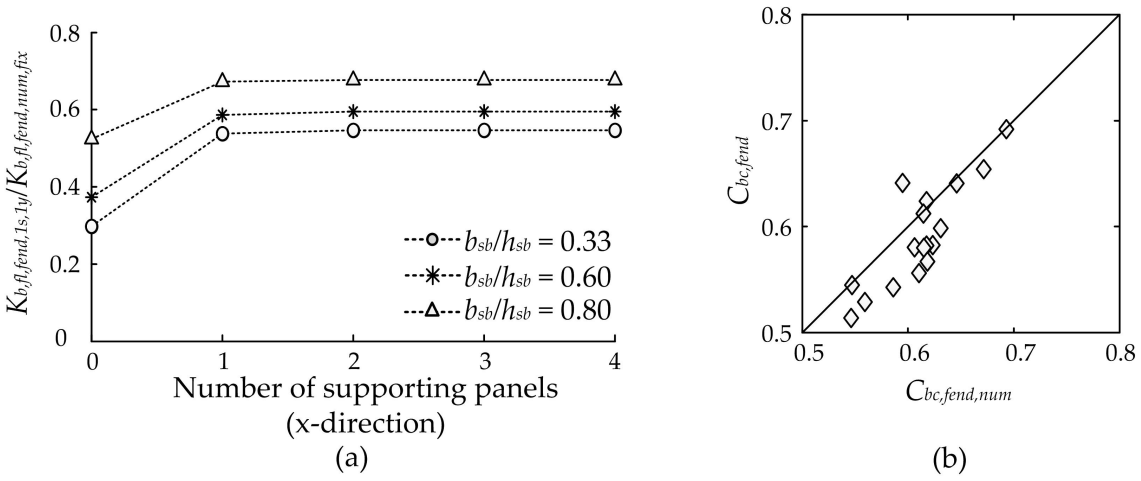

Fig. 5.29 (a) Effect of supporting floors on the end fixity of the loaded floors, (b) comparison of proposed $C_{bc,fend}$ values (Equation 5.17) with numerical results

in Figure 5.23c) provides significant resistance against rotation to the supporting beams, and increases the degree of floor end fixity. The degree of end fixity of the loaded floors (connected to supporting panels) can be related to the bending stiffness of the fixed support scenario of these floors (from Stage 1). It can be defined as the ratio of the bending stiffness of the loaded floors in a single storey, one y-bay numerical analysis ($K_{b,fl,fend,1s,1y}$) to that obtained for fixed-ended loaded floors ($K_{b,fl,fend,fix}$ from Stage 1). Figure 5.29 shows the variation of $K_{b,fl,fend,1s,1y}/K_{b,fl,fend,num,fix}$ with the number of supporting panels for three cases of b_{sb}/h_{sb}. The numerical results show that the addition of more than one supporting panel has a negligible effect on the change of bending stiffness.

The floor bending stiffness for the loaded panels alone (without supporting panels) depends on the stiffness of the supporting beams and columns. The ratio of b_{sb}/h_{sb} is also an influential parameter as it has a significant effect on the rotation of the loaded floor and provides its end fixity. Figure 5.29a illustrates that the bending stiffness of a single loaded panel (zero supporting panels) is considerable compared to the bending stiffness of its fixed-ended scenario (i.e from stage 1), but the case of having only two panels loaded at their middle columns due to tunnelling is not realistic. Therefore, the case where at least one supporting panel is available at each side of the one y-bay building is considered for the fixed–end approach.

The stiffness of the supporting beams, supporting columns (located on x_1 and x_3 in Figure 5.23c) and the floor of the first supporting panels from each side (panels x_0y_0 and x_3y_0 in Figure 5.23c) have the most significant effect on the degree of end fixity of the loaded

floors. Based on these parameters, the following modification coefficient $C_{bc,fend}$ is proposed to estimate the degree of end fixity of the loaded floor:

$$C_{bc,fend} = \frac{K_{c,Sfl} + K_{c,sb} + 2K_{c,col}}{K_{c,Lfl} + K_{c,Sfl} + K_{c,sb} + 2K_{c,col}} < 1.0 \tag{5.17}$$

The parameters are the same as that of Equation 5.4.

The coefficient $C_{bc,fend}$ can be used to evaluate the bending stiffness of the loaded floors in the first storey of a single y-bay building using:

$$K_{b,fl,fend,eq,1s,1y} = C_{bc,fend} \times K_{b,fl,fend,eq,fix} \tag{5.18}$$

where $K_{b,fl,fend,eq,fix}$ is obtained from Equation 5.16.

Figure 5.29b compares results of $C_{bc,fend}$ using Equation 5.17 with $C_{bc,fend,num} = K_{b,fl,fend,num,1s,1y}/K_{b,fl,fend,num,fix}$, an equivalent coefficient determined from numerical analyses. The results show that the equivalent values using Equation 5.17 give a satisfactory match to the numerical results.

5.5.4 Stage 3: effect of adding storeys

Numerical analyses were conducted to evaluate the stiffness effect of adding up to 10 storeys to the single y-bay building from stage 2, as shown in Figure 5.23d. The sizes of floors, beams and columns considered were the same as in stage 2 (Table 5.5). The area of applied displacements is consistent with stage 2, as indicated in Figure 5.23d. For a given number of x-bays (up to 10 from each side in the x-direction), numerical analyses were conducted sequentially by adding additional storeys. The first storey is used as a reference for which the bending stiffness is compared when additional storeys are added, thereby illustrating the additional bending stiffness each storey contributes.

Similar to the cantilever approach (Section 5.4.4), a column-floor stiffening effect coefficient $C_{cf,fend}$ (Equation 5.19) can be introduced to take into account the role of the columns in transferring the stiffness contribution of upper storeys to the foundation as well as the influence of the distance from the foundation to the considered floor. In the fixed–ended approach, the influence of a storey on the overall structural response is proportional to the relative stiffness of columns compared to both connected floors.

$$C_{cf,i} = \frac{2K_{c,col}}{2K_{c,col} + 2K_{c,Lfl}} \times \left(\frac{L_{col,i}}{h_{fl,i}}\right) \tag{5.19}$$

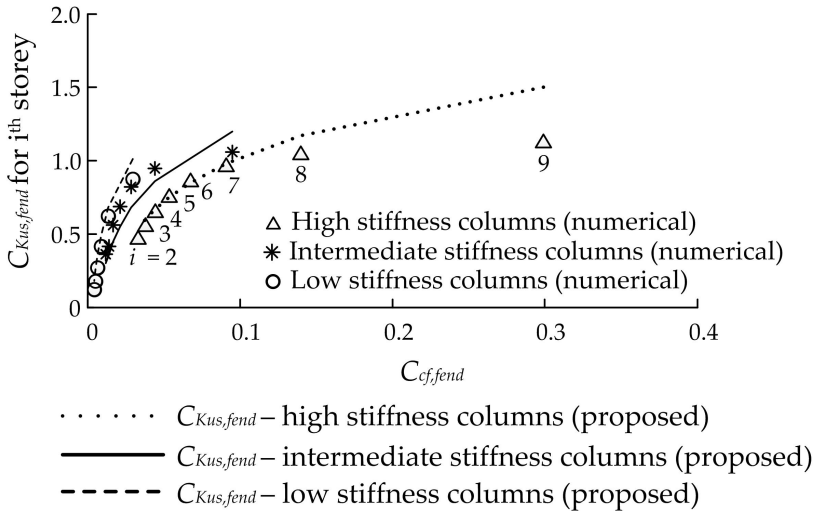

Fig. 5.30 Relationship between $C_{Kus,fend}$ and $C_{cf,fend}$ for buildings of varying column stiffness

where subscript i indicates a measurement for the i^{th} floor, $L_{col,i}$ is column height, and $h_{fl,i}$ is the total height between the i^{th} floor and the foundation, as shown in Figure 5.23d.

A coefficient $C_{Kus,fend,i}$ is defined as the ratio of the increased bending stiffness of the superstructure due to the addition of the i^{th} upper storey (subscript *us*) to the bending stiffness of the first storey. Since there is no rotation of the global building due to symmetry about the deflection line (i.e. loaded columns located on $x1$ in Figure 5.23c), the number of the supporting spans in the x-direction does not have an effect on $C_{Kus,fend}$.

The numerical analyses indicated that $C_{Kus,fend}$ has a logarithmic relationship with $C_{cf,fend}$, as illustrated in Figure 5.30 for cases of high, intermediate, and low column stiffness relative to the loaded floor stiffness ($2K_{c,col}/2K_{c,Lfl} = 0.426$, 0.105, and 0.031, respectively) in a 7, 8 and 9 storey building, respectively; the data can be reasonably well fitted with the following curve:

$$C_{Kus,fend,i} = \log_{10}(C_{cf,fend,i}) + \alpha_{Kus,fend} \quad \geq 0.0 \tag{5.20}$$

where $\alpha_{Kus,fend}$ is a parameter depending on the stiffness of the loaded beam, loaded floors and columns. Generally, an increase of the value of $\alpha_{Kus,fend}$ is obtained with the increase of stiffness of the beam and/or columns in upper storeys that have the same position as the loaded beam and columns of the first storey. Figure 5.31a illustrates the relationship between $\alpha_{Kus,fend,num}$ obtained from the curve fitting of the numerical results, and the ratio

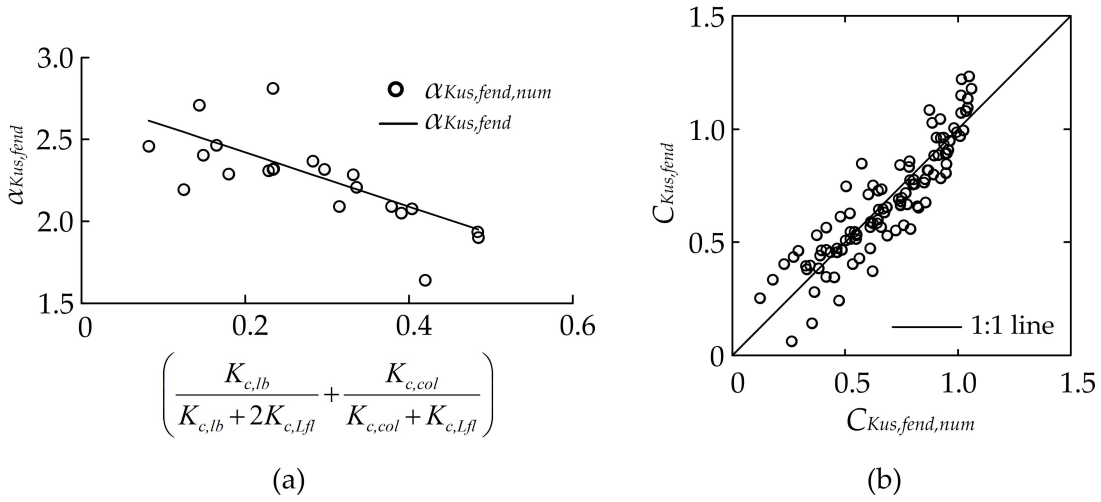

Fig. 5.31 (a) Comparison between $\alpha_{Kus,fend}$ values obtained from curve fitting of numerical results, and proposed values calculated by Equation 5.21, (b) $C_{Kus,fend}$ values: proposed method ($C_{Kus,fend}$) versus numerical results ($C_{Kus,fend,num}$)

$[K_{c,lb}/(K_{c,lb}+2K_{c,Lfl})+K_{c,col}/(K_{c,col}+K_{c,Lfl})]$. The numerical data in Figure 5.31a was fitted using the following expression:

$$\alpha_{Kus,fend} = -1.65 \times \left(\frac{K_{c,lb}}{K_{c,lb}+2K_{c,Lfl}}+\frac{K_{c,col}}{K_{c,col}+K_{c,Lfl}}\right)+2.75 \tag{5.21}$$

A comparison between the numerical and proposed analysis values of $C_{Kus,fend}$ is presented in Figure 5.31b showing a reasonably good agreement between them.

The stiffness contribution of each storey is obtained by multiplying $C_{Kus,fend,i}$ by its floor bending stiffness, $K_{b,fl,fend,eq,i,1y}$ (note that, similar to the cantilever approach, based on assumption [5] that floor parameters remain constant across all storeys, $K_{b,fl,fend,eq,i,1y} = K_{b,fl,fend,eq,1s,1y}$, which is calculated in stage 2 of the analysis). The bending stiffness of the entire multi-storey (subscript *ms*) single y-bay building ($K_{b,fl,fend,eq,ms,1y}$) is then obtained by summing the individual storey contributions:

$$K_{b,fl,fend,eq,ms,1y} = \sum_{i=1}^{m}\left(C_{Kus,fend,i} \times K_{b,fl,fend,eq,i,1y}\right) \tag{5.22}$$

Figure 5.32 compares the bending stiffness of single y-bay buildings computed using the proposed method (from stages 1 to 3) with their equivalent numerical results. The figure includes 155 data points including buildings of 1 to 9 storeys.

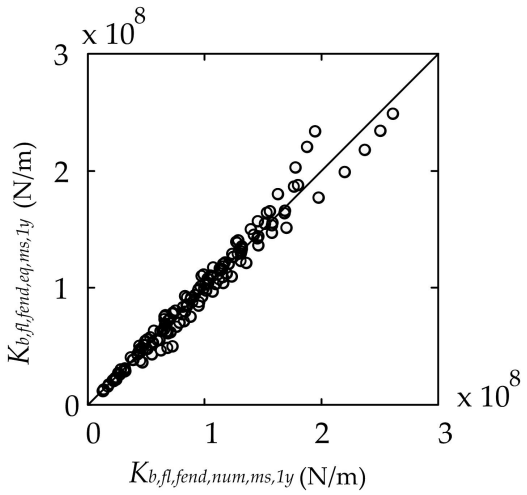

Fig. 5.32 Bending stiffness of single y-bay, multi-storey (up to 9 storeys) buildings: proposed method ($K_{b,fl,fend,eq,ms,1y}$) versus numerical results ($K_{b,fl,fend,num,ms,1y}$)

5.5.5 Numerical verification of stages 1 to 3

To validate the proposed method from stage 1 to stage 3, a single y-bay, six-storey building made of concrete with an elastic modulus of 30 GPa was numerically modelled in a way that the virtual columns (Figure 5.23c) which were removed in the previous simulations were added to the model, and the displacements were applied to their bases. Using this technique allows the transfer of the displacements through the columns to the floors, and eliminates the assumption of applying displacements uniformly to the loaded floor cross sections of the first storey.

Column dimensions were 0.3×0.3×3.2 m (b_{col}, h_{col} and L_{col}, respectively), floor and supporting beam dimensions were 0.3×0.5 m (b_{fb} or b_{sb}, and h_{fb} or h_{sb}, respectively), and slab dimensions were 4×6×0.15 m (B_{sl}, L_{sl} and t_{sl}, respectively).

Figure 5.33a shows the $C_{Kus,fend}$ values for the numerical and the proposed methods. There is a generally good agreement between the coefficients except for the coefficient of the second storey. To show the effect of this difference, the estimated bending stiffness of the building from one to 6 storeys is demonstrated in Figure 5.33b for the numerical and the proposed methods. It is indicated that the estimated bending stiffness values are in a good agreement.

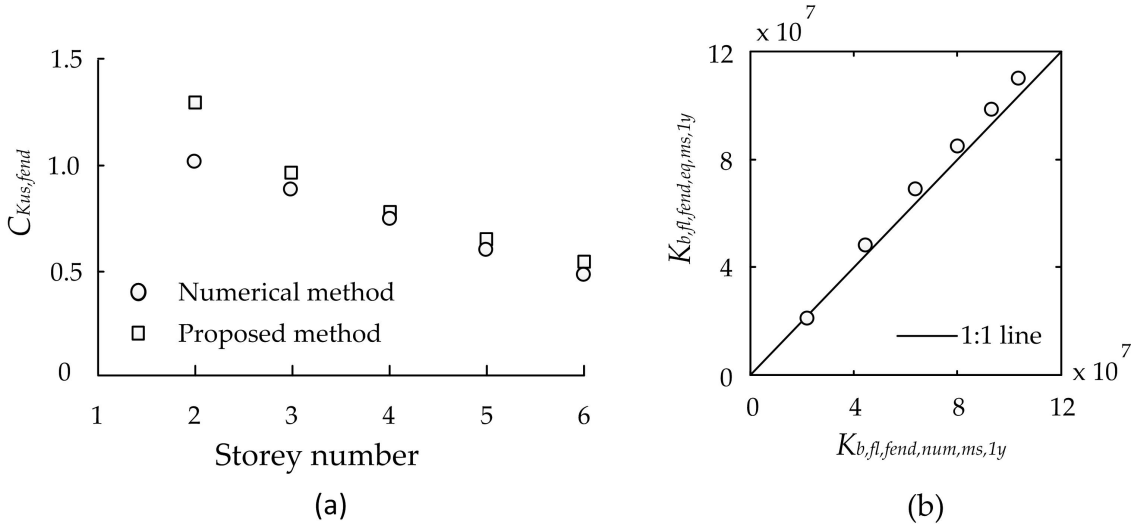

Fig. 5.33 (a) Comparison of $C_{Kus,fend}$ between numerical and the proposed methods, (b) comparison of bending stiffness values of the superstructure between the numerical and the proposed methods

5.5.6 Stage 4: effect of adding y-bays in direction of tunnel

This section considers the effect of adding bays in the direction of the tunnel (y-direction) to the bending stiffness of the building. Figure 5.34a demonstrates the change of $C_{Kus,fend}$ for each storey of a 5-storey building as the number of y-bays is increased from 1 to 3, based on the numerical analyses. The value of $C_{Kus,fend}$ for the i^{th} floor was calculated from the numerical results as $(K_{b,fl,i} - K_{b,fl,(i-1)})/K_{b,fl,1}$. Also included in Figure 5.34a are values obtained using the proposed method (Equation 5.20) for a single y-bay building.

Similar to the cantilever approach, the numerical results show that the addition of each y-bay increases the bending stiffness of the building superstructure by approximately 60% of the bending stiffness of a single y-bay building. For this reason, Equation 5.23 is proposed to estimate the bending stiffness of a multi-storey building with multiple y-bays (subscript *my*), $K_{b,fl,fend,eq,ms,my}$:

$$K_{b,fl,fend,eq,ms,my} = (1 + 0.6(n_y - 1)) \times K_{b,fl,fend,eq,ms,1y} \tag{5.23}$$

An example calculation of building stiffness using the proposed method is provided in Appendix B. Figure 5.34b shows a comparison of the bending stiffness of multi y-bay buildings obtained from the numerical analyses and those calculated using the proposed method (stages 1 to 4). The buildings range from 2 to 3 y-bays, and 1 to 7 storeys.

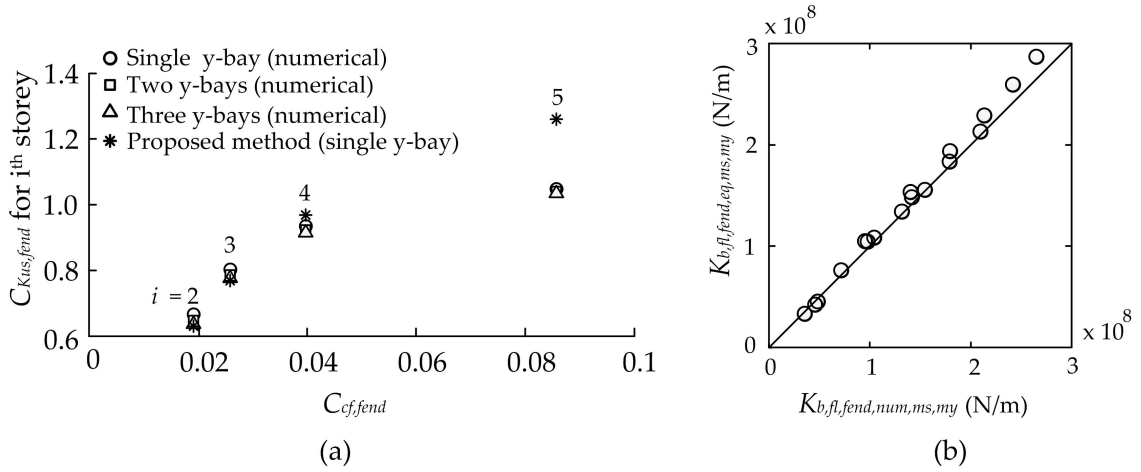

Fig. 5.34 (a) Comparison between numerical and proposed values of $C_{Kus,fend}$ considering buildings with different numbers of y-bays, (b) comparison of the numerical bending stiffness of multi y-bay buildings with their equivalent calculated values based on stages 1 to 4

5.5.7 Stage 5: considering multiple x-bays affected by ground displacements

The numerical simulations thus far only considered the case where only two middle panels of the building were subjected to downward displacements (i.e. affected by tunnelling settlements). As explained in Section 5.4.7, an increase in the influenced building length causes a large reduction of the bending stiffness since the length has a cubic effect on the bending stiffness (Equation 2.3).

Figure 5.35 shows a tunnel constructed under the centreline of a building. If the building is located entirely inside the displaced soil zone, the bending stiffness of the superstructure will have a small contribution to the global building bending stiffness because the ends of the structure are not constrained. Note that the global rotation of the building that occurs in the case of the cantilever approach does not happen in the case of the fixed–ended approach. The deflection and rotation of a building in the fixed–ended case is symmetric about the tunnel axis.

To consider the effect of the influenced length of the building, numerical simulations were performed to evaluate how bending stiffness of a storey decreases when more panels are affected by ground displacements. It was assumed that the building behaved like a fixed–ended beam subjected to multiple loads at the location of the columns, as shown in Figure 5.36. Multi-storey buildings with 1 y-bay and 16 x-bays were numerically simulated. Half of the model (8 x-bays) was analysed due to symmetry. The number of affected panels

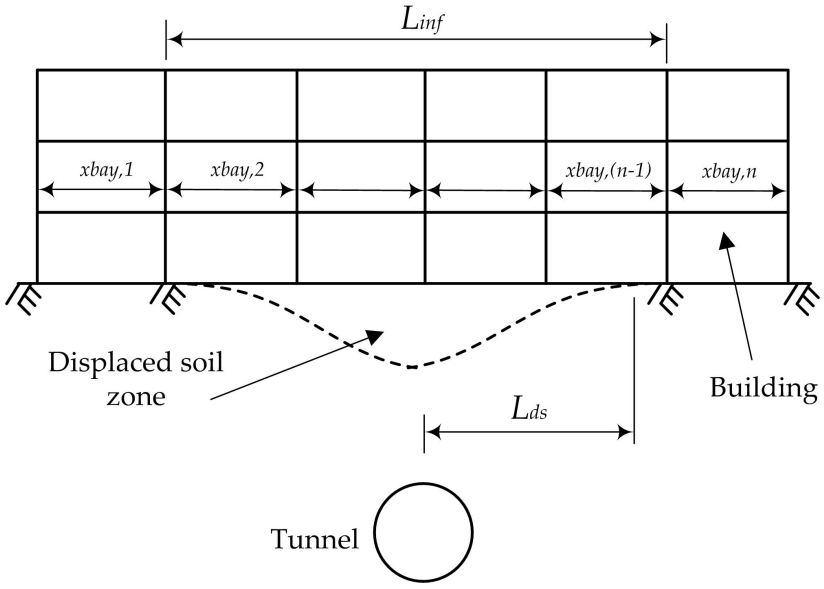

Fig. 5.35 Soil and building zones affected by tunnelling induced ground displacements

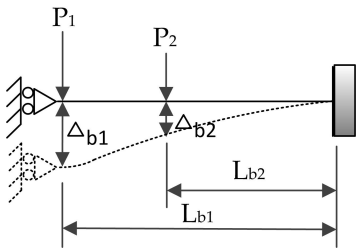

Fig. 5.36 A fixed–ended beam subjected to multiple loads

considered was 2, 4, 6 and 8; the bases of columns in the unaffected zone were fixed. Similar to the cantilever approach (Section 5.4.7), the displacement was modelled by applying forces at the locations of the affected columns; the applied forces changed linearly from a maximum value above the tunnel centreline to zero at the columns in the unaffected zone.

Expression 5.11 was used to approximate bending stiffness of a building subjected to multiple loads due to the complexity of an analytical expression. A similar reduction factor to the cantilever approach, $C_{K,reduct,fend}$, was introduced to quantify the reduction of the building bending stiffness due to the effect of multiple panels being affected by tunnelling. Figure 5.37a plots results for a single y-bay, 16 x-bay, 1 storey building when the number of affected panels is increased from 2 to 8 and illustrates that there is a dramatic reduction of the building bending stiffness when more than two panels are affected by ground displacements. As also observed in the cantilever approach, the results indicate that

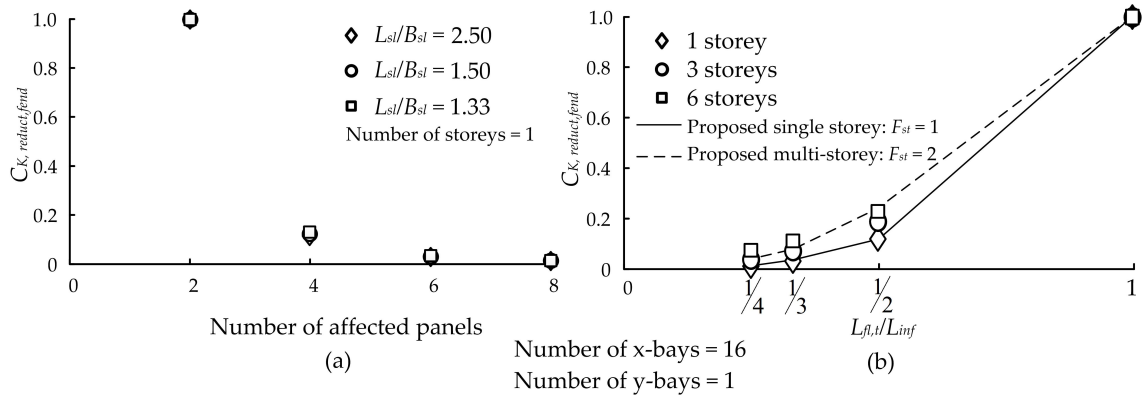

Fig. 5.37 (a) Reduction of building bending stiffness with the number of panels located in the displaced zone, (b) comparison between numerical and proposed values of $C_{K,reduct,fend}$

$C_{K,reduct,fend}$ is insensitive to the panel size (L_{sl}/B_{sl}). Figure 5.37b shows results for the same building but with additional storeys added; a slight increase in the value of $C_{K,reduct,fend}$ is noted for multi-storey buildings. Based on these numerical results, $C_{K,reduct,fend}$ can be expressed as:

$$C_{K,reduct,fend} = F_{st} \times \frac{L_{fl,t}^3}{L_{inf}^3} \tag{5.24}$$

where F_{st} =1 and 2 for one-storey and multi-storey buildings, respectively. In the fixed–ended approach, L_{inf} can be calculated as $L_{inf} = 2L_{ds}$ if $2L_{ds} \leq L_{bldg}$, or $L_{inf} = L_{bldg}$ if $2L_{ds} > L_{bldg}$, where L_{ds} is the half length of the displaced zone (see Figure 5.35). For practical purposes, L_{inf} should correspond to the location of a building column.

The final value of the building bending stiffness, $K_{b,fend,eq,bldg}$, can be calculated using:

$$K_{b,fend,eq,bldg} = C_{K,reduct} \times K_{b,fl,eq,ms,my} \tag{5.25}$$

where $C_{K,reduct,fend} = 1$ if tunnelling settlements only affect the two middle x-bays or calculated using Equation 5.24 otherwise.

5.5.8 Comparison with other methods

A 2D and 3D comparison of the proposed method is made with the approaches mentioned in Section 5.4.8. For the approach of Goh and Mair (2014), it is assumed that the two bays affected by tunnelling are located in the sagging area ($L_{sag,hog}$) to calculate $L_{sag,hog}^2/L_{bay}^2$.

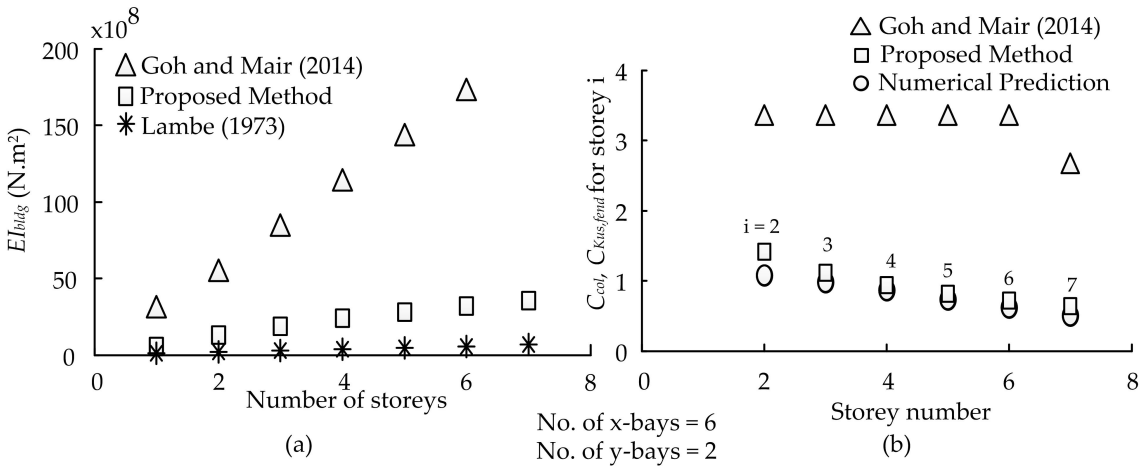

Fig. 5.38 (a) Comparison of EI_{bldg} between the proposed method and approaches suggested by Lambe (1973) and Goh and Mair (2014), (b) comparison between C_{col} and $C_{Kus,fend}$ of the numerical and proposed methods

The comparison is made for a multi-storey (1 to 7) two y-bay, 6 x-bay building with the parameters given in Table 5.6. This building was used for both 2D and 3D comparisons.

Table 5.6 Sizes of structural parts (1 to 7 storey building) considered in 2D and 3D comparative analyses

Parameter	L_{sl}	B_{sl}	t_{sl}	b_{fb}	b_{sb}	h_{fb} and h_{sb}	L_{col}
Dimension (m)	6.00	5.00	0.15	0.40	0.35	0.50	3.00

Figure 5.38a shows that the approach used by Lambe (1973) results in the lowest values of EI_{bldg} because it disregards the effect of the interaction between slabs through their connecting links. The values of EI_{bldg} of the proposed method are greater than those of the Lambe (1973) approach. The difference increases with the increase of building storeys. The method of Goh and Mair (2014) leads to the largest values of EI_{bldg} among the three considered methods. The main reason is that two bays are affected by tunnelling which result in a large value of $L^2_{sag,hog}/L^2_{bay}$ in the method of Goh and Mair (2014). It is worth noting that if the coefficient $C_{K,reduct,fend}$ is considered for the proposed method (when more than 2 bays are affected by tunnelling), the values of EI_{bldg} calculated based on the proposed approach of this research will decrease to a an even greater extent.

Figure 5.38b shows the values of C_{col} in the Goh and Mair (2014) method and $C_{Kus,fend}$ obtained from numerical results and the proposed method. It is shown that there is a good

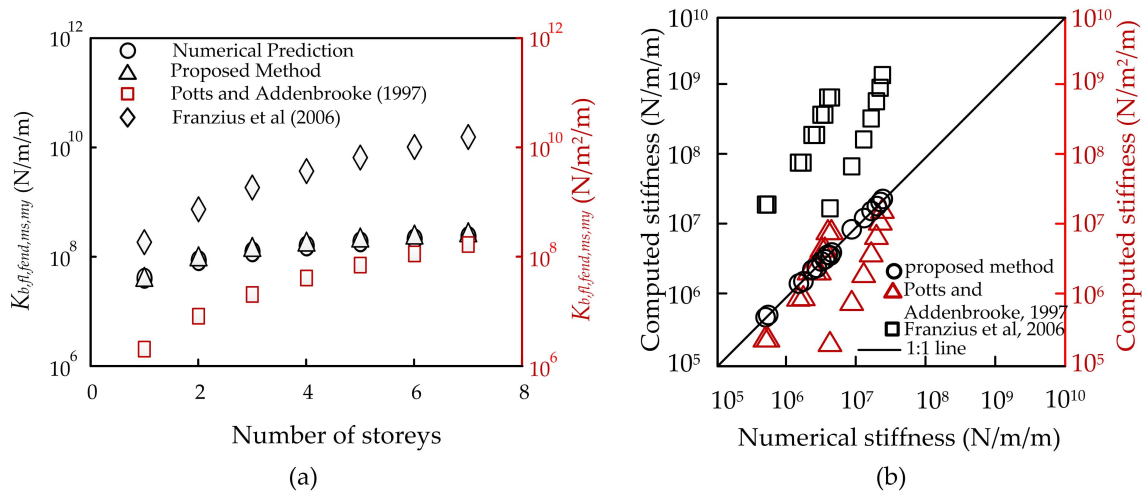

Fig. 5.39 (a) Comparison of 3D building bending stiffness (fixed–ended approach) using different methods, (b) comparing computed building bending stiffness using different methods with the numerically achieved bending stiffness for buildings of multiple y-bays

agreement between the numerical and the proposed values of $C_{Kus,fend}$ while the values of C_{col} from the Goh and Mair (2014) method are significantly higher.

A comparison of bending stiffness of the mentioned 3D building between the numerical prediction and the method proposed in this work, Potts and Addenbrooke (1997) and Franzius et al. (2006) is presented in Figure 5.39a. The bending stiffness values of the Franzius et al. (2006) method were too large to be plotted on a normal axis figure with the other methods. For this reason, the y-axis of Figure 5.39a was chosen to be logarithmic. It is worth noting that $L_{bldg} = 38.45$ m.

As explained in the cantilever approach, the moment of inertia of the building in the methods proposed by Potts and Addenbrooke (1997) and Franzius et al. (2006) are largely overestimated; the term $(L_{bldg}/2)^4$ in the approach of Potts and Addenbrooke (1997) yielded a very large value which in turn reduced the bending stiffness of the building to a great extent. In the method of Franzius et al. (2006), the overestimation of the building cross sectional moment of inertia resulted in the overestimation of the building bending stiffness. Both methods of Potts and Addenbrooke (1997) and Franzius et al. (2006) would appear to lead to unrealistic results; the reasons for this were presented in Section 5.4.8.

Figure 5.39b compares the bending stiffness of a range of multi y-bay buildings calculated by the proposed method of this work (based on stages 1 to 4), and the approaches of Potts and Addenbrooke (1997) and Franzius et al. (2006). There is a good agreement between the numerical results and those of the proposed method.

5.6 Summary

In this chapter, the bending behaviour of 3D concrete framed buildings was investigated in detail considering different parameters that affect the bending stiffness of a member. It should be mentioned that disregarding the 3D nature of buildings and overlooking the parameters that affect the bending stiffness of a member were limitations of the previous research. The results of this chapter overcome these limitations. Furthermore, different from the outcomes of the majority of previous work in which design charts were proposed to deal with specific scenarios of tunnel–building interaction, the approaches suggested in this chapter are applicable to a wide range of buildings with different tunnel–building relative locations.

The analysis started with an analogy between the bending behaviour of a single floor in a loaded panel and the bending deflection of a fixed-support beam. This analogy was essential to relate the outcomes of the numerical analyses to the results of beam analytical equations. Furthermore, the parameters on which bending stiffness of a beam depend, were determined from the mathematical equations of the beam deflection. After that, the contribution of the rest of the building superstructure to the bending of the loaded floor was investigated. The realistic boundary of the loaded floor was determined by considering the effect of the panels connected to the loaded floor in x-direction (perpendicular to the tunnel axis). The bending contribution of the upper floors (z-direction) as well as building storeys in the y-direction (parallel to tunnel axis) was then added to the analysis. Finally, a scenario where multiple panels in x-direction were influenced by tunnelling was numerically studied.

The analyses of this chapter only considered the superstructure, separately from the foundation. It was shown that the building does not deform as a singe member to obtain a uniform effect of ground displacements throughout the building height; the stiffness contribution of the lower storeys to the global building stiffness was more significant than that of the upper storeys.

Furthermore, two computationally efficient methods (cantilever and fixed–ended approaches) were proposed to obtain realistic estimates of the bending stiffness of concrete framed buildings influenced by tunnelling induced displacements. The cantilever approach assumes that the tunnel is located adjacent to the building while in the fixed–ended approach, the tunnel is constructed directly under the building. The methods depend on the actual parameters of the structural components of the building.

Various assumptions and simplifications were made within the methodology, leading to limitations of its applicability. The structural components of the building were assumed

to be linear elastic; in reality cracking will occur and non-linear behaviour (a reduction in structural stiffness) can be expected (Giardina et al., 2013; Son, 2015; Son and Cording, 2010). The effect of walls, façades and partitions within the building was also not considered in the analyses of this project. This may have an effect on the bending behaviour of the building, however the standard methodology applied in structural design of framed buildings is to omit the effect of walls and partitions (Mirhabibi and Soroush, 2013).

Chapter 6

Bending Stiffness Estimation of Raft Foundations

6.1 Introduction

This chapter investigates the behaviour of raft foundations numerically and proposes two methods to estimate the approximate foundation bending stiffness. The proposed methods depend on the location of the tunnel with respect to the building. Similar to the investigation of the building superstructure (Chapter 5), a cantilever method is proposed for the case where the tunnel is not located under the building plan area, and a fixed–ended method for the case where the tunnel axis coincides with the building centreline. It is worth noting that the values of foundation bending stiffness estimated in this chapter can be added algebraically with the bending stiffness of the superstructure calculated based on the methods proposed in Chapter 5 in order to obtain the final value of the building bending stiffness.

As presented in Section 2.3.3, differential settlement is not allowed under rigid foundations. It is assumed that the stiffness of the foundation is large enough to allow the foundation to behave as a rigid body and to produce a uniform or linearly varying ground bearing pressure. On the other hand, differential settlements are allowed in flexible foundations, and the created ground bearing pressure is not linear: it is large under columns and relatively small in other areas. It should be mentioned that in both types of foundation (rigid and flexible), the cause of the foundation deformation is the applied building load. In tunnel–building interaction analysis, several researchers (i.e. Franzius et al., 2006; Potts and Addenbrooke, 1997; Selby, 1999) have modelled the building as weightless and used a rough soil–building interface assuming that the deflection of the building occurs due to tunnelling induced ground displacements. This means that the building is attached to the soil and when the tunnel is

constructed, the induced ground movements will be transferred to the building and cause building deflections. It can be said that the behaviour of the building under its weight is disregarded, and the building is forced to follow the deformation of the soil.

As shown in Section 4.7, the recommended minimum elastic modulus of concrete in ACI-Building-Code (2011) is 21.5 GPa. In the case of raft foundations, even relatively thin foundations will be sufficiently rigid to modify ground deformations. Therefore, when ground displacements are created due to the construction of a tunnel, the stiffness and the weight of the existing buildings will be more influential on the building response than the shape of the surface settlement trough. This behaviour mainly relates to the rigidity of the concrete relative to that of the soil. Hence, assuming that the deformations of the building follow the shape of the ground settlement trough may not be realistic. Note that the role of building stiffness in redistributing the building load after the construction of the tunnel is investigated in Chapter 8.

The numerical analyses in this chapter depend on the elastic behaviour of raft foundations under an applied pressure, which approximately represents the building weight, when a new tunnel is constructed. In addition, the foundation and the soil are considered as one global system. Bending stiffness of the global foundation–soil is estimated rather than dealing with the structural part independently from the underlying soil. General assumptions, methodology and the detail of the proposed methods to estimate foundation bending stiffness are presented in the following sections.

6.2 General Assumptions

In this chapter, the soil and the foundation are assumed to be linear elastic. The tunnel is not modelled since the relative change of applied forces and created deformations does not affect the stiffness of the member in the linear-elastic range. Furthermore, ground displacements in the direction of the tunnel are assumed constant; this causes one-directional deformation (perpendicular to the tunnel axis) to the foundation. The deformation of the foundation is assumed to be similar to a beam. This assumption may apply to the deflected part of the foundation but does not represent the undeflected part which is located in the undeformed (unaffected) soil zone (Figure 6.1a, b). In the unaffected soil zone, the actual behaviour of the foundation is not similar to a beam; the interaction between the building weight through columns and the reaction of the underlying soil creates two-directional deformations, similar to plates.

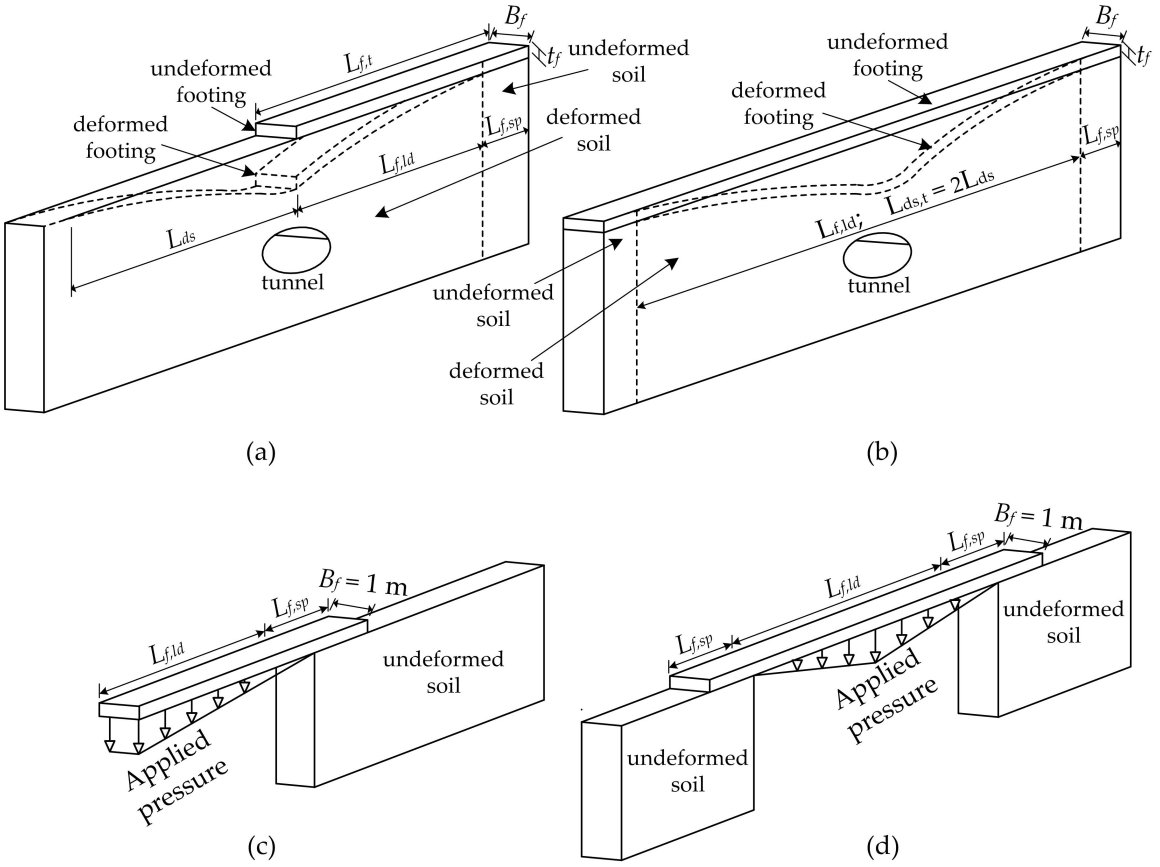

Fig. 6.1 View of tunnel–soil–foundation problem for a foundation with (a) cantilever behaviour, (b) fixed–ended behaviour, (c) numerical model of the cantilever behaviour, and (d) numerical model of the fixed–ended behaviour

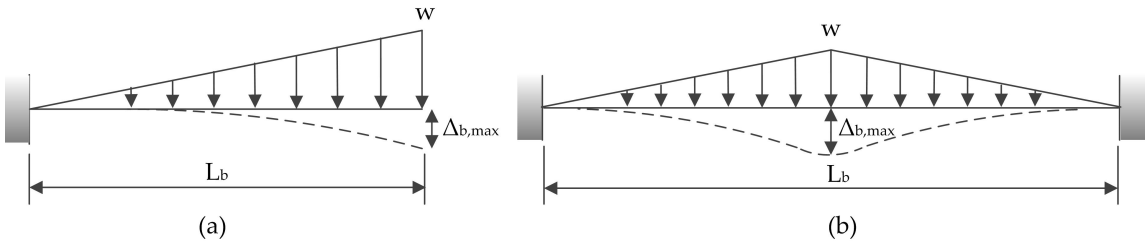

Fig. 6.2 A typical beam subjected to a linear load: (a) cantilever, (b) fixed–ended

When a tunnel is constructed under the foundation edge or outside the foundation plan area, the portion of the foundation located in the deformed soil zone is assumed to deflect similar to a cantilever beam fixed at one end and loaded linearly along its length, as shown in Figure 6.2a. The reason for choosing an analogy with a cantilever beam is that, in the case where the tunnel is not located directly under the foundation, the foundation will deform in a way that the end that located above the tunnel is subjected to a larger deformation compared to the far end. The far end, which is not or less affected by tunnelling, provides a degree of end–fixity to the foundation, resulting in a deformed shape similar to a cantilever beam. Furthermore, the foundation is not likely to include a sagging zone since the rigidity of the foundation is significantly larger than that of the soil and the foundation deflection will not follow the greenfield soil deformation shape. It should be noted that before the construction of the tunnel, settlements caused by the building weight have already occurred, and are not taken into consideration in the numerical analyses of this chapter. When a tunnel is constructed, the soil will move and, in turn, the weight of the building will cause the building to move and remain in contact with the soil. This gives a generally known trend of deformations induced in the foundation which is similar to the deflected shape of the beam shown in Figure 6.2a.

With regard to the case where the tunnel is constructed under the foundation centreline, the foundation in the deformed soil zone is assumed to deflect similar to a fixed–ended beam loaded linearly along its length, as shown in Figure 6.2b. The reason for choosing an analogy with a fixed–ended beam is that, in such cases, the foundation will not undergo a large unsymmetrical rotation (similar to the cantilever case) because of the symmetrical deflection around its centreline. Furthermore, the middle zone of the foundation deflects more than its ends. This deflection shape is similar to that of a beam fixed at its ends and loaded along its length.

Another assumption is that the foundation is sufficiently rigid to distribute the building load linearly over the underlying soil after the tunnel is constructed. It can be said that the

actual rigidity of the foundation is between perfectly rigid and perfectly flexible. It does not behave as a perfectly rigid body (leading to a uniform distribution of the building load), and it also does not completely follow ground displacements (to have the same sagging and hogging zones as the surface settlement trough). A linear distribution of the building weight (as in Figures 6.2a and b) over the deformed soil zone is an approximate representation of the foundation behaviour. Foundation deformations in this chapter are modelled by applying a linearly varying pressure to the foundation in which the maximum pressure is at the tunnel axis and reduces to zero at the beginning of the undeformed soil zone. More detail about the foundation loading is provided in Section 6.3.

6.3 Model Description and Material Properties

In the cantilever approach, the soil model was 60 m long and 25 m deep. The problem was 2D due to having negligible displacements in the direction of the tunnel; therefore, the width was taken as 1 m. The model size was chosen to eliminate boundary effects on the analysis results. The total number of meshing elements ranged from 19,110 to 35,100. The foundation had a thickness of t_f and consisted of two parts: a deformed part (or loaded part) with a length of $L_{f,ld}$ located in the displaced soil zone, L_{ds}, and a supporting part with a length of $L_{f,sp}$ located in the undisplaced soil zone. Figure 6.1a shows the general view of the tunnel–soil–foundation problem for the cantilever approach including various geometric parameters. $L_{f,ld}$ varied from 2.5 m to 22.5 m, $L_{f,sp}$ from 1 m to 20 m, and t_f from 0.3 m to 1 m in the numerical analyses.

In the fixed–ended approach, half of the problem was modelled due to symmetry. The same dimensions as the cantilever approach were used for the symmetric fixed–ended models. Figure 6.1b shows the general view of the tunnel–soil–foundation problem for the fixed–ended approach including various geometric parameters. It is worth noting that the soil–building interface was rough (tied) in all simulations. Furthermore, the elastic modulus of the soil was varied from 10 to 100 MPa and that of the concrete from 20 to 60 GPa.

In the numerical simulations, the tunnel and the zone of the displaced soil were not modelled. Instead, a linear pressure was applied to the deflected part of the foundation ($L_{f,ld}$) to simulate displacements, as shown in Figures 6.1c,d. The removal of the displaced soil was done for two main reasons. First, the created deformation is proportional to the applied load in a linear–elastic medium which means that the magnitude of the force is not important. The linear-elastic behaviour of the soil and the foundation is an assumption of this work. Second, applying a known linear force to the foundation without considering the underlying

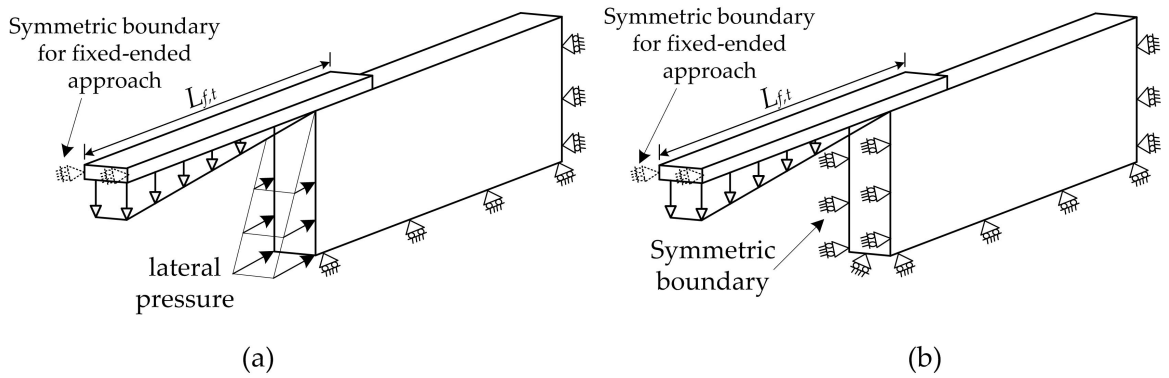

Fig. 6.3 Replacing the removed soil by applying (a) lateral pressure, (b) symmetric boundary

soil allows relating the numerically estimated foundation bending stiffness to the analytically computed stiffness using the equation of beam deflection (Equation 2.3), which is an essential element of this work. It should be noted that the displaced and undisplaced soil zones in Figures 6.1c,d relate to greenfield evaluations.

The part of the removed soil should be replaced by a boundary condition in the numerical model. This boundary should provide a lateral pressure determined according to the coefficient of lateral earth pressure (K_0), as shown in Figure 6.3a. The parameter K_0 is essential to account for horizontal soil stresses, and it also plays an important role in the numerical analyses of tunnelling problems (as stated in Section 3.6.5). However, an accurate estimation of K_0 is difficult practically. An approximate alternative of the lateral pressure is to apply a roller (symmetric) boundary to the model to replace the removed soil, as shown in Figure 6.3b. In some cases of low values of K_0, the application of a symmetric boundary condition leads to an overestimation of the soil stiffness compared to the real soil situation.

To investigate the effect of the symmetric boundary on the foundation bending stiffness compared to the case of applying a lateral pressure, two numerical models were simulated for each case of the cantilever and fixed–ended approaches. The removed soil from the model was represented by a lateral pressure in one model, and by a symmetric boundary in the other. For the lateral pressure boundary, soil weight density was 16 kN/m^3 and $K_0 = 0.5$. The length of the footing in the undeformed soil zone was 20 m. The deformed length of the foundation was varied from 5 m to 20 m in the cantilever approach, and from 10 m to 40 m in the fixed–ended method. The foundation thickness was $t_f = 0.5$ m.

Figure 6.4 presents the ratio of $K_{b,fnd,num}/K_{b,fnd,num,fix}$ (where $K_{b,fnd,num}$ is the numerically estimated bending stiffness of the foundation with the actual (soil) boundary, and $K_{b,fnd,num,fix}$ is the numerical bending stiffness with a fixed boundary; fnd denotes founda-

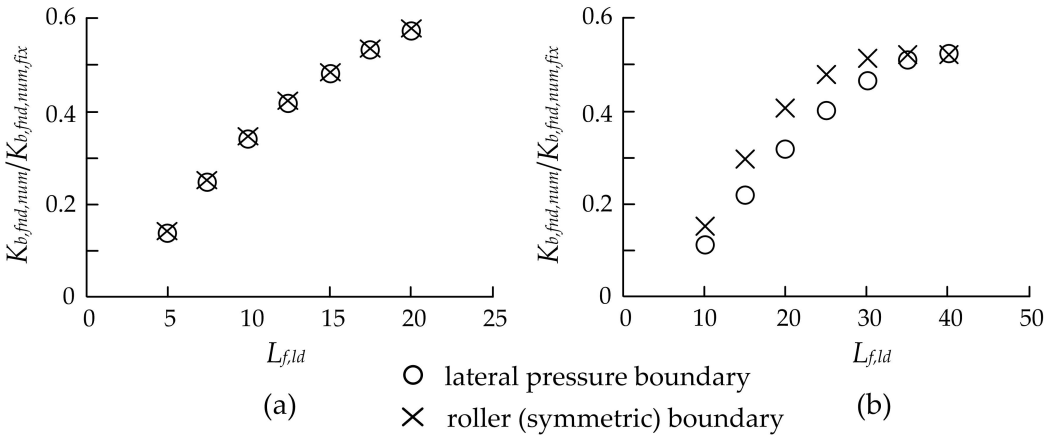

Fig. 6.4 Numerical bending stiffness of a foundation with lateral pressure and roller (symmetric) boundaries for (a) cantilever and (b) fixed–ended approaches

tion). For the mentioned case, Figure 6.4a shows that there is no practical difference between the results of lateral pressure and symmetric boundaries in the cantilever approach. However, an overestimation of the foundation bending stiffness is obtained for the symmetric boundary condition in the fixed–ended approach, as shown in Figure 6.4b.

6.4 Methodology

Equation 2.3 ($K_b = F_K((EI)_b/L_b^3)$, where K_b is the beam bending stiffness, $(EI)_b$ is the flexural rigidity and L_b is the length) is used to compute the analytical bending stiffness of the foundations with fixed supports; $F_K = 60/11$ for the cantilever case (Figure 6.2a), and $F_K = 1920/7$ for the fixed–ended case (Figure 6.2b). Furthermore, the term 'foundation' in this chapter is used for the global foundation consisting of the footing member and the underlying soil. When 'footing member' is used, it refers to the individual reinforced concrete part of the foundation without considering the boundary condition (i.e. the soil). The actual boundary of the foundations is soil (as shown in Figure 6.1), whereas Equation 2.3 considers a fixed boundary for beams (as in Figures 6.2a,b). This fixed boundary should be modified to represent the actual soil that works as a support for the footing. Sections 6.5 and 6.6 investigate the modification of the fixed boundary of Equation 2.3 to the actual boundary of the foundation for both cantilever and fixed–ended cases, respectively, and relate it to the elastic properties of the soil and the concrete and to the geometry of the footing member.

The investigation of the boundary condition for each approach (cantilever and fixed–ended) comprises three sections. The first section studies the effect of the elastic modulus

of the soil and concrete; the second section deals with the effect of the loaded part of the foundation on the global foundation bending stiffness; the third section investigates the influence of the supporting part. A method is proposed for each case to approximate the bending stiffness of the raft foundation. It should be noted that the realistic boundary condition of the foundation is related to the bending stiffness of the foundation with a fixed boundary condition (i.e. the foundation boundary condition = $K_{b,fnd,an,fix}/K_{b,fnd,num}$ where $K_{b,fnd,an,fix}$ is the analytical bending stiffness calculated using Equation 2.3). Note the subscripts *cant* and $fend$ are added to the notations of the following sections to represent *cantilever* and *fixed–ended*, respectively (e.g. $K_{b,fnd,cant,an,fix}$ for the cantilever case and $K_{b,fnd,fend,an,fix}$ for the fixed–ended case).

6.5 Cantilever Approach

This section deals with the cantilever case shown in Figure 6.1a.

6.5.1 Effect of soil and concrete elastic modulus on foundation boundary

Soil and concrete elastic moduli have significant effects on the behaviour of the foundation. The soil underlying the footing acts as a support to the foundation. Numerical results shown in Figure 6.5a illustrate that as the soil elastic modulus in the undeformed zone increases, the numerical bending stiffness of the foundation approaches the analytical stiffness (an increase of foundation stiffness). In other words, as the undeformed soil elastic modulus increases, the boundary condition of the foundation approaches the fixed condition.

As explained in Section 2.2.3, the deflection of a member and the rotation allowed by the boundary condition are the main influential parameters affecting its bending stiffness. The stiff soil leads to the reduction of the foundation rotation.

Similar to the soil part, the concrete elastic modulus also plays an important role in determining the behaviour of the foundation, but in an opposite way to the soil. Figure 6.5b shows that the increase of E_c results in a decrease in the bending stiffness of the foundation and increases the difference between the analytical and numerical bending stiffness. This is because the increase of E_c increases the bending stiffness of the footing member (local stiffness of the concrete part). Because of this, the local deflection of the footing member decreases, and most of the effect of the applied pressure to the foundation is transferred to

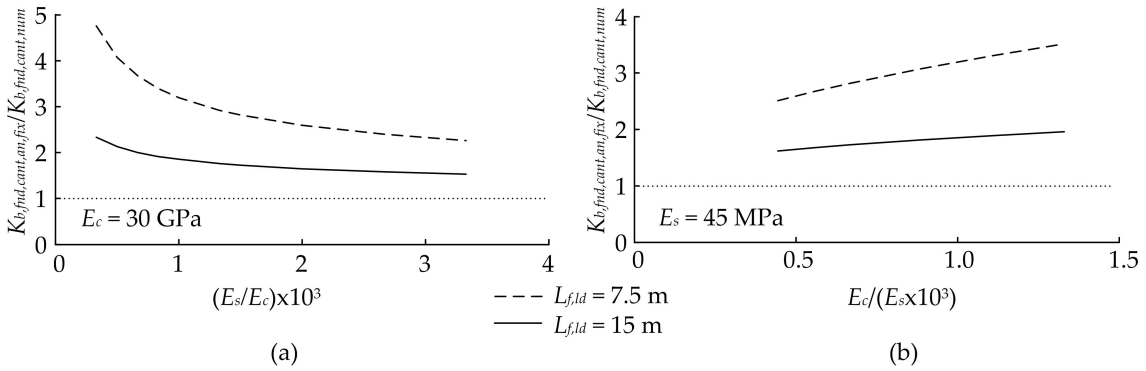

Fig. 6.5 Effect of (a) soil and (b) concrete elastic modulus on the foundation boundary condition ($K_{b,fnd,cant,an,fix}/K_{b,fnd,cant,num}$) for $t_f = 0.5$ m and $L_{f,sp} = 15$ m

the foundation boundary, which causes a rotation and reduces the global foundation bending stiffness.

In light of what was presented in this section, it should be noted that several researchers (Franzius et al., 2006; Miliziano et al., 2002; Potts and Addenbrooke, 1997) reported that the decrease of soil stiffness or the increase of building–soil relative stiffness led to the reduction of building deformations. The results obtained here are in agreement with the results obtained by these researchers, but there is a terminological difference between them. Most soil–structure interaction research has considered the soil and the building individually, and disregarded some influential parameters affecting the bending stiffness of a member. If only the footing member is considered, the increase of concrete elastic modulus will increase the local rigidity of the member to resist deflections, but this will cause a large rotation, which will in turn reduce the global bending stiffness. In a case where the boundary of a member is perfectly fixed, Equation 2.3 indicates that the increase of material elastic modulus will increase the member's bending stiffness, but this is not the case for a foundation resting on soil. Note that the comparison of the foundation bending stiffness is between the numerical simulation and its corresponding analytical case. In other words, the focus is on the difference between the numerical and the corresponding analytical bending stiffness for the same foundation material and geometrical properties.

6.5.2 Effect of $L_{f,ld}$ on foundation boundary

Equation 2.3 shows that the bending stiffness of the foundation is a function of $L^3_{f,ld}$. Apart from this, $L_{f,ld}$ also has an essential effect on the behaviour of the foundation boundary. It plays an important role on how much deformation effect is transferred to the boundary. For

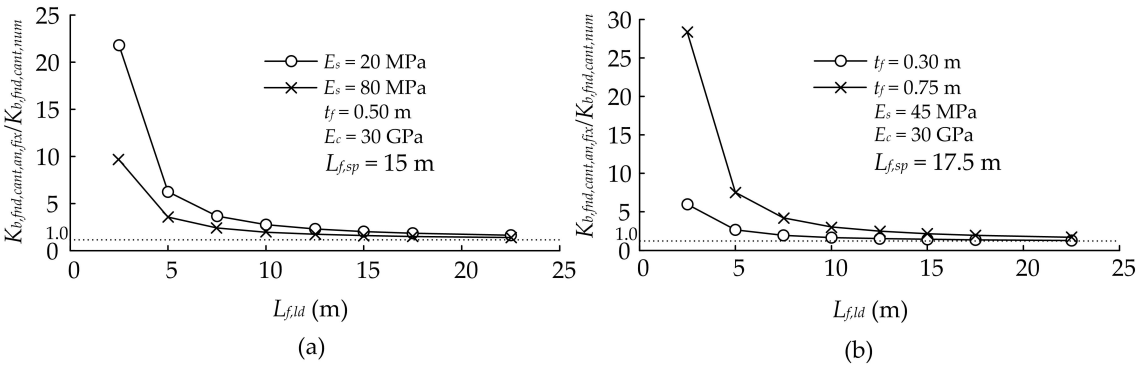

Fig. 6.6 Effect of $L_{f,ld}$ on the foundation boundary condition for different values of (a) soil elastic modulus and (b) foundation thickness

the footing member, the bending stiffness decreases as $L_{f,ld}$ increases, while the fixity of the boundary condition increases as the length decreases. This is because footing members with small lengths are very stiff and transfer most of the deformation effects to the boundary which in turn leads to a large boundary rotation. It should be mentioned that in the numerical models created to investigate $L_{f,ld}$, the supporting part ($L_{f,sp}$) was given a large length to ensure that it did not have any effect on the stiffness results (the effect of $L_{f,sp}$ is considered in the next section).

Figure 6.6a shows that there is a significant difference between the analytical and the numerical bending stiffness of the foundation for small lengths of $L_{f,ld}$. As $L_{f,ld}$ increases, the difference between the analytical and numerical foundation bending stiffness decreases. This is because as $L_{f,ld}$ increases, a smaller effect of the deformation is transferred to the foundation boundary, and less rotation occurs. It is also indicated in Figure 6.6a that the reduction of the foundation bending stiffness with $L_{f,ld}$ is higher in the case of $E_s = 20$ MPa compared to the case of $E_s = 80$ MPa. This is because the ratio of concrete to soil elastic modulus is higher, or in other words, the stiffness of the footing member is high relative to the stiffness of its support (soil).

Figure 6.6b shows the effect of $L_{f,ld}$ on the foundation boundary for two cases of t_f. In general, an increase of foundation thickness leads to an increased difference between the analytical and numerical bending stiffness of the foundation. Furthermore, the difference in the case of the larger t_f is more significant. The reason for this is that the increase of thickness increases the moment of inertia of the footing cross section, which in turn increases the stiffness of the footing member and causes a larger rotation at the foundation support (boundary).

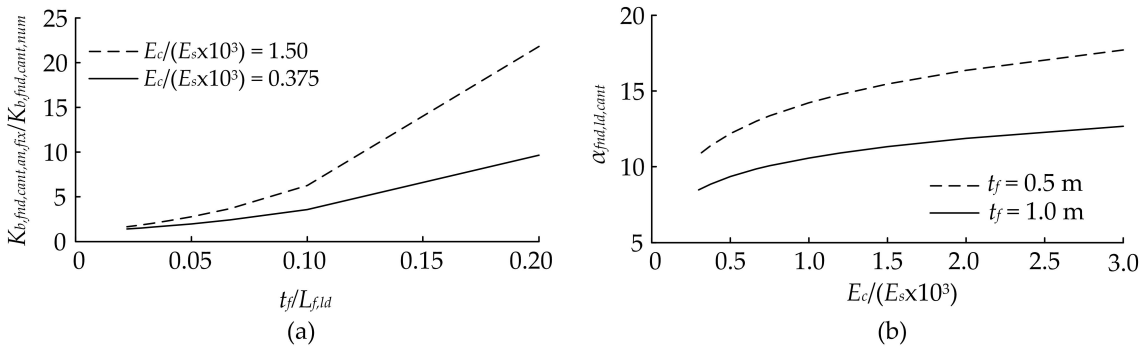

Fig. 6.7 (a) Effect of $t_f/L_{f,ld}$ on the foundation boundary for $t_f = 0.5$ m, (b) relationship between $\alpha_{fnd,ld,cant}$ and $E_c/(E_s \times 10^3)$

Figure 6.6b also illustrates that $L_{f,ld}$ and t_f have opposite effects on the foundation bending stiffness. This can give a parameter, $t_f/L_{f,ld}$, to quantify the effect of $L_{f,ld}$ on the boundary of the foundation. Figure 6.7a shows how the ratio $K_{b,fnd,cant,an,fix}/K_{b,fnd,cant,num}$ is influenced by $t_f/L_{f,ld}$.

A coefficient, $C_{bc,fnd,ld,cant}$, is introduced to be equivalent to $K_{b,fnd,cant,an,fix}/K_{b,fnd,cant,num}$ to approximately determine the boundary condition of the foundation based on the effect of the loaded part of the footing. Based on the numerical results, $C_{bc,fnd,ld,cant}$ can be fitted to the numerical data using Equation 6.1.

$$C_{bc,fnd,ld,cant} = \exp\left(\alpha_{fnd,ld,cant} \times \frac{t_f}{L_{f,ld}}\right) \geq 1.0 \tag{6.1}$$

where $\alpha_{fnd,ld,cant}$ is a parameter required to calculate $C_{bc,fnd,ld,cant}$. Data points of $\alpha_{fnd,ld,cant}$ achieved from the curve fitting of the numerical results to Equation 6.1 showed that there was a relation between $\alpha_{fnd,ld,cant}$ and $E_c/(E_s \times 10^3)$, as displayed in Figure 6.7b. Based on the numerical results, Equation 6.2 can be used to fit the data of $\alpha_{fnd,ld,cant}$.

$$\alpha_{fnd,ld,cant} = 5 \times \left(\frac{t_f + 10}{t_f}\right)^{0.4} \times \left(\frac{E_c}{E_s \times 10^3}\right)^{0.2} \tag{6.2}$$

Figure 6.8a shows a comparison between values of $\alpha_{fnd,ld,cant}$ computed using Equation 6.2 and those obtained from curve fitting of the numerical results. Furthermore, a comparison of the numerical values of $C_{bc,fnd,ld,cant}$ and computed values using Equation 6.1 is presented in Figure 6.8b. The figures show a good prediction of coefficients $\alpha_{fnd,ld,cant}$ and $C_{bc,fnd,ld,cant}$ using Equations 6.2 and 6.1, respectively.

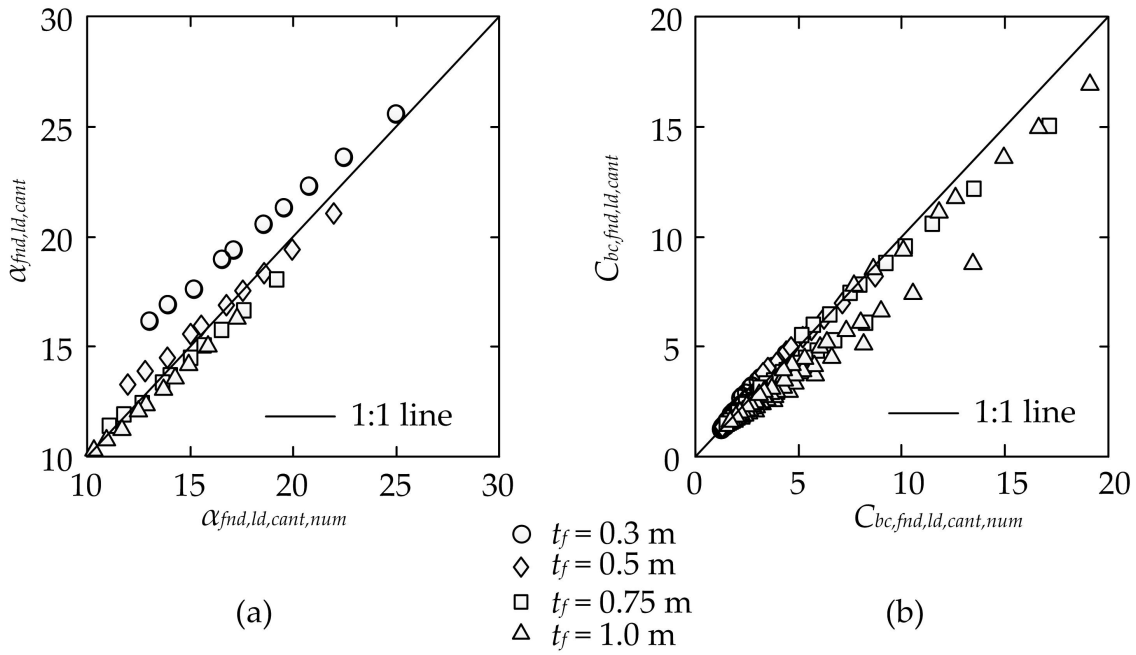

Fig. 6.8 Comparison between the numerical and calculated values of (a) $\alpha_{fnd,ld,cant}$ (Equation 6.2) and (b) $C_{bc,fnd,ld,cant}$ (Equation 6.1)

6.5.3 Effect of $L_{f,sp}$ on foundation boundary

$L_{f,sp}$ is part of the boundary in the foundation system and plays an important role in the determination of the foundation end fixity. This part provides resistance against foundation rotation, and its increase leads to the increase of the foundation bending stiffness. Figure 6.9a shows the variation of the ratio $K_{b,fnd,cant,an,fix}/K_{b,fnd,cant,num}$ with $L_{f,sp}$. It is displayed that small values of $L_{f,sp}$ result in significant differences between the analytical and numerical bending stiffness. An increase in $L_{f,sp}$ leads to an increase in the foundation bending stiffness up to a specific length. After that, the ratio $K_{b,fnd,cant,an,fix}/K_{b,fnd,cant,num}$ becomes constant. This specific length can be defined as the maximum length of $L_{f,sp}$ that has influence on the foundation bending stiffness, and denoted by $L_{f,sp,cant,max}$. Figure 6.9b demonstrates how t_f influences the relation between $L_{f,sp}$ and $K_{b,fnd,cant,an,fix}/K_{b,fnd,cant,num}$. It also indicates that the effect of $L_{f,sp}$ on $K_{b,fnd,cant,an,fix}/K_{b,fnd,cant,num}$ becomes negligible after a specific length ($L_{f,sp,cant,max}$).

The values of $K_{b,fnd,cant,an,fix}/K_{b,fnd,cant,num}$ in Figure 6.9 contain the effect of both: the deformed ($C_{bc,fnd,ld,cant}$) and undeformed foundation parts. If the effect of $C_{bc,fnd,ld,cant}$ is removed from $K_{b,fnd,cant,an,fix}/K_{b,fnd,cant,num}$ (by dividing $K_{b,fnd,cant,an,fix}/K_{b,fnd,cant,num}$ by $C_{bc,fnd,ld,cant}$), the remaining portion will be due to the effect of the supporting part. Fig-

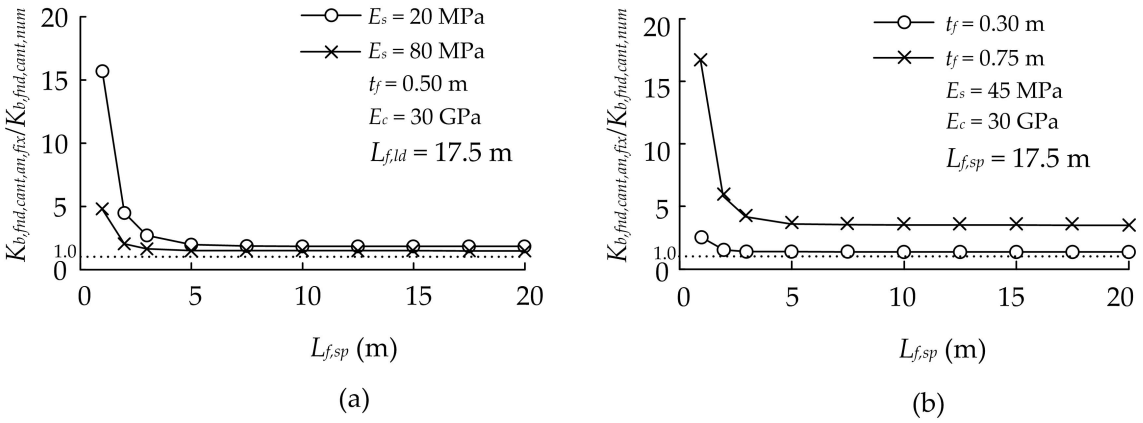

Fig. 6.9 Effect of $L_{f,sp}$ on the boundary condition for (a) variable E_s, and (b) variable t_f

ure 6.10a shows the values of $K_{b,fnd,cant,an,fix}/K_{b,fnd,cant,num}$, $C_{bc,fnd,ld,cant}$ calculated using Equation 6.1, and $C_{bc,fnd,sp,cant,num}$ obtained from taking away the effect of $C_{bc,fnd,ld,cant}$ from $K_{b,fnd,cant,an,fix}/K_{b,fnd,cant,num}$. The figure illustrates that the effect of the foundation supporting part on bending stiffness should be taken into consideration for the length $L_{f,sp,cant,max}$.

Figure 6.10b shows that numerical values of $L_{f,sp,cant,max}$ are considerably affected by the foundation thickness. It is worth noting that in addition to the foundation thickness, the ratio of $E_c/(E_s \times 10^3)$ and the length $L_{f,ld}$ are also influential parameters affecting $L_{f,sp,cant,max}$. The length $L_{f,sp,cant,max}$ decreases with the increase of $L_{f,ld}$ or the decrease of $E_c/(E_s \times 10^3)$. Equation 6.3 is introduced to estimate an appropriate value of $L_{f,sp,cant,max}$ based on t_f. This equation gives the upper bound values of $L_{f,sp,cant,max}$. The values of $L_{f,sp,cant,max}$ calculated using Equation 6.3 are also plotted on Figure 6.10b.

$$L_{f,sp,cant,max} = 13.5t_f \tag{6.3}$$

The ratio of $L_{f,sp,cant,max}/L_{f,sp}$ can be used as a parameter to quantify the effect of $L_{f,sp}$ on the foundation boundary condition. Figure 6.10c demonstrates that the ratio $L_{f,sp,cant,max}/L_{f,sp}$ has an exponential relationship with $K_{b,fnd,cant,an,fix}/K_{b,fnd,cant,num}$. A parameter, $C_{bc,fnd,sp,cant}$ is introduced to approximately determine the boundary condition of the foundation based on the effect of the supporting part of the footing. $C_{bc,fnd,sp,cant}$ was fitted to the numerical data using Equation 6.5. It should be noted that the fitting of $C_{bc,fnd,sp,cant}$ was done after the removal of the effect of $C_{bc,fnd,ld,cant}$ (Equation 6.1) from $K_{b,fnd,cant,an,fix}/K_{b,fnd,cant,num}$.

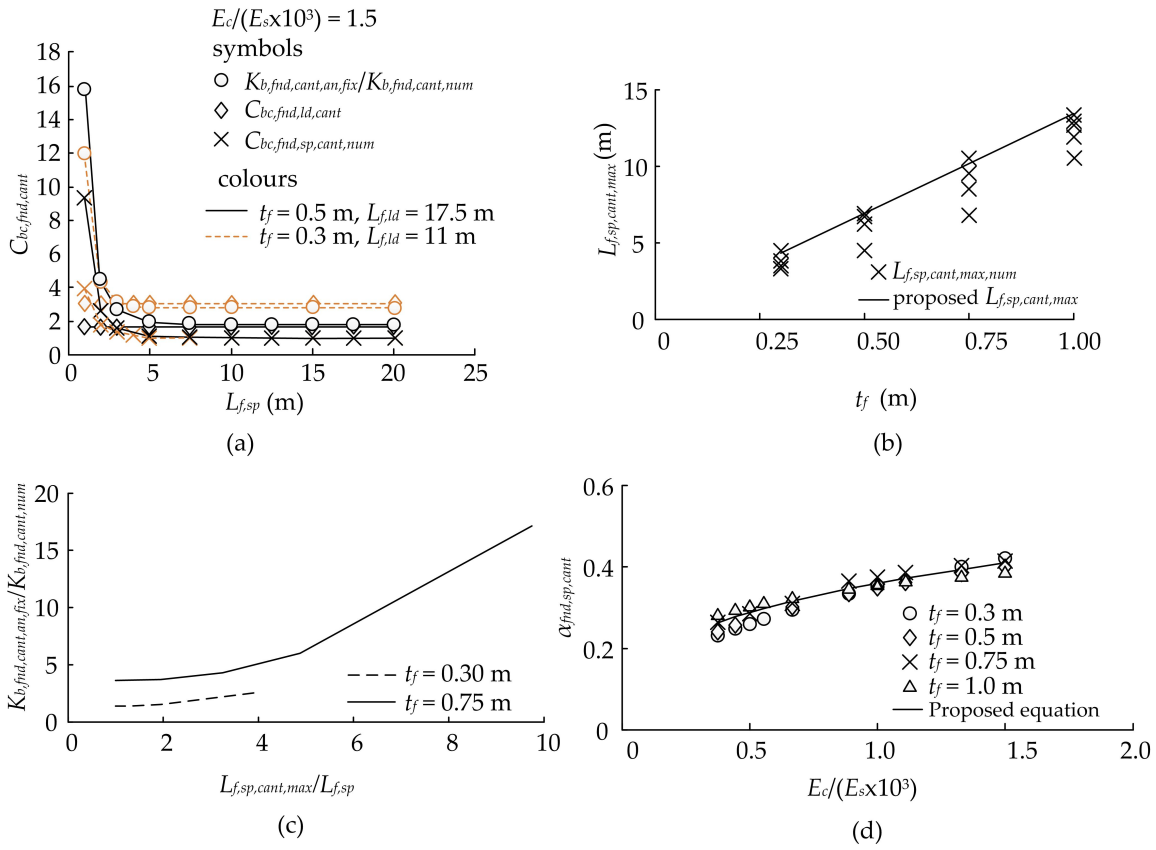

Fig. 6.10 (a) Weight of the coefficient $C_{bc,fnd,ld,cant}$ in $K_{b,fnd,cant,an,fix}/K_{b,fnd,cant,num}$, (b) numerical values of $L_{f,sp,cant,max}$ and the fitted values (Equation 6.3), (c) effect of $L_{f,sp,cant,max}/L_{f,sp}$ on the foundation boundary condition, (d) effect of $E_c/(E_s \times 10^3)$ on $\alpha_{fnd,sp,cant}$

$$C_{bc,fnd,sp,cant} = 0.8 \times \exp\left(\alpha_{fnd,sp,cant} \times \frac{L_{f,sp,cant,max}}{L_{f,sp}}\right) \geq 1.0 \tag{6.4}$$

Equation 6.4 is applicable for values of $L_{f,sp} \leq L_{f,sp,cant,max}$. For cases where $L_{f,sp} > L_{f,sp,cant,max}$, the value of $C_{bc,fnd,sp,cant} = 1.0$. Furthermore, it was noted that values of $L_{f,sp}$ smaller than $0.15L_{f,sp,cant,max}$ caused a dramatic rotation to the foundation, especially for thick foundations (i.e. $t_f \geq$0.5 m). For this reason, it is recommended to neglect values of bending stiffness for foundations with a supporting length of $L_{f,sp} < 0.15L_{f,sp,cant,max}$. Therefore, the length effect of the foundation supporting part is considered for values of $L_{f,sp}$ lying between $0.15L_{f,sp,cant,max}$ and $L_{f,sp,cant,max}$ ($0.15L_{f,sp,cant,max} \leq L_{f,sp} \leq L_{f,sp,cant,max}$).

Figure 6.10d shows the effect of $E_c/(E_s \times 10^3)$ on $\alpha_{fnd,sp,cant}$ for different values of t_f. It is demonstrated that there is a general increase of $\alpha_{fnd,sp,cant}$ with the increase of $E_c/(E_s \times 10^3)$, and can be expressed by Equation 6.5.

$$\alpha_{f,sp,cant} = 0.36 \times \left(\frac{E_c}{E_s \times 10^3}\right)^{0.32} \tag{6.5}$$

A final coefficient for estimating the boundary condition of the foundation can now be introduced by multiplying $C_{bc,fnd,ld,cant}$ by $C_{bc,fnd,sp,cant}$:

$$C_{bc,fnd,cant} = C_{bc,fnd,ld,cant} \times C_{bc,fnd,sp,cant} \geq 1.0 \tag{6.6}$$

To summarise, the analytically computed bending stiffness of the foundation using Equation 2.3 is divided by coefficient $C_{bc,fnd,cant}$ to obtain an equivalent stiffness value of the numerical results ($K_{b,fnd,cant,eq}$):

$$K_{b,fnd,cant,eq} = \frac{K_{b,fnd,an,fix}}{C_{bc,fnd,cant}} \tag{6.7}$$

Figure 6.11 presents a comparison of $K_{b,fnd,cant,num}$ with the equivalent numerical values of bending stiffness ($K_{b,fnd,cant,eq}$) for over 600 cases with variable parameters of $L_{f,ld}$, $L_{f,sp}$, t_f, E_c and E_s. The figure shows that the proposed method predicts the foundation bending stiffness to a good extent.

6.5.4 Verification example

To make a simple verification of the proposed method, numerical models were simulated to test the parameters that have an effect on the estimation of the foundation boundary condition. It is worth noting that the considered numerical models used to verify the proposed method

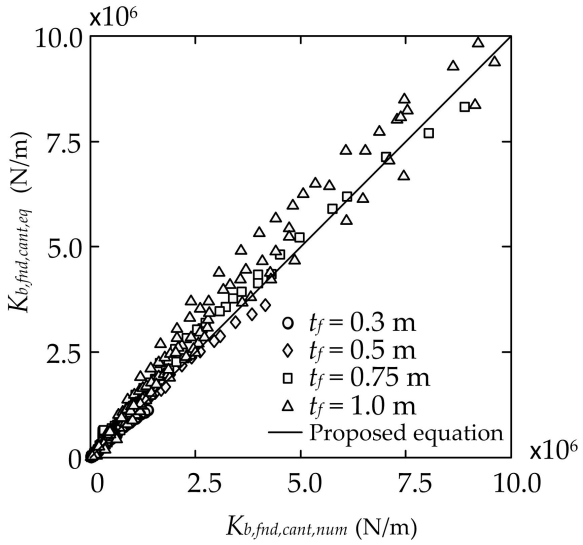

Fig. 6.11 Comparison between $K_{b,fnd,cant,eq}$ and $K_{b,fnd,cant,num}$

were not included in the development of the method. However, the considered dimensions and material properties were within the range of values used for the method development. The tested parameters in this example were: E_c/E_s, $L_{f,ld}$, $L_{f,sp}$ and t_f.

Figure 6.12a presents the results of the numerical and proposed values of $C_{bc,fnd,cant}$ for different values of $E_c/(E_s \times 10^3)$, and two values of t_f: 0.4 m and 1.0 m. For $t_f = 0.4$ m, $L_{f,sp} = 5$ m which is close to $L_{f,sp,cant,max} = 5.4$ m, while for $t_f = 1.0$ m, $L_{f,sp} = 5$ m is smaller than $L_{f,sp,cant,max} = 13.5$ m. In both cases, there is a good agreement between the numerical and proposed results.

The effect of changing $L_{f,ld}$ on $C_{bc,fnd,cant}$ is shown in Figure 6.12b for two values of t_f: 0.4 m and 0.75 m, with values of $L_{f,sp} = 5$ m and 15 m, respectively. A good agreement between the numerical and the proposed values of $C_{bc,fnd,cant}$ is observed. The effect of $L_{f,sp}$ on $C_{bc,fnd,cant}$ is presented in Figure 6.12c. An excellent agreement between the numerical and proposed values is obtained.

Figure 6.12d exhibits the effect of foundation thickness on $C_{bc,fnd,cant}$. Generally, the results are in reasonably good agreement. There is a notable difference between the numerical and the proposed results for t_f values greater than about 0.6 m. This difference is larger in the case of $L_{f,sp} = 5$ m. This indicates that for high values of t_f, a large rotation of the foundation occurred which was not well-captured by coefficient $C_{bc,fnd,cant}$.

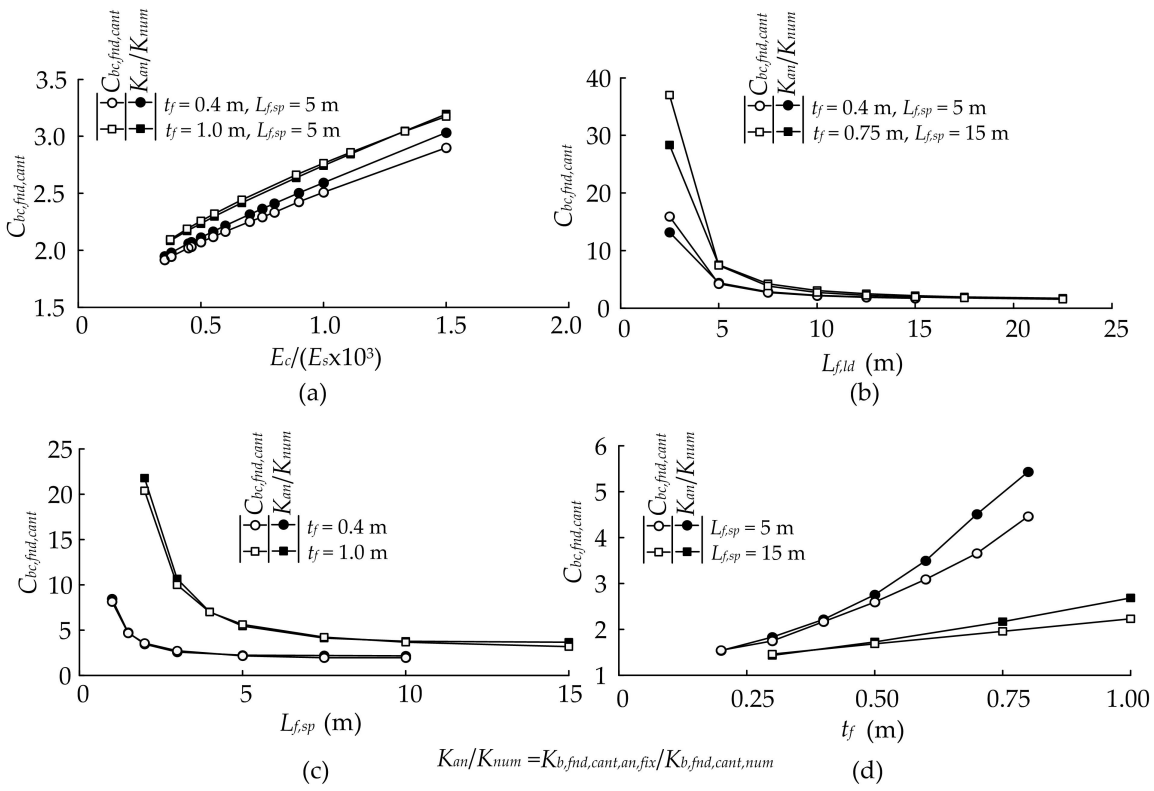

Fig. 6.12 Verification of the effect of (a) $E_c/(E_s \times 10^3)$ for $L_{f,ld} = 10$ m, (b) $L_{f,ld}$ for $E_c/(E_s \times 10^3) = 0.667$, (c) $L_{f,sp}$ for $L_{f,ld} = 10$ m and $E_c/(E_s \times 10^3) = 0.667$, (d) t_f for $L_{f,ld} = 10$ m and $E_c/(E_s \times 10^3) = 0.667$ on the estimation of $C_{bc,fnd,cant}$

6.6 Fixed-Ended Approach

This section deals with the fixed–ended case shown in Figure 6.1b.

6.6.1 Effect of soil and concrete elastic moduli on foundation boundary

As explained in the cantilever approach, the concrete and soil elastic moduli have opposing effects on the foundation bending stiffness. The increase of the soil elastic modulus leads to increasing the fixity of the foundation support (boundary), while a high value of concrete elastic modulus results in the settlement of the foundation and reduces the global foundation bending stiffness.

Numerical results shown in Figure 6.13a illustrate that the difference between the analytical ($K_{b,fnd,fend,an,fix}$) and numerical ($K_{b,fnd,fend,num}$) bending stiffness of the foundation reduces with the increase of the soil elastic modulus. Similar to the cantilever approach, this indicates that the foundation bending stiffness increases and the boundary condition of the foundation approaches the fixed condition.

The reason for the increase of the foundation bending stiffness due to a high soil elastic modulus in a fixed–ended situation is that a stiff soil reduces the deflection of the foundation and the embedding of the foundation ends into the underlying soil. Dissimilar to the cantilever approach, rotation of the foundation in a fixed–ended case is not significant because of symmetry.

Figure 6.13b demonstrates the effect of the concrete elastic modulus on the bending stiffness of the foundation. It is indicated that the difference between the analytical and numerical bending stiffness of the foundation increases with the increase of E_c. The reason for this is the same as that presented in the cantilever approach; when the footing member becomes stiff due to a high value of E_c, most of the effects of the applied pressure to the foundation will transfer to the boundary which will cause a significant deformation to the supporting soil.

6.6.2 Effect of $L_{f,ld}$ on foundation boundary

$L_{f,ld}$ plays an important role on how much deformation effect is transferred to the boundary. Considering only the footing member, the increase of $L_{f,ld}$ results in a cubic decrease of the foundation bending stiffness, while considering the global foundation, it leads to a significant reduction of the difference between the analytical and the numerical bending stiffness of the foundation. This is because footing members with small lengths are very stiff and transfer

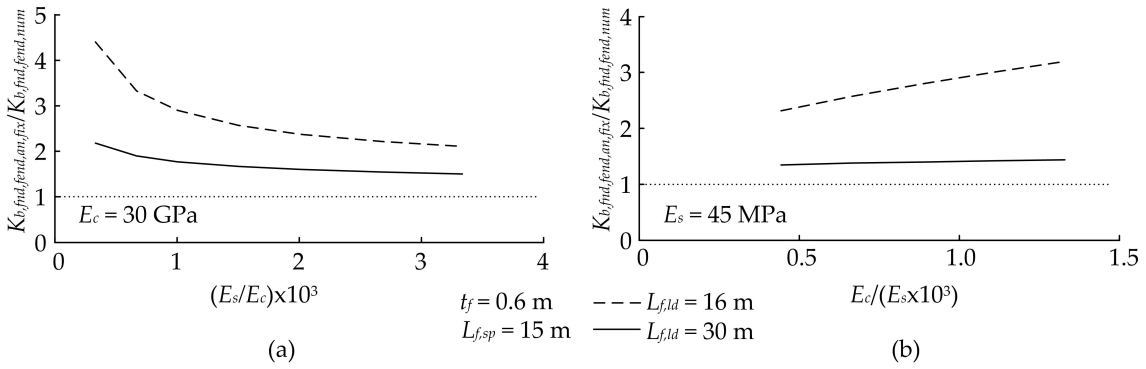

Fig. 6.13 Effect of (a) soil and (b) concrete elastic modulus on the foundation boundary condition ($K_{b,fnd,fend,an,fix}/K_{b,fnd,fend,num}$)

most of the deformation effects to the boundary. This in turn leads to a large boundary deformation. It should be mentioned that in the numerical models created to investigate $L_{f,ld}$, the supporting part ($L_{f,sp}$) was given a large value to ensure that it did not have any effect on the stiffness results.

Figure 6.14a presents the influence of $L_{f,ld}$ on the bending stiffness of the foundation for two different values of E_s, and Figure 6.14b demonstrates the effect for two different values of t_f. The data indicate that there is a significant difference between the analytical and the numerical bending stiffness of the foundation for small lengths of $L_{f,ld}$. Furthermore, Figure 6.14a shows that the reduction of the foundation bending stiffness is higher in the case of $E_s = 20$ MPa due to having a low stiffness support. On the other hand, Figure 6.14b demonstrates that there is a general trend that the increase of foundation thickness leads to increasing the difference between the analytical and numerical bending stiffness of the foundation, and the difference in the case of the larger t_f is more significant. In all these cases, when the stiffness of the footing member increases, the foundation boundary is subjected to greater deformation leading to a reduction in the bending stiffness.

The actions of $L_{f,ld}$ and t_f can give a parameter, $t_f/L_{f,ld}$, to quantify the effect of $L_{f,ld}$ on the boundary of the foundation. Figure 6.15a shows how the ratio $K_{b,fnd,fend,an,fix}/K_{b,fnd,fend,num}$ is influenced by $t_f/L_{f,ld}$. A coefficient, $C_{bc,fnd,ld,fend}$, is introduced to be an equivalent to $K_{b,fnd,fend,an,fix}/K_{b,fnd,fend,num}$ to approximately determine the boundary condition of the foundation in a fixed–ended approach based on the effect of the foundation loaded part. $C_{bc,fnd,ld,fend}$ was fitted to the numerical data using Equation 6.8.

$$C_{bc,fnd,ld,fend} = \alpha_{fnd,ld,fend} \times \exp\left(25 \times \frac{t_f}{L_{f,ld}}\right) \geq 1.0 \tag{6.8}$$

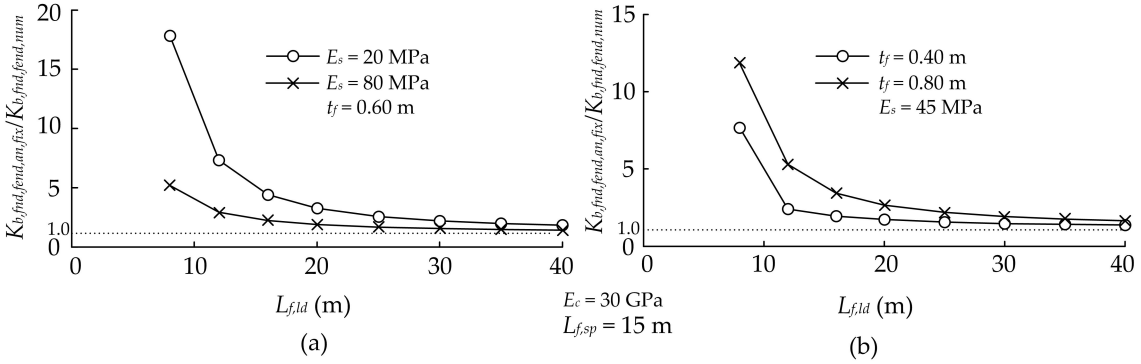

Fig. 6.14 The effect of $L_{f,ld}$ on the foundation boundary condition in the fixed–ended approach for different values of (a) soil elastic modulus and (b) foundation thickness

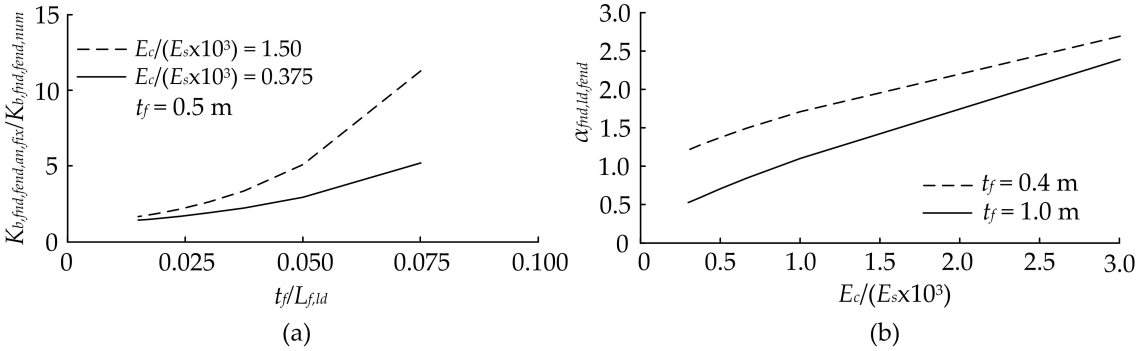

Fig. 6.15 (a) Effect of $t_f/L_{f,ld}$ on the foundation boundary, (b) relationship between $\alpha_{fnd,ld,fend}$ and E_c/E_s

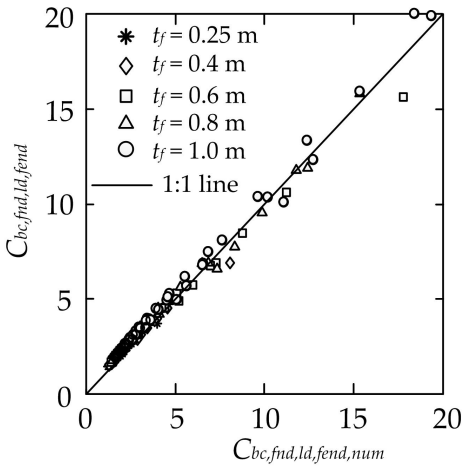

Fig. 6.16 Comparison between numerical and computed values of $C_{bc,fnd,ld,fend}$ (Equation 6.8)

where $\alpha_{fnd,ld,fend}$ is a parameter required to estimate $C_{bc,fnd,ld,fend}$. Data points of $\alpha_{fnd,ld,fend}$ achieved from the curve fitting of numerical results to Equation 6.8 showed that there was a relation between $\alpha_{fnd,ld,fend}$ and $E_c/(E_s \times 10^3)$, as displayed in Figure 6.15b. Based on the numerical results, a relation based on only $E_c/(E_s \times 10^3)$ does not fit the data well; an additional term, $8t_f/(t_f + L_{f,ld})$ should also be considered. Equation 6.9 can be used to fit the numerical data of $\alpha_{fnd,ld,fend}$ to a good extent. Figure 6.16 presents a good prediction of coefficient $C_{bc,fnd,ld,fend}$ using Equation 6.8.

$$\alpha_{fnd,ld,fend} = 1.3 \times \left(\frac{E_c}{E_s \times 10^3}\right)^{\left(\frac{8t_f}{t_f + L_{f,ld}}\right)} \tag{6.9}$$

6.6.3 Effect of $L_{f,sp}$ on foundation boundary

In the fixed–ended approach, $L_{f,sp}$ provides resistance against deformation of the foundation boundary. Figure 6.17a shows the variation of the ratio $K_{b,fnd,fend,an,fix}/K_{b,fnd,fend,num}$ with $L_{f,sp}$. It is shown that an increase in $L_{f,sp}$ leads to an increase in the foundation bending stiffness up to a specific length. After that, the ratio $K_{b,fnd,fend,an,fix}/K_{b,fnd,fend,num}$ becomes constant. Similar to the cantilever approach, this specific length can be defined as the maximum length of $L_{f,sp}$ that has influence on the foundation bending stiffness, and is denoted by $L_{f,sp,fend,max}$. Figure 6.17b demonstrates how t_f influences the relation between $L_{f,sp}$ and $K_{b,fnd,fend,an,fix}/K_{b,fnd,fend,num}$. It is also indicated that the effect of $L_{f,sp}$ on $K_{b,fnd,fend,an,fix}/K_{b,fnd,fend,num}$ becomes negligible after a specific length.

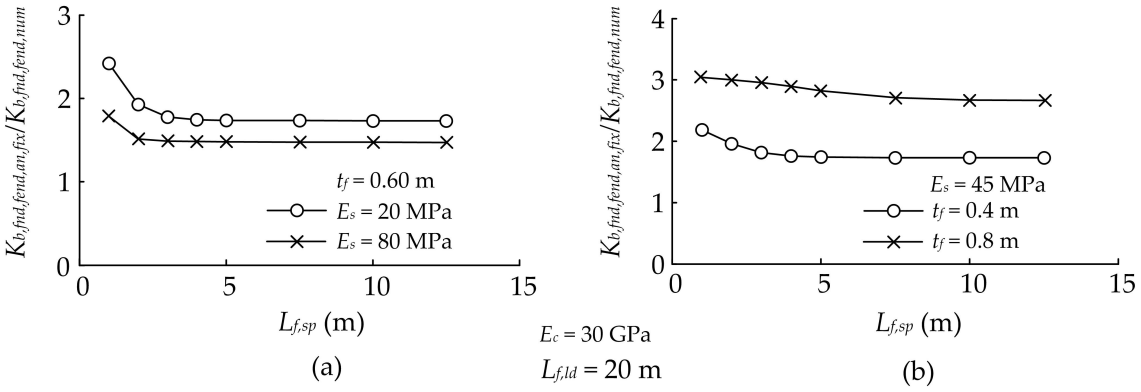

Fig. 6.17 Effect of $L_{f,sp}$ on $K_{b,fnd,fend,an,fix}/K_{b,fnd,fend,num}$ for different values of (a) $E_c/(E_s \times 10^3)$, and (b) t_f

It should be mentioned that the major effect of the footing member on the boundary condition was considered in $C_{bc,fnd,ld,fend}$. Figure 6.18a shows the values of $K_{b,fnd,fend,an,fix}/K_{b,fnd,fend,num}$, $C_{bc,fnd,ld,fend}$ calculated using Equation 6.8, and $C_{bc,fnd,sp,fend,num}$ obtained from taking away the effect of $C_{bc,fnd,ld,fend}$ from $K_{b,fnd,fend,an,fix}/K_{b,fnd,fend,num}$ (by dividing the value of $K_{b,fnd,fend,an,fix}/K_{b,fnd,fend,num}$ by $C_{bc,fnd,ld,fend}$). The data show that the coefficient $C_{bc,fnd,ld,fend}$ (calculated from Equation 6.8) estimates the major portion of $K_{b,fnd,fend,an,fix}/K_{b,fnd,fend,num}$, and leaves only a secondary role to the effect of the supporting length on the boundary condition. The reason for the secondary role of the supporting length is that the foundation does not experience rotation due to symmetry.

Figure 6.18b shows that numerical values of $L_{f,sp,fend,max}$ are affected by the foundation thickness. Similar to the cantilever approach, the thickness of the foundation is not the only influential parameter affecting $L_{f,sp,fend,max}$; $E_c/(E_s \times 10^3)$ and $L_{f,ld}$ also play an important role. The upper bound of the numerical data points plotted in relation to t_f was used to obtain the approximate value of $L_{f,sp,fend,max}$. This was done to eliminate the complexity of the problem since the effect of the supporting part has a secondary contribution to $K_{b,fnd,fend,an,fix}/K_{b,fnd,fend,num}$ compared to the contribution of $C_{bc,fnd,ld,fend}$. Equation 6.10 can be used to approximate $L_{f,sp,fend,max}$. The calculated values of $L_{f,sp,fend,max}$ using Equation 6.10 are also plotted on Figure 6.18b.

$$L_{f,sp,fend,max} = 2.25 \times \exp\left(1.25 \times t_f\right) \tag{6.10}$$

Numerical results shown in Figure 6.18c show that the estimation of the foundation boundary condition can be related to a parameter, $t_f^2/(L_{f,sp}L_{f,ld})$, based on an exponential

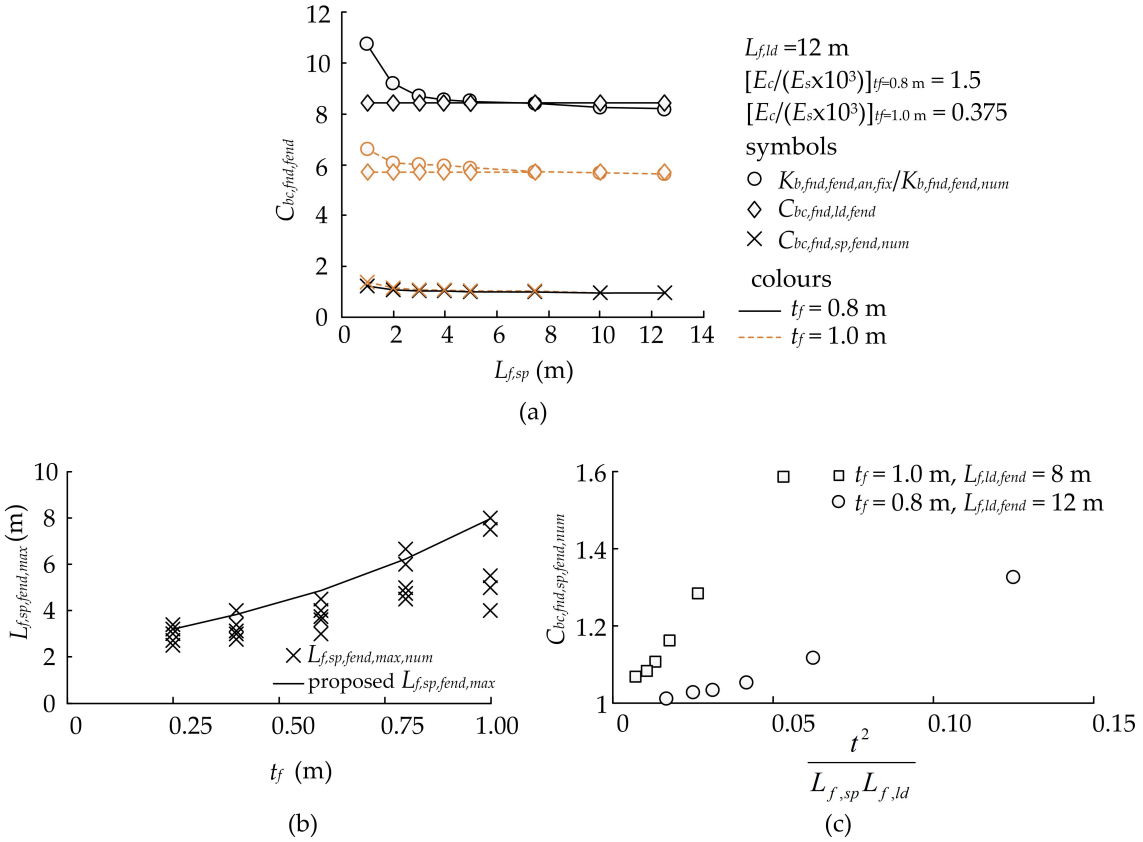

Fig. 6.18 (a) Weight of the coefficient $C_{bc,fnd,ld,fend}$ in $K_{b,fnd,fend,an,fix}/K_{b,fnd,fend,num}$, (b) numerical values of $L_{f,sp,fend,max}$ and the fitted values (Equation 6.10), (c) effect of $t_f^2/(L_{f,sp}L_{f,ld})$ on the foundation boundary condition

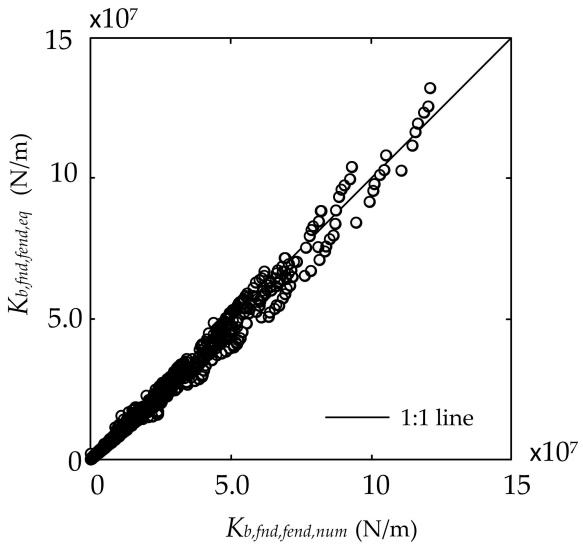

Fig. 6.19 Comparison between $K_{b,fnd,fend,eq}$ and $K_{b,fnd,fend,num}$

relationship, as expressed by Equation 6.11. It is worth noting that for values of $L_{f,sp} \geq L_{f,sp,fend,max}$, the coefficient $C_{bc,fnd,sp,fend}$ is not considered (i.e. $C_{bc,fnd,sp,fend} = 1.0$).

$$C_{bc,fnd,sp,fend} = \exp\left(4 \times \frac{t_f^2}{L_{f,sp} \times L_{f,ld}}\right) \geq 1.0 \tag{6.11}$$

A final coefficient for estimating the boundary condition of the foundation in the fixed–ended approach can now be introduced by multiplying $C_{bc,fnd,ld,fend}$ by $C_{bc,fnd,sp,fend}$:

$$C_{bc,fnd,fend} = C_{bc,fnd,ld,fend} \times C_{bc,fnd,sp,fend} \geq 1.0 \tag{6.12}$$

Finally, the analytically computed bending stiffness of the foundation using Equation 2.3 is divided by coefficient $C_{bc,fnd,fend}$ to obtained an equivalent stiffness value of the numerical results ($K_{b,fnd,cant,eq}$):

$$K_{b,fnd,fend,eq} = \frac{K_{b,fnd,an,fix}}{C_{bc,fnd,fend}} \tag{6.13}$$

Figure 6.19 presents a comparison of $K_{b,fnd,fend,num}$ with the equivalent numerical values of bending stiffness ($K_{b,fnd,cant,eq}$) for over 600 cases with variable parameters of $L_{f,ld}$, $L_{f,sp}$, t_f, E_c and E_s. The results show that the proposed method predicts the foundation bending stiffness to a good extent.

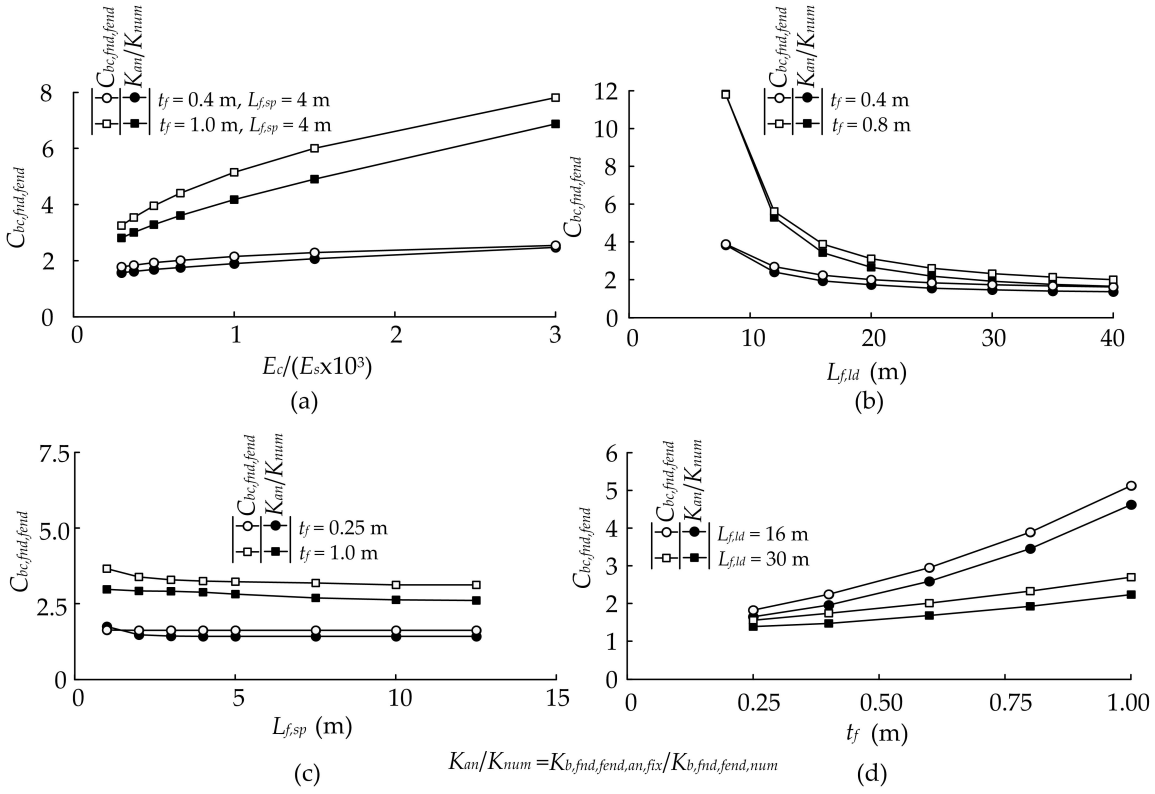

Fig. 6.20 Verification of the effect of (a) $E_c/(E_s \times 10^3)$ for $L_{f,ld} = 20$ m, (b) $L_{f,ld}$ for $L_{f,sp} = 12.5$ and $E_c/(E_s \times 10^3) = 0.667$, (c) $L_{f,sp}$ for $L_{f,ld} = 25$ m and $E_c/(E_s \times 10^3) = 0.667$, (d) t_f for $L_{f,sp} = 12.5$ m and $E_c/(E_s \times 10^3) = 0.667$ on the estimation of $C_{bc,fnd,fend}$

6.6.4 Verification example

To make a simple verification of the proposed method, numerical models were simulated to test the parameters that have an effect on the estimation of the foundation boundary condition. The considered numerical models used to verify the proposed method were not included in the development of the method, but the dimensions were within the range of values used in the method development. The tested parameters were: E_c/E_s, $L_{f,ld}$, $L_{f,sp}$ and t_f.

Figure 6.20a presents the results of the numerical and proposed values of $C_{bc,fnd,fend}$ for different values of $E_c/(E_s \times 10^3)$, and two values of t_f: 0.4 m and 1.0 m. $L_{f,sp} = 4$ m was chosen which was approximately equal to $L_{f,sp,fend,max} = 3.7$ m for $t_f = 0.4$ m, while it was smaller than $L_{f,sp,fend,max} = 7.85$ m for $t_f = 1.0$ m. In both cases, there is a reasonably good agreement between the numerical and proposed results; however, the agreement of the case where $t_f = 0.4$ m is better than that of $t_f = 1.0$ m.

The effect of changing $L_{f,ld}$ on $C_{bc,fnd,fend}$ is shown in Figure 6.20b for two values of t_f: 0.4 m and 0.8 m. A good agreement between the numerical and the proposed values of $C_{bc,fnd,fend}$ is observed. The difference between the numerically obtained and the proposed values of $C_{bc,fnd,fend}$ in the case of $t_f = 0.8$ m is greater compared to the case of $t_f = 0.4$ m. On the other hand, the effect of $L_{f,sp}$ on $C_{bc,fnd,fend}$ is presented in Figure 6.20c. There is also a reasonably good agreement between the numerical and the proposed values. Furthermore, Figure 6.20d exhibits the effect of the foundation thickness on $C_{bc,fnd,fend}$. Generally, the results are in reasonably good agreement.

6.7 Summary

This chapter investigated the bending behaviour of raft foundations located near newly constructed tunnels. As will be explained in Chapter 8, raft foundations constitute the major resistance of the building to bending deformations; therefore, special investigation is necessary to consider the foundation role in the tunnel–soil–building interaction analysis, which is disregarded to a great extent in the literature.

Two important zones of the soil were recognised in this chapter: the zone influenced by tunnelling (displaced zone), and the zone that was not influenced (undisplaced zone). The displaced soil zone was not modelled in the numerical analyses. Instead, a triangular pressure was applied to the footing to create deformations. The effects of the soil and concrete elastic moduli, the foundation length located in the displaced soil zone and that located in the undisplaced zone, on the bending behaviour of the foundation was also investigated. It was shown that the soil elastic modulus and the length of the footing in the undisplaced zone had a proportional effect on the foundation bending stiffness. Additionally, the increase of the footing length in the displaced zone led to the reduction of foundation rotation.

Furthermore, this chapter presented two methods based on numerical analyses to estimate the approximate bending stiffness of raft foundations. The methods consider two cases of tunnel–building relative location: a cantilever method for the case where the building is located under the edge or outside the building plan area, and a fixed–ended method for the case where the tunnel is under the building centreline. The footing and the underlying soil were considered together in the numerical simulations in order to calculate the bending stiffness of the global foundation.

Chapter 7

Mixed Empirical-Numerical Method for Investigating Tunnelling Effects on Structures

7.1 Introduction

The numerical simulation of a tunnel is an effective method for estimating the influence of tunnelling on buildings, however, as explained in Section 3.6.5, finite element methods generally predict a wider and shallower greenfield settlement trough than observed in practice. This issue can be overcome by the use of sophisticated soil constitutive models, although the input parameters for these models are generally not readily available. A wider/shallower input of greenfield displacements can affect the results of a soil–structure interaction analysis in two ways. First, for a given settlement trough shape, a smaller maximum settlement produces less distortions and therefore less damage to a building. Second, the width of the settlement trough can alter the response of the building; a building affected along its entire length will show less resistance to deformation compared to the same building subjected to ground displacements along part of its length. This feature, which relates to the end-fixity of the building, can be explained using a beam analogy. A relatively long building extending further outside the ground displacement zone can be thought of like a beam with a relatively stiff support that constrains the rotation of the beam (similar to a fixed ended beam), whereas a shorter building behaves like a beam with a more flexible support that allows a degree of rotation (similar to a simply supported beam).

The aim of this chapter is to describe the use of a two-stage mixed empirical-numerical (E–N) method to estimate the effect of the stiffness of a weightless building on ground displacements caused by tunnelling. In this method, realistic greenfield ground displacements, obtained from empirical or analytical relationships, are used as an input in a numerical analysis in order to determine the nodal reaction forces within the numerical mesh required to obtain the greenfield displacements (stage 1). The tunnel–building interaction is then solved in stage 2 by including the building within the model and applying the greenfield nodal reaction forces to the mesh. The applied numerical analysis adopts simple linear elastic constitutive soil behaviour; the effects of building weight on the tunnelling-induced response is therefore not considered in the analysis.

This chapter also includes the use of a conventional numerical analysis to estimate the tunnel–building interaction effect. The purpose of including the conventional numerical analysis is to provide results for comparison which might be obtained by a practising engineer considering this problem, using reasonably standard numerical modelling methods. Results from the two numerical analyses are compared and the importance of having an accurate input of greenfield displacements in evaluating structural distortions is demonstrated. Furthermore, this chapter adopts the methodology of Franzius et al. (2006) (Equations 3.30 and 3.31) for comparing the results. The method of Goh and Mair (2011b) and Mair (2013), in which the building is separated into sagging and hogging zones and the relative bending stiffness is estimated independently for each part, was also available for the comparison. Each method has its own advantages and limitations, however it was felt that treatment of the building as a single entity (as in the Franzius et al. (2006) method) was more logical for the analyses considered in this chapter since the fixity condition of the building ends (which is misrepresented by splitting the building into parts) plays an important role.

An investigation of the effect of volume loss and soil relative density on the tunnel-building interaction is also presented in this chapter. It should be mentioned that the proposed method in this chapter (mixed E–N) was used in Chapter 8 to estimate the effect of 3D buildings on tunnelling induced ground displacements.

7.2 Mixed Empirical-Numerical Approach (mixed E–N)

To address the issues related to poor prediction of tunnelling induced settlement trough shape using numerical methods, yet still take advantage of the capabilities of numerical modelling for soil-structure interaction analysis, several authors have incorporated an empirical or

analytical greenfield input into a numerical analysis, such as Selby (1999), Klar and Marshall (2008) and Wang et al. (2011) (see Section 3.7.1 for more detail).

Selby (1999) applied tunnelling induced ground surface movements to a finite element numerical model using Gaussian equations to estimate tunnelling effects on structures. Klar and Marshall (2008) applied Gaussian ground movements to all nodes of a finite difference numerical model in order to estimate tunnelling effects on pipelines. Wang et al. (2011) used a semi empirical method to investigate tunnelling effects on buried pipelines. The method of Selby (1999) and Klar and Marshall (2008) incorporated a two-stage analysis in which displacements are applied to the model in the first stage, and the reaction forces required to create the prescribed displacements are applied to the model in the second stage, after the structure is added to the model. In this way, the tunnelling process is not simulated directly in the numerical model, yet the soil-structure interactions caused by the greenfield input are simulated. The method of Wang et al. (2011) differs from the work of Klar and Marshall (2008) in that it was a displacement control modelling throughout the analysis. The soil boundary was subjected to displacements in both cases of greenfield and with the existence of the structure (i.e. assuming no effects of the structure on the boundaries). The effects of the tunnel construction were transferred to the other parts of the soil via the soil material model.

In the methodology of this chapter, the two-stage analysis approach was adopted. The method is referred to as the mixed empirical-numerical (mixed E–N) method because an empirical/semi-analytical relationship was used for the greenfield input. In the first stage of the analysis, all nodes in the numerical mesh of the soil model are forced to displace according to the empirical functions (displacement input to the model) and the nodal reaction forces are recorded. Note that the numerical model in stage 1 includes elements that represent the soil and the building, however the elements associated with the building are not activated (i.e. a virtual building exists that does not affect the analysis). This ensures that no changes occur to the global model in stage 2 in terms of boundaries, dimensions and node numbering. In the second stage, the model is returned to its original condition and the structure is activated. The recorded nodal forces are then applied to all nodes of the soil model. Using this approach, the difference between the greenfield deformations and the deformations obtained when the structure is added represents the soil-structure interaction effect.

Results are provided from both conventional numerical analyses (Figure 7.1a), in which the greenfield displacements and soil-structure interactions are evaluated using the numerical model, as well as the mixed E–N method (Figure 7.1b). The soil depth above the tunnel,

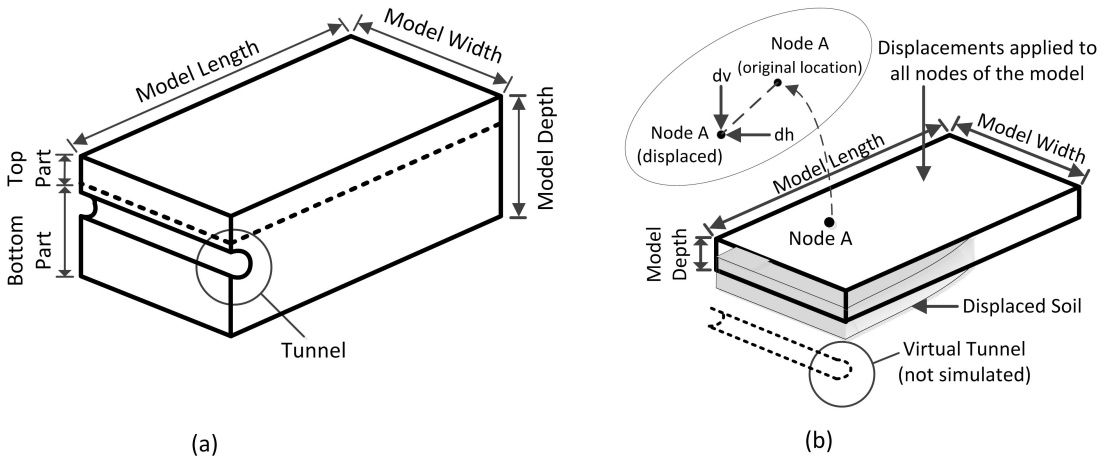

Fig. 7.1 (a) 'Conventional' numerical model and (b) mixed E-N method

denoted by 'top part', is used for the mixed E–N analysis; the 'bottom part' is excluded from the mixed E–N modelling.

The analyses presented here follow the procedure set out in Klar and Marshall (2008). The main difference is that the structure in this chapter is a 3D beam of finite length located on the surface, whereas for Klar and Marshall (2008) the structure was a buried pipeline of infinite length (achieved using appropriate boundary conditions). The assumptions inherent to the Klar and Marshall (2008) approach include: (1) the structure is continuous and always in contact with the soil, (2) both the soil and the structure are homogeneous linear elastic, (3) the tunnel is not affected by the existence of the structure, and (4) the soil responds to loading from the structure as an elastic half-space, disregarding the presence of the tunnel. In this chapter, analyses were carried out considering both vertical and horizontal ground movements, thereby including both deflections and axial deformations of surface structures.

A semi-analytical approach similar to that presented in Franza and Marshall (2015b) was used to obtain the greenfield displacement input. Franza and Marshall (2015b) obtained a closed-form solution that was able to represent greenfield displacements around a tunnel in sand based on data obtained from geotechnical centrifuge testing. Their proposed method provided good accuracy of vertical displacement predictions, however the solutions over-predicted subsurface horizontal movements. The semi-analytical solution for horizontal (S_h) and vertical (S_v) greenfield displacements used in this chapter are presented in Section 3.6.2 which is an expanded form of the approach proposed by Franza and Marshall (2015b), and modified by the same authors to include a wider set of centrifuge data. Note that any input of greenfield can be incorporated into this analysis methodology.

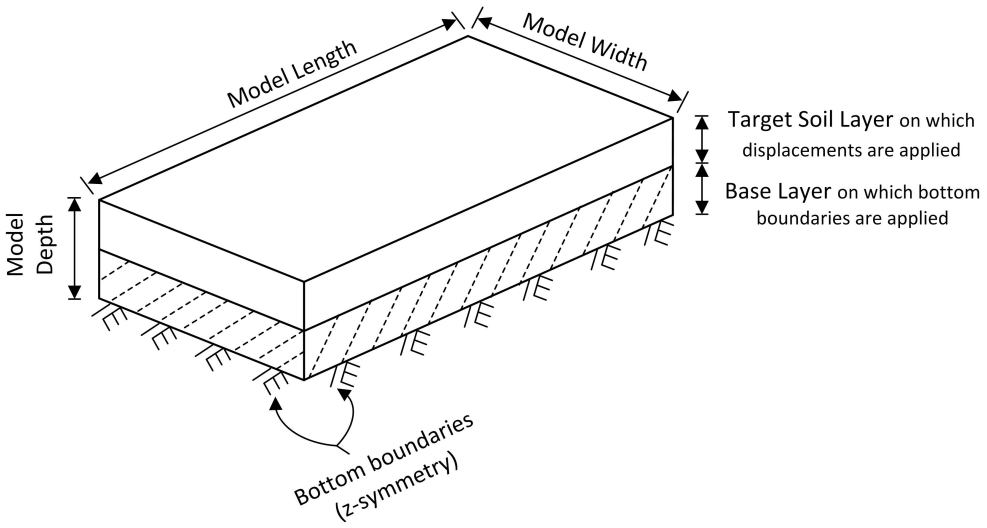

Fig. 7.2 Mixed E–N model with base layer

In Klar and Marshall (2008), the base of the mesh was forced to displace according to the input greenfield displacements even when the equivalent nodal forces were applied in the second stage of the analysis. This approach requires that the base of the mesh is not affected by the existence of the included structure (i.e. by the loading due to soil-structure interaction), which was the case for the Klar and Marshall (2008) analysis. This approach creates issues for analyses of structures above relatively shallow tunnels. This chapter proposes a method to address this constraint by using the following technique. As shown in Figure 7.1a, the targeted part of the soil is located above the tunnel crown. Instead of applying fixities and imposing greenfield displacements to the base of the model in stage 2 of the analysis, a 'base layer' is added to the bottom of the model (illustrated in Figure 7.2) which has the same properties as the top (target) layer (or could include other properties in the case of layered soil analyses) and is fixed in the vertical direction along its bottom. In this way, the soil responds to soil-structure interaction loading (i.e. reaction forces applied by the structure to the soil due to structure stiffness and distortions) in a way similar to an elastic half-space.

In stage 1, soil nodes in the target layer of the mesh are moved according to the greenfield displacements, while movements in the base layer are not imposed; they depend on the displacements applied to the target layer and the properties of the soil. The equivalent nodal forces from the target layer are then recorded and, in stage 2, after resetting the mesh displacements and adding the structure, the nodal forces in the target layer are applied to the mesh. It will be shown later that the use of the base layer provides an effective method for evaluating the effect of a structure on the entire depth of the target layer (Figure 7.2).

7.3 Model Description

7.3.1 Conventional numerical Model

In the conventional numerical analyses, a 4.65 m diameter tunnel was modelled within a soil domain $43D_t$ long and $10D_t$ deep, as illustrated in Figure 7.3; a unit length mesh was used in the direction of the tunnel axis. Two tunnel depths were considered, with C_t/D_t=2.4 and 4.4, as well as three relative tunnel-building eccentricities, $e/L_{bldg} = 0.0,\ 0.5$ and 0.75. A 60 m long beam (also 1 m wide in direction of tunnel axis) was attached to the soil surface using a tie constraint (does not allow slip or separation). The total number of elements was between 60,000 and 110,000. Equations 3.30 and 3.31 were used to evaluate ρ^*_{mod} and α^*_{mod}, respectively. Five buildings were analysed, as described in Table 7.1. The flexural and axial rigidity of the buildings, EI and EA, were chosen based on realistic values presented by Farrell (2010). The properties were selected so that they include low, medium and high stiffness structures. It is worth noting that the elastic modulus of the concrete was 23 GPa, and the other material models are given in Section 4.7.

Table 7.1 Building properties for conventional numerical and mixed E–N simulations

Cases	Beam thickness, t_B (m)	EI (kNm^2/m)	EA (kN/m)
1	0.10	1.9×10^3	2.3×10^6
2	0.25	3.0×10^4	5.8×10^6
3	0.50	2.4×10^5	1.2×10^7
4	1.00	1.9×10^6	2.3×10^7
5	3.00	5.2×10^7	6.9×10^7

The tunnel was excavated instantaneously along its length. The displacement controlled method described by Cheng et al. (2007), where increments of contraction are induced along the tunnel periphery, was used to simulate the tunnelling process. An oval-shaped pattern was assumed for the displacements around the tunnel, where maximum settlements occur at the tunnel crown and no movements occur at the invert, as shown in Figure 7.3. Tunnel boundary displacements were directed towards the centre of the converged tunnel. This displacement pattern matches closely to data obtained from centrifuge experiments (Marshall, 2009; Zhou, 2014), and has provided good predictions of ground displacements when compared with the stress control method (Cheng et al., 2007).

Three cases of volume loss and two cases of soil relative density were considered for each tunnel/building scenario, as listed in Table 7.2. The chosen values of tunnel volume loss (V_{lt}) are based on the available centrifuge test data. In the numerical model, displacements

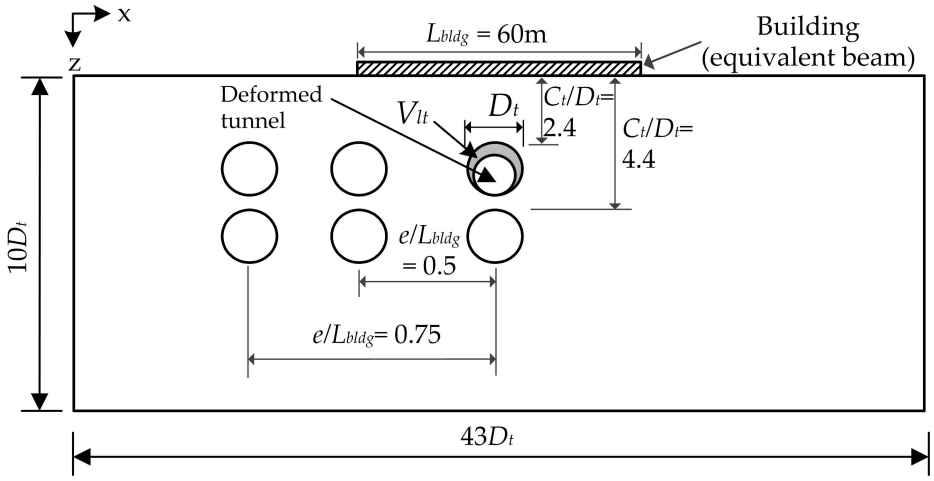

Fig. 7.3 Illustration of numerical model showing dimensions, depths and locations of the tunnel

of the tunnel boundary were increased until the volume loss at the surface in the greenfield situation matched that of $V_{ls,surf}$ in Table 7.2. This was done to ensure a fair comparison of numerical results with those from the mixed E–N since the most important zone is at the surface where the tunnel-building interaction takes place.

7.3.2 Mixed E–N model

In the mixed E–N analyses, a soil model of the same dimensions as the conventional numerical model was used. The analyses, summarised in Table 7.2, were based on centrifuge experiment data. The input of the tunnelling induced greenfield displacements to the mixed E–N model was obtained using Equations 3.17, 3.18, and 3.20 in Section 3.6.2. The depth of the target and base layers for both tunnel depth cases ($C_t/D_t = 2.4$ and 4.4) were 10 m and 35 m, respectively, except for simulations where the effect of the size of the target/base layers was investigated. Three tunnel volume losses (V_{lt}) of 0.96%, 1.76% and 3.94% were considered; these result in the soil volume losses ($V_{ls,surf}$) at the ground surface shown in Table 7.2. Two cases of soil relative density were considered: I_d= 90% and 30%. The element types and elastic properties of the soil and the building were the same as the conventional numerical model. It should be noted that the centrifuge data for the case $I_d = 90\%$ was from Marshall et al. (2012) and that of the case $I_d = 30\%$ was from Franza (2016).

Table 7.2 Mixed E–N analyses: tunnel and surface soil volume losses

C_t/D_t	I_d (%)	V_{lt} (%)	$V_{ls,surf}$ (%)
2.4	90%	0.96	0.92%
2.4	90%	1.76	1.55%
2.4	90%	3.94	2.50%
2.4	30%	0.96	2.50%
2.4	30%	1.76	4.12%
2.4	30%	3.94	6.82%
4.4	90%	0.96	1.68%
4.4	90%	1.76	2.77%
4.4	90%	3.94	4.40%
4.4	30%	0.96	2.74%
4.4	30%	1.76	4.85%
4.4	30%	3.94	9.50%

7.4 Mixed E–N Model Results

This section includes the results related to the validation of the mixed E–N method and its comparison to the results obtained from the conventional numerical analyses. It should be mentioned that the results presented throughout this section are related to the case $I_d = 90\%$.

7.4.1 Greenfield input

In addition to predicting a wide settlement trough, conventional numerical methods are also not able to replicate the complex distribution of soil volume loss that occurs above a tunnel in a drained granular soil, where shear strains can lead to contraction or dilation of the soil. The amount of contraction/dilation of the soil, which depends on its relative density, the depth of the tunnel, and the magnitude of tunnel volume loss, ultimately leads to a change in the shape of the settlement trough (Marshall et al., 2012; Zhou et al., 2014). This necessitates the use of more complex empirical relationships compared to the standard Gaussian curve generally applied to settlements above tunnels in clay.

Figure 7.4 shows greenfield vertical and horizontal displacements for the conventional numerical and mixed E–N models for $C_t/D_t = 2.4$. The centrifuge test data, on which the semi-analytical expressions (and therefore mixed E–N analyses) are based are also illustrated. The figure presents data at two depths ($z/z_t = 0.0$ and $z/z_t = 0.37$) and at two values of surface volume loss ($V_{ls,surf}$=1.55% and 2.5%). The vertical displacement data illustrate the wide/shallow settlement trough obtained using the conventional numerical model. For horizontal displacements at the surface, the magnitude of maximum horizontal displacement

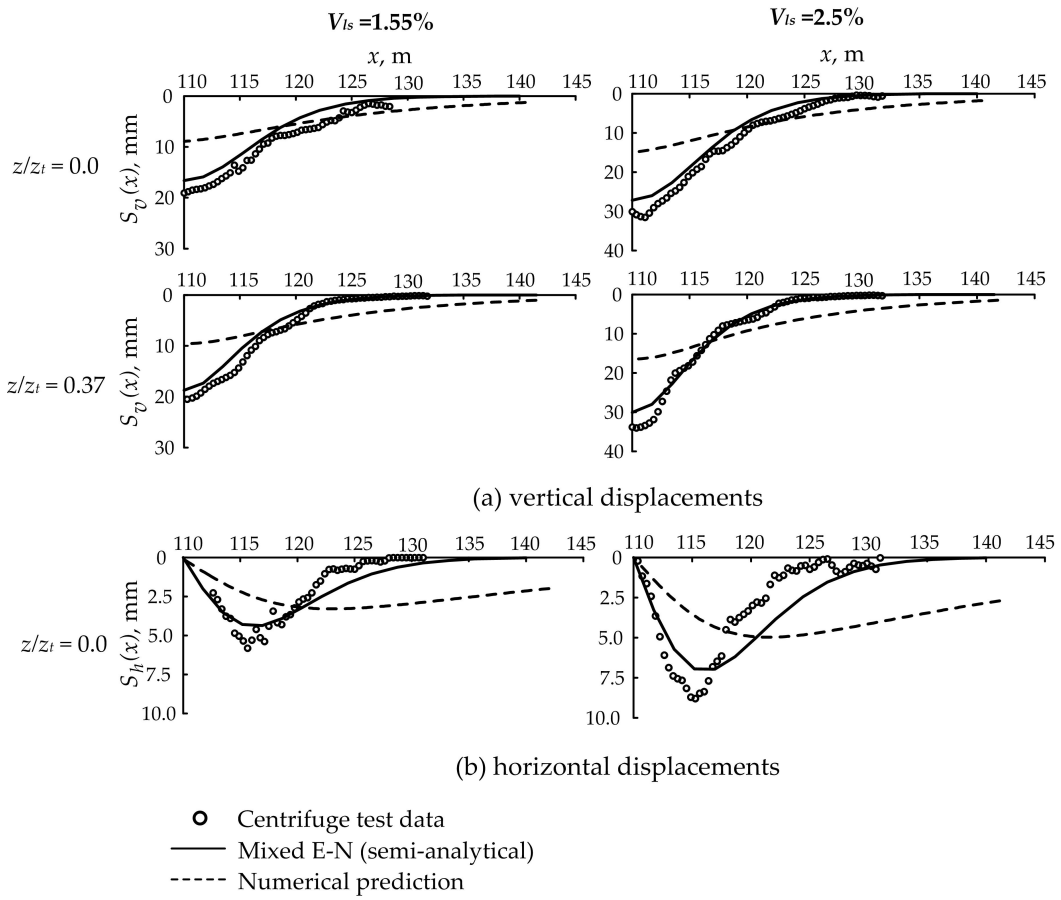

Fig. 7.4 Tunnelling induced greenfield ground displacements for $C_t/D_t = 2.4$: (a) vertical, (b) horizontal

from the conventional numerical analyses is considerably less than the experimental data, and occurs much further away from the tunnel. This has an impact on the soil-building interaction analysis, since the building in the conventional numerical model will be subjected to ground displacements along a greater length compared to what is expected (assuming that the centrifuge test data gives a good representation of reality). The semi-analytical expressions are shown to give a good fit to the centrifuge data, hence the greenfield inputs for the mixed E–N analyses are a good reflection of what is expected in reality.

For the same value of surface volume loss, the value of maximum settlement and the trough width are both significantly influential on the degree of effect of ground displacements on buildings. Therefore, any inaccuracy in the prediction of the maximum settlement or the trough width will lead to larger inaccuracy in the estimation of the building damage caused by displacements. In the proposed method of Burland (1995) to evaluate the risk of damage to

buildings, the assessment of building damage was linked to the maximum ground settlement; a building is likely to experience damage if the maximum ground settlement exceeds 10 mm. The importance of using realistic ground movements as input to tunnel–building interaction analyses was also confirmed by Heath and West (1996).

The input of tunnel volume loss for the centrifuge and the semi-analytical methods was the same (0.96%, 1.76% and 3.94%), but this was not achievable with the numerical modelling since the mechanism of predicting ground displacements between the centrifuge experiment and the numerical simulation was different. For this reason, the surface settlements of the conventional numerical analysis and the semi-analytical solution were equalised and used for the purpose of comparison and also for the estimation of building stiffness effect on tunnelling induced ground movements. Table 7.3 shows values of volume loss at different depths for the centrifuge experiment, conventional numerical modelling and semi-analytical (mixed E–N) solution. It is worth mentioning that the tunnel volume loss in the numerical modelling was calculated after a surface volume loss equal to that of the semi-analytical solution was predicted.

Table 7.3 Achieved volume losses at different depths by different prediction methods of ground displacements due to tunnelling

depth	soil volume loss, V_{ls} %		
	centrifuge	semi-analytical	numerical
Tunnel	3.94	3.94	1.10
$z/z_t = 0.37$	2.20	2.33	2.50
$z/z_t = 0.0$	2.75	2.50	2.50
Tunnel	1.76	1.76	0.66
$z/z_t = 0.37$	1.60	1.46	1.55
$z/z_t = 0.0$	2.0	1.55	1.55
Tunnel	0.96	0.96	0.40
$z/z_t = 0.37$	1.0	0.87	0.93
$z/z_t = 0.0$	1.25	0.92	0.93

Table 7.3 shows that the value of volume loss in the centrifuge case changes along the soil depth. This change is also captured by the semi-analytical method while no change in the volume loss value was obtained along the soil depth in the conventional numerical analysis. The large volume loss difference between the tunnel and outside the tunnel (contraction) in the conventional numerical analysis is due to the effect of Poisson's ratio. For $\nu_s = 0.5$, the tunnel and surface volume losses will be the same due to no change in the initial and final

volume. In addition, there was no induced plastic strains in the soil except in an insignificant area around the top and sides of the tunnel boundary.

7.4.2 Applying displacements and equivalent nodal forces to the soil model

The results of different simulations showed that the nodal reaction forces recorded in the first stage in which displacements were applied to the model, resulted in the same prescribed displacements when they were applied to the model in the second stage. Vertical and horizontal displacements of both the applied displacements and the applied nodal reaction forces for various soil depths were compared to each other, and the displacement curves of both cases at each depth completely lied on each other without any difference between them. It should be noted that the comparison of the results was done for the greenfield situation where there were no structures.

7.4.3 Effect of top and base layer thickness

Three depths of the top layer (2.5 m, 5 m and 10 m) were tested for the building Case 5 (Table 7.1). The results of different depths of the top layer did not show any dissimilarities and their settlement curves exactly lied on each other. This explains that the depth of the top layer for a constant model depth does not have an effect on the simulations.

Figure 7.5 shows the effect of base layer thickness on the mixed E–N results for different building cases (Table 7.1) at a tunnel volume loss of 1.76% and tunnel depths corresponding to $C_t/D_t = 2.4$ and 4.4. The thickness of the base layer was varied from 5 to 35 m. Results based on the approach of Klar and Marshall (2008) in which the base of the model (target layer thickness = 10 m with no base layer) was assumed to follow greenfield displacements are also included. Figure 7.5a illustrates that displacements decrease with the increase of the base layer thickness. The maximum displacements are greatest when there is no base layer (i.e. the Klar and Marshall (2008) case). The effect of the base layer was constant for values of thickness greater than 25 m (data coincides with base layer = 25 m line). The larger displacements for the less thick base layer cases is caused by the effect of the constraint at the bottom of the base layer, which prevents the reduction of downwards movements near this boundary. Since the first stage of the analysis is a displacement controlled process in which all soil nodes in the top part are forced to displace by a certain amount, relatively large reaction forces are created in the nodes, including the effect of the applied displacements as well as the bottom boundary. When the structure is added to the analysis in stage 2,

these nodal reactions force the building to displace more compared to the larger base layer thickness cases due to the extra reaction forces created by the effect of the nearby bottom boundary.

The stiffness of the building also has an impact on the soil-building interaction. Figure 7.5b shows that the base layer thickness has little effect when it is greater than 5 m for the more flexible equivalent beam in building case 2, where the beam thickness t_B is 0.25 m. In the case of a fully flexible building, the base layer effects are negligible. The stiffer the building, the greater the required thickness of the base layer.

For deeper tunnels, the effect of the bottom boundary on the soil-building interaction reduces since the influence of the building at the base of the target layer is not as significant. Figure 7.5c shows three simulations in which the thickness of target layer was either 10 or 20.5 m for a tunnel depth corresponding to $C_t/D_t = 4.4$ and building case 5 ($t_B = 3$ m). The mixed E–N analysis with a base layer of 25 m provided the same result for both target layer thicknesses. The Klar and Marshall (2008) results are shown to match more closely with the mixed E–N results as the thickness of the top layer is increased.

7.4.4 Effect of nodes and nodal force components on each other

When both vertical and horizontal greenfield displacements are included together in the tunnel-building interaction, there will be a strong inter-dependence of horizontal and vertical nodal reaction forces required to produce the specified greenfield displacements. Vertical nodal reaction forces due to the applied displacements are affected by horizontal reaction forces on the nodes. Similarly, the horizontal nodal reaction forces are affected by vertical reaction forces on the nodes. This is because each force component of a node subjected to a displacement consists of two main parts: a part comes from the material resistance and the other comes from the effect of other force components in different directions, as illustrated in Figure 7.6a. Because of this, any significant change in the vertical or horizontal reaction forces will have a considerable impact on the displacement results.

In addition, the closely located nodes also have a great effect on each other. Some nodal forces are in the opposite direction to the others in order to achieve equilibrium. For instance, the displacement applied to node 1 in Figure 7.6b is large and needs a large force of F_{v1}. This large value already creates some movement in the adjacent node 2 leading to a smaller force F_{v2} compared to the scenario that F_{v1} did not exist. The action of forces F_{v1} and F_{v2} generates a displacement at node 3 larger than the required value; therefore, the force on this node must act in the opposite direction to prevent it from exceeding the applied displacement value.

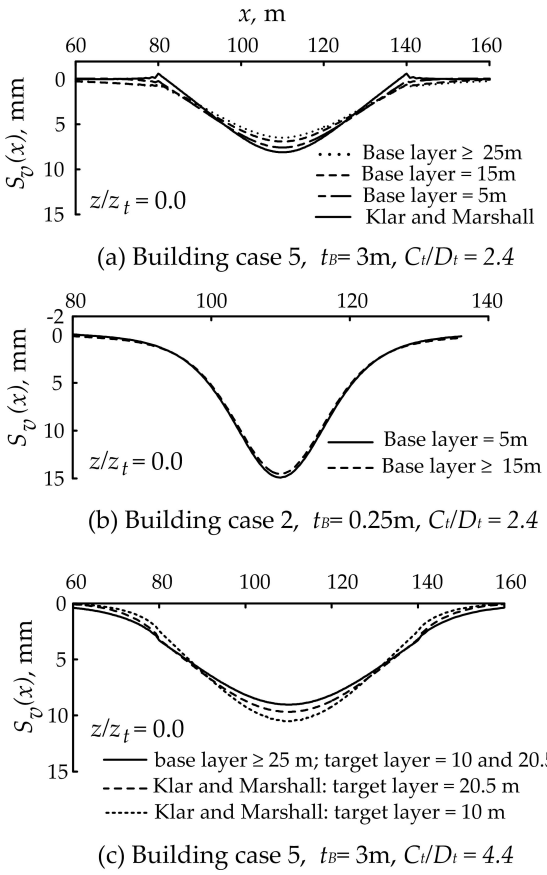

Fig. 7.5 Effect of base layer thickness on soil-building interaction: $V_{lt} = 1.76\%$

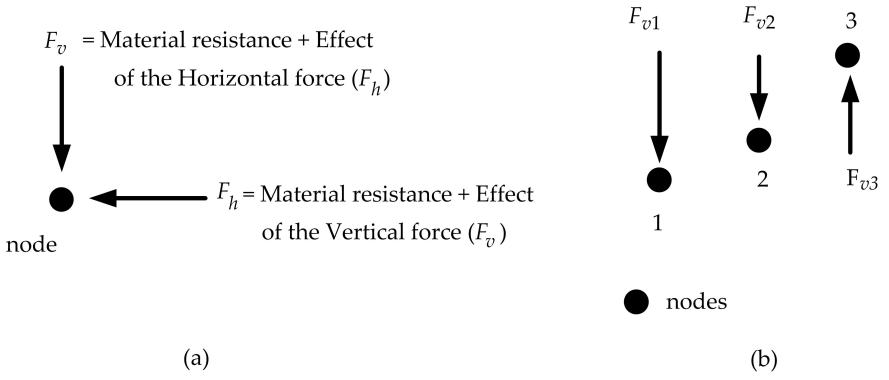

Fig. 7.6 (a) Horizontal and vertical nodal reaction forces, and (b) equilibrium of the vertical nodal forces to create the originally applied displacements

This causes the nodes to behave in a way that the regular pattern of the applied displacements (i.e. vertically downward for vertical and horizontally towards the tunnel) is not reproduced for the nodal reaction forces.

To understand the influence of horizontal and vertical force components on each other, a model was analysed three times. In the first time, both vertical and horizontal displacements were applied to the model and the nodal reaction forces were achieved. After that, a simulation was run in which the horizontal component was reduced to half with actual vertical component, and then, the third simulation was run in which the vertical component was reduced to half with actual horizontal component. Figure 7.7 exhibits the vertical and horizontal displacements obtained from these simulations.

As shown in Figures 7.7a and b, when nodal reaction forces are determined from specific values of applied displacements, a decrease of the horizontal nodal forces for constant values of vertical forces results in an increase of the vertical displacements. This is because vertical nodal forces face less resistance due to the lack of the horizontal components. Conversely, when the vertical components of the nodal forces are reduced to half with constant horizontal values, vertical displacements will face a great reduction of more than half of their original values, as shown in Figures 7.7a and b. This is because of the action of horizontal nodal forces which decreases the effect of the vertical forces.

With regard to the horizontal displacements, the results show that these displacements increased at the ground surface when the values of horizontal nodal forces were reduced to half of their original values, as shown in Figure 7.7c. In contrast, horizontal displacements faced a great reduction when the values of the vertical nodal forces were reduced to half with constant horizontal forces, as shown in Figure 7.7c. A different trend appears with subsurface horizontal displacements. As shown in Figure 7.7d, in both cases where the vertical and horizontal forces were reduced, horizontal displacements underwent a reduction compared to their applied greenfield displacements but the displacements of the case where horizontal forces decreased to half, faced a marginally bigger reduction.

It is indicated in Figures 7.7c and d that the nodes close to the surface generally start to move away from the tunnel, while deeper nodes move towards the tunnel. The reason for the changes happened to the horizontal displacements is strongly related to the direction of the forces created at the nodes when the model was subjected to displacements. The reaction forces of the nodes close to the surface are initially outwards from the tunnel due to the reaction forces towards the tunnel in the lower soil layers. When vertical forces decrease, horizontal forces close to the surface push the nodes away from the tunnel to a greater extent. The opposite action happens at the lower layers as most of the nodal reaction

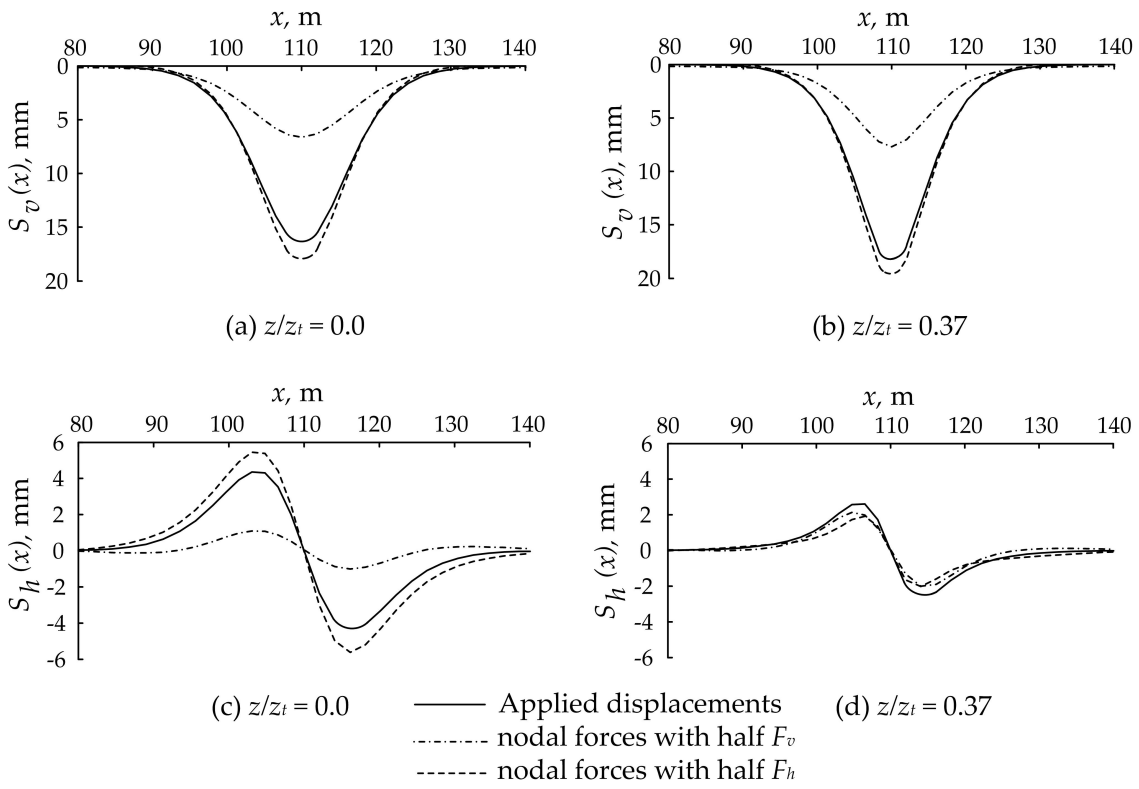

Fig. 7.7 Effect of vertical and horizontal components of nodal forces on each other at different depths for $V_{lt} = 1.76\%$

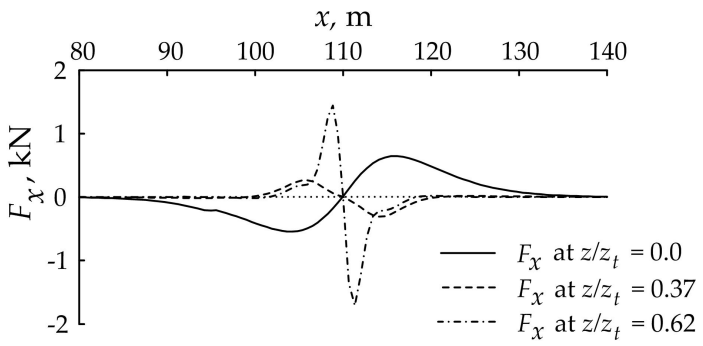

Fig. 7.8 Horizontal force distribution at different depths for $V_{lt} = 1.76\%$

forces are directed towards the tunnel. Figure 7.8 presents horizontal forces at three depths of $z/z_t = 0.0$, $z/z_t = 0.37$ and $z/z_t = 0.62$ achieved from the case where both horizontal and vertical displacements were applied to the model. It is illustrated that horizontal forces at the lower layers (i.e. $z/z_t = 0.62$) are large and towards the tunnel. These forces decrease gradually at shallower depths like $z/z_t = 0.37$, and then, they start to change their directions away from the tunnel.

The effect of each component on the other is due to that the medium is continuum and Poisson's ratio transfers the effect of each direction to the other. Figure 7.9 shows the effect of Poisson's ratio on the interaction between horizontal and vertical displacements at the ground surface for a tunnel volume loss of 1.76% after the horizontal forces are reduced to half of their original values. It is illustrated that the increase of the Poisson's ratio from 0 to 0.40 results in an increase of the vertical displacements.

Based on the mentioned reasons, when both vertical and horizontal displacements are applied to a model in the first stage of the analysis, all components of the nodal reaction forces should be applied to the model in the second stage of analysis. This includes the forces in the directions of x and y. If a 3D modelling is performed for such a plane strain analysis, the forces in the z direction should also be applied in the second stage because some reaction forces in that direction will still be created in the nodes due to the effect of Poisson's ratio.

7.4.5 Interaction effects of horizontal and vertical displacements

The analyses presented here consider the effect of both vertical and horizontal greenfield displacements, which may be important in the tunnel-building interaction analysis. For example, consider the case where the tunnel is located directly beneath the building centreline as shown in Figure 7.10; vertical displacements drag the building downwards and, at the same

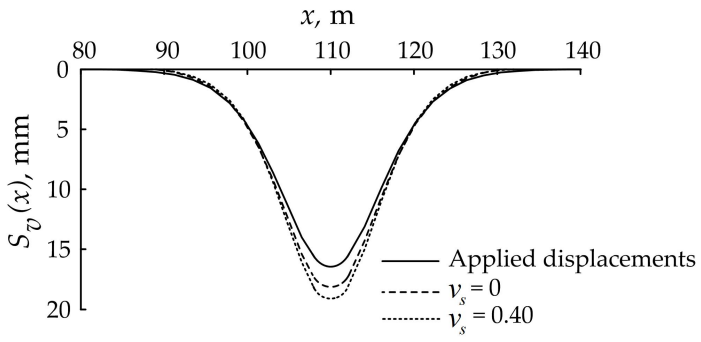

Fig. 7.9 Effect of Poisson's ratio on the interaction between vertical and horizontal displacement components at the ground surface for $V_{lt} = 1.76\%$ (the horizontal forces are reduced to half of their original values for the cases of $\nu_s = 0$ and 0.40)

time, horizontal displacements pull the portion of the building above the tunnel (at the ground or foundation level) horizontally towards its centre. The horizontal displacements act to compress the building horizontally and increase its resistance against bending deformations (because of the compression applied at the bottom fibre), thereby increasing its resistance to vertical displacements. In addition, the action of the downwards displacements also creates horizontal strains in the building. In the case where only vertical or horizontal displacements are applied to the model, these interactions are neglected.

The interaction between vertical and horizontal displacements of both the soil and the structure is illustrated in Figures 7.11a and b for two buildings (Cases 3 and 5 from Table 7.1). These figures show building displacements from analyses where only vertical S_v, only horizontal S_h, or both S_v and S_h were applied to the models. Interestingly, the application of both vertical and horizontal soil movements results in a smaller building maximum vertical displacement compared to the analysis for only S_v; this is consistent with the upwards building deflections obtained when only S_h was applied (due to the compressive action of S_h). Also note that for the stiffer Case 5 building the interaction effects between vertical and horizontal input soil displacements is minimal.

Figures 7.11c and d show the horizontal strains, ε_h, induced in the building. There is a significant difference between the case where both displacement components are applied and when they are applied separately. When the building is flexible (i.e. beam thickness is small; Figure 7.11c), most of the effect of S_h is transferred to the building and horizontal strains due to vertical displacements play a minor role, hence the 'Only S_h' line matches closely with the case where both displacements are applied. As bending stiffness of the building increases (i.e. larger beam thickness; Figure 7.11d), the resistance of the building

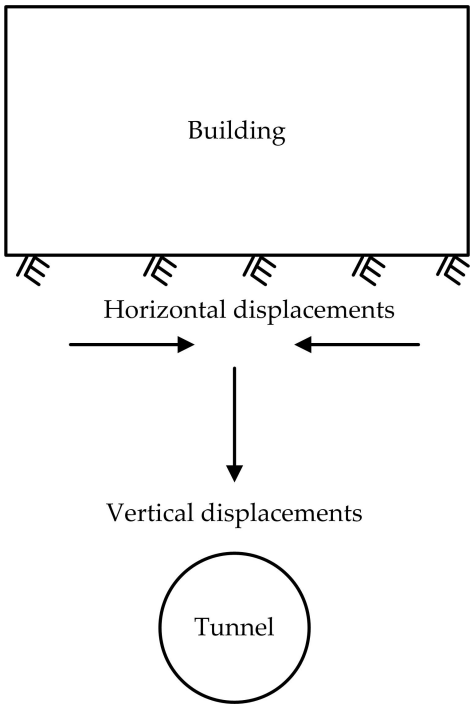

Fig. 7.10 Interaction between horizontal and vertical displacements for $e/L_{bldg} = 0$

against deformations (bending and axial) increases. Because axial stiffness is significant, only a minimal axial effect is transferred from the soil to the building. Tensile horizontal strains occur at the middle of the beam because of the coupling between beam bending and soil horizontal ground movements. On the other hand, when S_v and S_h are applied together, significant compressive horizontal strains are induced due to the action of S_v.

In scenarios where the tunnel is located below the edge or outside the building plan area (i.e. $e/L_{bldg} \geq 0.5$), analysis results indicated a negligible tendency of horizontal movements to reduce vertical displacements (i.e. no practical difference was found when both S_h and S_v were applied and when only S_v was applied to the model). This outcome relates to the end constraints of the building, which affects its ability to resist deformations. Moreover, horizontal displacements used within the mixed E–N method (based on centrifuge test data) have a narrow trough and do not cover a significant proportion of the buildings with $e/L_{bldg} \geq 0.5$. Further discussion on this aspect is given later in the chapter.

It is worth noting that when equivalent beams are used instead of actual buildings, there will be a coupling effect between the cross sectional flexural (EI) and axial (EA) rigidity of the beam on the axial and bending behaviour. For a specific beam length, a change in the thickness leads to a change in the bending and axial behaviour of the beam. A larger

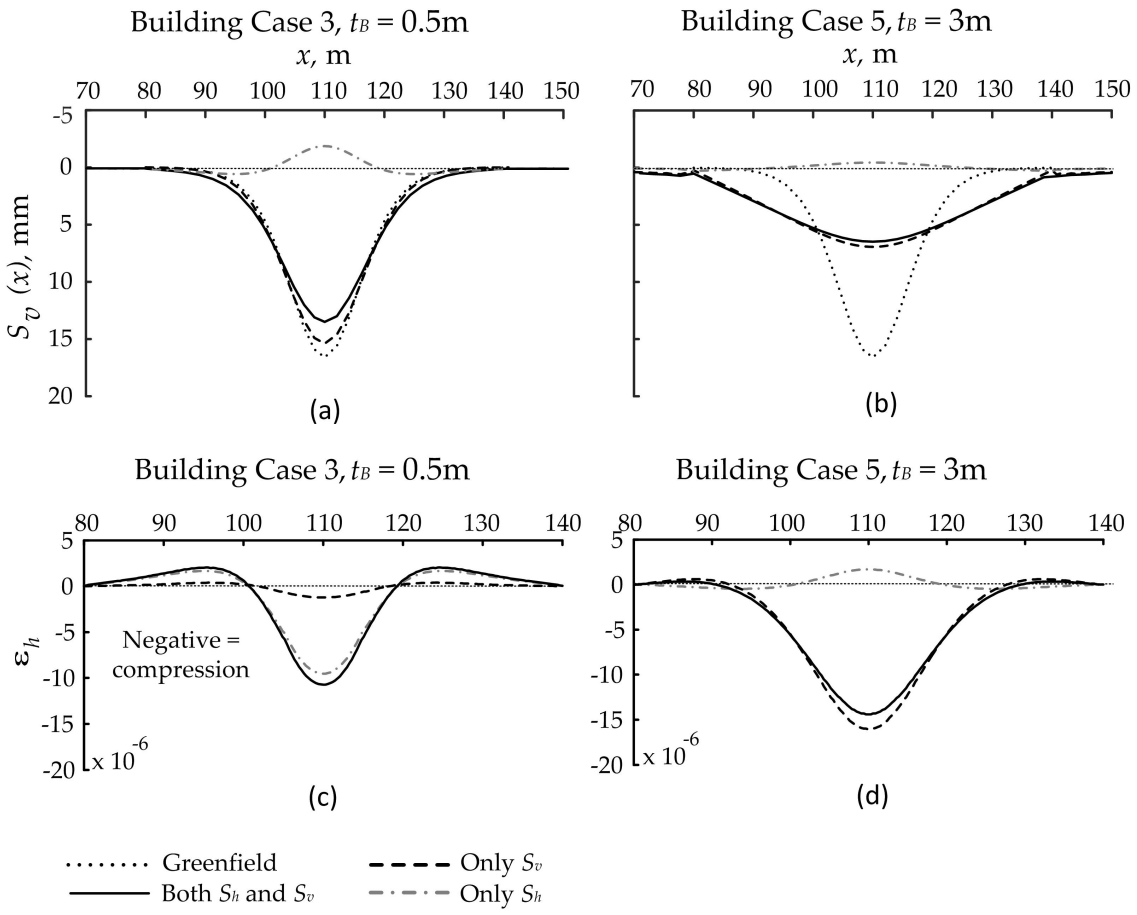

Fig. 7.11 Effect of applying ground displacement components separately to a model: (a) and (b) ground displacements in the presence of a building; (c) and (d) horizontal strains created in the building. Tunnel volume loss = 1.76%

axial effect is transferred to the beam when the axial rigidity decreases. Similarly, the beam experiences a larger bending effect when flexural rigidity reduces. This change may alter the behaviour of the beam to some extent due to the occurrence of the coupling effect between EI and EA. For instance, a decrease in EA induces larger horizontal displacements in the beam which in turn results in larger compressive stresses that may reduce vertical displacements. To understand this effect clearly, beams should be analysed for both cases of having constant EA with variable EI, and constant EI with variable EA, as done by Potts and Addenbrooke (1997). However, this issue does not have an effect on the comparative results reported here since this feature is present in both the conventional numerical and mixed E–N analyses. Furthermore, investigating the impact of using equivalent beams rather than the actual building is not the focus of this chapter.

In the following sections, unless otherwise stated, results are based on analyses where both S_h and S_v were applied together to investigate the effect of building stiffness on ground displacements caused by tunnelling.

7.5 Comparison of Mixed E–N with Numerical Results

Results presented in this section are based on three cases of tunnel location: $e/L_{bldg} = 0$, 0.5 and 0.75. Results relate to cases with $C_t/D_t = 2.4$ with $V_{ls,surf}$ = 1.55% or $C_t/D_t = 4.4$ with $V_{ls,surf}$ = 2.77%.

7.5.1 Bending modification factors for $e/L_{bldg} = 0$

Figure 7.12 presents bending modification factors from conventional numerical and mixed E–N analyses for $e/L_{bldg} = 0$, 0.5 and 0.75 and for two tunnel depths corresponding to $C_t/D_t = 2.4$ and 4.4. For the case of $e/L_{bldg} = 0$ when $C_t/D_t = 2.4$, Figure 7.12a shows that the bending modification factors from the mixed E–N method are generally lower than those from the conventional numerical analysis. The difference is small for low values of relative bending stiffness and increases as the relative bending stiffness increases.

The results in Figure 7.12a indicate that ground displacements due to tunnelling have less of an effect on buildings based on the mixed E–N method compared to the conventional numerical analyses; i.e. buildings in the mixed E–N method have a greater relative structure-soil stiffness and are less affected by ground displacements compared to the conventional numerical analyses. The reason for this relates to the relative position and extent of the building in relation to the extent of the greenfield settlement trough, which is depicted in

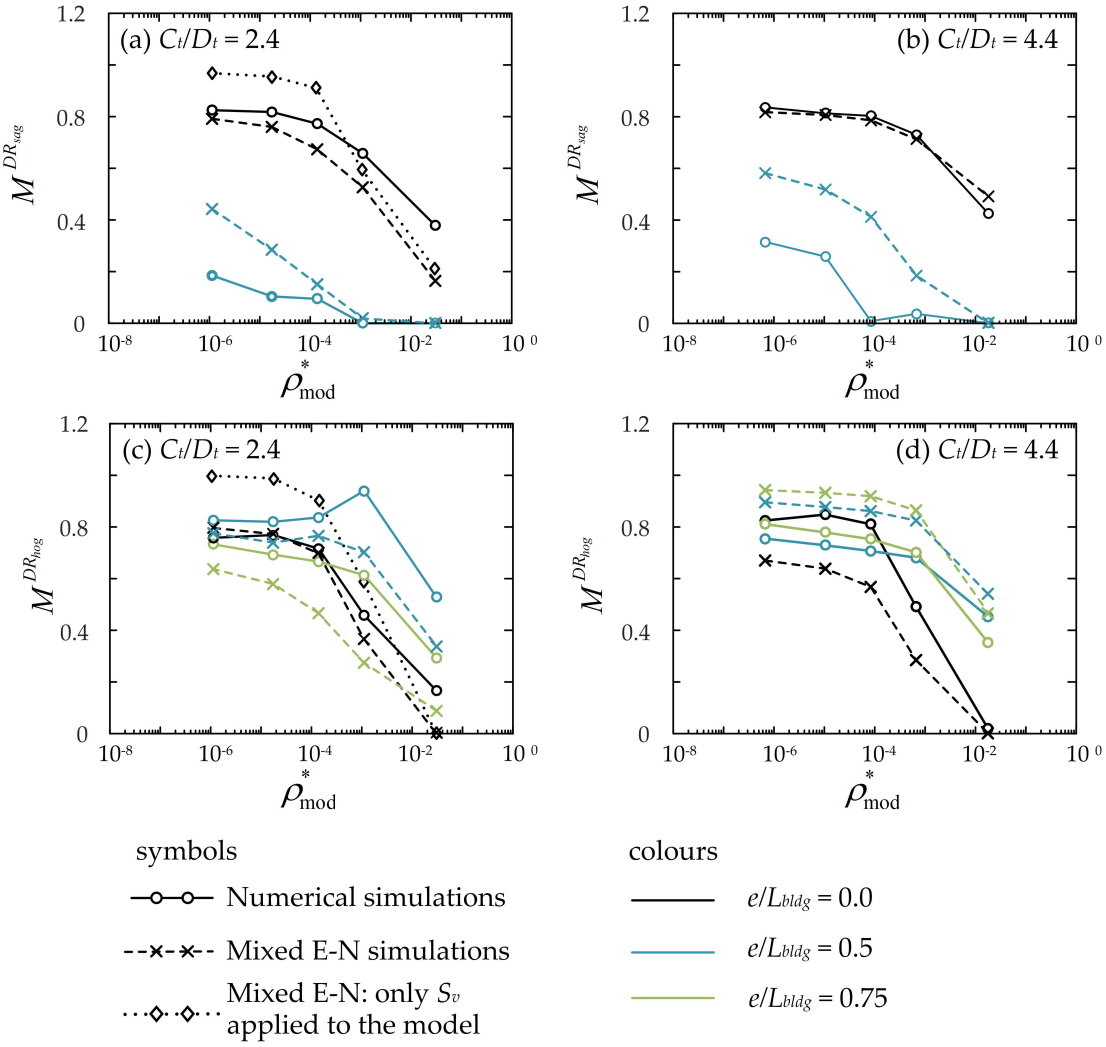

Fig. 7.12 Comparison of bending modification factors between conventional numerical and mixed E–N methods for $V_{ls,surf} = 1.55\%$ and 2.77% for C_t/D_t =2.4 and 4.4, respectively

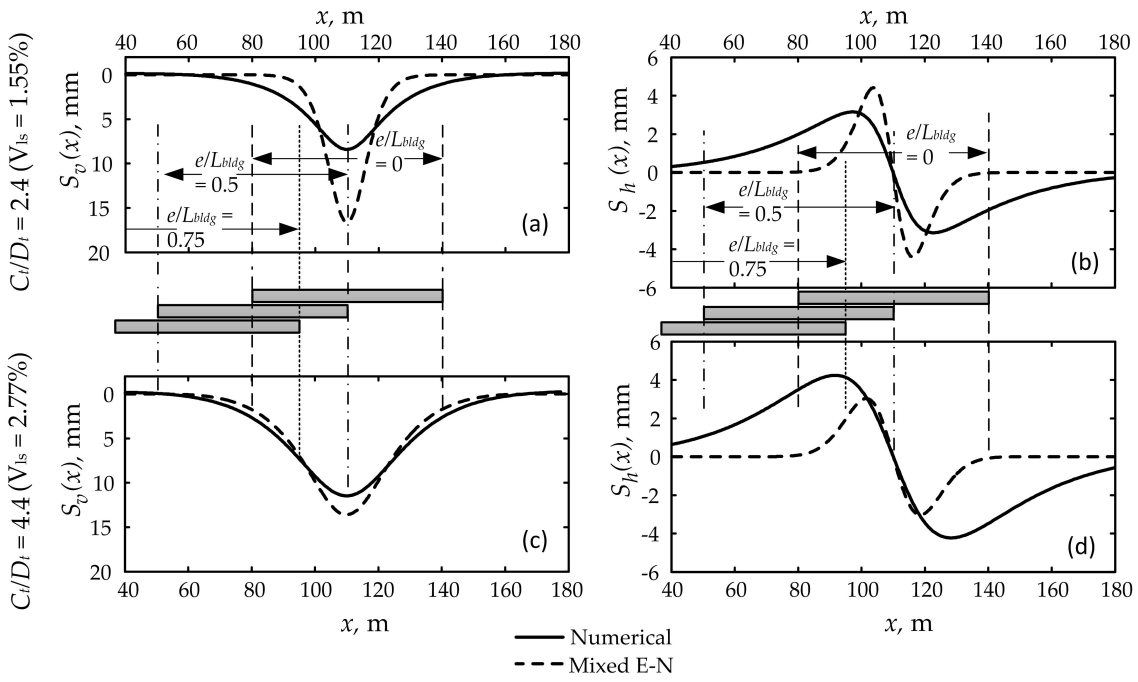

Fig. 7.13 Tunnelling induced surface greenfield movements predicted by conventional numerical and mixed $E-N$ methods

Figure 7.13a. The building with $e/L_{bldg} = 0$ extends a considerable distance past the extent of the mixed E–N greenfield settlement trough, whereas it is inside the greenfield settlement trough for the conventional numerical model. The section of the building located outside the affected soil zone in the mixed E–N analysis provides support to the section of the building affected by soil displacements (like a fixed end support that prevents rotation at the location where the building first becomes affected by ground movements), thereby increasing the building's resistance to deformation. This feature is not explicitly captured by the relative stiffness equations proposed by Potts and Addenbrooke (1997) and Franzius et al. (2006).

Figure 7.13b illustrates that greenfield horizontal movements in the conventional numerical analyses are greater over a wider area compared to the mixed E–N analyses (for $e/L_{bldg} = 0$). The effect of the resulting compression applied to the building, which contributes to the resistance of the building against bending, is therefore more pronounced in the conventional numerical analyses compared to the mixed E–N analyses. The horizontal displacements outside the building area in the conventional numerical analyses (which do not exist in the mixed E–N analyses) also increase the building resistance against bending deformations.

To demonstrate how horizontal displacements influence the value of bending modification factors, mixed E–N simulations were performed where only vertical displacements were included for the case $C_t/D_t = 2.4$, as shown in Figures 7.12a and c. The data show that exclusion of horizontal displacements (only S_v) results in larger values of M^{DR} (greater deformation of the building) compared to the case where both S_h and S_v were applied. The additional deformation of the building was also demonstrated in Figures 7.11a and b where excluding S_h effectively removed a component of upwards beam deflection. Note that the effects of horizontal displacements on building deformations were also reported by Potts and Addenbrooke (1997) in their numerical analyses and Farrell et al. (2014) based on geotechnical centrifuge tests.

In the work of Potts and Addenbrooke (1997), the existence of a building with a very low bending stiffness led to an increase in the vertical ground displacements. The reason for this was related to the action of horizontal movements which applied a compression to the building. This action of horizontal movements was restricted by the building axial stiffness and due to having a very low bending stiffness, an increase of vertical settlements happened.

In the work of Farrell et al. (2014), four buildings were modelled using aluminium plates of low to high stiffness in the centrifuge. They declared that the existence of the very flexible buildings resulted in distortions larger than the greenfield values. They related this effect to the action of horizontal shear stresses at the base of the building which led to an increase of curvature.

For the case of $C_t/D_t = 4.4$ and $e/L_{bldg} = 0$, the values of $M^{DR_{sag}}$ computed from both conventional numerical and mixed E–N analyses are very similar, as shown in Figure 7.12b. This indicates similar building effects on ground displacements despite the slightly narrower settlement trough in the mixed E–N analyses, as displayed in Figure 7.13c. This is mainly due to the existence of large horizontal displacements beneath and adjacent to the building in the conventional numerical analyses (Figure 7.13d), which counteract the reduction of relative bending stiffness caused by the wider settlement trough.

In terms of $M^{DR_{hog}}$ for $e/L_{bldg} = 0$, the mixed E–N analysis outcomes are generally lower than those from the numerical simulations. The difference is relatively small for the case of $C_t/D_t = 2.4$ (Figure 7.12c) but more pronounced for $C_t/D_t = 4.4$ (Figure 7.12d). This again illustrates that buildings in the mixed E–N analyses showed greater relative structure-soil bending stiffness than in the conventional numerical analyses. This is because the narrower settlement trough in the mixed E–N analyses has a proportionally higher impact (increase) on the resulting relative stiffness than the effect of the difference in horizontal displacements between the two analyses for the case of $e/L_{bldg} = 0$.

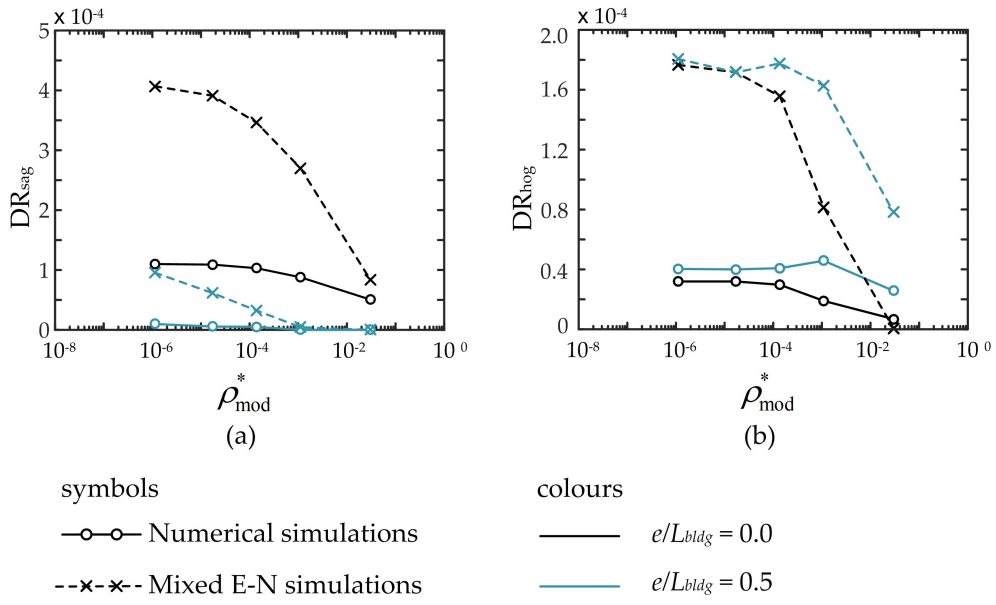

Fig. 7.14 Comparison of (a) sagging and (b) hogging deflection ratios obtained from conventional numerical and mixed E–N analyses for $C_t/D_t = 2.4$ and $V_{ls,surf} = 1.55\%$

The calculation of M^{DR} includes a normalisation against the greenfield displacements, hence it does not fully demonstrate the effect of the different greenfield settlement trough inputs within the conventional numerical and mixed E–N analyses. The level of flexural distortion of the structure estimated by the two methods varies considerably more than indicated in the M^{DR} data. For instance, Figure 7.14 shows that the deflection ratios, DR, in the sagging and hogging zones calculated with the mixed E–N analyses are notably higher than those from the conventional numerical analyses for $C_t/D_t = 2.4$, especially at low values of relative bending stiffness. The same observation applies for the case of $e/L_{bldg} = 0.5$. The potential for building damage is proportional to deflection ratio (Mair et al., 1996) rather than modification factor, hence these results illustrate the importance of correctly estimating and incorporating greenfield ground displacements within preliminary risk assessments and numerical analyses.

The use of the normalisation against the greenfield displacements seems to show a greater degree of building distortions for curves of small curvature. Based on the distortions caused to the settlements curves, Figure 7.15a shows a significant effect of a 1 m thick beam on surface displacements when $C_t/D_t = 2.4$ which is greater than the effect of the same building when $C_t/D_t = 4.4$ (Figure 7.15b). However, due to the location of the building on the settlement curve, the parameter $M^{DR_{hog}}$ shows a smaller degree of displacement effects on

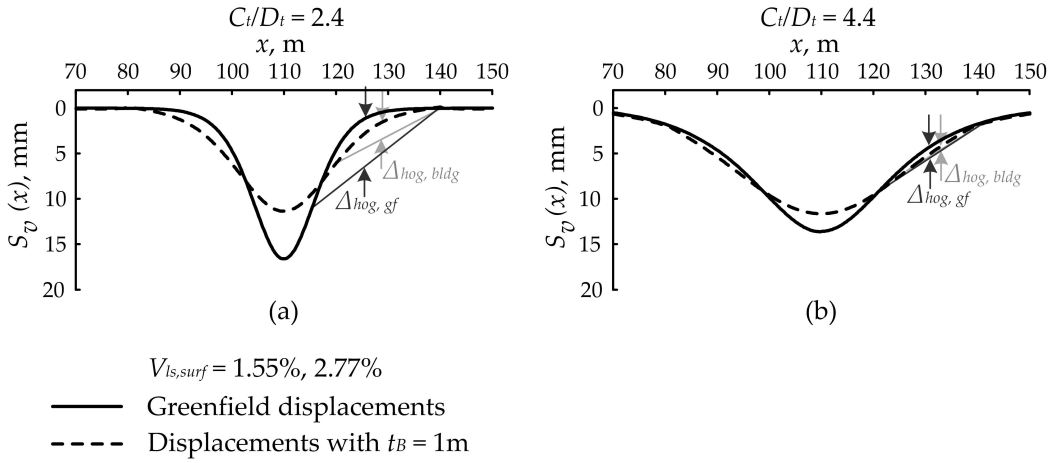

Fig. 7.15 Effect of a 1 m building on vertical ground surface displacements in the mixed E–N methods for $C_t/D_t = 2.4$ and 4.4

the building in the case of $C_t/D_t = 4.4$. To better imagine the effect of ground displacements on the building, a simple comparison of the deflection ratios can help. When $C_t/D_t = 2.4$, the greenfield deflection ratio was 22.2×10^{-5}. The addition of a 1 m thick beam reduced this deflection ratio to 8.16×10^{-5}. This gave an $M^{DR_{hog}}$ of 0.368. When $C_t/D_t = 4.4$, the greenfield deflection ratio was 5.81×10^{-5}. The addition of a 1 m thick beam reduced this deflection ratio to 1.66×10^{-5}. This gave an $M^{DR_{hog}}$ of 0.286. The distortions occurred to the surface settlement curve in Figures 7.15a and b indicate that the building in the case of $C_t/D_t = 2.4$ showed a greater stiffness than that of $C_t/D_t = 4.4$ but this is not shown by the ρ^*_{mod}–M^{DR} curves due to the consideration of a ratio between the greenfield situation and its corresponding case where the building exists.

7.5.2 Bending modification factors for $e/L_{bldg} > 0$

For the cases where the tunnel was not located under the building centreline ($e/L_{bldg} = 0.5$ and 0.75), it is important to describe the effects of the rotational constraint provided by the soil outside the tunnel influence area, where settlements are low. Figure 7.16 illustrates how building length affects results for $e/L_{bldg} = 0.5$ and $C_t/D_t = 2.4$. Two building lengths are considered: 60 m (where the building extends far outside the greenfield displacement profile), and 30 m (where most of the building is affected by greenfield displacements).

The portion of the 60 m building outside the displacement zone provides a degree of constraint to the deformed part of the building, which reduces rotation (i.e. tilting of entire building) but results in greater distortion (i.e. bending strains) compared to the 30 m building,

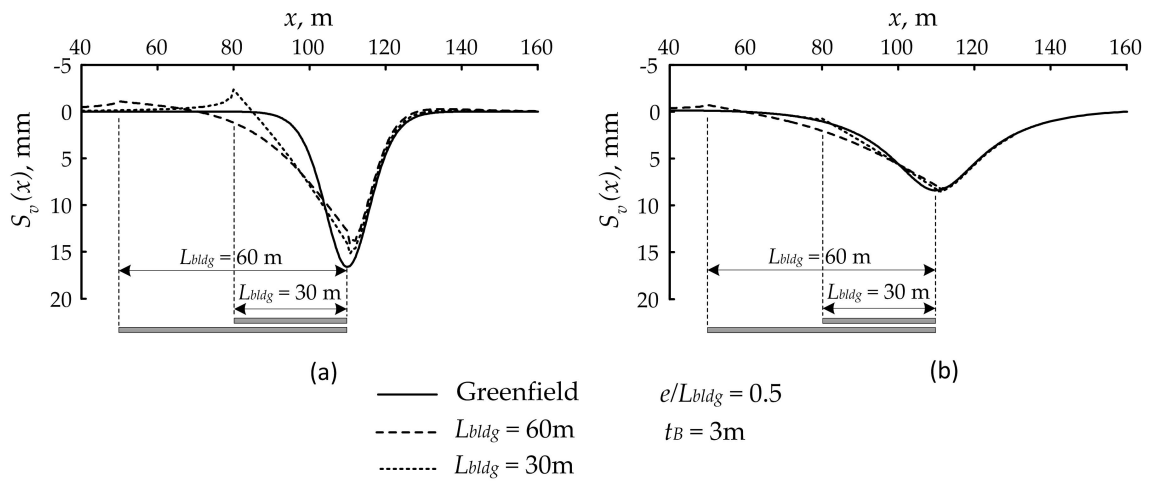

Fig. 7.16 Effect of building length on ground displacements due to tunnelling for $C_t/D_t = 2.4$: (a) mixed $E-N$ and (b) conventional numerical analyses

which undergoes significant rotation but little distortion. The resistance of a building to rotation is important when considering its response to ground displacements; as building length increases outside the displaced soil zone, so does its ability to resist rotation. Note that for the symmetric case where $e/L_{bldg} = 0$, rotation is not permitted and therefore the building bending stiffness is relatively high. Currently available methods for evaluating relative stiffness do not account for the effect of building length in relation to the displaced soil zone.

On the other hand, Figure 7.16 shows that the modification caused to the ground displacements by the existence of the building is greater in the mixed E–N method than the conventional numerical analysis. This is also because a larger part of the building in the mixed E–N method is located outside the displaced zone due to a narrower trough width.

For $e/L_{bldg} = 0.5$ and 0.75, Figure 7.12a and b show that values of $M^{DR_{sag}}$ from the mixed E–N method for $C_t/D_t = 2.4$ and 4.4 are higher than those from the conventional numerical analyses. Values of $M^{DR_{sag}}$ indicate stiffer buildings (relative to the soil) in the conventional numerical analyses because of the action of the large horizontal displacements in the conventional numerical analyses, which causes a significant increase to the building's resistance to bending deformations.

The values of $M^{DR_{hog}}$ from the mixed E–N analyses are generally lower than those from the conventional numerical analyses for $e/L_{bldg} = 0.5$, 0.75 and $C_t/D_t = 2.4$, especially for higher values of relative bending stiffness, as shown in Figure 7.12c. There is an interesting transition point observable in Figure 7.12c for the conventional numerical analysis results at

about $\rho^*_{mod} \geq 1.1 \times 10^{-3}$, where hogging occurs in the entire building length (corresponding to the point where $M^{DR_{sag}} = 0$ in Figure 7.12a), resulting in a marked increase of $M^{DR_{hog}}$.

A different trend of $M^{DR_{hog}}$ is obtained for $C_t/D_t = 4.4$ (Figure 7.12d), where values from the mixed E–N analyses are higher than the conventional numerical analyses. Since vertical greenfield displacements from both methods are similar (see Figure 7.13c), the greater ability of the conventional numerical analysis buildings to resist hogging zone distortions (i.e. lower values of $M^{DR_{hog}}$) must be due to the effect of the larger magnitude and wider profile of the greenfield horizontal displacements in the conventional numerical analyses.

7.5.3 Axial modification factors

Figure 7.17 presents the axial modification factors from the conventional numerical and mixed E–N analyses for $e/L_{bldg} = 0$, 0.5 and 0.75, and $C_t/D_t = 2.4$, 4.4. Figures 7.17a and b present the compressive strain modification factors, $M^{\varepsilon_{hc}}$; Figures 7.17c and d give the tensile modification factors, $M^{\varepsilon_{ht}}$. For $e/L_{bldg} = 0$, the data show that the conventional numerical analysis results for $M^{\varepsilon_{hc}}$ are larger than those of the mixed E–N analyses, whereas $M^{\varepsilon_{ht}}$ values are smaller (for both $C_t/D_t = 2.4$ and 4.4). The difference in modification factors between the conventional numerical and mixed E–N analyses decreases with the increase in relative axial stiffness factor.

To help understand the different axial responses from the two methods, it is important to note that the greenfield soil is in compression horizontally within the zone bounded by the peak values of S_h, and in tension outside this region. As shown in Figure 7.13b and d, for structures with $e/L_{bldg} = 0$, the greenfield displacement profile from the conventional numerical analysis encompasses the entire building. The effect is that the building is completely in compression and values of $M^{\varepsilon_{hc}}$ are greater for the conventional numerical analysis than the mixed E–N method (Figure 7.17a, b). In the mixed E–N method, peak horizontal displacements are closer to the tunnel centreline and the structure is subjected to both tensile and compressive forces from the soil. This produces values of $M^{\varepsilon_{ht}}$ (tension) from the mixed E–N method that are greater than zero for the considered configurations (Figure 7.17c, d). Franzius et al. (2006) also obtained no tensile strains in the building in their numerical analyses for the non-eccentric structures.

For the case of $e/L_{bldg} > 0$, Figure 7.17 shows that both $M^{\varepsilon_{hc}}$ and $M^{\varepsilon_{ht}}$ from the conventional numerical analyses are larger than those from the mixed E–N analyses for both $C_t/D_t = 2.4$ and 4.4. The high values of axial modification factors from the conventional numerical analyses is mainly related to the effect of the proportion of the building located

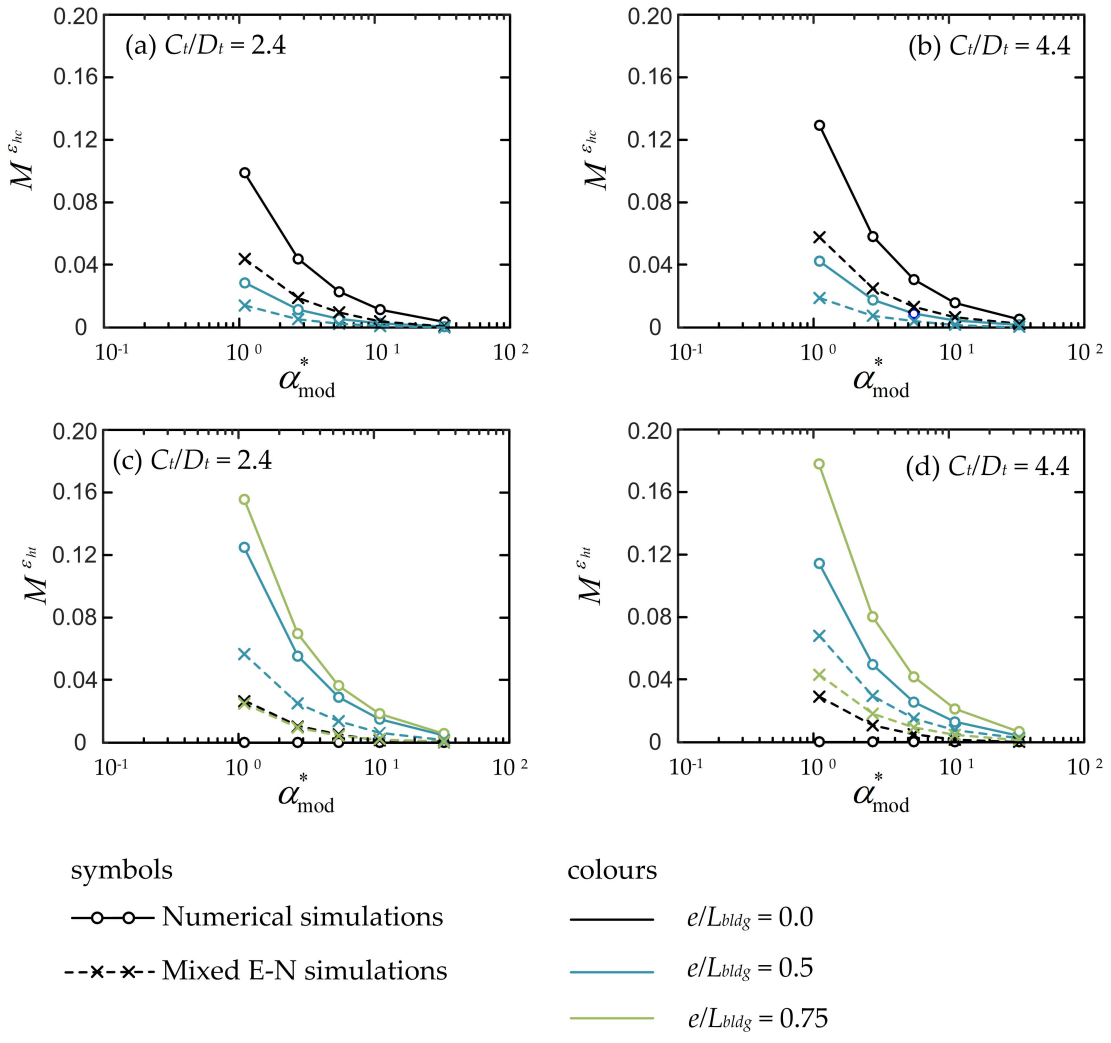

Fig. 7.17 Comparison of axial modification factors between conventional numerical and mixed E–N methods for $C_t/D_t = 2.4$ ($V_{ls,surf} = 1.55\%$) and $C_t/D_t = 4.4$ ($V_{ls,surf} = 2.77\%$)

inside the displaced soil zone, which as a result experiences more axial distortion from horizontal ground displacements than buildings in the mixed E–N analyses where the horizontal displacement profile is narrower (see Figure 7.13). It should be noted that the influence of building length on induced horizontal strains in the building was also mentioned by Franzius et al. (2006). After numerically testing buildings with different lengths, they concluded that the effect of building length on induced horizontal strains in the building was greater than its effect on the deflection ratios.

7.6 Effect of Volume Loss on the Tunnel–Building Interaction

The results showed a very small effect of varying volume loss on the bending and axial modification factors. For the purpose of investigation, the cases of $e/L_{bldg} = 0.0$ (where the building rotation is not allowed) and $e/L_{bldg} = 0.75$ (where building rotation is allowed) are considered for a tunnel depth corresponding to $C_t/D_t = 2.4$. Estimated values of $M^{DR_{sag}}$ and $M^{DR_{hog}}$ for $e/L_{bldg} = 0.0$, $C_t/D_t = 2.4$ and three different values of greenfield surface volume loss are presented in Figure 7.18. It should be mentioned that the comparison between the results of the conventional numerical and mixed E–N methods is not the aim of this section; the results of each method for different values of volume loss are discussed independently.

Figures 7.18a and b display bending modification factors of the sagging zone for the mixed E–N and conventional numerical analyses, respectively, for the case where $e/L_{bldg} = 0.0$ (there is no sagging zone in the case $e/L_{bldg} = 0.75$). It is shown that the difference between the results of various greenfield surface volume losses in each analysis case is not considerable. For $\rho^*_{mod} = 1.11 \times 10^{-3}$ in the mixed E–N results, there is slightly more distortion to the building with $V_{ls,surf} = 1.55\%$ compared to the other volume loss cases (Figure 7.18a). For the relatively low stiffness buildings in the conventional numerical case, there is a slight increase of building distortions due to ground displacements with the increase of the surface volume loss (Figure 7.18b).

The reason for having a negligible effect of changing volume loss on the modification factors is that the results of bending and axial modification factors are ratios between the greenfield situation and its corresponding case where the building is present. The changes happening in the presence of a building are proportional to those of the greenfield situation. This can result because the trough width and the inflection points of settlement curves in each method (conventional numerical and mixed E–N) do not vary significantly with the

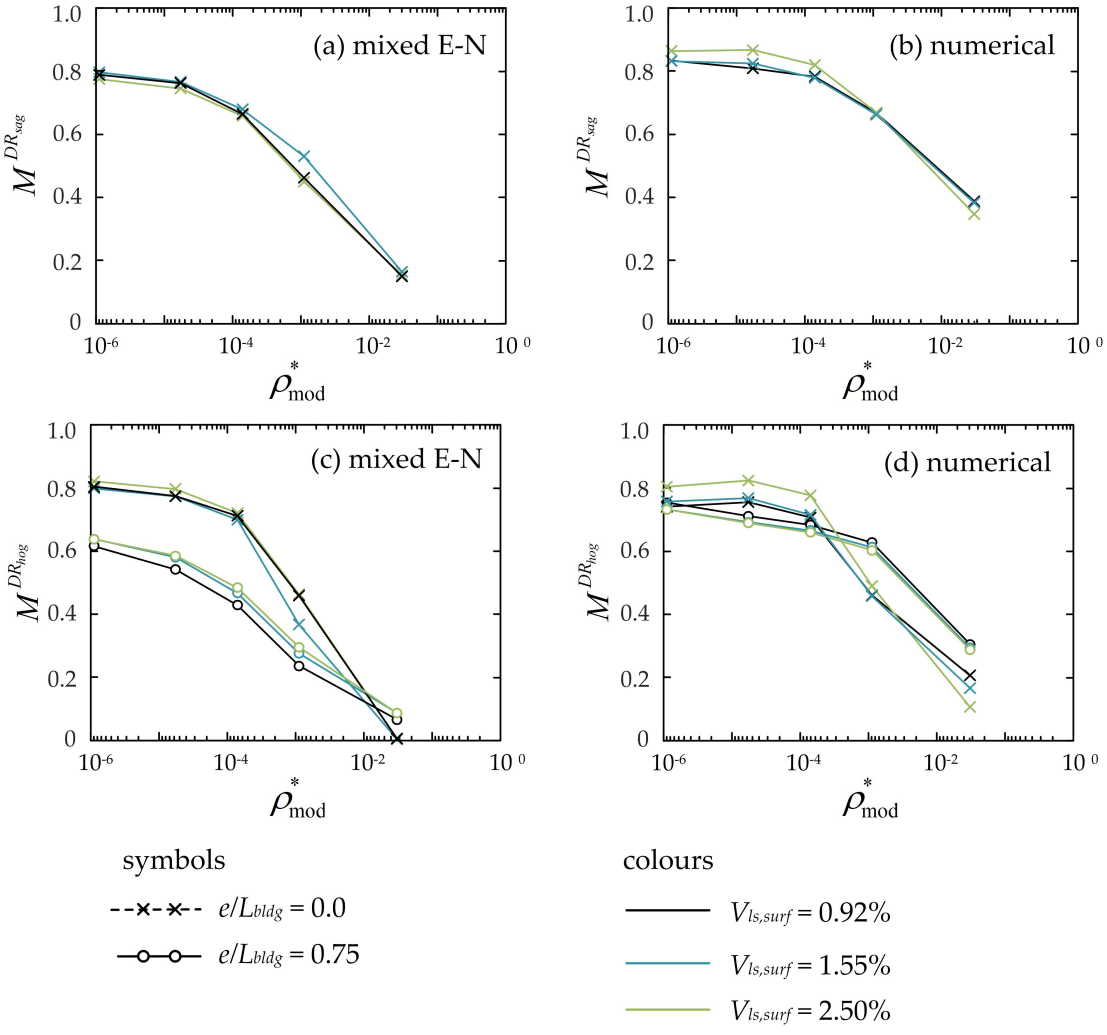

Fig. 7.18 Bending modification factors obtained from conventional numerical and mixed E–N modelling for different values of surface volume loss for $C_t/D_t = 2.4$

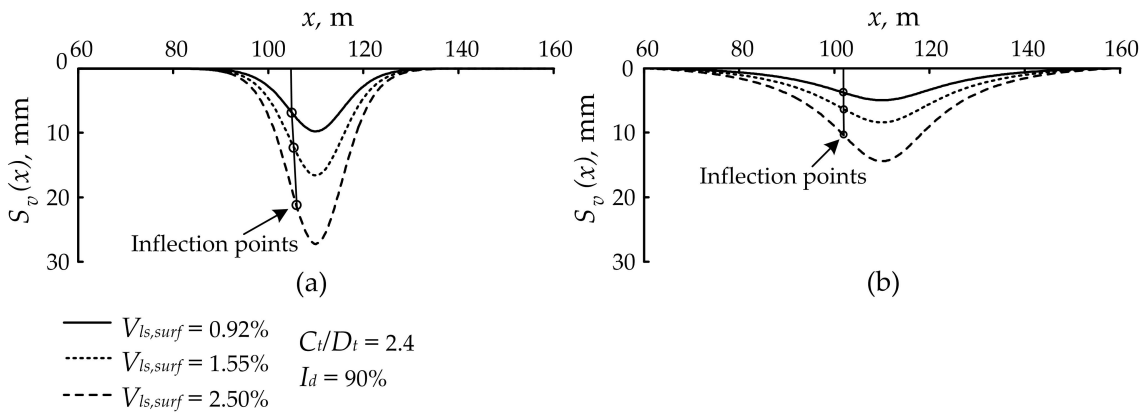

Fig. 7.19 Surface settlement curves for different surface volume losses predicted by (a) mixed E–N and (b) numerical simulations

change of volume loss. Figure 7.19a shows the ground surface settlement for three surface volume losses (0.92%, 1.55% and 2.50%), and illustrates that there is a negligible difference between the position of the inflection points of each volume loss case. It also exhibits that the width of the settlement troughs does not vary considerably. Therefore, the building in all three cases is similar in terms of the building length located in the displaced soil zone and the parameters affecting the building rotation, such as the building part located in the undisplaced soil zone. The small difference between the volume loss cases is due to a small change in the width of sagging and hogging parts of the settlement curve with the change of volume loss.

Figures 7.18c and d present the results of bending modification factors of the hogging zone for the mixed E–N and conventional numerical analyses, respectively, and for both cases of $e/L_{bldg} = 0.0$ and 0.75. For the mixed E–N analysis results (Figure 7.18c), the results of the hogging zone in the case $e/L_{bldg} = 0.0$ are very similar except a slightly less distortion of the building case of $\rho^*_{mod} = 1.11 \times 10^{-3}$ for $V_{ls,surf} = 1.55\%$ compared to the other cases. With regard to the case $e/L_{bldg} = 0.75$, the buildings where $V_{ls,surf} = 0.92\%$ are generally less distorted by ground displacements compared to the other cases. This is likely due to the slightly narrower settlement trough when $V_{ls,surf} = 0.92\%$ (Figure 7.19). Regarding the conventional numerical analysis results (Figure 7.18d), the data show similarities between the results of different volume loss cases except for the case $e/L_{bldg} = 0.0$ and $V_{ls,surf} = 2.50\%$ in which relatively flexible buildings are more distorted than those of other volume loss cases. It is worth noting that slightly more distortion also occurred to the relatively flexible buildings where $e/L_{bldg} = 0.0$ and $V_{ls,surf} = 2.50\%$ in the sagging zone (Figure 7.18b). In both cases,

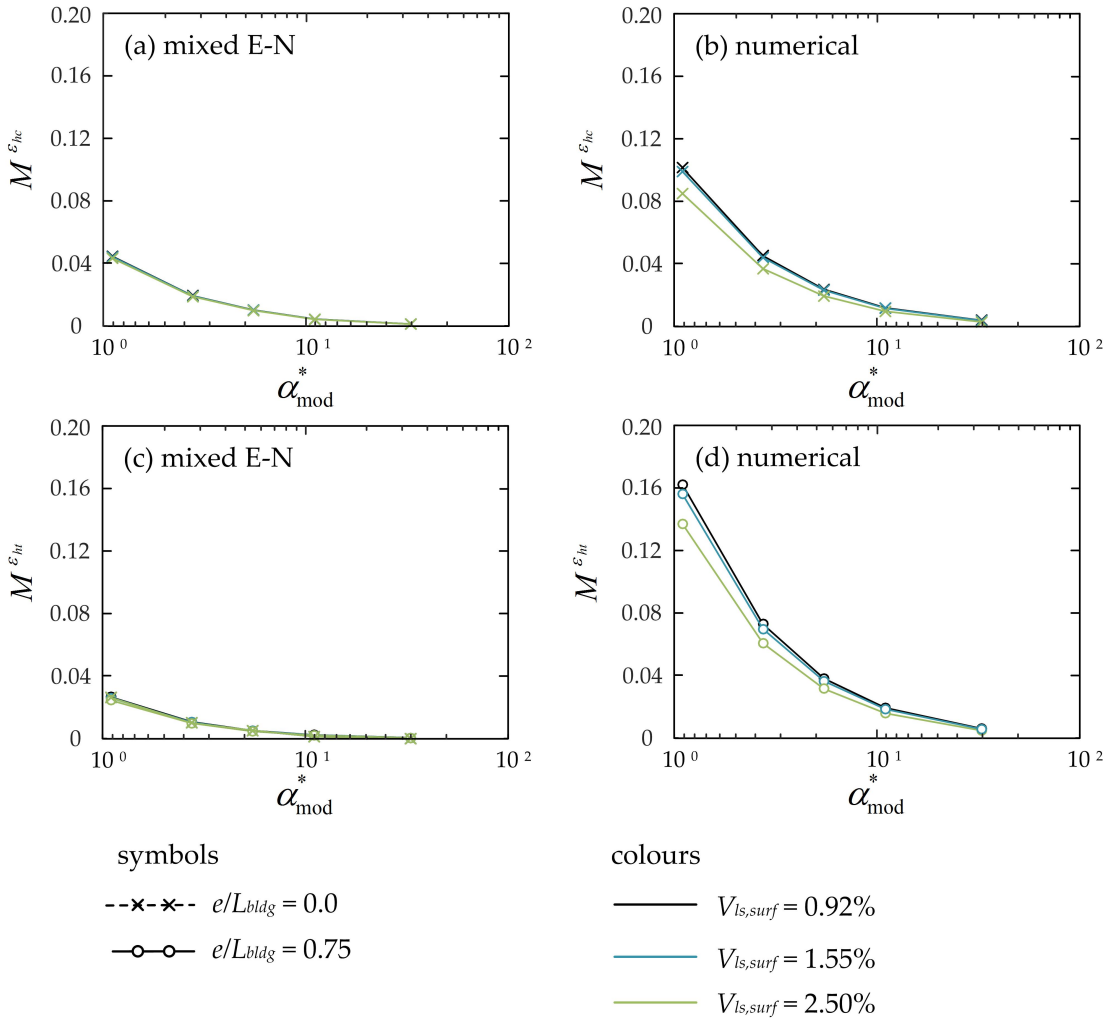

Fig. 7.20 Axial modification factors obtained from conventional numerical and mixed E–N modelling for different values of greenfield surface volume loss

the stiff building with $\rho^*_{mod} = 3 \times 10^{-2}$ experiences less distortion compared to the building of the other volume loss cases in the conventional numerical simulations. Furthermore, a similar trend of having a slightly greater effect of ground displacements on less stiff buildings and smaller effect on stiff buildings is obtained for the cases of $V_{ls,surf} = 0.92\%$ and 1.55%. This effect would appear to be due to the plastic behaviour of the soil in the conventional numerical models. The increase of building bending stiffness reduces the curvature of the settlement curve in all volume loss cases, but the amount of this reduction is greater for the settlement curves of larger volume losses.

With regard to the axial modification factors, there is no effect of volume loss change on $M^{\varepsilon_{hc}}$ of the mixed E–N analysis for $e/L_{bldg} = 0$ (Figure 7.20a), whereas the building of

the case $V_{ls,surf} = 2.50\%$ in the conventional numerical simulation results experienced less axial distortions compared to the other cases, as shown in (Figures 7.20b) for $e/L_{bldg} = 0$. Similarly, there is no effect of the volume loss change on $M^{\varepsilon_{ht}}$ for both cases of $e/L_{bldg} = 0$ and 0.75 in the mixed E–N simulation results (Figure 7.20c). However, the building of the case $V_{ls,surf} = 2.50\%$ in the conventional numerical simulation results underwent less axial distortions, as shown in Figure 7.20d for $e/L_{bldg} = 0.75$ (there was no induced tensile strains in the building for the case $e/L_{bldg} = 0$).

The reason for having similar results in the elastic mixed E–N analyses is that any change that happens to the greenfield situation of each analysis case with different surface volume losses is proportional to that of its corresponding case in the presence of a building. With regard to the difference between the results of the building in the case $V_{ls,surf} = 2.50\%$ with that of the other cases in the conventional numerical analyses, it should be mentioned that larger horizontal strains were created in the building during high volume losses, but the rate of increase of horizontal strains in the greenfield case was more than that induced in the building. For instance, in the case of having a beam with 0.50 m thickness, the maximum greenfield horizontal compressive strain produced from 0.92%, 1.55% and 2.50% surface volume losses were 2.65×10^{-4}, 4.46×10^{-4} and 7.64×10^{-4}, respectively, while the maximum compressive strain induced in the building at each case was 0.63×10^{-5}, 1.03×10^{-5} and 1.49×10^{-5}, respectively. The values show that larger strains were induced in the building in the case of high volume losses, however, the ratio of horizontal compressive strains at each case gives axial modification factors of 2.38×10^{-2}, 2.31×10^{-2} and 1.95×10^{-2} which show an opposite trend from that of the horizontal strain values induced in the building.

7.7 Effect of Soil Relative Density on the Tunnel–Building Interaction

A change in the soil relative density leads to a change in the soil behaviour. For a constant tunnel volume loss, the induced displacements due to tunnelling in a soil with a low relative density are larger than those in a soil with a high relative density. In addition, the trough width of the settlement curve is wider in a soil with a low relative density due to creating higher ground losses. If settlement troughs are normalised by the maximum settlement for different cases of relative density, the normalised trough of looser soils will be narrower (Zhou et al., 2014). This large settlement of soils with low relative density is more obvious for soils with relative densities under 60% (Coelho et al., 2006).

A low relative density causes contraction to the soil during tunnelling while a high relative density results in soil dilation. The terms 'contraction' and 'dilation' are related to the volume changes that occur in the soil because of shear strains (Poulos, 1971). This behaviour is due to the interlocking of soil particles during shearing. For a dense soil, particles are not sufficiently free to move around one another. Therefore, a dilation of the soil occurs when these particles are subjected to motion. In a loose soil, the existing voids in the soil mass allow the particles to move sufficiently freely around one another and to fill the gaps between them which in turn leads to a contraction of the soil (Cox, 2008; Houlsby, 1991).

The investigation of this characteristic of soil (volume change) is difficult using conventional numerical analyses because of the variation of soil volume loss with depth, however, the mixed E–N method can be used to investigate this aspect, with some limitations. Strength parameters of the soil, such as friction angle and dilation angle, and cohesion, cannot be included in the analysis. Furthermore, the elastic modulus of the soil should be estimated accurately to achieve realistic results.

Figures 7.21a and b show surface vertical and horizontal displacements, respectively, created in a soil with relative densities of 90% and 30%. As shown in Table 7.2, the achieved surface volume loss for a tunnel volume loss of 1.76% was 1.55% for $I_d = 90\%$ and 4.12% for $I_d = 30\%$. It is shown that a larger ground area in the soil of low relative density is displaced compared to the case of high relative density for the same tunnel volume loss. This can significantly affect the behaviour of the building. In an elastic analysis, smaller displacements are applied to the soil in the case of having a high relative density while greater displacements are applied to the model in the case of low relative density. However, the magnitude of the nodal reaction forces induced in the case of the higher relative density is relatively larger than that of the low relative density since the elastic modulus of a loose soil is smaller than that of a dense soil. In terms of building location relative to the displaced soil, the building shows a larger bending stiffness when the soil has a high relative density because less soil beneath the building experiences deformations which in turn, provides a better support to the building. Apart from the effect of the tunnel–building relative location and the magnitude of soil elastic modulus, centrifuge tests performed by Farrell et al. (2014) showed that the increase of volume loss resulted in a gradual decrease of soil stiffness and an increase in the building relative stiffness. The effects related to the soil elastic modulus are not shown in this section since the value of the soil elastic modulus was kept constant throughout the soil depth for all cases of different relative densities.

To visualise the influence of the soil elastic modulus on the tunnel-building interaction, a comparison was made between two models having the same soil relative density of 30% but

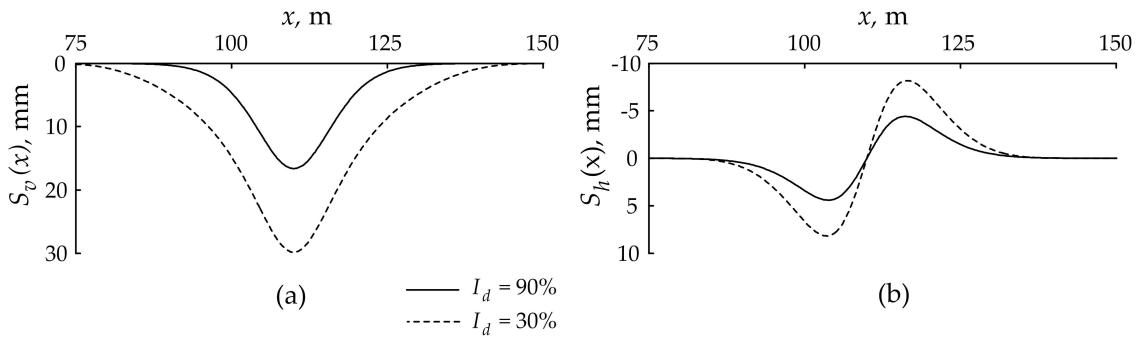

Fig. 7.21 Comparison of greenfield (a) vertical and (b) horizontal surface displacements for soil relative densities of 90% and 30%, $C_t/D_t = 2.40$ and $V_{lt} = 1.76\%$

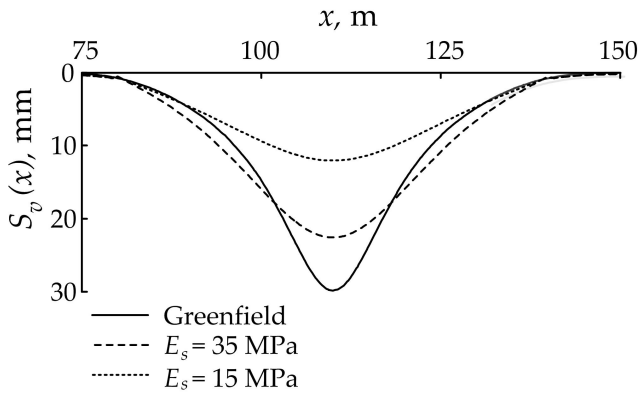

Fig. 7.22 Comparison of vertical surface displacements for a soil with a relative density of 30%, $C_t/D_t = 2.4$ and in the presence of a building with 1 m height

different elastic moduli of 15 MPa and 35 MPa in the presence of a building. Figure 7.22 shows the effect of a model building with 1 m thickness on ground displacements due to tunnelling for the mentioned soil types with $C_t/D_t = 2.4$. It is illustrated that the surface settlement of the soil with a low elastic modulus is considerably reduced by the effect of the building and there is a negligible distortion to the surface settlement trough width. For a higher elastic modulus, the effect of the building on ground displacements decreases significantly in addition to an increase in the settlement trough width. This is due to applying larger forces from the soil to the building when having greater soil elastic modulus.

For a constant value of E_s throughout the soil depth, Figure 7.23a shows the values of $M^{DR_{sag}}$ for tunnel locations corresponding to $e/L_{bldg} = 0$ and 0.5, and $I_d = 90\%$ and 30%. For $e/L_{bldg} = 0$, there is a greater effect of ground displacements on low stiffness buildings in the sagging zone for the relative density of 90%. Stiffer buildings change this

trend and are less affected by ground displacements from soils of high relative density. For $e/L_{bldg} = 0.5$, Figure 7.23a illustrates that buildings in the case $I_d = 90\%$ are affected by ground displacements to a greater extent than that of the case $I_d = 30\%$ for all values of relative bending stiffness.

For the hogging part of the settlement curve, as shown in Figure 7.23b, the effect of ground displacements on flexible buildings is greater in the case $I_d = 90\%$ compared to the case $I_d = 30\%$ when $e/L_{bldg} = 0$. For eccentric cases, buildings of the case $I_d = 30\%$ are more distorted than those of the case $I_d = 90\%$. In these cases, a considerable part of the building in the case of $I_d = 90\%$ is located inside the undisplaced soil zone and provides an effective support to the building against rotation. This is because the predicted settlement trough is narrower compared to that of $I_d = 30\%$. It should be noted that since the parameter E_s is constant throughout the soil depth, the differences obtained between different cases of soil relative density are mainly related to the width of the predicted settlement trough, relative position of the building and the tunnel, and the effect of horizontal displacements. The effect of these parameters are explained in detail in Section 7.5.

With regard to the axial modification factors, as shown in Figure 7.23c,d, no practical effect of the soil relative density on the compressive and tensile modification factors is achieved. The changes that occur in the greenfield situation of different I_d cases are proportional to the changes that occur in their corresponding situations when a building is present.

7.8 Summary

A mixed empirical-numerical (mixed E–N) method was presented in this chapter to predict the response of buildings to realistic inputs of tunnelling induced ground movements. A modified semi-analytical method was used to obtain the greenfield displacements, however any input could be incorporated into the methodology. The input greenfield displacements were based on centrifuge test data and included both horizontal and vertical displacements. The mixed E–N method allows the application of horizontal and vertical displacements to the model either together or separately, thereby allowing a detailed evaluation of the coupling effect of the two displacements. The proposed mixed E–N method eliminates the role of material models in predicting ground displacements due to tunnelling. Dissimilar to the previously proposed methods, the mixed E–N method allows the estimation of the building effect on the whole layer of soil above the tunnel.

Results obtained from the proposed mixed E–N method were compared against conventional numerical analyses in which the tunnel was simulated, resulting in wider settlement

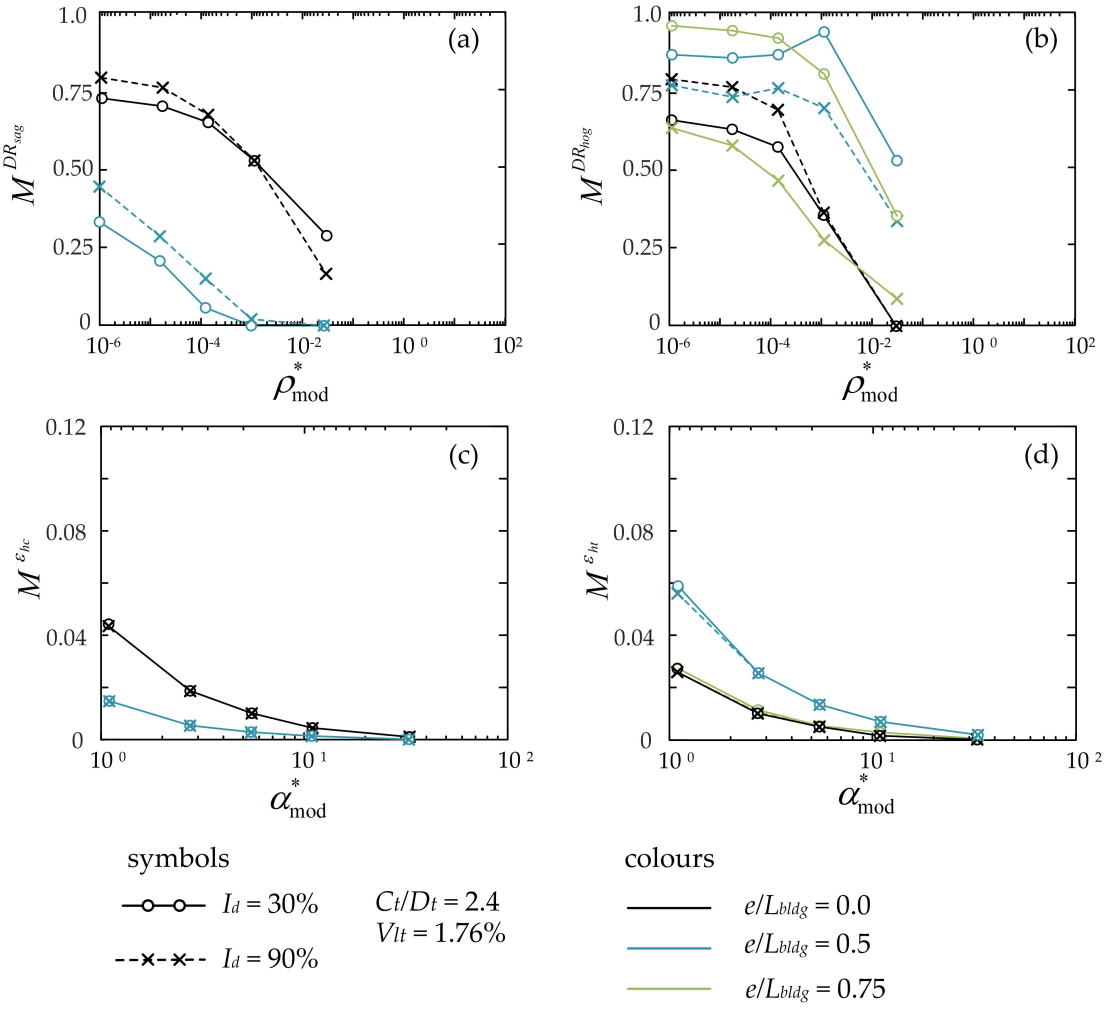

Fig. 7.23 (a)–(b) Bending and (c)–(d) axial modification factors computed for soils with relative densities of 90% and 30%

troughs and greater horizontal displacements than expected in reality. It was shown that the action of the unrealistic horizontal displacements in the conventional numerical analyses increased the resistance of the building against bending deformations quite considerably in some scenarios. In contrast, the wide settlement trough predicted in the conventional numerical analysis resulted in the reduction of the building ability to resist bending deformations. It was shown that the proposed mixed E–N method led to more realistic estimation of tunnelling effects on structures due to the input of more accurate ground movements, and predicting a narrower settlement trough.

This chapter also investigated the effect of the change of volume loss and soil relative density on the tunnel–building interaction. The variation of the volume loss did not have an effect on the bending and axial modification factors since the changes that occurred in the greenfield situations were proportional to their corresponding cases in the presence of a building.

With regard to the effect of relative density, mixed E–N results showed that building behaviour changed considerably with the change of the relative density. For the same value of tunnel volume loss, a soil with a low relative density experienced larger settlements and wider trough widths than a soil with a high relative density. Furthermore, the effect of ground displacements on the building was dependent on the tunnel–building relative distance, the geometry of the settlement curve and the extent of the building in the displaced and undisplaced soil zones.

It is worth noting that the dilation/contradiction that occurs in sands has a significant effect on the ground displacements induced by tunnelling. Conventional numerical methods are not sufficiently capable of capturing this property during tunnelling. The proposed mixed E–N method is an efficient tool to investigate the effect of dilation/contraction of the soil on the tunnel–building interaction analysis, however an accurate estimation of the soil elastic modulus is necessary to obtain good results. Moreover, soil strength parameters cannot be included in the simulations since the method is purely for elastic analysis.

Chapter 8

Effect of Concrete Framed Buildings on Tunnelling Induced Ground Movements

8.1 Introduction

It was explained in Section 3.7 that in the majority of the literature, buildings have been considered as a single entity to estimate their bending stiffness, and the individual contribution of the foundation and the superstructure to the global building stiffness is not considered. The stiffness contribution of each storey to the global superstructure bending stiffness was explained in Chapter 5. It was shown that the stiffness contribution of each building storey changes with its distance from the foundation. In this chapter, the soil and 3D buildings, consisting of the foundation and the superstructure, are modelled together to investigate how the foundation and the superstructure of a 3D building behave when subjected to tunnelling induced ground displacements. The degree of the stiffness contribution of the foundation and the superstructure to the resistance capacity of the global building in a full soil-structure domain will be investigated.

This chapter consists of three main sections. The first section deals with the behaviour of a weightless building (foundation and superstructure) when subjected to tunnelling. The second section studies the effect of the building weight on ground displacements due to tunnelling. The third section proposes an equivalent method to replace a 3D weightless building with a 2D beam in the numerical analyses.

It is worth noting that the conventional numerical analysis is used for the simulations related to the behaviour of a 3D building (weightless and weighted) in the global soil–building system (i.e. in Sections 8.2 and 8.3). For the weighted building (Section 8.3), the conventional numerical analysis is the only option since the strength parameters of the

soil should be taken into consideration, which is not possible for the elastic mixed E–N method. The use of the conventional method for the weightless building case in Section 8.2 is because of three reasons. First, a comparison with the weighted analysis of Section 8.3 can be obtained. Second, conventional numrical methods are common techniques used by geotechnical engineers to analyse tunnel–building interaction. Third, the aim is to focus on the general behaviour of the 3D building when affected by tunnelling, rather than quantifying the interaction between the tunnel and the building.

For Section 8.4 in which an equivalent beam method is proposed, the mixed E–N method (Chapter 7) is used to model tunnelling. This choice is because of the following reasons. The method quantifies the effect of building stiffness on ground displacements (i.e. the behaviour of the building is converted to equations). Using the conventional numerical modelling leads to the prediction of minimum effects of buildings on ground displacements since a wide settlement trough is predicted, and in the majority of the modelling cases, the building is located inside the soil zone influenced by tunnelling. The use of the mixed E–N method shows a stiffer situation of the building due to predicting a narrower settlement trough. Furthermore, the displaced and undisplaced soil zones as well as the effect of the building boundary condition are more appreciable in the mixed E–N modelling compared to the conventional numerical analysis.

8.2 Stiffness Effect of Weightless Buildings

This section examines the effect of the foundation and the superstructure of a weightless building on tunnelling induced ground displacements. The degree of effect of the foundation and the superstructure is also investigated to show the stiffness contribution of the building structural parts to the global building bending stiffness. The effect of the 3D building stiffness is then compared to its equivalent beam using the approaches of Lambe (1973) and Potts and Addenbrooke (1997).

8.2.1 Model description

The soil was taken as an elastic perfectly plastic material with properties presented in Section 4.7. The tunnel was located at a depth to axis level of 15 m, and had a diameter of $D_t = 4.65$ m. Three tunnel locations were modelled: a location in which the tunnel and the building centrelines coincided ($e/L_{bldg} = 0$), a location where the tunnel was constructed under the building edge ($e/L_{bldg} = 0.5$), and a case where there was a distance of 16.75 m

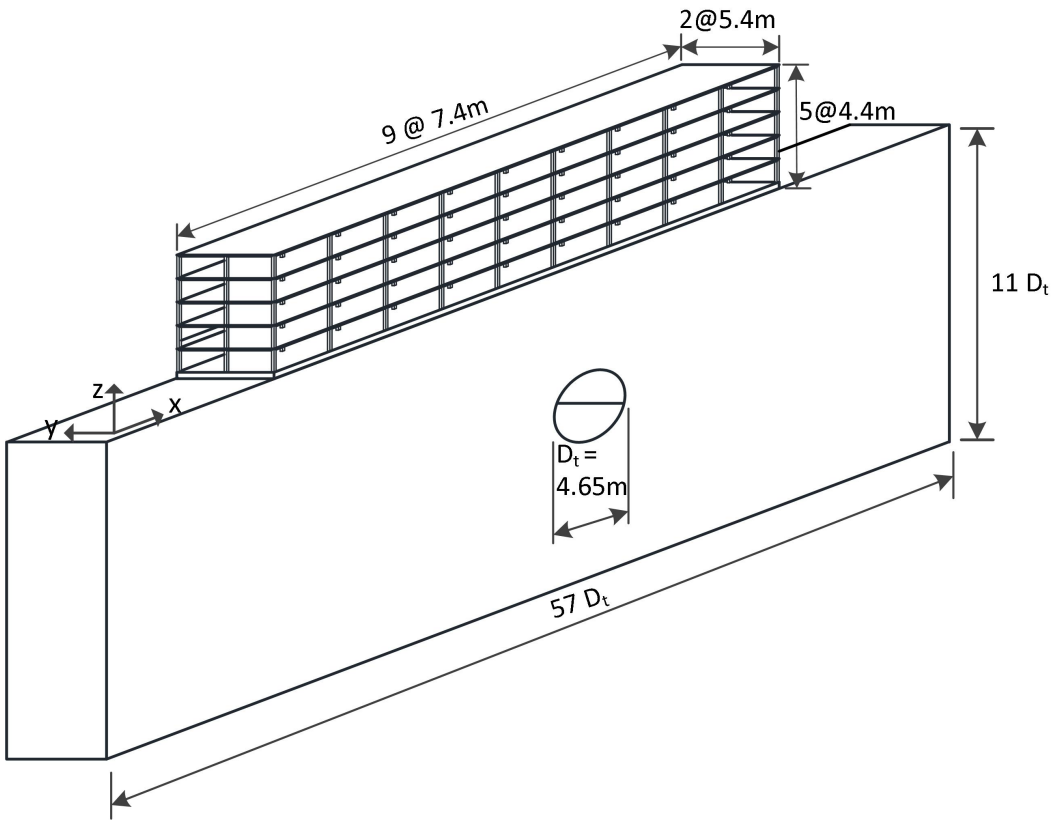

Fig. 8.1 Tunnel – soil – building model

between the tunnel centreline and the building edge ($e/L_{bldg} \geq 0.75$). The tunnel was excavated instantaneously along its entire length, creating a plane-strain scenario in the x-z plane; the effect of tunnel advancement in the y direction was not considered. The soil model was $57D_t$ long and $11D_t$ deep, as shown in Figure 8.1. Meshing and the boundary locations in the model were chosen after testing different scenarios to eliminate their effects on results. The total number of elements of the model ranged from 201,000 to 346,000.

The building consisted of 3 to 9 bays in the x-direction and two bays in the y-direction, as shown in Figure 8.1. The reason for choosing a two y-bay building in the numerical analyses of this section is to have a representative building in terms of stiffness. It should be noted that the symmetric boundaries, which were applied to the soil in the y-direction, were not applied to the building. This means that the building was assumed continuous in the y-direction but as a jointed building (i.e. each two bays were separated from each other as an independent building). The building material was assigned a modulus of elasticity of 30 GPa. The raft foundation had dimensions of $(22.6 \text{ to } 67) \times 11.20 \times (0.30 \text{ and } 0.60)$ m length $\times$ width $\times$ thickness. Column dimensions were 0.40×0.40 m in cross-section with a

clear height of 3.80 m. Beam dimensions were $0.40 \times 0.60 \times 7$ m in the long direction and $0.40 \times 0.60 \times 5$ m in the short direction (cross sectional width $\times$ height $\times$ clear length). The slabs were $7 \times 5 \times 0.16$ m clear length $\times$ clear width $\times$ thickness. The building was attached to the soil using the tie constraint in which the slip or separation of the surfaces was not allowed.

The model included a first stage to introduce soil insitu stresses and bring the model to equilibrium. The inner tunnel elements were then removed and tunnel excavation was simulated using the displacement control method described in Section 7.3.1. Additionally, the simulations were performed at a tunnel volume loss of 0.62% which produced a greenfield surface volume loss of 1.55%. For the tunnel-soil-building analyses, the building was included in the model and the same process of applying displacements to the tunnel boundary was used (applying the same magnitude of displacements as the greenfield situation at the tunnel boundary).

8.2.2 Effect of foundation and superstructure stiffness on ground displacements

This section presents numerical results of three tunnel locations: $e/L_{bldg} = 0$, 0.5 and ≥ 0.75. Figure 8.2a compares greenfield displacements to those obtained when including a foundation of thickness t_f = 0.30 m and a 5 storey building (including the foundation) with a length of 67 m for $e/L_{bldg} = 0$. It is worth noting that rotation of the building is negligible when $e/L_{bldg} = 0$ due to symmetry. Results in Figure 8.2a illustrate that the building stiffness has an effect on surface settlements but that the major effect is due to the foundation stiffness. The addition of the 5-storey building does show an effect on the displacement profile, however this is less significant than the effect of the foundation.

The results for a 0.60 m thick foundation are presented in Figure 8.2b, which again illustrates that the influence of the foundation bending stiffness on surface ground displacements is the most significant component. The data show that there is a slightly greater effect of the 0.60 m foundation on ground displacements compared to the effect of the 0.30 m foundation, while the effect of the superstructure is similar in both cases.

Figure 8.3 displays the degree to which the stiffness of the foundation and the upper storeys affects ground displacements. The parameter $S_{v,max}$ refers to the maximum settlement of the ground surface in the presence of the building, and $S_{v,max,gf}$ is the maximum greenfield settlement. The ratio of $S_{v,max}/S_{v,max,gf}$ is 1.0 when there is no building. For the foundation thickness of 0.30 m, $S_{v,max}/S_{v,max,gf}$ decreases to 0.95 when the foundation is added (0

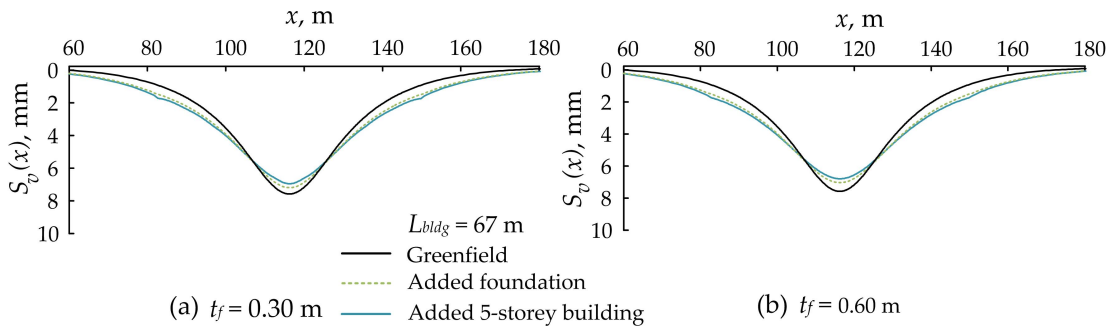

Fig. 8.2 Effect of a 5-storey building on tunnelling induced ground displacements for $e/L_{bldg} = 0$

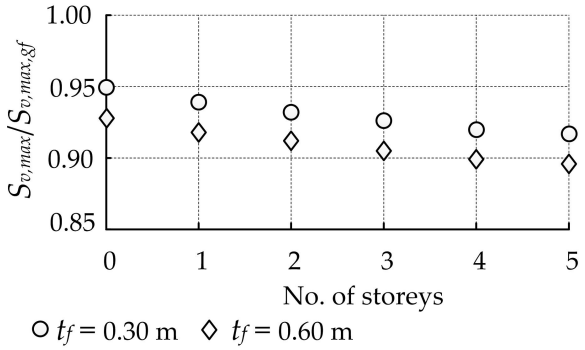

Fig. 8.3 The effect of building foundations and number of storeys on maximum ground settlements for $e/L_{bldg} = 0$

storeys), then reduces slightly as additional storeys are added, reaching a value of 0.92 when a 5 storey building is added. The stiffness of the foundation reduces the maximum settlement by 5%; the 5 storey superstructure reduces this by an additional 3.2%.

Figure 8.3 also shows data for the 0.6 m thick foundation; the foundation reduces the maximum settlement by approximately 7% and, similar to the 0.30 m thick foundation case, the addition of the 5 storey superstructure reduces the maximum settlement by a further 3.20%.

These results indicate that there is a considerable difference between the amount of stiffness contribution of the foundation and that of the superstructure to the bending stiffness of the whole building. Therefore, estimating the stiffness of all storeys equally in a building without considering their position with respect to the foundation may lead to an overestimation of the global building stiffness.

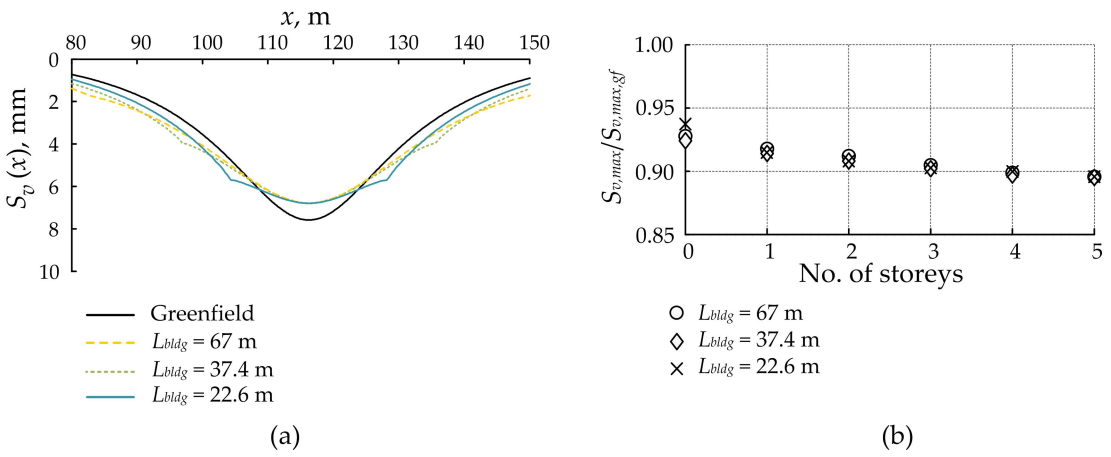

Fig. 8.4 (a) The effect of building length on ground displacements (5-storey building), and (b) effect of number of storeys for different building lengths (t_f = 0.60 m) for $e/L_{bldg} = 0$

Figure 8.4a shows the effect of building length on ground displacements, considering lengths of 67 m, 37.4 m and 22.6 m. The trough width of the surface settlement curves predicted in the analyses varies slightly, but not to a significant degree. Increasing building length causes a slightly wider trough width and marginally smaller maximum settlement. This effect is further discussed in Section 8.2.3. Figure 8.4b shows that there is no practical difference of the degree of stiffness contribution of the building structural parts for buildings with different lengths. The foundation of the 22.6 m long building shows a negligibly smaller effect on ground displacements compared to the other building cases.

When $e/L_{bldg} = 0.5$, the building is flexible to rotate. In addition, a small part of the building may be located in the undisplaced soil zone (the zone which is not influenced by tunnelling). This means that the degree of building rotation will be reasonably high. Figure 8.5a shows the effect of the foundation and the superstructure of a 5 storey building on tunnelling induced ground movements. It is shown that the effect of the building on the displacements is very small. Furthermore, there is no practical difference between the effect of the foundation and that of the whole building. The main cause for showing a small bending stiffness is the rotation that happens to the building. Figure 8.5b demonstrates the effect of a 5 storey building with variable lengths on the tunnelling induced ground displacements. The difference between the curve of greenfield displacements and that of the other cases with the existence of a building decreases with the decrease of the building length. Generally, the trough width of the settlement curve slightly increases due to the presence of a building, and the maximum ground settlement negligibly increases. The increase of the settlement trough width becomes imperceptible for lengths $L_{bldg} = 37.4$ and 22.6 m.

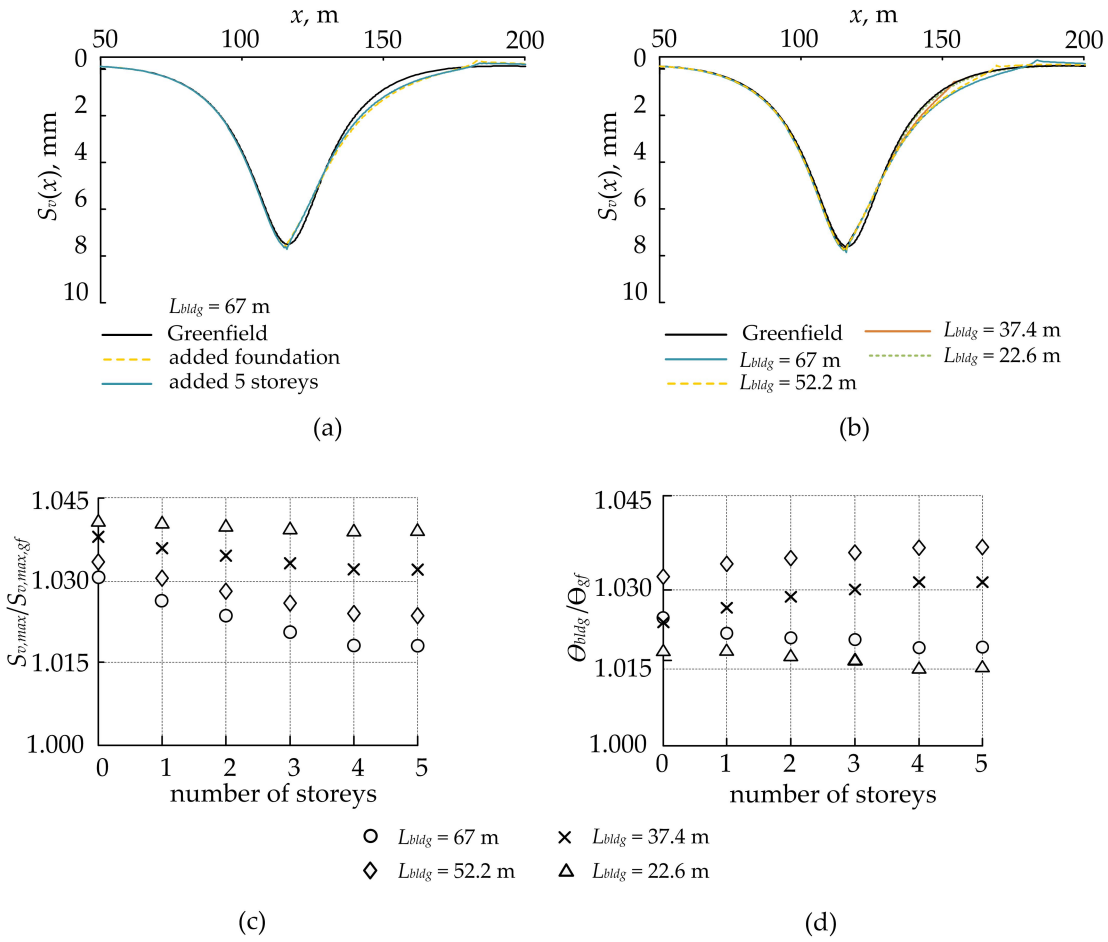

Fig. 8.5 (a) Effect of the foundation and the superstructure of a weightless building on ground displacements due to tunnelling, (b) effect of buildings with different lengths on ground displacements, (c) effect of number of storeys for different building lengths, and (d) the rotation of the buildings relative to the slope of the greenfield settlement curve for $e/L_{bldg} = 0.5$ and $t_f = 0.30$ m

The effect of the existence of a building with different lengths on the maximum ground displacement is presented in Figure 8.5c. The increase of the maximum ground settlement due to the presence of a foundation with a length $L_{bldg} = 67$ m is 2.9%. This effect increases gradually with the decrease of the length until it becomes 3.9% for $L_{bldg} = 22.6$ m. This shows that the rotation of the building increases with the decrease of the length. Additionally, for a specific building length, the existence of building storeys leads to a decrease in the effect of the building on the maximum ground settlement. For $L_{bldg} = 67$ m, the presence of the foundation and 5 storeys (together) causes an increase of 1.18% to the maximum ground settlement (which was 2.9% for the presence of only the foundation). For a reasonably large length, the existence of building storeys increases the resistance of the building against bending deformations. This effect rate of the building storeys decreases for smaller lengths. For $L_{bldg} = 22.6$ m, the existence of a 5 storey building causes an increase of 3.7% (which was 3.9% for the presence of only the foundation).

Figure 8.5d presents the rotation of buildings with variable lengths. θ_{bldg} in Figure 8.5d denotes the rotation of the building (difference in vertical coordinates of the building ends divided by the length), and θ_{gf} is the slope of the greenfield settlement curve under the building. The figure shows that buildings having $L_{bldg} = 67$ m and 22.6 m experience a decrease in their rotation as the number of storeys increases while an opposite trend occurs with building lengths of $L_{bldg} = 52.2$ m and 37.4 m. For the length $L_{bldg} = 67$ m, Figure 8.5b shows that there is a small part of the building located in the undisplaced soil zone. This gives a small resistance to the building against rotation. The addition of building storeys slightly increases this resistance and reduces the building rotation, as illustrated in Figure 8.5a. For a small length of $L_{bldg} = 22.6$ m, the majority of the building is located in the sagging zone of the settlement curve which causes a compression to the building and slightly increases its resistance against rotation. For intermediate lengths of $L_{bldg} = 52.2$ m and 37.4 m, the building does not have any portion in the undisplaced soil zone, and a significant part is located in the hogging zone of the settlement curve which pushes the building to rotate. As a consequence, the rotation of the building increases with the increase of the building storeys since a larger effect is transferred when the local stiffness of the building member increases by adding more storeys (building member considers only the building excluding the whole system of the building–soil).

When $e/L_{bldg} \geq 0.75$, the deformed part of the building is located inside the hogging zone of the settlement curve. In addition, a larger part of the building is located in the undisplaced soil zone compared to the case of $e/L_{bldg} = 0.5$. This means that the degree of building rotation will be relatively less than that of the case $e/L_{bldg} = 0.5$. Figure 8.6a

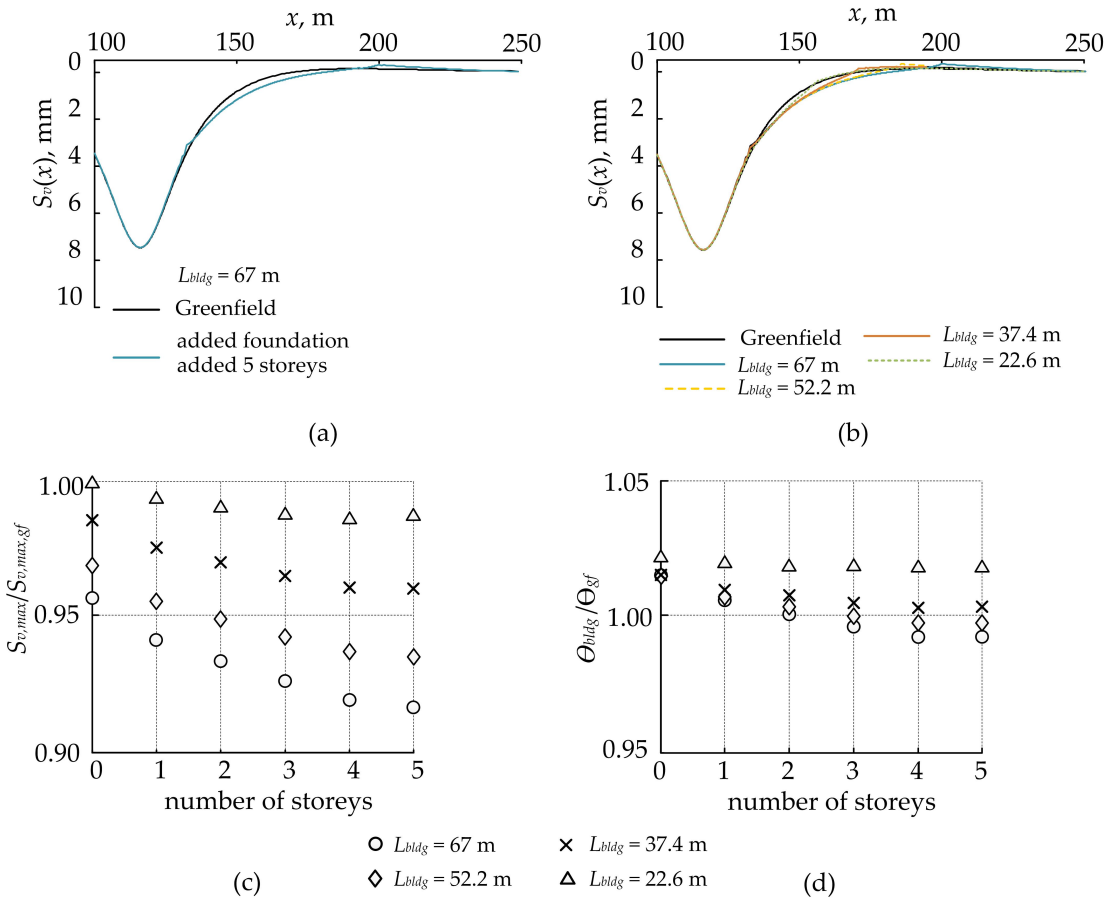

Fig. 8.6 (a) Effect of the foundation and the superstructure of a weightless building on ground displacements due to tunnelling, (b) effect of buildings with different lengths on ground displacements, (c) effect of number of storeys for different building lengths, and (d) the rotation of the buildings relative to the slope of the greenfield settlement curve for $e/L_{bldg} \geq 0.75$ and $t_f = 0.30$ m

shows that there is no practical difference between the effect of the foundation and that of a 5 storey building on tunnelling induced ground movements for $L_{bldg} = 67$ m. This indicates that the contribution of the superstructure to the global building bending stiffness is very small when the building is subjected to rotation. Figure 8.6b demonstrates the effect of a 5 storey building with variable lengths on the tunnelling induced ground displacements for the case $e/L_{bldg} \geq 0.75$. Similar to the case $e/L_{bldg} = 0.5$, the difference between the curve of greenfield displacements and that of the other cases with the existence of a building decreases with the decrease of the building length. Generally, there is a slight increase of the settlement trough width due to the presence of a building, and the maximum ground settlement negligibly decreases.

The effect of the existence of a building with different lengths on the maximum ground displacement for the case of $e/L_{bldg} \geq 0.75$ is presented in Figure 8.6c. It is illustrated that there is a decrease in the maximum settlement under the building in two ways. There is a decrease due to the increase of the building length, and there is also a decrease because of the increase of the building storeys. The decrease of the maximum settlement under the building due to the increase of the building length is because of adding a degree of constraint to the building against rotation. Additionally, the decrease due to the increase of the building storeys is because of increasing the flexural rigidity of the building member. For $L_{bldg} = 67$ m, the presence of the foundation and 5 storeys (together) causes a decrease of 7.7% to the maximum ground settlement while the foundation alone causes a reduction of 4%. This degree of effect decreases with the decrease of the building length until reaching 0% and 1.3% for the foundation and a 5 storey building, respectively, for the case $L_{bldg} = 22.6$ m. The effect of a building with a length $L_{bldg} = 67$ m is greater than that of $L_{bldg} = 22.6$ m by 6.4%. This is because of the building part located in the undisplaced soil zone in the case of $L_{bldg} = 67$ m.

Figure 8.6d presents the rotation of buildings with variable lengths for the case $e/L_{bldg} \geq 0.75$. The figure shows that buildings with a large length (i.e. $L_{bldg} = 67$ m) experience less rotation, and slightly decrease the slope of the settlement curve under the building. Their rotation increases with the decrease of their length until they cause a slight increase to the slope of the settlement curve under the building (i.e. when $L_{bldg} = 22.6$ m). It is worth noting that the foundation alone in all cases leads to an increase in the slope of the settlement curve under the building. For large lengths, the increase of the building storeys decreases the slope of the settlement curve gradually. When there is a small length of the building (i.e. $L_{bldg} = 22.6$ m), the superstructure does not show an effect on the slope of the settlement curve.

8.2.3 Comparison of 3D buildings and equivalent beams

To display the difference between the behaviour of a 3D building and an equivalent 2D beam, the bending stiffness of the modelled building (Section 8.2.1 for $t_f = 0.30$ m) was calculated based on the approaches proposed by Lambe (1973) and Potts and Addenbrooke (1997). For the former approach, the values of EI of all slabs and the foundation are added together to obtain the EI of the whole building. Using a 5-storey building as an example, the analysis is based on 5 slabs of 0.16 m thickness and a foundation of 0.30 m thickness with a width of 1 m.

For the approach of Potts and Addenbrooke (1997), a five storey building has 6 slabs of 0.16 m thickness and 4.4 m centre to centre distance between the successive slabs. The parallel axis theorem is used to calculate the moment of inertia of the 6 slabs with respect to the building centreline. Table 8.1 shows the calculated values of EI for the building based on the two approaches as well as the value of E_{beam} used in the equivalent beam for a 2-, 4- and 5-storey building. An equivalent beam of 1 m width and 1 m height was used to model the building (I_{beam} was kept constant and E_{beam} was varied to achieve the value of EI). Furthermore, two tunnel locations of $e/L_{bldg} = 0$ and $e/L_{bldg} = 0.5$ were considered for the comparison.

Table 8.1 Building properties for the approaches of Potts and Addenbrooke (1997) and Lambe (1973)

	No. of storeys	EI_{bldg}(Nm^2/m)	E_{beam}(N/m^2/m)
Potts and Addenbrooke	2	1.86×10^{11}	2.23×10^{12}
	4	9.3×10^{11}	11.15×10^{12}
	5	16.26×10^{11}	19.52×10^{12}
Lambe	2	8.80×10^{7}	1.06×10^{9}
	4	10.85×10^{7}	1.3×10^{9}
	5	11.87×10^{7}	1.42×10^{9}

Figure 8.7a displays results obtained when adopting the equivalent beam using the Lambe (1973) and the Potts and Addenbrooke (1997) approaches as well as the results obtained from the numerical simulation of a 5-storey 3D building with a length of 67 m and a foundation thickness of 0.30 m when $e/L_{bldg} = 0$. The figure shows that the approach of Potts and Addenbrooke (1997) results in a nearly perfectly rigid building with a significant effect on ground displacements. The over-estimation of the effect of building stiffness on ground displacements of this method was also recognised by Potts and Addenbrooke (1997).

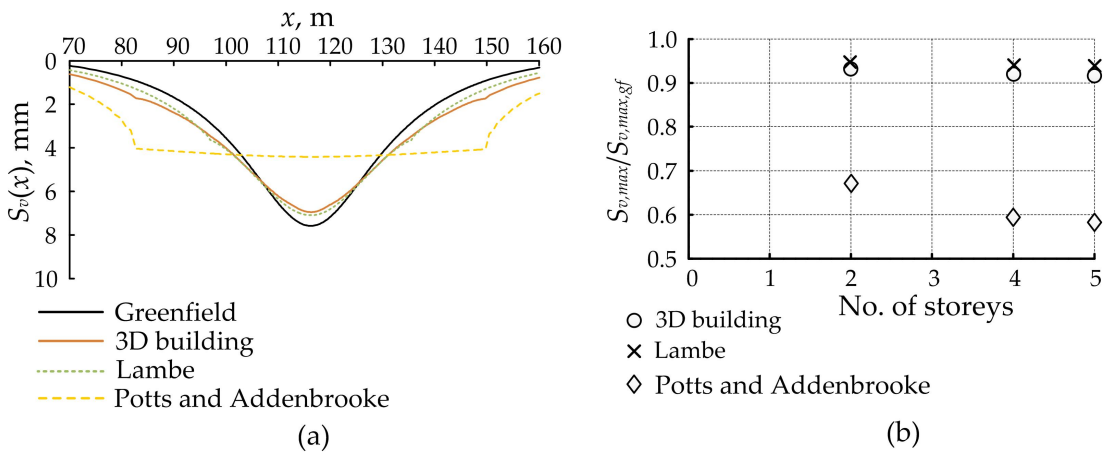

Fig. 8.7 (a) Ground displacements from 3D building model and equivalent beams, and (b) effect of number of storeys on maximum settlement for 3D building model and equivalent beams (building length = 67 m) for $e/L_{bldg} = 0$

Mirhabibi and Soroush (2013) also showed that the structural effect is highly overestimated when using the 2D equivalent beam based on Potts and Addenbrooke's approach compared to a 3D building. This occurs in part because of the inability of the method to consider the decrease of stiffness contribution of the upper storeys to the building global stiffness; the building is considered as a single entity and the use of the parallel axis theorem leads to a significant increase of the building cross sectional moment of inertia when including several upper storeys. Figure 8.7b shows that the degree of stiffness effect of the Potts and Addenbrooke (1997) beam is significantly larger than that of the other methods and approaches a fully rigid case after the 4th storey. The stiffness of the beam does not allow deformations, leading to an overall 'sinking' of the beam into the soil with an increase in trough width and reduction in the maximum soil settlement compared to the other cases.

In the Lambe (1973) approach, the interaction between the building storeys is neglected and the building global stiffness is calculated by adding together the EI of all the slabs and the foundation. The results in Figure 8.7a show that, for the case considered, the Lambe method agrees well with the 3D building model, but with a slightly smaller impact of the building stiffness on ground displacements. The similarity between the results from the Lambe (1973) approach and the 3D building model is due to the fact that the foundation is the same in both cases. Figure 8.7b illustrates that the stiffness contribution of the upper storeys to the building global stiffness in the Lambe (1973) beam is very low; 2 storeys reduce the maximum settlement by an additional 0.40% compared to the foundation alone, and the 5 storey superstructure reduces the maximum settlement by 1%. The degree of stiffness

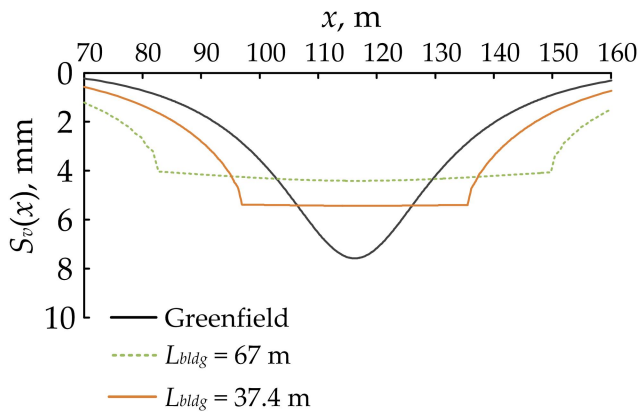

Fig. 8.8 Effect of length of a stiff building on ground displacements for $e/L_{bldg} = 0$

contribution of upper storeys in the Lambe (1973) approach is smaller than that of the 3D building model (1.70% for 2 storeys and 3.20% for 5 storeys).

It is worth noting that the length of the building has an effect on the soil-building interactions but this effect is not significant for relatively flexible buildings. Figure 8.8 shows results for the Potts and Addenbrooke (1997) beams with lengths of 67 m and 37.4 m. The increase in the building length results in an increase of the trough width and a decrease of the maximum settlement since the response of the building is effectively rigid. Moreover, the 'sinking' of the shorter building into the soil is appreciably greater than that of the longer building. This widening and shallowing effect was also observed for the 3D building numerical analysis, however the effect was much less pronounced since the 3D building was much less stiff.

For $e/L_{bldg} = 0.5$, the allowance of the building rotation reduces the effect of the building on ground displacements significantly. Figure 8.9a shows the numerical results of a 3D building and equivalent beam methods of Potts and Addenbrooke (1997) and Lambe (1973) for a tunnel location corresponding to $e/L_{bldg} = 0.5$. It is shown that the difference between the effect of the 3D building and the equivalent beam of Lambe (1973) is negligible. Additionally, both have insignificant effects on ground settlements. With regard to the equivalent beam of Potts and Addenbrooke (1997), it is illustrated that the beam underwent a large rotation but remained rigid.

Figure 8.9b demonstrates the degree of effect of the buildings on the maximum ground settlement. It is exhibited that both the 3D building and the Lambe (1973) equivalent beam resulted in an increase of the maximum ground settlement. It is also shown that the Lambe (1973) beam behaved slightly more flexibly than the 3D building. Furthermore, the increase

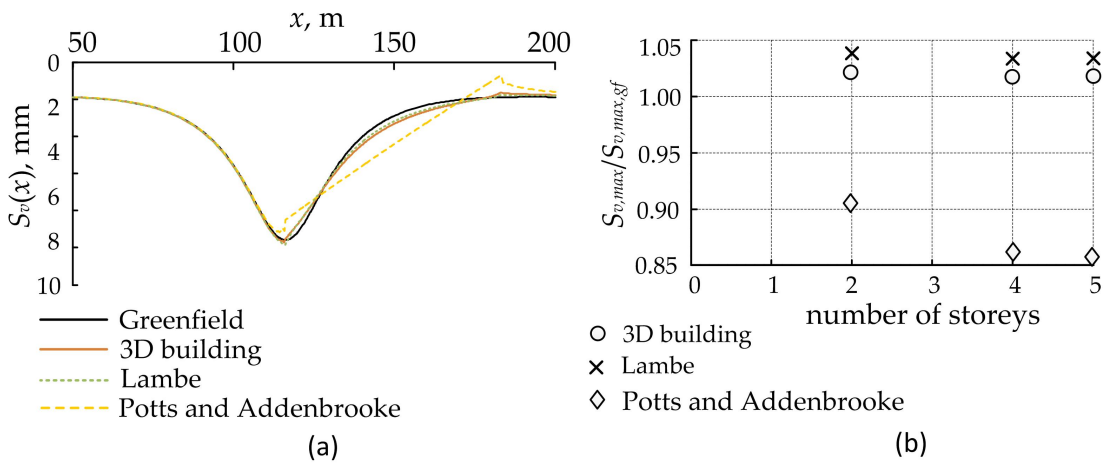

Fig. 8.9 (a) Ground displacements from 3D building model and equivalent beams, and (b) effect of number of storeys on maximum settlement for the 3D building model and the equivalent beams for a 5 storey building with $L_{bldg} = 67$ m and $e/L_{bldg} = 0.5$

of storeys did not show a noticeable effect on the results. On the other side, the equivalent beam of Potts and Addenbrooke (1997) caused a decrease to the maximum ground settlement. Furthermore, the increase of the building storeys showed an appreciable effect on the results.

8.3 Effect of Building Weight

Despite the fact that several researchers have considered both the stiffness and the weight of buildings in their analyses (Section 3.7), there is still not a good understanding of the effect of building stiffness and weight together on tunnel–building interaction, and the relation between the stiffness and the weight of a structure when influenced by tunnelling. This section investigates how the bending stiffness and the weight of a building are interconnected, and how they, together, contribute to the behaviour of the global building when affected by tunnelling.

The section starts with an explanation of the stages taken into consideration prior to the construction of a building to show the assumptions made during the analysis and design stages. The effects of these design assumptions and the changes that may happen to the building after the construction of a tunnel are then discussed. The influence of these assumptions are then numerically examined to predict the behaviour of a 3D weighted building (with actual structural members) when affected by tunnel excavation.

8.3.1 Building analysis and design

The possibility of constructing a tunnel in an urban area is very likely not considered in the design of an existing building. Therefore, the assumptions made during the design stage of these buildings are vitally important to be considered in the tunnel–building interaction analysis.

The stages considered prior to building construction are briefly explained in Section 2.2.1 which mainly consist of 'analysis' and 'design'. It was clarified that the analysis stage included the determination of possible loads, moments and torques that may be imposed to the building, and the induced shear forces, bending and torsional moments in the structural parts were calculated. The design stage started after the analysis of the building, and included the determination of a cross section to each structural member by specifying the required dimensions and material properties. The achieved stiffness (axial, bending and torsion) of each member is then obtained from the specified dimensions and material properties given to them in the design stage. It is worth noting that there are additional (serviceability) checks required by building construction codes to ensure that the obtained bending stiffness of the members during the design is sufficient for the applied loads.

In a concrete framed building, the design stage in which cross sectional dimensions of the members are determined is performed for individual members separately from each other using different design approaches. For example, slabs are mainly designed as two-way flexural members in which a double curvature is produced, beams are one-way flexural members with a single curvature, and columns are mainly designed for compression. Furthermore, in the case of static vertical loads, beams are considered as slab supports that constrain slab vertical movement and rotation to a certain degree, columns are beam supports that constrain beam vertical movement and rotation to a certain degree, and footings are column supports constraining their vertical movement.

The foundation, which is in direct contact with the soil and is the most important support in the building system, is supported by the underlying soil and can be designed in different ways. As explained in Section 2.3.3, a raft foundation can be designed as flexible or rigid. The flexible footing has some degree of flexibility to allow the occurrence of differential settlement, while differential settlement is not allowed in the rigid foundation.

The behaviour of the two types of foundations (flexible and rigid) is different, however they both depend on the same principle of gaining equilibrium with the underlying soil pressure. The stages of analysis and design are similar to the building structural members described previously, and bending stiffness of the footing is achieved from the design process in which the underlying soil has an important role. Figure 8.10a shows a typical footing

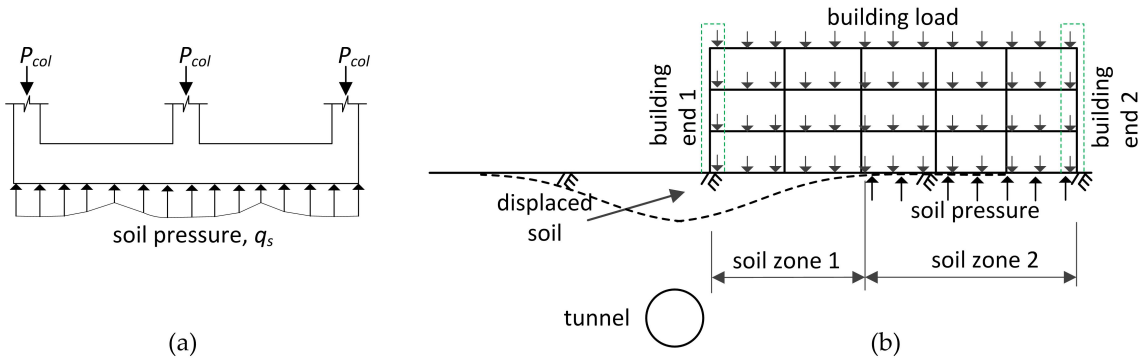

Fig. 8.10 (a) Building load – soil pressure equilibrium on foundations, (b) tunnel–building interaction problem

subjected to building loads through columns (P_{col}). These loads have to reach equilibrium at some point with the subgrade reaction from the underlying soil, q_s (after some settlement due to the weight of the building). q_s depends on the properties of the soil, especially the soil elastic modulus, E_s. Various methods have been proposed by researchers to estimate these properties (Bowles, 1997; Terzaghi, 1955; Vesic, 1961). It is also shown in Figure 8.10a that the foundation does not behave as a beam supported at discrete locations that resists bending moments over unsupported lengths; instead, its whole length is supported by the underlying soil. Moreover, its function is to distribute the building load over an area of soil to prevent excessive and differential settlements (Tomlinson and Boorman, 2001), as explained in Section 2.3.

If a tunnel is constructed close to a building, as shown in Figure 8.10b, changes occur which impact the assumptions and principles on which the building and the foundation were designed. Because of the occurrence of stiffness degradation due to the increase of shear strains in the soil as a consequence of the tunnel volume loss, stress redistribution will happen under the building foundation, and the subgrade reaction (q_s) will decrease in the displaced soil zone (Lee and Ng, 2005; Mair, 2008; Tatsuoka et al., 1997). The occurrence of this reduction in q_s will disturb the equilibrium between the building loads and the subgrade reaction. In this situation, the foundation will not be able to resist the forces applied by the superstructure load and will have to deflect until it regains its equilibrium with the underlying soil. If the soil settlement is small, the foundation may not suffer damage or failure. When the soil settlement exceeds an allowable limit, the foundation will crack or fail because it has not been designed to behave as a beam and to resist the building load without a support from the soil. It is worth mentioning that most of the buildings affected by tunnelling are relatively old and have lost a certain amount of strength and stiffness due to previous actions,

such as repair works (Cording et al., 2008); this may increase the level of disturbance due to tunnelling (required to reach a state of equilibrium).

By design, the foundation and the building will not have sufficient bending stiffness to prevent building deformations when a tunnel is constructed beneath it. As defined in Section 2.2.3, bending stiffness is the resistance of a member against bending deformations. In a mathematical relationship presented by Equation 2.3, the essential parameters influencing the bending stiffness of the member are the cross sectional flexural rigidity (EI), the member's length (L_b), the applied force and the boundary condition of the member.

When the tunnel passes the building and the effect of the tunnel advancement is eliminated, the deformations that happen to the building become one-way (i.e. in the direction perpendicular to the tunnel axis). As explained in Section 2.2.3 and also shown in Equation 2.3, the flexural rigidity of the building, EI_{bldg}, has a proportional effect on the bending stiffness and reduces deformations. Conversely, building length located in the displaced soil zone (soil zone 1 in Figure 8.10b) has an inversely proportional effect which reduces the value of bending stiffness dramatically. In addition, the boundary condition also plays an important role in the resistance of the building against deformation. The boundary condition of the building depends on the properties of the soil and the length of the building located in the undisplaced soil zone (soil zone 2 in Figure 8.10b). In terms of bending stiffness, the role of the boundary is to specify the capacity of the building (as one global member) to resist the applied moments, and this depends on how much rotation is allowed by the boundaries.

Given the above knowledge about bending stiffness, a larger length of a building in the displaced soil zone leads to a lower bending stiffness, while a larger length in the undisplaced soil zone provides more resistance to the building against deformations. The building shown in Figure 8.10b experiences a significant rotation since it is not constrained at end 1. If soil zone 2 (in Figure 8.10b) is not available or is very small, the results of previous chapters showed that the building bending stiffness did not have an impact on ground displacements. A degree of boundary condition is introduced with an increase in the length of soil zone 2. Furthermore, if the part of the building located in the displaced soil zone undergoes cracking its stiffness will decrease significantly (Son and Cording, 2005, 2010). If the local stiffness of the building members is very high (i.e. a building with stiff reinforced concrete walls cast monolithically with the slabs, and acted upon by a relatively small load) or the underlying soil is very soft, tilting of the building may occur (as also mentioned by Son and Cording, 2010). Additionally, a building with a small length affected by ground displacements, or an unrealistically stiff building, may separate from the soil during ground settlements due to

tunnelling. This separation happened in the centrifuge tests performed by Farrell (2010) and also discussed by Giardina et al. (2015).

This section investigates the possible building design parameters that experience changes due to tunnelling. Namely, the investigation includes the effects of the creation of plasticity in the soil, building rotation, building weight, and the lengths located inside the displaced and undisplaced soil zones.

8.3.2 Model description

Th geometry and parameters of the soil and the building model, building bays, tunnel simulation and considered locations are the same as presented in Section 8.2.1. Only the thickness of 0.30 m was considered for the foundation of the building. Furthermore, three tunnel volumes losses of 0.4%, 0.62% and 1.04% were examined, which produced greenfield surface volume losses of $V_{ls,surf} = 1\%$, 1.55% and 2.5%, respectively. Furthermore, the self weight of the building was applied as body forces with a unit weight of 25 kN/m^3, and the considered live load values were 2.5, 5.0, 7.5 and 10.0 kPa applied to the surface of the foundation and the slab of each storey. In the following sections, each case of the considered building weight is referred to by the value of the applied live load. For instance, an applied live load of 2.5 kPa implies a live load of 2.5 kPa on the slab of each storey and the foundation, plus the building self weight. A model of the soil and the building is shown in Figure 8.1.

The interface between the building and the soil was chosen to be a surface to surface contact which has both normal and tangential response. The detail of the soil–building interface is given in Section 4.9. For the following sections, the term 'rough' interface is used for the cases where a rough contact was assumed for the tangential behaviour, and 'frictionless' interface is used where frictionless behaviour was assumed.

8.3.3 Effect of tunnel volume loss and tunnel location on tunnel-building interaction

As mentioned earlier, the occurrence of tunnel volume loss results in the degradation of soil stiffness due to strains (Mair, 2008), which in turn causes a disturbance to the equilibrium system of the soil pressure – building loads shown in Figure 8.10a. Figures 8.11a,b,c show the effect of building weight on the tunnelling induced ground movements for three tunnel locations with a greenfield surface volume loss of $V_{ls,surf} = 1.55\%$. Four settlement cases

are considered: the greenfield case, the existence of a weightless 3D building, the existence of a weighted building with 5.0 kPa and 10.0 kPa live loads.

When a tunnel is constructed under the building centreline ($e/L_{bldg} = 0$), bending stiffness of the weightless building reduces maximum settlement and increases the settlement trough width, as shown in Figure 8.11a. When the building weight is included, the maximum ground displacement is close to the greenfield value or slightly larger. The settlement trough under the building is also broadened. Additionally, the building edges embed into the soil. The presence of a 5.0 kPa live load gives practically the same maximum value of ground surface settlement as that of the greenfield situation. The increase of the applied live load to 10.0 kPa creates plastic zones in the underlying soil and increases ground surface settlements. This increase of surface displacements is a consequence of the tendency of the building to regain equilibrium with the underlying soil pressure which was disturbed by the construction of the new tunnel.

In the presence of the building weight, the bending stiffness of the building seems to mainly affect the distribution of the building load on the underlying soil rather than reducing ground displacements, as was also noted by Maleki et al. (2011) and Mroueh and Shahrour (2003). Additionally, it can be said that the case where the tunnel is constructed under the building centreline shows the stiffest response of the building since the rotation of the building does not occur due to symmetry. When the tunnel is located under the building edge ($e/L_{bldg} = 0.5$), the role of bending stiffness decreases significantly due to the occurrence of building rotation. Figure 8.11b exhibits that even for a weightless building, there is not a significant influence of building bending stiffness on ground displacements. The inclusion of the building weight in the analysis leads to an increase in the ground surface settlements in the sagging zone which are slightly larger than those of the case $e/L_{bldg} = 0$. Furthermore, the trough width also increases, but the amount of increase is less than when the tunnel is under the building centreline. The main reason for this is the influence of building rotation when $e/L_{bldg} = 0.5$, which decreases the embedding of the building into the soil in the hogging zone and increases ground settlements (in both sagging and hogging zones) due to the building weight.

When there is an offset of 16.75 m between the building edge and the tunnel centreline, and the building is located in a place where it is less affected by tunnelling, the influence of the building weight and bending stiffness on ground displacements decreases significantly, as shown in Figure 8.11c. The maximum settlement under the building is not considerably affected but there is an increase in the width of the settlement trough. Additionally, building rotation occurs but with a smaller extent than for $e/L_{bldg} = 0.5$. This is because a portion

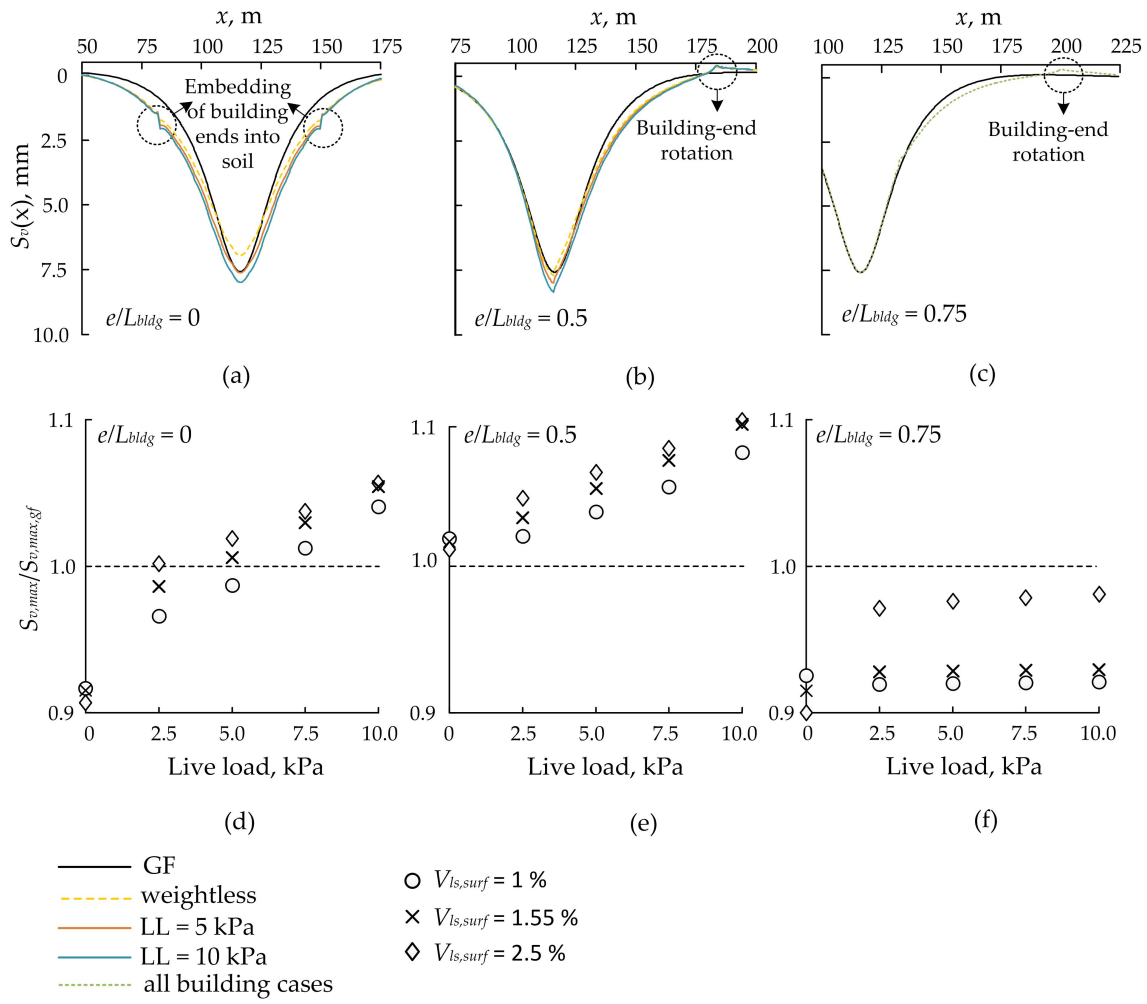

Fig. 8.11 (a), (b), (c) Effect of building weight and bending stiffness on ground displacements due to tunnelling for $V_{ls,surf} = 1.55\%$ and a rough building–soil interface; (d), (e), (f) degree of effect of building weight on the maximum ground displacement under the building

of the building is located in the undisplaced soil zone (soil zone 2 in Figure 8.10b) which restricts the rotation of the building.

To show the effect of the weight of a building (for a specific bending stiffness) on the maximum ground settlement under the building, the maximum ground surface settlement in the presence of the building is normalised by the maximum greenfield settlement and shown in Figures 8.11d,e,f for $e/L_{bldg} = 0$, 0.5 and 0.75, and for three greenfield surface volume losses of $V_{ls,surf} = 1\%$, 1.55% and 2.5%. For all locations of the tunnel, Figures 8.11d,e,f show the increase of tunnel volume loss leading to the creation of greater plasticity in the soil and a larger influence of the building on ground displacements. Moreover, the increase of building weight also results in an increase in the ground displacements. The cases of zero live loads in Figures 8.11d,e,f are for weightless buildings.

For $e/L_{bldg} = 0$, where there is no building rotation, the stiffness of a weightless building reduces maximum ground displacements to a certain extent. As the building weight is added, the reduction of maximum ground displacements decreases. The building tends to reduce ground displacements for low building weights of 2.5 and 5 kPa live load when $V_{ls,surf} = 1\%$, and for 2.5 kPa live load when $V_{ls,surf} = 1.55\%$, as shown in Figure 8.11d. For all other cases, building weight increases maximum ground displacements relative to the greenfield values. For a high greenfield surface volume loss of 2.5%, the weight of the building increases ground displacements even for the lower values of the applied loads. When $e/L_{bldg} = 0.5$, where there is a significant building rotation, there is a slight increase in the maximum ground displacements by the existence of a weightless building. For the weighted buildings, the weight for all surface volume losses leads to an increase in maximum ground displacements, as shown in Figure 8.11e. The occurrence of building rotation causes the building to show little resistance against deformations. Therefore, there is no effect of the bending stiffness except to distribute the building load over an area of soil. As the value of e/L_{bldg} increases to 0.75, despite having a significant building rotation, a large part of the building is located inside the undisplaced soil zone, thereby increasing building resistance to bending deformations. This causes a reduction in the maximum soil displacement under the building for both cases of weighted and weightless buildings, as shown in Figure 8.11f.

It is interesting that for a weightless building, the increase of tunnel volume loss results in a reduction of maximum ground displacements, whereas for weighted buildings, an increase in volume loss results in an increase of maximum ground displacements, as shown in Figures 8.11d, e, f. This is because as the tunnel volume loss increases, a greater area of the soil under the building reaches its plastic limit, thereby experiencing more of an effect from the building. These plastic zones reduce with the decrease of the tunnel volume loss.

This is the reason that the trend of the effect of a weightless building on maximum ground displacements is opposite to that of a weighted building. The effect is similar between a weighted and a weightless building in that maximum ground displacements are more influenced by the existence of a building when the tunnel volume loss increases. For a weighted building, the increase of the tunnel volume loss leads to an increase in maximum ground displacements while for a weightless building, a decrease occurs.

It is worth noting that the reduction of ground displacements in some cases within Figures 8.11d,e,f is partly due to the utilisation of an interface which does not allow separation of the building and the soil. The use of a no-tension interface gives a more realistic condition to the numerical simulations, as suggested by Giardina et al. (2015). Furthermore, using elastic behaviour for the building also has an effect on the results. Son and Cording (2010) showed that using an elastic structure in a numerical analysis leads to much stiffer behaviour of the building compared to a scenario where cracks are allowed to develop in the building.

Using a frictionless interface between the soil and the building, in addition to the previously used rough interface, will give a better depiction of the building response to tunnelling. However, as previously discussed, the separation between the two surfaces still does not happen. When a rough interface is used between the soil and the building, the load of the building will be well–redistributed over the underlying soil, which in turn may decrease or increase the effect of the building weight on the ground displacements. This redistribution is not so effective when using a frictionless interface. For the case of $e/L_{bldg} = 0$, a frictionless interface leads to a slightly larger maximum settlement and a narrower trough width with less embedding of the building edges into the soil, as shown in Figure 8.12a. Compared to the rough interface, the frictionless behaviour of the interface does not allow the transfer of the building load from the portion located in the displaced soil zone where maximum strains happen, to the building edges. This results in a greater maximum settlement and smaller settlements under the edges. For the case of $e/L_{bldg} = 0.5$, settlement curves of both interface types are very similar, as shown in Figure 8.12b. The settlement trough of the frictionless case is slightly narrower than that of the rough case. Different from the case of $e/L_{bldg} = 0$, the maximum settlement of the frictionless case is marginally smaller than that of the rough case. The reason for this is that a building with a rough interface eliminates the curvature of the settlement curve (under the building) in the sagging zone and makes it close to an inclined line while there is a very small curvature when a frictionless interface is used, and the portion of the settlement curve in the sagging zone will not become an inclined line. Similar to the case of $e/L_{bldg} = 0$, this shows that a building with a frictionless interface is slightly less stiff compared to the same building with a rough interface. With regard to

the tunnel location of $e/L_{bldg} = 0.75$, there is also a negligible difference between the two interfaces, as shown in Figure 8.12c. Similar to the other cases, the settlement trough of the frictionless case is slightly narrower than that of the rough case, but the effect on the ground maximum settlement under the building is very similar in both cases.

Figures 8.12d,e,f show the degree of building effect on the maximum soil settlement under the building for different tunnel locations. Figures 8.12d,e illustrate that in the majority of the considered cases, the existence of a weighted building leads to an increase in the maximum ground settlement when $e/L_{bldg} = 0$ and 0.5. It should be noted that in the simulations of both interface cases, there is a limited amount of plasticity created in the soil by the existence of the building. This is because of two main reasons. The first reason is related to the soil. A linear elastic material with a Mohr–Coulomb failure criterion is used to model the soil, and this leads to an underestimation of the ground displacements and the creation of soil plasticity (Ehsan, 2013; Pickles and Henderson, 2005; Ti et al., 2009). Furthermore, it has been reported by researchers that tunnelling does not tend to cause plastic changes to the soil, and a nonlinear elastic model can present a good prediction of tunnelling induced ground displacements (Cheng et al., 2007; Dasari, 1996; Giardina et al., 2015). Indeed, the greenfield model in this research showed no plastic zones at the soil surface or subsurface except a small region around the tunnel. The second reason is related to the building. Before the construction of the tunnel, a region of soil in the vicinity of building column bases reached plasticity. When the tunnel was constructed, the plastic region formed around the column bases located approximately above the tunnel axis decreased, especially for the cases of low applied live loads. This is because building load was transferred from the highly affected columns above the tunnel, to the less affected columns further away.

It is worth noting that the role of the building load in creating soil plasticity is greater than that of the tunnel volume loss. Figures 8.11d,e and 8.12d,e exhibit that for a low building load, the effect of a building on ground displacements increases with the increase of tunnel volume loss. When the building weight increases, the trend of the effect of different tunnel volume losses approach a single value and their difference reduces. In the case of $e/L_{bldg} = 0$ (Figures 8.11d and 8.12d), the trend of effect of all greenfield surface volume losses (1%, 1.55% and 2.5%) approach the same failure point when the building load is increased. In the case of $e/L_{bldg} = 0.5$ (Figures 8.11e and 8.12e), the trend of effect of $V_{ls,surf} = 1\%$ is different from the trend of the others ($V_{ls,surf} = 1.55\%$ and 2.5%) which approach a single value. In the presence of the building load, some plasticity is induced in the soil due to the occurrence of tunnel volume loss. The increase of building weight causes greater plasticity to the soil and reduces the difference between various tunnel volume loss cases.

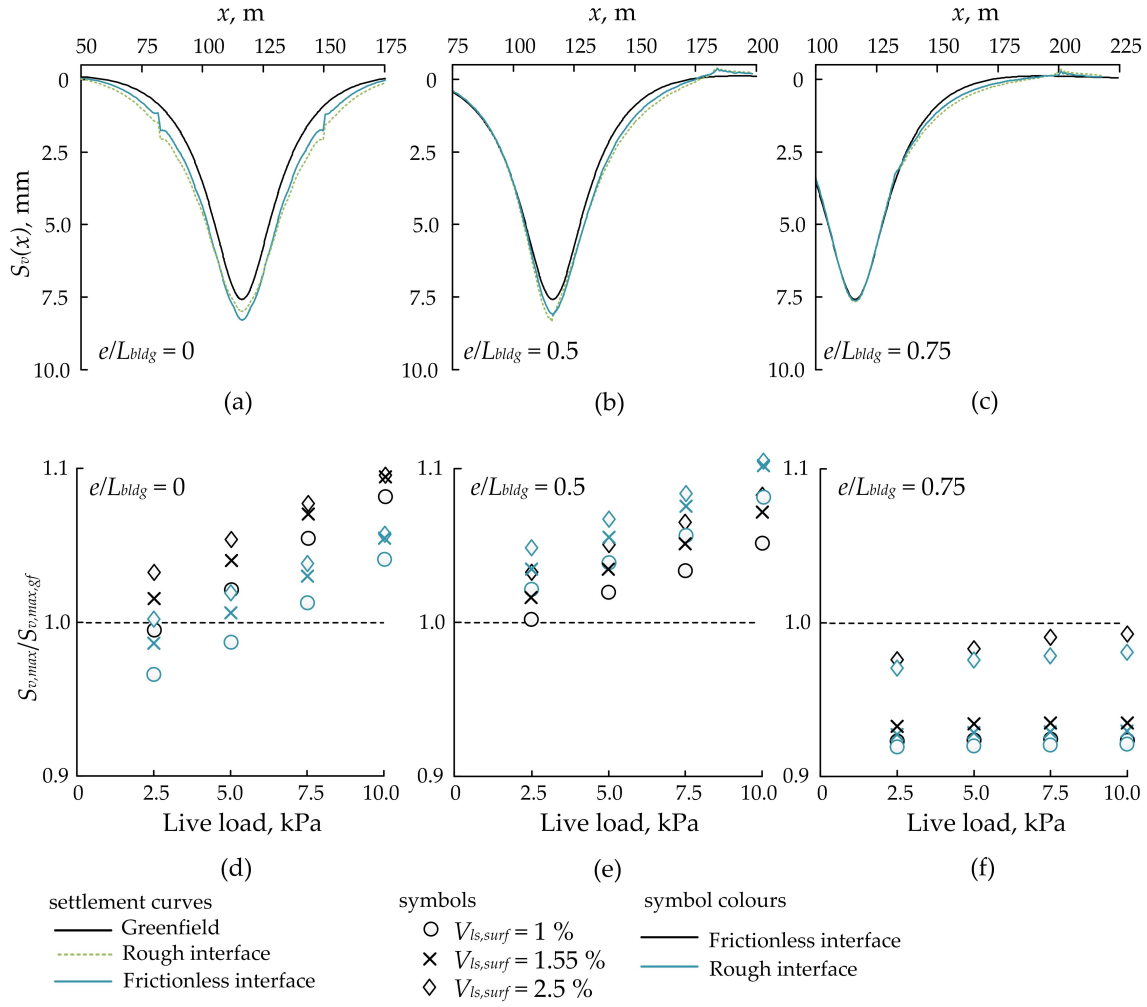

Fig. 8.12 (a), (b), (c) Effect of building weight and bending stiffness on ground displacements due to tunnelling for $V_{ls,surf} = 1.55\%$, live load of 10 kPa, and a rough and frictionless building–soil interface; (d), (e), (f) degree of effect of building weight on the maximum ground displacement under the building for a frictionless and a rough building–soil interface

Figures 8.12d,e,f also illustrate that a change in the soil–building interface changes the building response to tunnelling. It is shown that for a tunnel location of $e/L_{bldg} = 0$, a frictionless interface causes a larger increase to the ground maximum settlement under the building while for the case where $e/L_{bldg} = 0.5$, an opposite trend is created. This is mainly because of the occurrence of building load redistribution due to tunnelling effects. For the case of $e/L_{bldg} = 0.75$ where a smaller building part is affected by tunnelling, the role of the soil–building interface decreases and both results lead to similar effects.

Figures 8.13a,b exhibit the degree of increase and decrease of bottom column loads due to tunnelling for different values of $V_{ls,surf}$. The interior row of the bottom columns in the x–direction (first storey, Figure 8.14) are considered in Figure 8.13. The terms $P_{col,in}$ and $P_{col,fi}$ denote initial (before tunnel construction) and final (after tunnel construction) column loads, respectively. Figure 8.13a shows the degree of column load redistribution for the case of $e/L_{bldg} = 0$ where the building rotation is not allowed. It is illustrated that the load of the two middle columns (5 and 6) decreased; the load was redistributed over the other columns, especially the edge ones (columns 1 and 10). Additionally, the increase of tunnel volume loss for a constant building load resulted in an increase in the degree of load redistribution. For the case of $e/L_{bldg} = 0.5$ where building rotation is allowed, the load of the columns located directly above the tunnel axis (column 1) decreased to a greater extent than that of the others, as shown in Figure 8.13b. There was also a slight load decrease of the neighbouring column (column 2). After that, a small load increase occurred in columns 3, 4, 5 and 6. Interestingly, there was also a load decrease of the end column (column 10) which was due to the global rotation of the building; it caused a pulling force to the end columns and reduced their initial applied loads. Figure 8.13b also clarifies that for a constant building load, the increase of the tunnel volume loss resulted in an increase in the redistribution of the column loads.

In addition to the effect of tunnel volume loss on the load redistribution of the columns, the magnitude of the applied loads to the columns also has a significant role. Figures 8.13c,d show the degree of column load redistribution for two live load cases of 5 and 10 kPa, at a greenfield surface volume loss of 1.55%. It is displayed that the increase of the building load leads to a decrease in the load transfer between columns. This shows that the capability of the building bending stiffness to transfer load between columns is influenced by the applied load. Bending stiffness with a relatively small applied load is capable of transferring a greater load between columns.

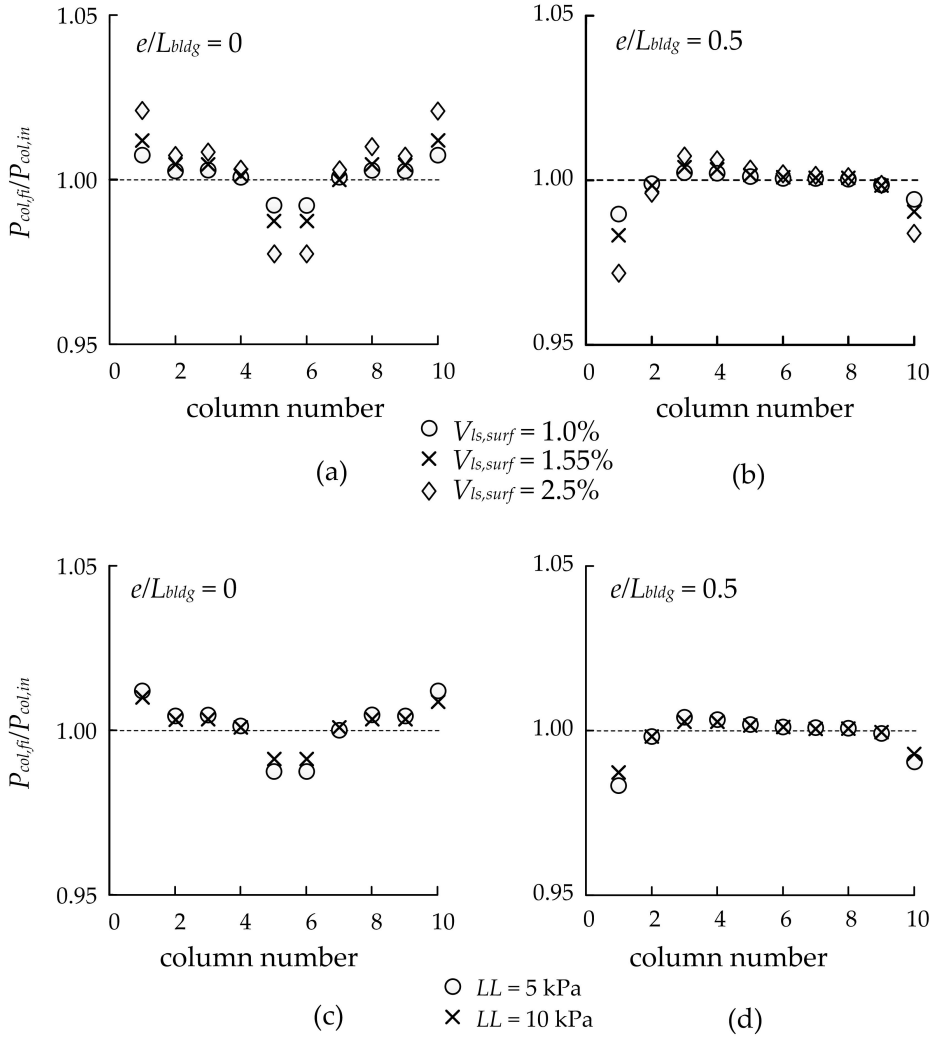

Fig. 8.13 (a), (b) Degree of column load redistribution for the 5 kPa live load case and variable $V_{ls,surf}$; (c), (d) degree of column load redistribution for a volume loss of 1.55%, and live load cases of 5 and 10 kPa

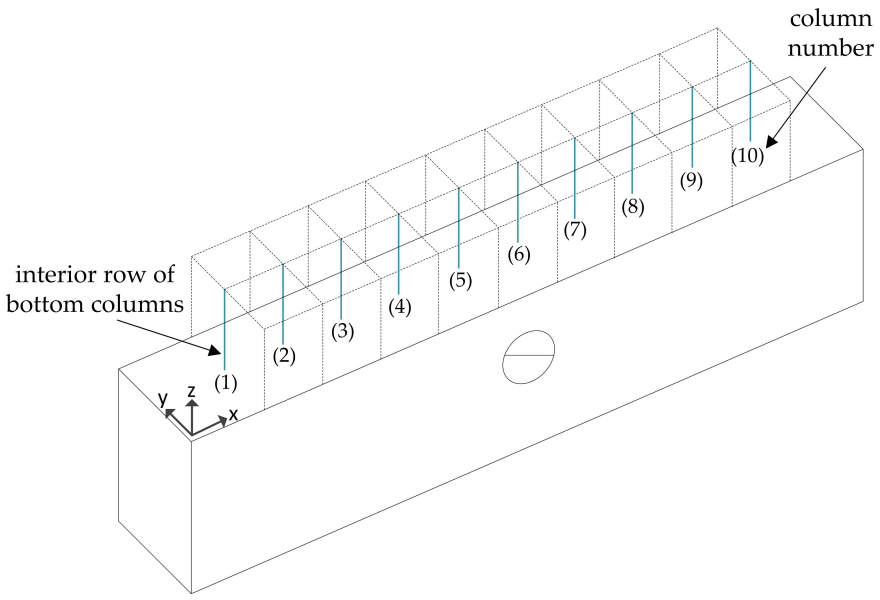

Fig. 8.14 Interior row of bottom columns

8.3.4 Effect of building length in the displaced and undisplaced soil zones

To investigate how building length affects the interaction between a newly constructed tunnel and an existing building, different numerical models were analysed considering various building lengths and tunnel locations. Figure 8.15 shows the results of vertical ground displacements, the degree of building effect on maximum ground displacement under the building, and building rotation for a live load case of 10 kPa and a greenfield surface volume loss of 1.55% with different building lengths and tunnel locations.

When $e/L_{bldg} = 0$ where no rotation of the building is allowed due to symmetry, Figure 8.15a displays that the decrease of the building length results in a decrease of the building effect on ground displacements. It is exhibited that the maximum ground settlement created by a building with $L_{bldg} = 67$ m is greater than that created by a building with $L_{bldg} = 22.6$ m. Furthermore, the trough width of the settlement curve in the case of $L_{bldg} = 67$ m is greater than that of $L_{bldg} = 22.6$ m. The reason for this is that the whole building lies in the displaced soil zone and as the length increases, the building weight will be applied to a wider soil area and will induce greater plasticity in the soil.

When $e/L_{bldg} = 0.5$ and rotation of the building is allowed, the behaviour of the building is influenced by the variation of its length. Figure 8.15b shows that the effect of a 22.6 m and a 67 m building on the maximum ground settlement is very similar while the longer

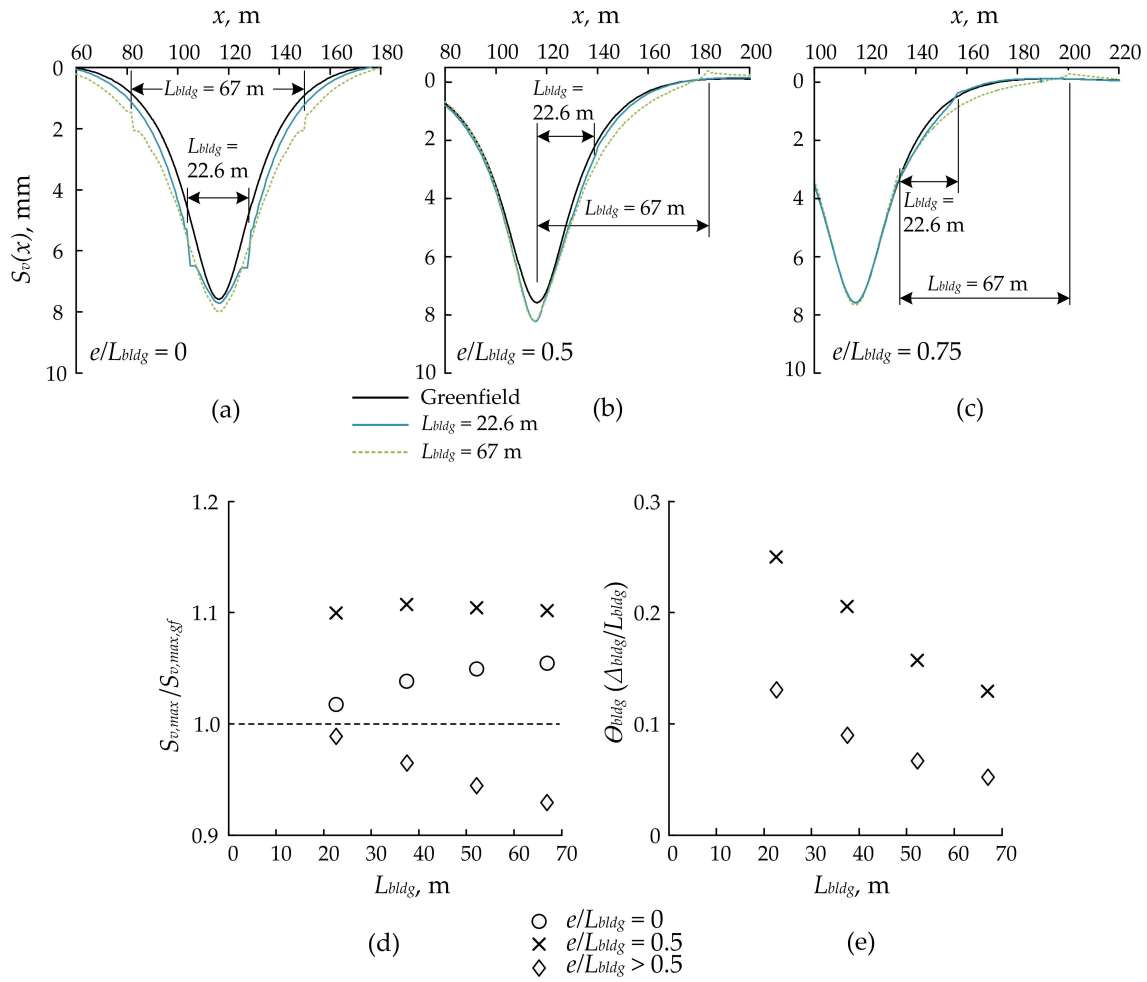

Fig. 8.15 (a), (b), (c) Effect of building existence on ground surface displacements for variable e/L_{bldg}, a live load case of 10 kPa and a greenfield surface volume loss of 1.55%, (d) the degree of building effect on maximum soil displacements under the building, (e) building rotation when the tunnel is not located under the building plan area

building leads to a wider settlement trough. The Figure also shows that the soil in the vicinity of the end of the building furtherest from the tunnel is affected by the building rotation when $L_{bldg} = 67$ m whereas this effect is negligible for the building of $L_{bldg} = 22.6$ m. The building having $L_{bldg} = 22.6$ m is completely located in the displaced soil zone and due to the occurrence of a large rotation, its bending stiffness does not have a significant effect on the ground displacements. Building influence in this case is due to its weight which results in an increase in ground settlements. When $L_{bldg} = 67$ m, a part of the building is located in the undisplaced or less displaced soil zone which provides an amount of bending resistance to the building. The end rotation of the building (far end from the tunnel) in the case $L_{bldg} = 67$ m is due to the building resistance to bending deformations obtained from the building part located in the undisplaced soil zone. Similarly, when there is an offset of 16.75 m between the tunnel axis and the building edge, as shown in Figure 8.15c, a building with $L_{bldg} = 22.6$ m has a minimum effect on ground displacements, resulting in a small increase in the settlement trough width. It is also exhibited that there is a large rotation of the building. When the length increases to 67 m, a greater modification occurs to the ground surface settlement and a wider trough is created.

To better illustrate how building length in the displaced and undisplaced soil zones affect tunnelling induced ground displacements, the degree of building effect on the maximum ground settlement under the building and the building rotation are plotted in Figures 8.15d,e, respectively. When $L_{bldg} = 22.6$ m for the case of $e/L_{bldg} = 0$, Figure 8.15d displays that there is a small increase of the ground surface maximum settlement due to the existence of the building. Building effect on the maximum ground settlement increases with increasing building length until reaching its maximum value when $L_{bldg} = 67$ m (based on the cases considered in this section). This is because, in the considered cases of this section, the building is always located in the displaced soil zone when $e/L_{bldg} = 0$. A larger area of soil is influenced by the building and greater plasticity is induced.

When $e/L_{bldg} = 0.5$, there is not a significant effect of the building length on the maximum ground settlement under the building. This is because a large rotation of the building happens and building resistance against bending deformations will be minimum. Figure 8.15d shows that the effect of the building on maximum ground settlement slightly increases with length until $L_{bldg} = 37.4$ m. After that, there is a minor building influence on the ground maximum settlement for longer buildings. This confirms that for building lengths of 22.6 m and 37.4 m, the whole building is located in the displaced soil zone while for longer buildings, a part of the building is located in the less affected or undisplaced soil zone and produces some building resistance against rotation. Additionally, the general effect of a building on

ground maximum settlement when $e/L_{bldg} = 0.5$ is greater than that of $e/L_{bldg} = 0$ due to the occurrence of building rotation.

The influence of the building part located in the undisplaced soil zone on ground displacements becomes more obvious when $e/L_{bldg} > 0.5$. Figure 8.15d illustrates that the presence of a building with a small length of 22.6 m approximately follows the greenfield deformations except slightly increasing the settlement trough width and negligibly decreasing the maximum ground settlement under the building. The increase of the building length leads to a fairly considerable reduction of the maximum ground settlement under the building, and a relatively significant increase of the settlement trough width.

The length of the building in the undisplaced soil zone has an important role in restricting the rotation of the buildings. Figure 8.15e shows the rotation happening to a building with different lengths at two tunnel locations corresponding to $e/L_{bldg} = 0.5$ and when there is an offset of 16.75 m between the tunnel axis and the building edge ($e/L_{bldg} > 0.5$). It is shown that a relatively large building rotation occurs when the length is small while building rotation decreases significantly with the increase of the length.

8.4 Proposing a 2D Equivalent Method to Estimate Building Bending Stiffness

This section presents a method to calculate the global building bending stiffness by combining the methods proposed to estimate the bending stiffness of the superstructure (Chapter 5) and that of the foundation (Chapter 6), then to convert it to a 2D beam. The 2D beam is given equivalent elastic properties of the 3D building so that the 2D beam can replicate the behaviour of the 3D building.

In this section, after describing the numerical model, the effect of the building superstructure and the relative soil–building elastic modulus on ground displacements in a global soil–building system is investigated using the mixed E–N method. A method is then proposed to replace the 3D building by a 2D equivalent beam in the numerical analysis. The equivalent method aims to replicate the complex 3D behaviour of buildings when influenced by tunnelling.

8.4.1 Model description

To investigate the behaviour of the global building in the soil–building system, two buildings were modelled. The properties of the buildings are presented in Table 8.2. It is worth noting

that the dimensions of the column cross section depended on the dimensions of the floor and supporting beam cross sections. The building of model 1 (Table 8.2) consisted of 5 storeys. The foundation, 2 storeys and 5 storeys were considered in the numerical analyses. The building of model 2 (Table 8.2) comprised 6 storeys. The foundation, 2, 4 and 6 storeys were considered in the analyses. In both building models, only one bay in the y-direction was analysed. It should be mentioned that the model 1 building was a one y-bay building of that simulated in Section 8.2.1. The reason for using a one y-bay building in this section is to simplify numerical models since the number of bays is not influential in this section. This is because the equivalent method presented in this section depends on the methods of Chapter 5 for the estimation of the superstructure bending stiffness, which deals with both single and multiple y-bay buildings.

With regard to the soil, its elastic modulus was varied from 15 MPa to 60 MPa. The model dimensions and the considered tunnel locations were the same as those presented in Section 8.2.1. The depth and the diameter of the tunnel were 13.645 m and 4.65 m, respectively. The mixed E–N method (Chapter 7) was used to simulate tunnelling. The simulations were done at a surface volume loss of 1.55%. The required coefficients for the greenfield input are presented in Table 3.1 for $C_t/D_t = 2.4$ and $I_d = 90\%$. In addition, a tie constraint, in which slip or separation was not allowed, was sued to attach the building to the soil. It is worth noting that the model had 65,000 to 115,000 elements.

Table 8.2 Sizes of structural parts considered in 3D weightless building analyses

Parameter	L_{sl}	B_{sl}	t_{sl}	b_{fb} and b_{sb}	h_{fb} and h_{sb}	L_{col}	L_{bldg}	t_f
model 1	7	5	0.16	0.4	0.6	3.8	22.6 to 67	0.8
model 2	5.7	4.2	0.15	0.3	0.5	3	18.3 to 42.3	0.5

8.4.2 Effect of building storeys on the global building behaviour

The contribution of foundation and superstructure bending stiffness to the stiffness of the global building was investigated in Section 8.2 using conventional numerical simulations in which the tunnel was modelled. It was explained in Chapter 7 that the simulation of the tunnel and the utilisation of conventional soil material models resulted in predictions of a wider trough width than reality. This narrowness of the trough width does not lead to realistic response of the building since, in most cases, the majority of the building length is located inside the displaced soil zone, and no length or a small part is located in the undisplaced soil area, which has an effect on the building end fixity. For this reason, the effect of the

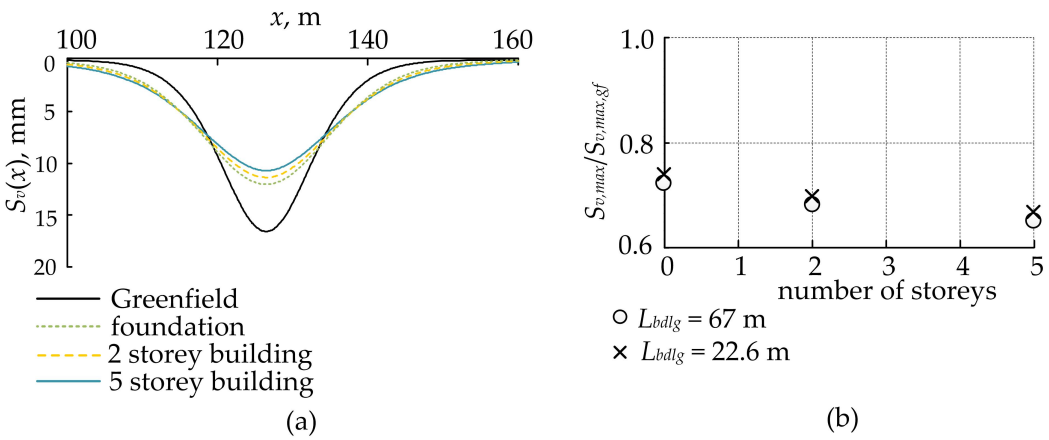

Fig. 8.16 (a) Effect of a 3D building (model 1) on ground displacements due to tunnelling, (b) effect of number of storeys on the maximum settlement for $e/L_{bldg} = 0$ and $E_s = 35$ MPa

superstructure is re-investigated in this section using the mixed E–N method which may lead to a narrower trough width of the settlement curve. Furthermore, in the investigation of the superstructure in Chapter 5, the soil and the foundation were excluded in the analyses. The study presented in this section leads to a better understanding of the behaviour of the superstructure in a soil–building system.

Figure 8.16a shows the effect of a 5 storey building (model 1) on ground displacements due to tunnelling for a tunnel location corresponding to $e/L_{bldg} = 0$. Similar to the results of Section 8.2, the major effect of the building on ground displacements was again due to the foundation. Figure 8.16b presents the degree of effect of the foundation and a 2 and 5 storey building on ground displacements for building lengths of $L_{bldg} = 67$ m and 22.6 m. The degree of effect in both cases is very similar. The existence of the foundation reduced the maximum ground settlement by about 27%. This degree of effect increases to 34% for a 5 storey building, indicating that the superstructure has an additional effect of 7%.

Figure 8.17a shows the effect of building model 1 on ground displacements for a tunnel location of $e/L_{bldg} = 0.5$. It is illustrated that the effect of the building on ground displacements is small. Figure 8.17b shows the degree of effect of the foundation and a 2 and 5 storey building on ground displacements for different building lengths. It is shown that the effect of the building on the displacements increases with the increase of building storeys, especially for buildings with large lengths. The increase of the storey number results in the increase of the flexural rigidity of the building which in turn increases the building resistance to bending deformations. When the building has a large length, the degree of the end fixity increases which, together with the increase of building storeys, leads to the increase of

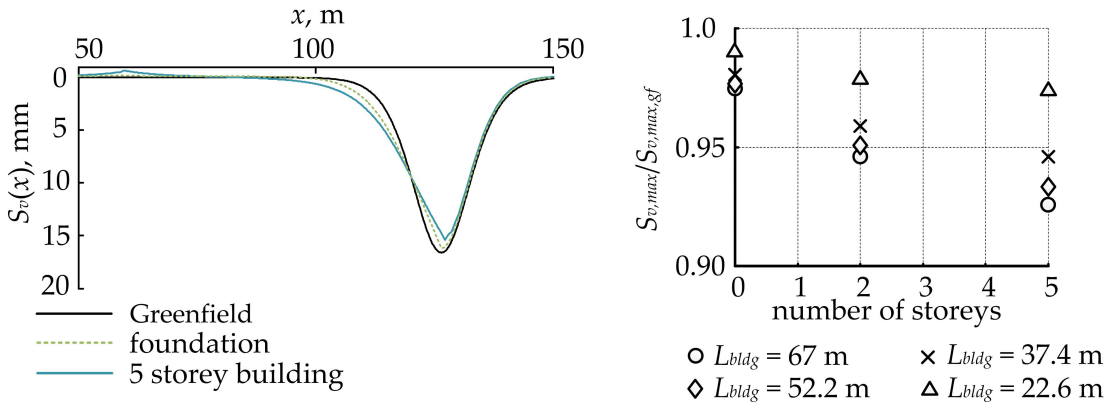

Fig. 8.17 (a) Effect of a 3D building (model 1) on ground displacements due to tunnelling, (b) effect of number of storeys on the maximum settlement for $e/L_{bldg} = 0.5$ and $E_s = 35$ MPa

the building bending resistance to a greater extent. For $L_{bldg} = 67$ m, the presence of the foundation reduced the maximum ground settlement by 2.5% while the presence of the whole building reduced the maximum settlement by 7.4%. For $L_{bldg} = 22.6$ m, the existence of the foundation caused a reduction of 1% to the maximum settlement while the whole building caused a reduction of 2.6%.

8.4.3 Effect of relative building–soil elastic modulus on the global building behaviour

The effect of the relative building–soil elastic modulus was investigated in Chapter 6 for the undisplaced zone of the soil. In this section, the effect of the building–soil elastic modulus is studied for the global soil–building system.

Figure 8.18a illustrates the effect of a building on ground displacements due to tunnelling for variable $E_c/(E_s \times 10^3)$, $e/L_{bldg} = 0$ and $L_{bldg} = 67$ m. The effect of the building on the displacements increases with the increase of $E_c/(E_s \times 10^3)$; in another words, the effect increases with the increase of the building elastic modulus. To avoid confusion with the conclusions drawn in Chapter 6, it should be noted that in this section, the effect of one entity (building) on the other entity (soil) in the soil–building system is measured while in Chapter 6, the bending stiffness of the global foundation (a footing supported by soil) was estimated. Simply having a large effect of the building on ground displacements does not mean having a high building bending stiffness. Both the building part and the underlying

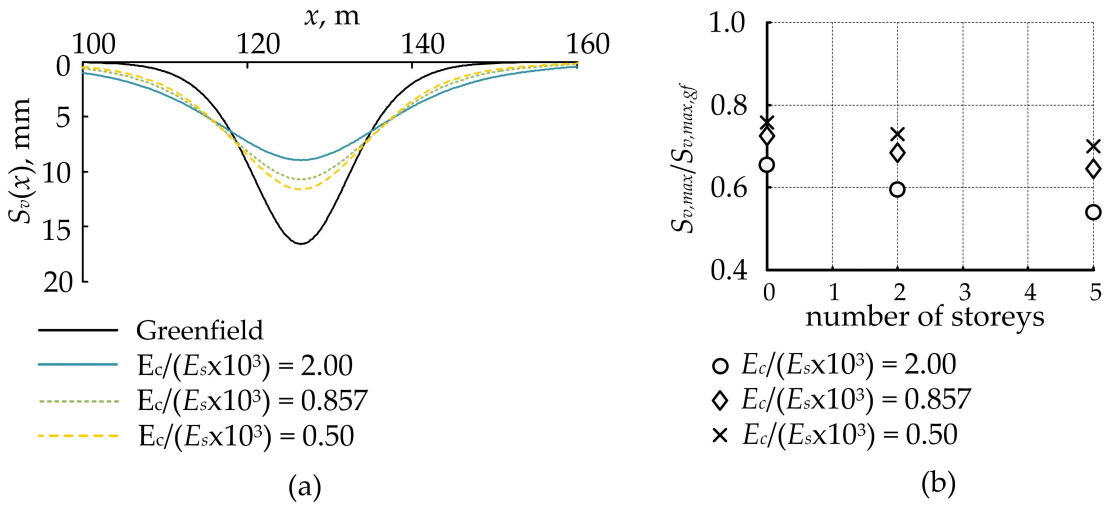

Fig. 8.18 (a) Effect of a 3D building on ground displacements due to tunnelling, (b) effect of number of storeys on the maximum settlement for variable $E_c/(E_s \times 10^3)$, $e/L_{bldg} = 0$ and $L_{bldg} = 67$ m

soil are parameters of the building bending stiffness, meaning that they are interconnected rather than being separate entities. For instance, in an elastic analysis where the weight of the building is not considered, when the soil is of small stiffness, it will apply small forces to the building to deflect. In such case, a large effect of the building on ground deformations is obtained while the bending stiffness of the building is relatively small due to having a low stiffness support (soil).

Figure 8.18b shows the reduction of the maximum ground displacement due to the existence of a building for variable values of $E_c/(E_s \times 10^3)$, $e/L_{bldg} = 0$ and $L_{bldg} = 67$ m. For $E_c/(E_s \times 10^3) = 2$, the foundation caused a reduction of 34% and a 5 storey building caused a reduction of 46% to the maximum ground settlement. For $E_c/(E_s \times 10^3) = 0.5$, the maximum ground settlement was reduced by 24% and 30% due to the existence of the foundation and a 5 storey building, respectively. It is indicated that the effect of the superstructure on the maximum ground settlement increases with the increase of $E_c/(E_s \times 10^3)$; for the case of $E_c/(E_s \times 10^3) = 2$, the effect of a 5 storey superstructure is 12% while for the case of $E_c/(E_s \times 10^3) = 0.5$, the superstructure effect becomes 6%.

8.4.4 An equivalent beam method

To obtain the bending stiffness of the global building ($K_{b,bldg}$), the bending stiffness of the superstructure based on the proposed method in Chapter 5 and that of the foundation

based on the method in Chapter 6 were algebraically added together. In order to represent the building by a simple 2D beam in the numerical analyses of the tunnel–soil–structure interaction, an analogy was made between the 3D building and an elastic beam resting on an elastic foundation (soil), hereafter called an equivalent beam. Similar to Chapters 5 and 6, a fixed–ended analogy was made for the case $e/L_{bldg} = 0$ and a cantilever analogy for the case $e/L_{bldg} \geq 0.5$. The Poisson's ratio of the equivalent beam was the same as that of the building. In a numerical model, the 3D building was analysed and its effect on the surface settlement curve was determined. The equivalent beam was then modelled in a numerical analysis and its elastic modulus was changed in a trial and error process until its effect on surface displacements was approximately equal to that of its corresponding 3D building.

The equivalent beam was assumed to be a 1×1 m elastic beam loaded by a linearly distributed force (the same as that applied to the foundation in Chapter 6, Figure 6.2). The initial elastic modulus, E_b, was calculated using Equation 2.3 ($K_b = F_K((EI)_b/L_b^3)$, where K_b is the beam bending stiffness, $(EI)_b$ is the flexural rigidity and L_b is the length) with $F_K = 60/11$ and $F_K = 1920/7$ for the cantilever and the fixed–ended cases, respectively. Equation 2.3 is based on a fixed boundary. There are two different coefficients to determine the boundary condition of the building: C_{bc} for the superstructure (Chapter 5) and $C_{bc,fnd}$ for the foundation (Chapter 6). These two coefficients are determined based on two different load cases; therefore, none of them independently represents the realistic boundary condition of the equivalent beam. Furthermore, the portion with which each boundary coefficient contributes to the equivalent beam boundary is not known since the effect of the foundation on ground displacements was shown to be greater than that of the superstructure (Section 8.2.2), but this is not quantified. As the first trial, the coefficient C_{bc} was divided by $C_{bc,fnd}$ ($C_{bc}/C_{bc,fnd}$) in order to approximately determine the end fixity of the equivalent beam in the soil–structure system. E_b was then calculated from $K_{b,bldg} = (C_{bc}/C_{bc,fnd}) \times [F_K \times (EI)_b/L_b^3]$, where $K_{b,bldg}$ is the algebraic addition of the foundation and superstructure bending stiffness.

It should be noted that in some cases, the whole building may lie in the displaced soil zone due to the width of the settlement trough. In the methods proposed in Chapters 5 and 6 to estimate the stiffness of the superstructure and the foundation, it was assumed that at least a small part of the structure was located in the undisplaced soil zone. An assumption is necessary to be made here to overcome the problem where the whole building is in the displaced zone since the methods of Chapters 5 and 6 do not work in cases where the length of the building in the undisplaced soil zone is zero. Furthermore, the method of estimating the bending stiffness of the superstructure is different from that of the foundation, requiring different assumptions for considering the length located in the undisplaced zone. For this

reason, for the case of the superstructure, the influenced length of the building was assumed to be the length of the whole building disregarding the settlement trough width. For the case of the foundation, the length of the undeformed (supporting) part was assumed to be 0.15 times the maximum supporting length ($L_{f,sp} = 0.15L_{f,sp,max}$, Equations 6.3 and 6.10 for the cantilever and fixed–ended approaches, respectively). For buildings with large lengths extending to the undisplaced soil zone, the point where the ground settlement became smaller than 1 mm was assumed to be the start point of the foundation supporting part (undisplaced zone).

The trial and error process of the numerical models showed that $C_{bc}/C_{bc,fnd}$ alone does not represent the realistic boundary condition of the beam. For this reason, an extra parameter was added to account for the effects of $E_c/(E_s \times 10^3)$ and the number of building storeys. The addition of the extra parameter was based on the numerical results of the effects of building storeys and $E_c/(E_s \times 10^3)$ on tunnelling induced ground displacements presented in Sections 8.4.2 and 8.4.3, respectively. A coefficient, $C_{bc,b,eq}$, was introduced to determine the realistic boundary condition of the equivalent beam based on the numerical results:

$$C_{bc,b,eq} = \left(\frac{C_{bc}}{C_{bc,fnd}}\right) \times \left(\frac{2}{n_{st}^{0.2}}\right) \times \exp\left(-0.35 \times \frac{E_c}{E_s \times 10^3}\right) \tag{8.1}$$

where n_{st} is the number of the building storeys.

The final elastic modulus of the beam is then calculated as:

$$E_b = \frac{K_{b,bldg} \times L_{inf}^3}{C_{bc,b,eq} \times F_K \times I_b} \tag{8.2}$$

Note that when adding the foundation and superstructure bending stiffness, either the superstructure bending stiffness should be divided by the building width, or the foundation stiffness should be multiplied by the building width before the addition of their bending stiffness is done.

Figures 8.19a,b,c show a comparison between the effect of a 3D building and that of a 2D equivalent beam on ground displacements due to tunnelling for $e/L_{bldg} = 0$ and $L_{bldg} = 67$ m. The building is that of model 1 in Table 8.2. The comparison is made for the foundation and a 2 and 5 storey building. An excellent agreement between the results of the 3D building and that of the equivalent beam is achieved.

Figures 8.19d,e,f,g show the degree of effect of the foundation and a 2 and 5 storey building (3D building and 2D equivalent beam - model 1 in Table 8.2) on the maximum ground settlement for $e/L_{bldg} = 0$ and different building lengths. The Figures show a good agreement of the results between the 3D building and the equivalent beam analyses.

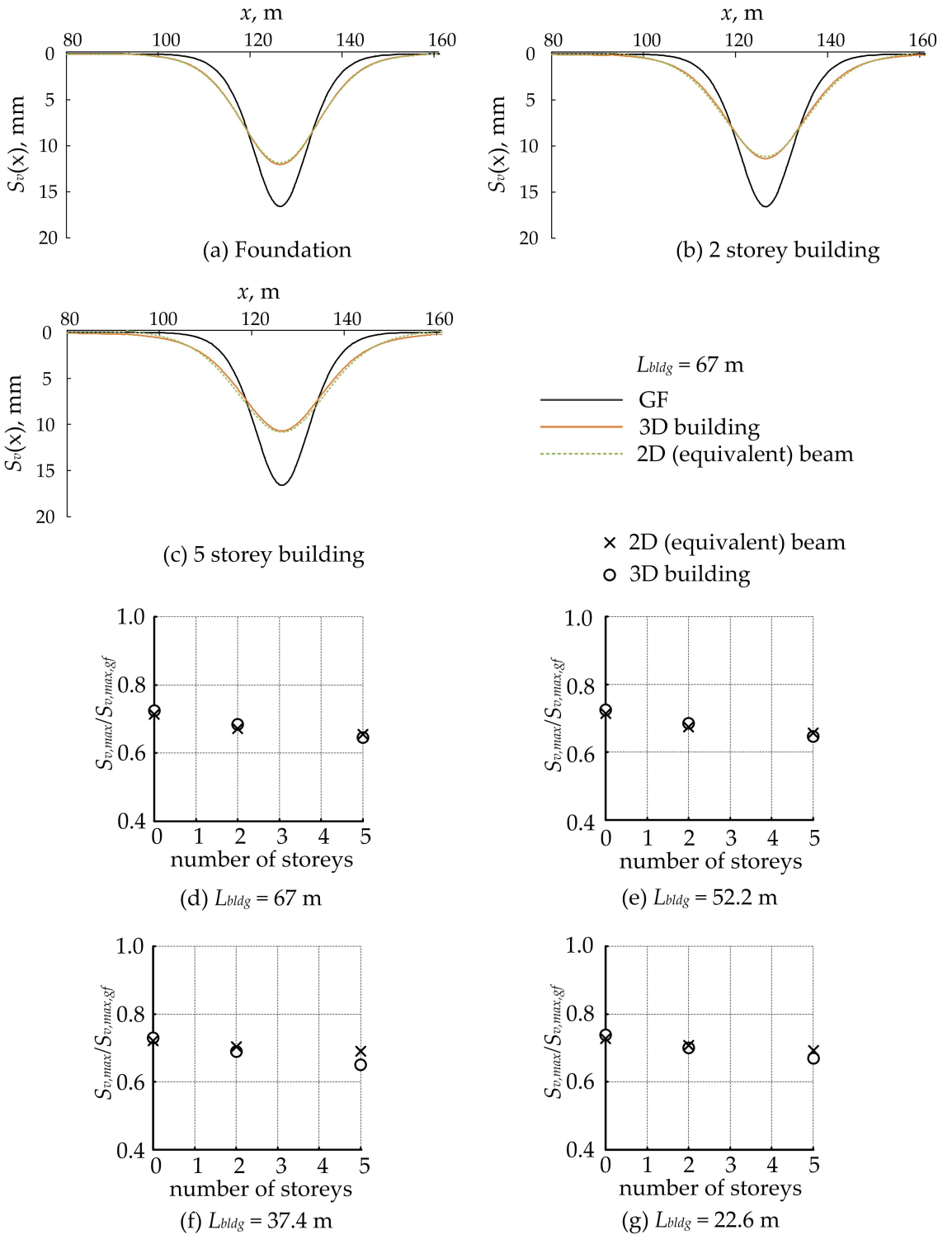

Fig. 8.19 Comparison of the predicted building effect on (a), (b), (c) ground displacements, and (d), (e), (f), (g) the maximum ground settlement between a 3D building and its equivalent beam for $e/L_{bldg} = 0$

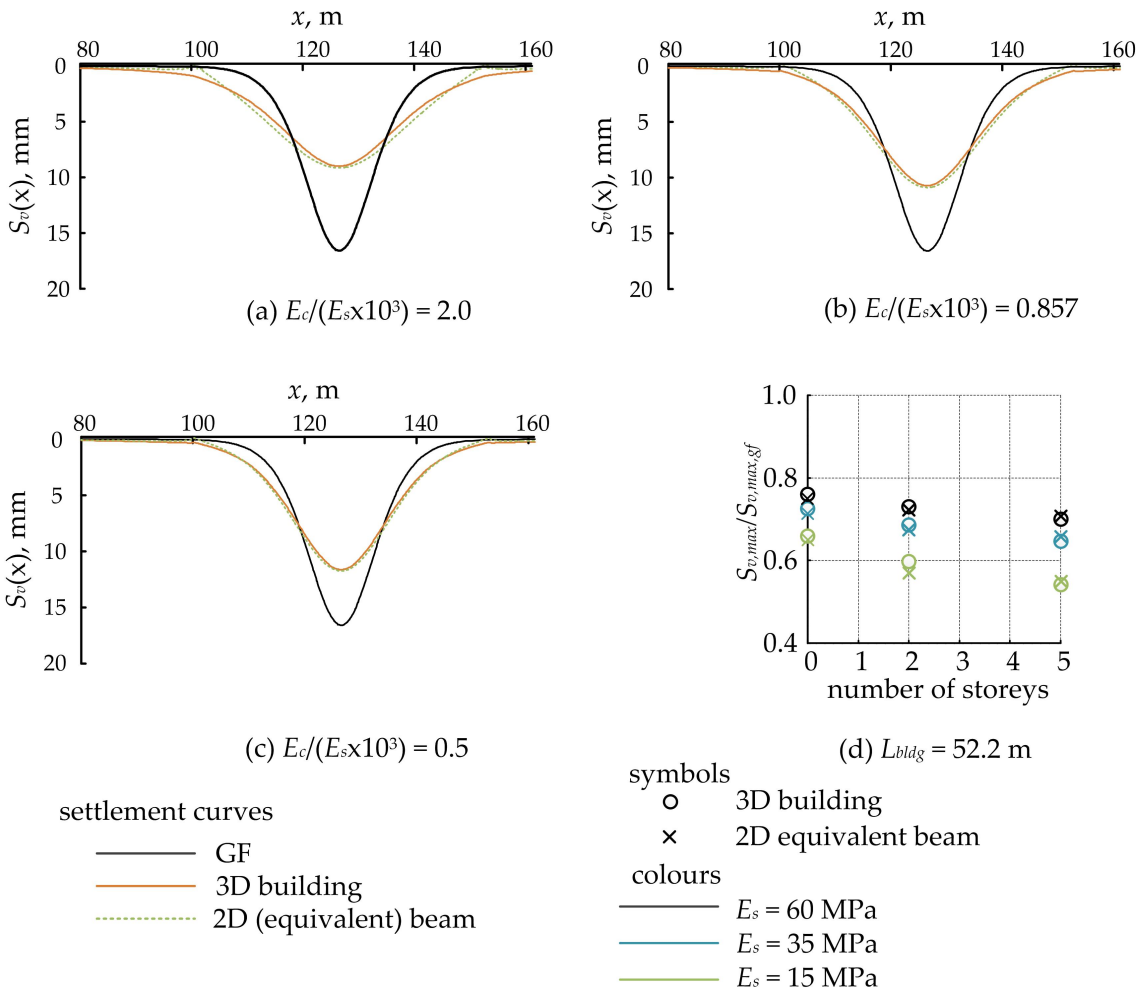

Fig. 8.20 Comparison of the predicted building effect (a), (b), (c) on ground displacements, and (d) on the maximum ground settlement between a modelled 3D building and an equivalent beam for a 5 storey building (model 1) with $e/L_{bldg} = 0$ and variable ratios of building–soil elastic moduli

Figures 8.20a,b,c illustrate that there is a good agreement between the numerical results of the 3D building and that of the equivalent beam for different values of $E_c/(E_s \times 10^3)$. The agreement is very good for the prediction of the maximum ground settlement, as shown in Figure 8.20d. Both Figures 8.19 and 8.20 illustrate that generally, the settlement trough width predicted with the 3D building and the equivalent beam is also in a good agreement. With regard to the symmetric rotation of the building ends, Figures 8.20a,b,c illustrate that the equivalent beam experienced slightly more end rotation than that of the 3D building. This is mainly because the part of the building located in the undisplaced soil zone is smaller than $L_{f,sp,max}$, which is seemingly not well-captured by the equivalent beam, especially for high values of $E_c/(E_s \times 10^3)$.

Figure 8.21 presents the numerical results of the 3D building of model 2 in Table 8.2. Figures 8.21a,b,c,d show the effect of the building (3D and the equivalent beam) on ground displacements for $e/L_{bldg} = 0$ and $E_c/(E_s \times 10^3) = 1.0$. It is indicated that generally, there is a good agreement between the results of the 3D building and that of the equivalent beam. The effect of the building on ground displacements is captured well by the equivalent beam up to 4 storeys. For the 6 storey building, the symmetric end rotation of the equivalent beam is more than that of the 3D building, as shown in Figure 8.21d. For a building with a larger length, such as that of Figure 8.19c, there is negligible difference between the end rotation of the 3D building and that of the equivalent beam. As the length of the building decreases, a slight difference between the end rotation of the 3D building and the equivalent beam occurs. The assumption of having at least $0.15L_{f,sp,max}$ in the undisplaced zone to estimate the bending stiffness of the building may have an influence on the behaviour of the equivalent beam. The difference of end rotation between the 3D building and the equivalent beam is also shown in Figures 8.21e,f where the length of the building is $L_{bldg} = 30.3$ m and 18.3 m, respectively. It should also be noted that for the 6 storey buildings shown in Figures 8.21d and e, it would appear that the equivalent beam generally behaves more flexibly than the 3D building, and undergoes larger settlements.

As explained previously, when the tunnel is located outside the building plan area, the building bending stiffness will decrease due to the occurrence of global building rotation. Numerical results of the 3D building and the equivalent beam for the case $e/L_{bldg} \geq 0.5$ are presented in Figure 8.22. Generally, there is excellent agreement between the results of the equivalent beam and the 3D building.

Figures 8.22a,b,c show the numerical results of $e/L_{bldg} = 0.5$ for three building lengths of $L_{bldg} = 42.3$ m, 30.3 m and 18.3 m. The building undergoes an appreciable rotation in all length cases since the length of the foundation supporting part is relatively small. The equiv-

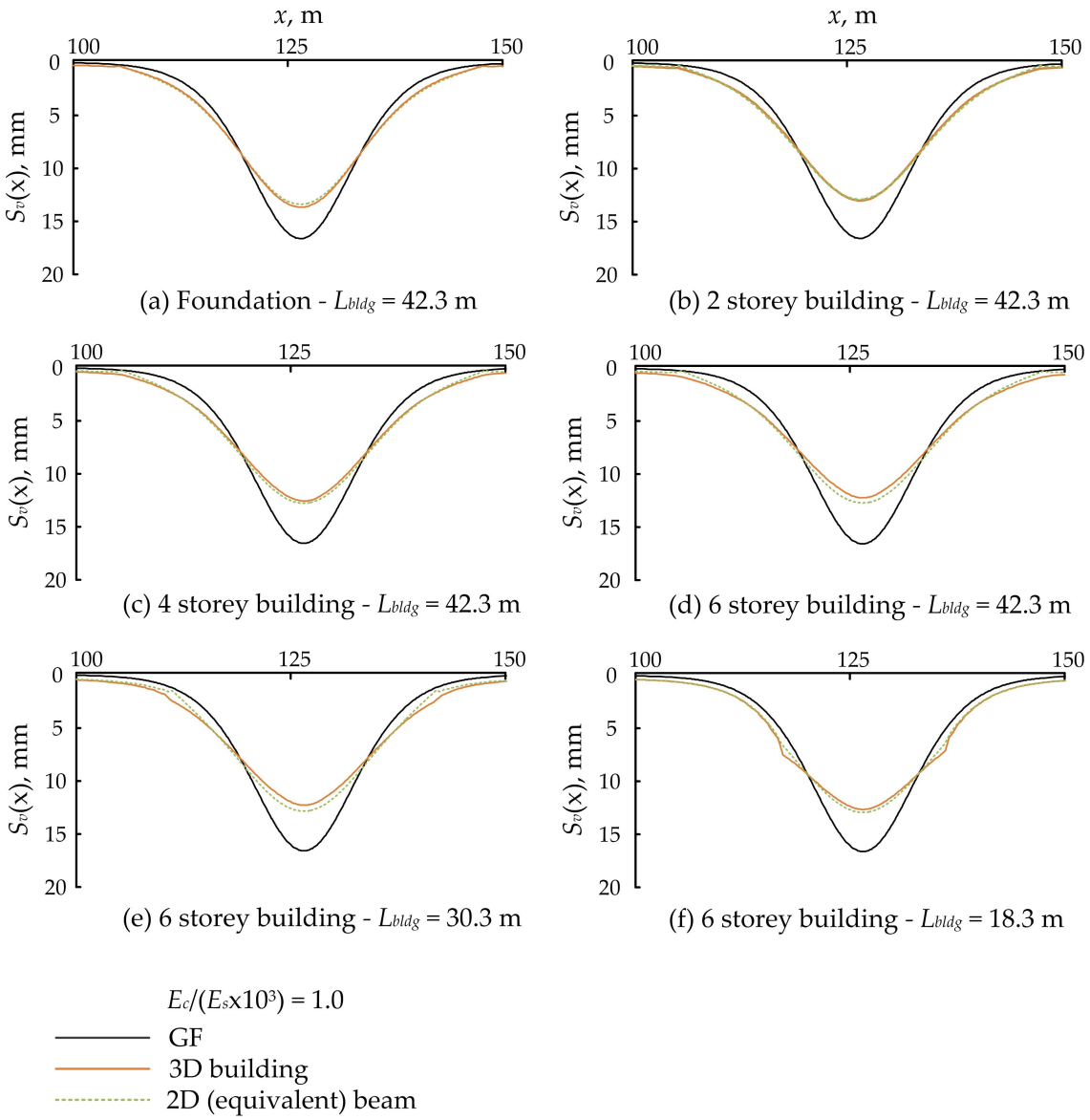

Fig. 8.21 Comparison of the predicted building effect between a 3D building and an equivalent beam on ground displacements due to tunnelling for the building of model 2 (Table 8.2) with $e/L_{bldg} = 0$

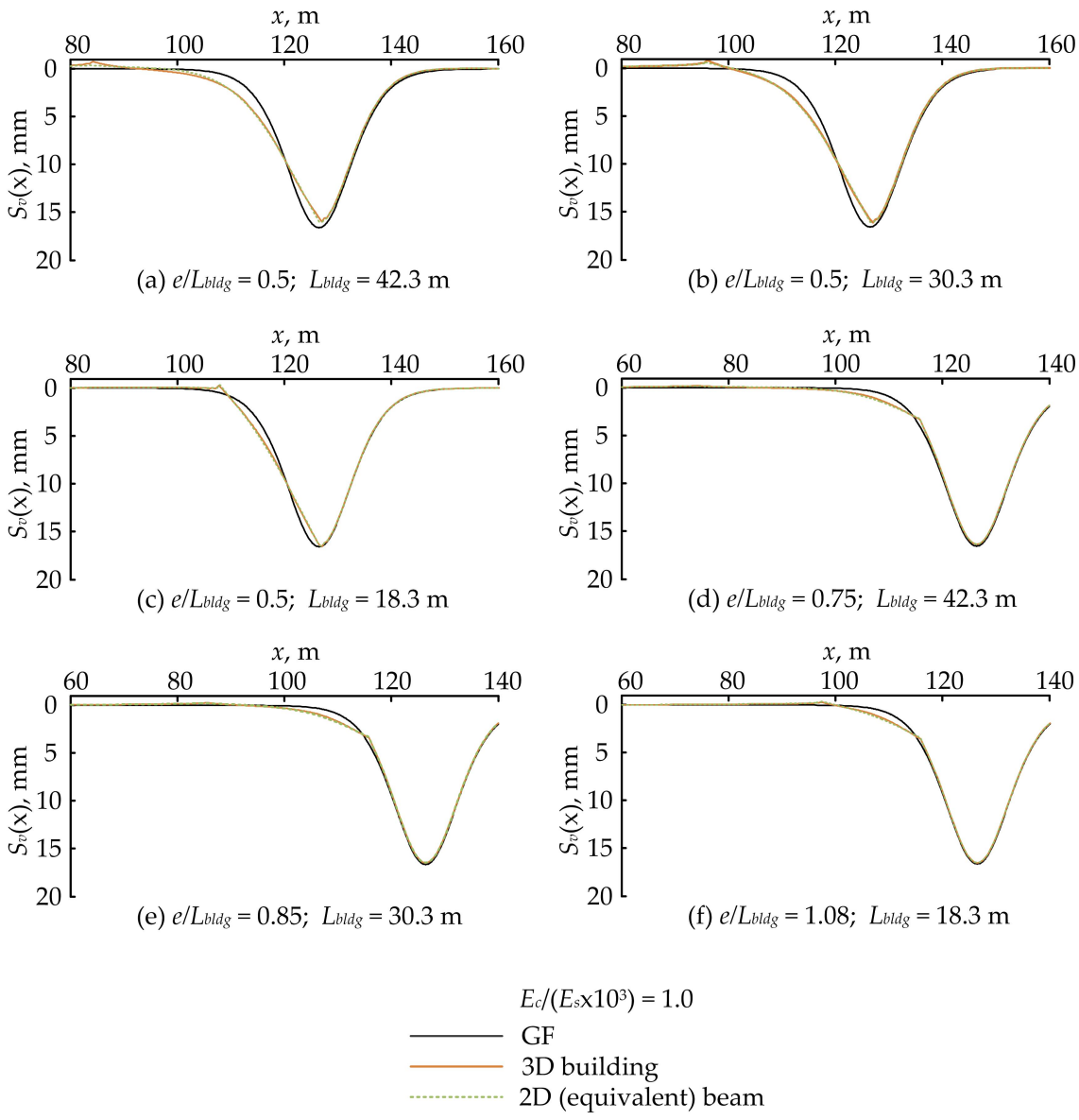

Fig. 8.22 Comparison of the predicted building effect between a 3D building and an equivalent beam on ground displacements for the building of model 2 (Table 8.2) with variable tunnel location and building length

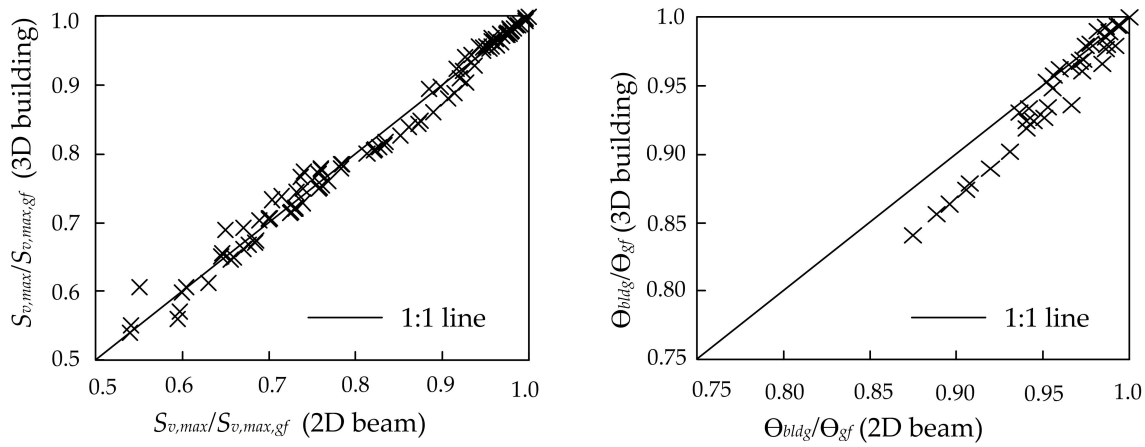

Fig. 8.23 (a) Comparison between the stiffness effect of 3D building and 2D equivalent beam on maximum ground displacements under the building, (b) comparison of building rotation between 3D buildings and 2D equivalent beams.

alent beam shows good capability to capture the rotation of the building. Figures 8.22d,e,f show the numerical results for the case where there is an offset of 10.575 m between the building edge and the tunnel centreline ($e/L_{bldg} \geq 0.75$). In the cases of $L_{bldg} = 42.3$ m and 30.3 m, there is a significant part of the building in the undisplaced soil zone which provides a good resistance of the building against rotation. Figures 8.22d,e show that there is no rotation of the building end located in the undisplaced soil zone. For a smaller length (i.e. $L_{bldg} = 18.3$ m), there is a rotation of the building end. In all cases, the results of the equivalent beam showed good agreement with that of the 3D building.

Figure 8.23a compares the stiffness effect of 3D buildings and 2D equivalent beams on the maximum ground settlement under the building. Figure 8.23b demonstrates a comparison between the rotation experienced by 3D buildings and that of the equivalent beams when affected by tunnelling. The presented data points are from various numerical analyses including different tunnel locations, building storeys and dimensions. The figure shows good agreement between the results of both methods.

8.5 Summary

This chapter investigated the effect of 3D global buildings (foundation and superstructure) on ground displacements due to tunnelling in a soil–building domain. The analyses considered both weighted and weightless buildings. In the weightless analyses, the effect of the founda-

tion and individual storeys on the global building behaviour was investigated. The results showed that the contribution of the foundation stiffness to the global building stiffness was greater than that of the superstructure. Furthermore, the contribution of building storeys to the global building bending stiffness decreased with the increase of the storey distance from the foundation. It should be mentioned that the results of the weightless analyses were used to propose a method to replace a 3D building by an equivalent beam in an elastic numerical analysis.

The assumptions made in the analysis and design stages of a building were explained for the case of weighted buildings. Considering these assumptions in the tunnel–soil–building interaction is missing to a great extent in the literature. It was demonstrated that prior to the construction of a new tunnel, the building is in equilibrium with the underlying soil. Tunnelling causes disturbance to this equilibrium and changes the building behaviour by imposing rotation and settlement to the building. This leads to the creation of two building zones: the portion located in the displaced soil zone and that is located in the undisplaced zone. These changes due to the construction of a new tunnel have negative consequences on the building. For example, failure can occur due to the crack development in the structural parts as a result of produced ground deformations, and the load of the building may be redistributed which can add extra load to some columns.

Results showed that building bending stiffness had an important role in redistributing the building weight over the underlying soil after the construction of the tunnel. Ground displacements due to tunnelling generally increased due to the weight of the building; the increase of the weight or the tunnel volume loss led to a larger increase in ground displacements. Additionally, it was shown that the portion of the building located in the undisplaced soil zone reduced building bending deformations. It is worth noting that the results showed the necessity of considering both the weight and the stiffness of buildings together in the analyses of tunnel–soil–building interaction.

The aim of this chapter was to show that (1) a building does not act as a single entity (in a global soil–building domain) when affected by tunnelling, and (2) the assumptions made in the analysis and design stages of buildings prior to tunnelling should be accurately considered in the analysis of tunnel–building interaction. The adoption of a rather simple numerical model (i.e. elastic building, Mohr-Coulomb soil) here was mainly to focus the analysis on the intended aim. The utilisation of more sophisticated material models considering complex soil, structure, and soil-structure interaction behaviour would lead to more accurate results.

Chapter 9

Conclusions and Recommendations for Further Research

Tunnelling has become an inevitable option in crowded urban areas to reduce surface traffic volume and accommodate required infrastructure. Tunnelling in an area where there are existing buildings may cause damage to surface and subsurface structures. Therefore, a detailed analysis of the global tunnel–soil–structure problem is necessary prior to the construction of a new tunnel.

The research of this thesis focused on the interaction between a newly constructed tunnel and existing buildings with shallow foundations. This issue has been studied numerically using different approaches. The focus in previous works was mainly on investigating specific scenarios or obtaining design charts for geotechnical engineers. This provides a good general appreciation of tunnelling effects on buildings, but there are still various limitations that reduce the applicability of these design charts. For example, specific types of soils are taken into account, and the 3D nature of buildings is not considered well. Furthermore, several main parameters that influence the deformation of a 3D building when affected by tunnelling have not been investigated adequately. This thesis studies the 3D behaviour of buildings considering the main parameters that affect the building bending deformation based on mathematical relationships of the stiffness of a structural member. Furthermore, computationally efficient methods are suggested to compute the bending stiffness of 3D buildings. These methods can be easily used by engineers to quantify the role of building stiffness in the global interaction problem.

In addition to suggesting simplified methods to estimate building bending stiffness, this thesis proposes a new method to study the tunnel–building interaction problem using realistic ground displacement values. This method solves problems related to the prediction of ground

displacements due to tunnelling, such as the wideness and shallowness of the settlement trough. Additionally, a detailed analysis of the 3D behaviour of buildings in a global soil–building system is presented, and the interconnection between the weight and the stiffness of a building is investigated.

This chapter presents a summary of the outcomes of the various chapters in this thesis, and suggests recommendations for further research to gain a better understanding of building behaviour in the tunnel–soil–structure interaction.

9.1 Conclusions

9.1.1 Estimation of superstructure stiffness

Chapter 5 presented two methods for the evaluation of the response of framed buildings located above newly constructed tunnels. The methods are for two different tunnel locations: a cantilever approach for the case where the tunnel is constructed outside the building plan area, and a fixed–ended approach for the case where the tunnel is located under the building centreline. It should be noted that these methods are to some extent unconventional, but depending on rigorous finite element analysis results, it is shown that they capture the actual 3D response of buildings and foundations to tunnelling induced ground movements more accurately than previously proposed methods. The methods are based on an analogy of building behaviour to that of a cantilever beam in the cantilever approach, and a fixed–ended beam in the fixed–ended approach. A set of empirical-type equations was developed based on numerical evaluations of the stiffness of 3D framed buildings obtained using Abaqus (finite element analyses).

The analytical expression of the relevant beam (cantilever or fixed–ended) was first adjusted to quantify the bending stiffness of a fixed ended floor in a panel affected by tunnelling induced settlements. This expression was then further developed to account for the number of building bays perpendicular to the tunnel (affecting the end-fixity condition), the number of building storeys, and the number of building bays in the direction of the tunnel axis (all assuming only one building bay perpendicular to the tunnel was affected). Finally, a method to account for scenarios where multiple building bays are affected was proposed.

In the literature, there is a lack of a detailed understanding of how structural elements of a building contribute to the stiffness of the entire building system. Moreover, the 3D nature of buildings is mainly replaced by 2D beams or frames in the current methods of building stiffness estimation. Results of this research, which depend on the analyses of 3D buildings,

demonstrated that the foundation of the building plays a major role in determining its effective stiffness; the contribution of upper storeys was shown to decrease with storey number. The factors influencing the stiffness contribution of each storey to the global building bending stiffness was demonstrated; the ratio of column to floor stiffness was shown to be proportional to the degree of stiffness contribution. Furthermore, the ratio of the length to height of the building was also shown to be proportional to the degree of stiffness contribution.

The proposed methods were validated by comparing their results with numerical simulations of a 3D building. The results showed good agreement of the building bending stiffness estimated by the proposed methods and the numerical simulations. Furthermore, results of the proposed methods as well as available 2D and 3D approaches for estimating building bending stiffness were compared against the outcomes of the numerical analyses. The proposed methods agree well with the numerical analyses and capture important trends of the change of building bending stiffness with number of storeys and building fixity condition that other methods do not. The methods offer the advantage of being very computationally efficient compared to numerical analysis, yet achieve a good level of accuracy for the wide range of framed building characteristics considered.

9.1.2 Estimation of foundation stiffness

Chapter 6 proposed two methods to estimate the bending stiffness of a raft foundation for two cases of tunnel location: a cantilever approach for the case where the tunnel is constructed outside the building plan area, and a fixed–ended method for the case where the tunnel is located under the building centreline. For the cantilever approach, it was shown that tunnelling caused one side of the foundation to experience greater settlements than the other side. In the fixed–ended case, the raft foundation underwent large deformations at the middle. The development of the methods depended on the deflection equation of a beam (Equation 2.3).

In the currently available methods to compute building bending stiffness, buildings are considered as a single entity and a specific attention is not paid to the foundation, especially in the case of a raft foundation which is the most influential building part to determine the response of the building to tunnelling. Numerical results of this work showed that there were two significant parts in foundations based on their behaviour during tunnelling: a loaded part which was located in the displaced soil zone and subjected to deformations due to tunnelling induced ground movements, and a supporting part located in the undisplaced soil zone which provided support to the loaded part. It was determined that the length of the building subjected

to deflections, the length that is not affected by deformations, the cross sectional flexural rigidity of the building and the properties of the soil underlying the undeformed foundation part are the main parameters to estimate bending stiffness. Furthermore, it was explained that the soil elastic modulus in the undisplaced soil zone increased the resistance of the foundation against the rotation and bending deflection. The length of the foundation in the undisplaced soil zone was also essential to increase the foundation bending stiffness. Based on these numerical outcomes, the fixed boundary assumed for the beam in the equation of beam deflection was modified according to the properties of the foundation and the underlying soil, and linked to the soil and concrete elastic moduli and to the length of the building in the displaced and undisplaced soil zones.

The numerical results demonstrated that based on the definition of bending stiffness of a member, the building and the soil should be considered as one global system. Both the soil and the building member influence the bending stiffness of the global building. Dealing with the building as a separate part from the soil does not allow a realistic prediction of the behaviour of the building.

9.1.3 Mixed empirical–numerical method

A mixed empirical-numerical (mixed E–N) method to predict the response of buildings to realistic inputs of tunnelling induced ground movements was presented in Chapter 7. A modified semi-analytical method was used to obtain the greenfield displacements, however any input could be used in the methodology. The input greenfield displacements were based on centrifuge test data and included both horizontal and vertical displacements. The mixed E–N method allows the application of horizontal and vertical displacements to the model either together or separately, thereby allowing a detailed evaluation of the coupling effect of the two displacements. Results obtained from the proposed mixed E–N method were compared against conventional numerical analyses in which the tunnel was simulated, resulting in wider settlement troughs and greater horizontal displacements than expected in reality. It was shown that the action of the unrealistic horizontal displacements in the conventional numerical analyses increased the resistance of the building against bending deformations quite considerably in some scenarios.

With regard to bending modification factors when $e/L_{bldg} = 0$, it was shown that buildings in the mixed E–N analyses were distorted slightly less by ground displacements compared to buildings in the conventional numerical analyses for the sagging and hogging zones. Moreover, higher tensile and lower compressive strains were induced in buildings in the

mixed E–N analyses compared to the conventional numerical simulations. It should be noted that no tensile strains were produced in the conventional numerical analyses due to the very wide horizontal displacement profile.

For eccentric buildings, there was no practical difference between the bending modification factors of the mixed E–N and conventional numerical analyses in the hogging zone while modification factors of the sagging zone in the mixed E–N analyses were significantly higher than those from the conventional numerical analyses. Furthermore, both axial modification factors (compressive and tensile) computed from the mixed E–N method were lower than those estimated from the conventional numerical analyses.

Comparison of deflection ratios between the conventional numerical and mixed E–N methods showed that buildings in the mixed E–N method were distorted by tunnelling induced ground displacements to a greater extent than buildings in the conventional numerical analyses. This demonstrated the importance of incorporating accurate inputs of greenfield ground movements within numerical analyses of tunnel-building interaction.

The effect of volume loss on the modification factors was also investigated in Chapter 7. It was concluded that there was not a significant effect of changing volume loss value on the bending and axial modification factors. This was mainly because the position of the inflection points and the width of the settlement trough did not change considerably by varying the volume loss.

The influence of soil relative density on the tunnel-building interaction was examined for two relative densities of $I_d = 90\%$ and 30%. For a given tunnel volume loss, larger displacements occur in the soil with low relative density due to the contraction of the soil during tunnel volume loss. This causes a large soil area to experience settlements. It was shown that the degree of effect of ground displacements on buildings changed according to the geometry of the settlement curves, and the displaced and undisplaced soil zones. It is worth noting that the effect of relative density on the tunnel-building interaction in sands can not conveniently be investigated using conventional numerical analyses of tunnelling because of the occurrence of a complex dilation/contraction in sands due to volume loss. The proposed mixed E–N method is a good tool for this investigation, however, an accurate estimation of the soil elastic modulus is needed in order to obtain realistic results. Additionally, the strength parameters of the soil can not be included in the analysis.

9.1.4 Building effects on ground displacements

Chapter 8 presented the effects of 3D buildings on ground displacements due to tunnelling in a global soil–building system. Both cases of weightless and weighted buildings were considered. In addition, an equivalent beam method was proposed to model the building as a beam in a 2D finite element analysis. The main conclusions are summarised as below.

Weightless buildings

In the numerical simulations of weightless buildings, the stiffness effect of different components of concrete framed buildings (foundation and building storeys) on tunnelling induced ground displacements was investigated. Additionally, the effect of the building length and the relative tunnel–building location on the behaviour of the building in the tunnel–soil–structure system was studied.

The numerical results showed that in a building, the effect of foundation stiffness on ground displacements caused by tunnelling is significantly higher than that of the superstructure. Furthermore, the stiffness effect of structural members on ground displacements decreases considerably with the increase of the member distance from the ground. Similar to the conclusions of Section 9.1.2, higher storeys in a building show less contribution to the building's ability to resist soil deformations.

Results showed that representing the building as an equivalent beam using the Potts and Addenbrooke (1997) method greatly overestimates the stiffness effect of the building on ground displacements caused by tunnelling. The available methods in the literature to represent the 3D building by an equivalent beam disregard the stiffness contribution of different structural members to the global building stiffness.

The results of Chapters 5 and 6 in addition to the numerical results of Chapter 8 for weightless buildings were used to propose an equivalent beam method to represent the 3D building in a 2D analysis. Results showed that the proposed equivalent beam method can replicate the behaviour of the 3D building to a good extent.

Weighted buildings

In the numerical analyses of weighted buildings, the influence of the building weight and bending stiffness together on the tunnel–building interaction was studied. Moreover, the assumptions made in the analysis and design of the building prior to the construction of the tunnel were considered.

The results indicated that the stiffness and the weight of a building were strongly interconnected. This interconnection comes from the design and the analysis stages of the building prior to the construction stage. The loads acting on a building are calculated in the analysis stage of the building, and the geometry of the members and final material properties are given to the building in the design stage. Bending stiffness of the building is achieved in the design stage based on the calculated loads in the analysis stage. Furthermore, the general outcomes of this chapter showed that the occurrence of changes to the assumptions made to the building in the analysis and design stages, and the parameters on which bending stiffness of a member depend, are vitally important to be taken into consideration when investigating a building located close to a newly constructed tunnel.

The construction of a new tunnel close to an existing building causes a disturbance to the equilibrium state of building loads with the underlying soil pressure. The creation of plasticity in the soil after the tunnel construction is a reason of the building–soil equilibrium disturbance, and leads to an increase in ground surface settlements in the presence of a weighted building. Additionally, the increase of the tunnel volume loss and the applied building weight results in an increase in the plastic zones created within the soil.

It was also confirmed that the displaced and undisplaced soil zones by tunnelling have a great role in the tunnel–building interaction problem. The increase of the building length located in the displaced soil zone resulted in a larger building deformation, and in turn, caused an increase to the ground surface settlements. In contrast, the building part located in the undisplaced soil zone provided a support to the building against deformations.

A very influential parameter having an important role in the tunnel–building interaction is the allowance of the building rotation during the construction of a new tunnel. It was indicated that the resistance of a building to bending deformations reduced dramatically when the building was subjected to rotation. This case happens when a tunnel is constructed outside the plan area of a building. It was also shown that for a tunnel location having an eccentricity with the building, the length of the building located in the undisplaced soil zone decreased the flexibility of the building to rotation.

9.2 Recommendations for further research

The outcomes of this research have given a good understanding about the importance of considering 3D buildings together with the underlying soil in a three dimensional domain in order to predict a realistic behaviour of the global soil–building system. However, there

are features that require further investigations to eliminate the assumptions made during the analyses. The recommendations for further research are outlined in the following points.

- In the proposed methods to estimate the bending stiffness of building parts, the building was assumed to be elastic and the propagation of cracks was not allowed. It was explained in the literature that the development of cracks reduces the stiffness of buildings to a great extent. It would be important to revise the proposed methods using a building model that allows the development of cracks so that more realistic values of building bending stiffness are achieved.

- It was assumed in the numerical simulations of 3D buildings that the dimensions of each structural member (i.e. beams, columns), and the span of building panels in each direction were the same in all building storeys. Furthermore, the dimensions of the column cross sections depended on the dimensions of the connected beams. Considering buildings with different span lengths and variable dimensions of structural members will result in more general equations to calculate bending stiffness of various buildings.

- The superstructure and the foundation were treated separately from each other whereas they are strongly interconnected. The connection of the columns and the foundation certainly change the bending behaviour of the footing. Analysing the whole building including the superstructure and the foundation may lead to different results from the algebraic addition of the superstructure and foundation bending stiffness.

- The building, as an independent member, was three dimensional in the analyses of this research but the global problem was two dimensional since the effect of the tunnel head advancement was not considered. In other words, the deflection of the soil and the building was in one plane (perpendicular to the tunnel axis). Consideration of the tunnel head advancement will be an essential further work to represent the tunnel–building interaction problem in numerical analyses closer to the reality.

- In the proposed methods to estimate the bending stiffness of the foundation, the soil was assumed to behave as a linearly elastic material. Adopting a non-linear elastic material to represent the soil will lead to more realistic results since linear elasticity does not capture the degradation of soil properties due to strains when the tunnel is constructed.

- In the investigation of analysis and design assumptions made prior to the construction of a building (before tunnelling), a rather simple numerical model (i.e. elastic building, Mohr-Coulomb soil, and rough and frictionless interfaces between the soil and foundation, preventing slip and separation) was intentionally adopted in order to focus the analysis on the intended aim. More sophisticated analyses considering complex soil, structure, and soil-structure interaction behaviour would undoubtedly give results that vary somewhat to those presented here, however the main conclusions would not deviate from those listed in this research.

References

Abdullah, M. H. and Taha, M. R. (2013). A review of the effects of tunneling on adjacent piles. *Electronic Journal of Geotechnical Engineering*, 18:2739–2762.

ACI-Building-Code (2011). *ACI 318-11 Building Code Requirements for Structural Concrete and Commentary*. American Concrete Institute, Retrieved 8.

ACI-Committee-336 (2002). Suggested analysis and design procedures for combined footings and mats. *American Concrete Institute*, 336.2R-88.

Addenbrooke, T. I. (1996). *Numerical analysis of tunnelling in stiff clay*. PhD thesis, Imperial College London (University of London).

Addenbrooke, T. I., Potts, D. M., and Puzrin, A. M. (1997). The influence of pre-failure soil stifiness on the numerical analysis of tunnel construction. *Geotechnique*, 47(3):693–712.

Alshkane, Y. M. A. (2015). *Numerical modelling investigation of rock mass behaviour under gravity dams*. PhD thesis, University of Nottingham.

Arya, C. (2009). *Design of Structural Elements: Concrete, steelwork, masonry and timber designs to British Standards and Eurocodes*. Taylor & Francis, 3rd edition.

Atkinson, J. and Potts, D. (1977). Stability of a shallow circular tunnel in cohesionless soil. *Geotechnique*, 27(2):203–215.

Attewell, P. and Woodman, J. (1982). Predicting the dynamics of ground settlement and its derivitives caused by tunnelling in soil. *Ground engineering*, 15(8).

Attewell, P. B. and Yeates, J. (1984). Tunnelling in soil. ground movements and their effects on structures. *P. B. Attewell and R. K. Taylor (editors), Surrey University Press*, pages 132–215.

Attewell, P. B., Yeates, J., and Selby, A. R. (1986). Soil movements induced by tunnelling and their effects on pipelines and structures.

Augarde, C. E. (1997). *Numerical modelling of tunnelling processes for assessment of damage to buildings*. PhD thesis, University of Oxford.

Azevedo, R. F., Parreira, A. B., and Zornberg, J. G. (2002). Numerical analysis of a tunnel in residual soils. *Journal of Geotechnical and Geoenvironmental Engineering*, 128(3):227–236.

Baumgart, F. (2000). Stiffness-an unknown world of mechanical science? *Injury-International Journal for the Care of the Injured*, 31(2):14–23.

Beer, F. P., Johnston Jr, E. R., Mazurek, D. F., and Eisenberg, E. R. (2012). *Mechanics of materials*. McGraw Hill Brasil, 6th edition.

Bhatt, P., MacGinley, T. J., and S., C. B. (2006). *Reinforced concrete: design theory and examples*. Taylor & Francis, 3rd edition.

Bilotta, E., Paolillo, A., Russo, G., and Aversa, S. (2017). Displacements induced by tunnelling under a historical building. *Tunnelling and Underground Space Technology*, 61:221–232.

Biot, M. (1937). Bending of an infinite beam on an elastic foundation. *Journal of Applied Mechanics*, (203).

Bloodworth, A. G. (2002). *Three-dimensional analysis of tunnelling effects on structures to develop design methods*. University of Oxford.

Bobet, A. (2001). Analytical solutions for shallow tunnels in saturated ground. *Journal of Engineering Mechanics*, 127(12):1258–1266.

Bobet, A. (2010). Numerical methods in geomechanics. *The Arabian Journal for Science and Engineering*, 35(1B):27–48.

Boone, S. (2001). Assessing construction and settlement-induced building damage: a return to fundamental principles. *Underground Construction*, 34(2):559–570.

Boone, S. J. (1996). Ground-movement-related building damage. *Journal of geotechnical engineering*, 122(11):886–896.

Borst, R. d., Crisfield, M. A., Remmers, J. J. C., and Verhoosel, C. V. (2012). *Non-linear finite element analysis of solids and structures*. John Wiley & Sons Ltd, 2nd edition.

Boscardin, M. D. and Cording, E. J. (1989). Building response to excavation-induced settlement. *Journal of Geotechnical Engineering*, 115(1):1–21.

Bowles, J. E. (1997). *Foundation analysis and design*. McGraw-Hill, 5th edition.

British-Standard (1986). Code of practice for foundations, formerly cp 2004. *British Standard, London*.

Broms, B. B. and Bennermark, H. (1967). Stability of clay at vertical openings. *Journal of Soil Mechanics & Foundations Div*.

Bull, J. W. (1993). *Soil-Structure interaction: numerical analysis and modelling*. CRC Press.

Burd, H., Houslby, G., Augarde, C., and Liu, G. (2000). Modelling tunnelling-induced settlement of masonry buildings. *Proceedings of the Institution of Civil Engineers-Geotechnical Engineering*, 143(1):17–30.

Burland and Wroth (1974). *Settlement of buildings and associated damage*. Pentech Press.

Burland, J. (1995). *Assessment of risk of damage to buildings due to tunnelling and excavation*. Imperial College of Science, Technology and Medicine.

Burland, J. B., Broms, B. B., and de Mello, V. F. (1976). Behaviour of foundations and structures. In *6th European conference on SM&FE, Vienna*, pages 495–546.

Camós, C., Molins, C., and Arnau, O. (2014). Case study of damage on masonry buildings produced by tunneling induced settlements. *International Journal of Architectural Heritage*, 8(4):602–625.

Castaldo, P., Calvello, M., and Palazzo, B. (2013). Probabilistic analysis of excavation-induced damages to existing structures. *Computers and Geotechnics*, 53:17–30.

Celestino, T., Gomes, R., and Bortolucci, A. A. (2000). Errors in ground distortions due to settlement trough adjustment. *Tunnelling and Underground Space Technology*, 15(1):97–100.

Cheng, C., Dasari, G., Chow, Y., and Leung, C. (2007). Finite element analysis of tunnel–soil–pile interaction using displacement controlled model. *Tunnelling and Underground Space Technology*, 22(4):450–466.

Cheng, C., Dasari, G., Leung, C., Chow, Y., and Rosser, H. (2004). 3D Numerical study of tunnel-soil-pile interaction. *Tunnelling and Underground Space Technology*, 19(4):381–382.

Clough, G. and Schmidt, B. (1981). Design and performance of excavation and tunnels in soft clays. soft clay engineering. *Developments in geotechnical engineering*, 20:567–634.

Coduto, D. P. (2001). *Foundation design: principles and practices*. Prentice Hall, 2nd edition.

Coelho, P., Haigh, S., and Madabhushi, S. (2006). Effects of successive earthquakes on saturated deposits of sand. In *Physical Modelling in Geotechnics, Two Volume Set: Proceedings of the Sixth International Conference on Physical Modelling in Geotechnics, 6th ICPMG'06, Hong Kong, 4-6 August 2006*, volume 1, page 443. CRC Press.

Cording, E., Long, J., Son, M., Laefer, D., Ghahreman, B., and Gyeongsan, G. (2010). Assessment of excavation-induced building damage. *Earth Retention Conference 3: proceedings of the 2010 Earth Retention Conference*.

Cording, E. J., Son, M., Laefer, D. F., et al. (2008). Examples of building response to excavation and tunneling. In *Movimientos de edificios inducidos por excavaciones: Criterios de dano y gestion del riesgo, Universidad y Empresa: Abriendo Caminos, Jornada Tecnica, Barcelona, Spain*, pages 69–94.

Courant, R. (1943). Variational methods for the solution of problems of equilibrium and vibrations. *Bull. Amer. Math. Soc*, 49(1):1–23.

Cox, M. R. B. (2008). *The influence of grain shape on dilatancy*. The University of Arizona.

Das, B. M. (2010). *Principles of geotechnical engineering*. Cengage Learning, 7th edition.

Dasari, G., Rawlings, C., and Bolton, M. (1996). Numerical modelling of a NATM tunnel construction in london clay. *Geotechnical aspects of underground construction in soft ground*, pages 491–496.

Dasari, G. R. (1996). *Modelling the variation of soil stiffness during sequential construction.* PhD thesis, University of Cambridge.

Davies, A. J. (2011). *The finite element method: An introduction with partial differential equations*. Oxford university press, 2nd edition.

Davis, M. E. (1984). *Numerical methods and modeling for chemical engineers*. John Wiley & Sons.

Dimmock, P. S. and Mair, R. J. (2008). Effect of building stiffness on tunnelling-induced ground movement. *Tunnelling and Underground Space Technology*, 23(4):438–450.

Dolezalová, M. (2002). Approaches to numerical modelling of ground movements due to shallow tunnelling. In *Planning and Engineering for the Cities of Tomorrow. Second International Conference on Soil Structure Interaction in Urban Civil Engineering*.

Duggal, S. (2009). *Design of steel structures*. Tata McGraw-Hill Education, 3rd edition.

Dutta, S. C. and Roy, R. (2002). A critical review on idealization and modeling for interaction among soil–foundation–structure system. *Computers & structures*, 80(20):1579–1594.

Eberhardt, E. (2001). Numerical modelling of three-dimension stress rotation ahead of an advancing tunnel face. *International Journal of Rock Mechanics and Mining Sciences*, 38(4):499–518.

Ehsan, R. (2013). A study of geotechnical constitutive models using plaxis 2d. *ICE Thames Valley Branch G&S Papers Competition*.

Einstein, H. H. and Schwartz, C. W. (1979). Simplified analysis for tunnel supports. *Journal of Geotechnical and Geoenvironmental Engineering*, 105(ASCE 14541).

Elkayam, I. (2013). *Tunneling Induced Ground Displacements and Their Effects on Structures*. PhD thesis, Senate of the Technion - Israel Institute of Technology.

Eng, C. C. Y. B. (2003). Finite element study of tunnel-soil-pile interaction. *MSc Dissertation, National University of Singapore*.

Fargnoli, V., Gragnano, C., Boldini, D., and Amorosi, A. (2015). 3d numerical modelling of soil–structure interaction during epb tunnelling. *Géotechnique*, 65(1):23–37.

Farrell, R. (2010). *Tunnelling in sands and the response of buildings*. PhD thesis, University of Cambridge.

Farrell, R. and Mair, R. (2012). Centrifuge modelling of the response of buildings to tunnelling. In *Proc. of the International Symposium on Geotechnical Aspects of Underground Construction in Soft Ground*, pages 343–351.

Farrell, R., Mair, R., Sciotti, A., and Pigorini, A. (2014). Building response to tunnelling. *Soils and Foundations*, 54(3):269–279.

Farrell, R., Mair, R., Sciotti, A., Pigorini, A., and Ricci, M. (2012). The response of buildings to tunnelling: a case study. In *Proceedings of 7th International Symposium on Geotechnical Aspects of Underground Construction in Soft Ground, May, Rome*.

Fattah, M. Y., Shlash, K. T., and Salim, N. M. (2012). Prediction of settlement trough induced by tunneling in cohesive ground. *Acta Geotechnica*, 8(2):167–179.

Finno, R. J. and Clough, G. W. (1985). Evaluation of soil response to EPB shield tunneling. *Journal of Geotechnical Engineering*, 111(2):155–173.

Finno, R. J., Voss Jr, F. T., Rossow, E., and Blackburn, J. T. (2005). Evaluating damage potential in buildings affected by excavations. *Journal of geotechnical and geoenvironmental engineering*, 131(10):1199–1210.

Franza, A. (2016). *Tunnelling and its effects on piles and piled structures*. PhD thesis, University of Nottingham.

Franza, A. and Marshall, A. (2015a). Analytical investigation of soil deformation patterns above tunnels in sandy soil. In *Proceedings of the XVI ECSMGE, Geotechnical Engineering for Infrastructure and Development*, pages 467–472.

Franza, A. and Marshall, A. (2015b). Semi-analytical prediction of ground movements due to shallow tunnels in sand. In *Proceedings of the XVI ECSMGE, Geotechnical Engineering for Infrastructure and Development*, pages 461–466.

Franzius, J., Potts, D., and Burland, J. (2005). The influence of soil anisotropy and k0 on ground surface movements resulting from tunnel excavation. *Géotechnique*, 55(3):189–199.

Franzius, J. N. (2003). *Behaviour of buildings due to tunnel induced subsidence*. PhD thesis, University of London.

Franzius, J. N., Potts, D. M., Addenbrooke, T. I., and Burland, J. B. (2004). The influence of building weight on tunnelling-induced ground and building deformation. *Soils and Foundations*, 44(1):25–38.

Franzius, J. N., Potts, D. M., and Burland, J. B. (2006). The response of surface structures to tunnel construction. *Proceedings of the ICE-Geotechnical Engineering*, 159(1):3–17.

Galli, G., Grimaldi, A., and Leonardi, A. (2004). Three-dimensional modelling of tunnel excavation and lining. *Computers and Geotechnics*, 31(3):171–183.

Geddes, J. D. (1991). Discussion of "Building response to excavation-induced settlement" by Marco D. Boscardin and Edward J. Cording (january, 1989, vol. 115, no. 1). *Journal of Geotechnical Engineering*, 117(8):1276–1278.

Gere, J. (2004). *Mechanics of materials*. Bill Stenquist, 4th edition.

Gere, J. and Goodno, B. (2009). *Mechanics of materials*. Cengage Learning.

Ghoneim, M. A. and El-Mihilmy, M. T. (2008). *Design of reinforced concrete structures*, volume 2. Al-Balagh press, Egypt, 2nd edition.

Giardina, G., DeJong, M., and Mair, R. (2014a). Important aspects when modelling the interaction between surface structures and tunnelling in sand. In *Geotechnical Aspects of Underground Construction in Soft Ground-Proceedings of the 8th Int. Symposium on Geotechnical Aspects of Underground Construction in Soft Ground, TC204 ISSMGE-IS-SEOUL 2014*, pages 263–268.

Giardina, G., DeJong, M. J., and Mair, R. J. (2015). Interaction between surface structures and tunnelling in sand: Centrifuge and computational modelling. *Tunnelling and Underground Space Technology*, 50:465–478.

Giardina, G., Hendriks, M., and Rots, J. (2009). Coupled analysis of building damage due to tunneling. In *Proceedings of the Workshop on Computational Modeling on Concrete, Masonry and Fiber-reinforced Composites, Delft, The Netherlands, 17-18 June 2009*. TU Delft.

Giardina, G., Hendriks, M. A., and Rots, J. G. (2010). Numerical analysis of tunnelling effects on masonry buildings: the influence of tunnel location on damage assessment. In *Advanced Materials Research*, volume 133, pages 289–294. Trans Tech Publ.

Giardina, G., Hendriks, M. A., and Rots, J. G. (2014b). Damage functions for the vulnerability assessment of masonry buildings subjected to tunneling. *Journal of Structural Engineering*, 141(9):04014212.

Giardina, G., Marini, A., Hendriks, M. A., Rots, J. G., Rizzardini, F., and Giuriani, E. (2012). Experimental analysis of a masonry façade subject to tunnelling-induced settlement. *Engineering Structures*, 45:421–434.

Giardina, G., Van de Graaf, A. V., Hendriks, M. A., Rots, J. G., and Marini, A. (2013). Numerical analysis of a masonry façade subject to tunnelling-induced settlements. *Engineering Structures*, 54:234–247.

Gioda, G. and Swoboda, G. (1999). Developments and applications of the numerical analysis of tunnels in continuous media. *International Journal for Numerical and Analytical Methods in Geomechanics*, 23(13):1393–1405.

Goh, K. and Mair, R. (2011a). Building damage assessment for deep excavations in singapore and the influence of building stiffness. *Geotechnical Engineering*, 42:1–12.

Goh, K. and Mair, R. (2011b). The horizontal response of framed buildings on individual footings to excavation-induced movements. In *Proceedings of 7th International Symposium on Geotechnical Aspects of Underground Construction in Soft Ground, May, Rome*.

Goh, K. H. and Mair, R. J. (2014). Response of framed buildings to excavation-induced movements. *Soils and Foundations*, 54(3):250–268.

Gonzalez, C. and Sagaseta, C. (2001). Patterns of soil deformations around tunnels. Application to the extension of Madrid Metro. *Computers and Geotechnics*, 28(6):445–468.

Grant, R. and Taylor, R. (2000). Tunnelling-induced ground movements in clay. *Proceedings of the Institution of Civil Engineers-Geotechnical Engineering*, 143(1):43–55.

Guedes, P. d. M. and Pereira, C. S. (2000). The role of the soil k_0 value in numerical analysis of shallow tunnels. *Geotechnical aspects of underground construction in soft ground, Balkema, Rotterdam*, pages 379–384.

Gunaratne, M. (2006). *The foundation engineering handbook*. Taylor & Francis - Boca Raton, Florida.

Gunn, M. (1993). The prediction of surface settlement profiles due to tunnelling. In *PREDICTIVE SOIL MECHANICS. PROCEEDINGS OF THE WROTH MEMORIAL SYMPOSIUM, 27-29 JULY 1992, ST CATHERINE'S COLLEGE, OXFORD*.

Gupta, S. C. (1997). *Raft Foundation Design And Analysis With A Practical Approach*. New Age International.

Heath, G. and West, K. (1996). Ground movement at depth in london clay. In *International Journal of Rock Mechanics and Mining Sciences and Geomechanics Abstracts*, volume 8, page 381A.

Hergarden, H., Van der Poel, J., and Van der Schrier, J. (1996). Ground movements due to tunneling: influence on pile foundations. In *Proc. of the Int. Symp. on Geotechnical Aspects of Underground Construction in Soft Ground. London: AA Balkema*, pages 519–524.

Hetenyi, M. (1946). *Beams on elastic foundation*. University of Michigan Pres, Ann Arbor, Michigan.

Hetenyi, M. (1950). A general solution for the bending of beams on an elastic foundation of arbitrary continuity. *Journal of Applied Physics*, 21(1):55–58.

Hibbeler, R. C. (2012). *Structural analysis*. Pearson Prentice Hal, New Jersey, 8th edition.

Horvath, J. S. (1983). New subgrade model applied to mat foundations. *Journal of Geotechnical Engineering*, 109(12):1567–1587.

Houlsby, G. (1991). *How the dilatancy of soils affects their behaviour*. University of Oxford, Department of Engineering Science Oxford.

Hrennikoff, A. (1941). Solution of problems of elasticity by the framework method. *Journal of applied mechanics*, 8(4):169–175.

Huang, Y. H. (2004). *Pavement analysis and design*. Pearson Prentice Hall, 2nd edition.

Jacobsz, S. (2002). *The effects of tunnelling on piled foundations*. PhD thesis, Geotechnical Department. Cambridge, University of Cambridge.

Jacobsz, S., Standing, J., Mair, R., Hagiwara, T., and Sugiyama, T. (2004). Centrifuge modelling of tunnelling near driven piles. *Soils and Foundations*, 44(1):49–56.

Jurecic, N., Zdravkovic, L., and Jovicic, V. (2013). Predicting ground movements in london clay. *Proceedings of the Institution of Civil Engineers-Geotechnical engineering*, 166(5):466–482.

Kappen, J. M., Giardina, G., Hendriks, M. A., and Rots, J. G. (2013). 3D numerical analysis of tunnelling induced damage: The influence of the alignment of a masonry building with the tunnel axis. In *EURO: TUN 2013: 3rd International Conference on Computational Methods in Tunneling and Subsurface Engineering, Bochum, Germany, 17-19 April 2013*.

Katzenbach, R. and Breth, H. (1981). Nonlinear 3D analysis for natm in Frankfurt clay. In *Proceedings of the International Conference on Soil Mechanics and Foundation Engineering, 10th.*, volume 1, pages 315–318.

Kimmerling, R. E. (2002). Geotechnical engineering circular no. 6: Shallow foundations.

Kimura, T. and Mair, R. (1981). Centrifugal testing of model tunnels in soft clay. In *Proceedings of the 10th international conference on soil mechanics and foundation engineering*, pages 319–322. ISSMFE: International Society for Soil Mechanics and Foundation Engineering.

Klar, A. and Marshall, A. M. (2008). Shell versus beam representation of pipes in the evaluation of tunneling effects on pipelines. *Tunnelling and Underground Space Technology*, 23(4):431–437.

Kolymbas, D. (2005). *Tunnelling and tunnel mechanics: A rational approach to tunnelling*. Springer Science & Business Media.

Lambe, T. (1973). Predictions in soil engineering. *Geotechnique*, 23(2):151–202.

Lee, G. and Ng, C. (2002). Three-dimensional analysis of ground settlements due to tunnelling: Role of k0 and stiffness anisotropy. In *of: Proc. of the International Symposium on Geotechnical Aspects of Underground Construction in Soft Ground*, pages 617–622.

Lee, G. T. and Ng, C. W. (2005). Effects of advancing open face tunneling on an existing loaded pile. *Journal of Geotechnical and Geoenvironmental Engineering*, 131(2):193–201.

Lee, K., Rowe, R. K., and Lo, K. (1992). Subsidence owing to tunnelling. I. Estimating the gap parameter. *Canadian Geotechnical Journal*, 29(6):929–940.

Li, X.-q. and Zhu, C.-c. (2007). Numerical analysis on the ground settlement induced by shield tunnel construction. *Journal of Highway and Transportation Research and Development (English Edition)*, 2(2):73–79.

Li, Z. (2011). *Advanced concrete technology*. John Wiley & Sons.

Liu, G., Houlsby, G. T., and Augarde, C. E. (2000). 2-dimensional analysis of settlement damage to masonry buildings caused by tunnelling. *The Structural Engineer*, 79(1):19–25.

Liu, S. (2016). *Application of shakedown theory in the structural design of bituminous pavements*. PhD thesis, University of Nottingham.

Loganathan, N. and Poulos, H. (1998). Analytical prediction for tunneling-induced ground movements in clays. *Journal of Geotechnical and Geoenvironmental Engineering*, 124(9):846–856.

Loganathan, N., Poulos, H., and Xu, K. (2001). Ground and pile-group responses due to tunnelling. *Soils and foundation*, 41(1):57–67.

Losacco, N., Burghignoli, A., and Callisto, L. (2014). Uncoupled evaluation of the structural damage induced by tunnelling. *Géotechnique*, 64(8):646–656.

Lunardi, P. (2008). *Design and construction of tunnels: Analysis of Controlled Deformations in Rock and Soils (ADECO-RS)*. Springer Science & Business Media.

Mair, R. (1993). Unwin memorial lecture 1992. Developments in geotechnical engineering research: Application to tunnels and deep excavations. delivered at the ice on 17 march 1992.(abridged).(winner of 1994 geotechnical research medal). In *Proceedings of the Institution of Civil Engineers-Civil Engineering*, volume 97, pages 27–41. Thomas Telford-ICE Virtual Library.

Mair, R. (2008). Tunnelling and geotechnics: new horizons. *Géotechnique*, 58(9):695–736.

Mair, R. (2013). Tunnelling and deep excavations: Ground movements and their effects. In *Proc., 15th European Conf. on Soil Mechanics and Geotechnical Engineering—Geotechnics of Hard Soils—Weak Rocks (Part 4)*, pages 39–70. IOS Press, Amsterdam.

Mair, R., Gunn, M., and O'REILLY, M. (1982). Ground movement around shallow tunnels in soft clay. *Tunnels & Tunnelling International*, 14(5).

Mair, R. and Taylor, R. (1997). Theme lecture: Bored tunneling in the urban environment. In *Proceedings of the Fourteenth International Conference on Soil Mechanics and Foundation Engineering (Hamburg, 1997), Balkema*, pages 2353–2385.

Mair, R., Taylor, R., and Bracegirdle, A. (1993). Subsurface settlement profiles above tunnels in clays. *Geotechnique*, 43(2).

Mair, R., Taylor, R., and Burland, J. (1996). Prediction of ground movements and assessment of risk of building damage due to bored tunnelling. In *Fourth International Symposium of International Conference of Geotechnical Aspects of on Underground Construction in Soft Ground*, pages 713–718. AA Balkema.

Mair, R. J. (1979). *Centrifugal modelling of tunnel construction in soft clay*. PhD thesis.

Maleki, M., Sereshteh, H., Mousivand, M., and Bayat, M. (2011). An equivalent beam model for the analysis of tunnel-building interaction. *Tunnelling and Underground Space Technology*, 26(4):524–533.

Maraš-Dragojević, S. (2012). Analysis of ground settlement caused by tunnel construction. *Građevinar*, 64(07):573–581.

Marshall, A. (2009). *Tunnelling in sand and its effect on pipelines and piles*. PhD thesis, University of Cambridge.

Marshall, A., Farrell, R., Klar, A., and Mair, R. (2012). Tunnels in sands: the effect of size, depth and volume loss on greenfield displacements. *Géotechnique*, 62(5):385.

McCormac, J. C. and Brown, R. H. (2014). *Design of reinforced concrete*. John Wiley & Sons, 9th edition.

McHenry, D. (1943). A lattice analogy for the solution of stress problems. *Journal of the Institution of Civil Engineers*, 21(2):59–82.

Melis, M. and Rodriguez Ortiz, J. (2001). Consideration of the stiffness of buildings in the estimation of subsidence damage by epb tunnelling in the madrid subway. In *Response of buildings to excavation induced ground movements, Proc. intern. conf., London*, pages 17–18.

Meyerhof, G. (1953). Some recent foundation research and its application to design. *The Structural Engineer*, 31(6):151–167.

Miliziano, S., Soccodato, F., and Burghignoli, A. (2002). Evaluation of damage in masonry buildings due to tunnelling in clayey soils. In *of: Proc. of the International Symposium on Geotechnical Aspects of Underground Construction in Soft Ground*, pages 335–340.

Mirhabibi, A. and Soroush, A. (2013). Effects of building three-dimensional modeling type on twin tunneling-induced ground settlement. *Tunnelling and underground space technology*, 38:224–234.

Moaveni, S. (1999). *Finite element analysis: theory and application with ANSYS*. Printice-Hall, Inc., New Jersey.

Moh, Z., Ju, D. H., and Hwang, R. (1996). Ground movements around tunnels in soft ground. In *Proceedings of the International Symposium on Geotechnical Aspects of Underground Construction in Soft Ground. London: Balkema AA*, pages 725–730.

Möller, S. C. (2006). *Tunnel induced settlements and structural forces in linings*. Univ. Stuttgart, Inst. f. Geotechnik.

Mroueh, H. and Shahrour, I. (2003). A full 3-d finite element analysis of tunneling–adjacent structures interaction. *Computers and Geotechnics*, 30(3):245–253.

Mroueh, H. and Shahrour, I. (2008). A simplified 3d model for tunnel construction using tunnel boring machines. *Tunnelling and Underground Space Technology*, 23(1):38–45.

Murthy, V. N. S. (2007). Advanced foundation engineering.

Naeini, S. A., Ziaie Moayed, R., and Allahyari, F. (2014). Subgrade reaction modulus (ks) of clayey soils based on field tests. *Journal of Engineering Geology*, 8(1):2021.

Nghiem, H. M. (2009). *Soil-pile-structure interaction effects on high rises under seismic shaking*. ProQuest.

Oettl, G., Stark, R., and Hofstetter, G. (1998). A comparison of elastic–plastic soil models for 2d fe analyses of tunnelling. *Computers and Geotechnics*, 23(1):19–38.

O'reilly, M. and New, B. (1982). Settlements above tunnels in the United Kingdom - their magnitude and prediction. *Tunnelling*, 82:173–181.

Osman, A., Bolton, M., and Mair, R. (2006). Predicting 2d ground movements around tunnels in undrained clay. *Géotechnique.*, 56(9):597–604.

Panet, M. and Guenot, A. (1982). Analysis of convergence behind the face of a tunnel. In *proc. Tunnelling. London 82, the institution of mining and metalluragy*, pages 197–204.

Pasternak, P. (1954). On a new method of analysis of an elastic foundation by means of two foundation constants. *Gosudarstvennoe Izdatelstvo Literaturi po Stroitelstvu i Arkhitekture, Moscow*.

Peck, R. B. (1969). Deep excavations and tunnelling in soft ground. In *Proc. 7th int. conf. on SMFE*, pages 225–290.

Peiro, J. and Sherwin, S. (2005). Handbook of materials modeling. volume i: Methods and models. *Department of Aeronautics, Imperial College, London, UK*, pages 1–32.

Pickhaver, J., Burd, H., and Houlsby, G. (2010). An equivalent beam method to model masonry buildings in 3d finite element analysis. *Computers & Structures*, 88(19):1049–1063.

Pickles, A. and Henderson, T. (2005). Some thoughts on the use of numerical modelling in geotechnical design practice. *Proceedings of Underground Singapore 2005 and Special Session Numerical Analysis in Geotechnical Engineering*, pages 1–2.

Potts, D. (2003). Numerical analysis: a virtual dream or practical reality. *Géotechnique*, 53(6):535–573.

Potts, D. and Addenbrooke, T. (1997). A structure's influence on tunnelling-induced ground movements. *Proceedings of the ICE-Geotechnical Engineering*, 125(2):109–125.

Potts, D. M., Zdravkovic, L., and Zdravković, L. (2001). *Finite element analysis in geotechnical engineering: application*, volume 2. Thomas Telford.

Poulos, S. J. (1971). *The stress-strain curves of soils*. Geotechnical Engineers Incorporated.

Prakash, S. and Sharma, H. D. (1990). *Pile foundations in engineering practice*. John Wiley & Sons.

Puzrin, A., Burland, J., and Standing, J. (2012). Simple approach to predicting ground displacements caused by tunnelling in undrained anisotropic elastic soil. *Géotechnique*, 62(4):341.

Rampello, S., Callisto, L., Viggiani, G., and Soccodato, F. M. (2012). Evaluating the effects of tunnelling on historical buildings: the example of a new subway in rome/auswertung der auswirkungen des tunnelbaus auf historische gebäude am beispiel einer neuen u-bahnlinie in rom. *Geomechanics and Tunnelling*, 5(3):275–299.

Rankin, W. J. (1988). Ground movements resulting from urban tunnelling: predictions and effects. *Geological Society, London, Engineering Geology Special Publications*, 5(1):79–92.

Rao, N. K. (2011). *Foundation design: theory and practice*. John Wiley & Sons.

Rao, S. S. (2004). *The finite element method in engineering*. Elsevier Science & Technology Books, 4th edition.

Reddy, J. N. (2006). *An introduction to the finite element method*. McGraw-Hill New York, 3rd edition.

Reissner, E. (1958). A note on deflections of plates on a viscoelastic foundation. *Journal of Applied Mechanics*, 25(1):144–145.

Rowe, R., Lo, K., and Kack, G. (1983). A method of estimating surface settlement above tunnels constructed in soft ground. *Canadian Geotechnical Journal*, 20(1):11–22.

Roylance, D. (2001). Finite element analysis. *Department of Materials Science and Engineering. Massachusetts Institute of Technology Cambridge, MA*, 2139.

Sagaseta, C. (1987). Analysis of undraind soil deformation due to ground loss. *Geotechnique*, 37(3):301–320.

Schmidt, B. (1969). *Settlements and ground movements associated with tunneling in soil*. PhD thesis, University of Illinois at Urbana.

Schuster, M., Juang, C., Roth, M., Hsiao, E., and Kung, G. (2007). Serviceability limit state for probabilistic characterization of excavation-induced building damage. *Probabilistic Applications in Geotechnical Engineering (GSP 170)*, 1(10).

Schuster, M., Juang, C., Roth, M., Rosowsky, D., et al. (2008). Reliability analysis of building serviceability problems caused by excavation. *Géotechnique*, 58(9):743.

Schuster, M., Kung, G. T.-C., Juang, C. H., and Hashash, Y. M. (2009). Simplified model for evaluating damage potential of buildings adjacent to a braced excavation. *Journal of Geotechnical and Geoenvironmental Engineering*, 135(12):1823–1835.

Selby, A. (1999). Tunnelling in soils–ground movements, and damage to buildings in workington, UK. *Geotechnical & Geological Engineering*, 17(3-4):351–371.

Selvadurai, A. P. (1979). *Elastic analysis of soil-foundation interaction*. Elsevier.

Shafiqu, Q. S. M., Taha, M. R., and Chik, Z. (2008). Finite element analysis of tunnels using the elastoplastic–viscoplastic bounding surface model. *ARPN Journal of Engineering and Applied Sciences*, 3(3):178–188.

Simpson, B., Atkinson, J., and Jovicic, V. (1996). The influence of anisotropy on calculations of ground settlements above tunnels. *Geotechnical aspects of underground construction in soft ground*, pages 591–594.

SIMULIA, A. (2012). 6.12. *ABAQUS Analysis User's Manual*.

Smith, B. S. and Coull, A. (1991). *Tall building structures: analysis and design*. Wiley New York.

Son, M. (2015). Response analysis of nearby structures to tunneling-induced ground movements in sandy soils. *Tunnelling and Underground Space Technology*, 48:156–169.

Son, M. and Cording, E. J. (2005). Estimation of building damage due to excavation-induced ground movements. *Journal of Geotechnical and Geoenvironmental Engineering*, 131(2):162–177.

Son, M. and Cording, E. J. (2010). Responses of buildings with different structural types to excavation-induced ground settlements. *Journal of Geotechnical and Geoenvironmental Engineering*, 137(4):323–333.

Sugiyama, T., Hagiwara, T., Nomoto, T., Nomoto, M., Yutaka, A., Mair, R., Bolton, M., and Soga, K. (1999). Observations of ground movements during tunnel construction by slurry shield method at the docklands light railway lewisham extension—east london. *Soils and foundations*, 39(3):99–112.

Sun, E. Q. (2006). Shear locking and hourglassing in MSC nastran, Abaqus, and Ansys. In *Msc software users meeting*.

Swoboda, G. (1979). Finite element analysis of the new austrian tunnelling method (natm). In *Proceedings of the 3rd International Conference on Numerical Methods in Geomechanics, Aachen*, volume 2, pages 581–586.

Tatsuoka, F., Jardine, R., Presti, D. L., Benedetto, H. D., and Kodaka, T. (1997). Characterising the pre-failure deformation properties of geomaterials. volume 4, pages 2129–2164.

Taylor, R. (1995a). Centrifuges in modelling: principles and scale effects. *Geotechnical centrifuge technology*, pages 19–33.

Taylor, R. (1995b). Tunnelling in soft ground in the uk. *of: Underground construction in soft ground*, pages 123–126.

Terzaghi, K. (1955). Evaluation of coefficients of subgrade reaction. *Géotechnique*, 5(4):297–326.

Ti, K. S., Huat, B. B., Noorzaei, J., Jaafar, M. S., and Sew, G. S. (2009). A review of basic soil constitutive models for geotechnical application. *Electronic Journal of Geotechnical Engineering*, 14:1–18.

Timoshenko, S. (1940). *Strength of materials*. D. Van Nostrand Company, Inc., 2nd edition.

Timoshenko, S. P. and Woinowsky-Krieger, S. (1959). *Theory of plates and shells*. McGraw-hill.

Tomlinson, M. (1994). *Pile design and construction practice*. Taylor & Franics group, 4th edition.

Tomlinson, M. J. and Boorman, R. (2001). *Foundation design and construction*. Pearson education, 7th edition.

Vafaeian, M. and Mirmiran, S. (2003). Applicability of elastic analysis for predicting the settlement distribution around tunneling in soft ground (technical note). *International Journal of Engineering-Transactions B: Applications*, 16(3):217.

Vermeer, P. A. and Borst, D. R. (1984). Non-associated plasticity for soils, concrete and rock. *HERON, 29 (3), 1984*.

Vermeer, P. A., Ruse, N., and Marcher, T. (2002). Tunnel heading stability in drained ground. *Felsbau*, 20(6):8–18.

Verruijt, A. and Booker, J. (1996). Surface settlements due to deformation of a tunnel in an elastic half plane. *Geotechnique*, 46(4):753–756.

Vesic, A. S. (1961). Beams on elastic subgrade and the winkler's hypothesi. *Proceedings of the 5th International Conference on Soil Mechanics and Foundation Engineering, Paris*, 1:845–850.

Vlasov, V. Z. and Leont'ev, N. N. (1966). Beams, plates and shells on elastic foundations. *Translated from Russian by Israel Program for Scientific Translations, NASA TT F-357, TT 65-50135, Washington D.C.*

Vorster, T., Klar, A., Soga, K., and Mair, R. (2005). Estimating the effects of tunneling on existing pipelines. *Journal of Geotechnical and Geoenvironmental Engineering*, 131(11):1399–1410.

Vorster, T. E. (2005). *The effects of tunnelling on buried pipes*. PhD thesis, University of Cambridge.

Wang, Y., Shi, J., and Ng, C. W. (2011). Numerical modeling of tunneling effect on buried pipelines. *Canadian Geotechnical Journal*, 48(7):1125–1137.

Wang, Y., Tham, L., and Cheung, Y. (2005). Beams and plates on elastic foundations: a review. *Progress in Structural Engineering and Materials*, 7(4):174–182.

Wight, J. K. and MacGregor, J. G. (2009). *Reinforced concrete Mechanics and design*. Pearson Education International, Upper Saddle River, New Jersey, 5th edition.

Winkler, E. (1867). *Die Lehre von der Elasticitaet und Festigkeit*. Dominicus.

Wongsaroj, J., Soga, K., and Mair, R. (2007). Modelling of long-term ground response to tunnelling under st james's park, london. *Géotechnique*, 57(1):75–90.

Yahya, S. and Abdullah, R. (2014). A review on methods of predicting tunneling induced ground settlements. *EJGE*, 19:5813–5826.

Yeo, C. H., Hou LEE, F., Chee TAN, S., HASEGAWA, O., SUZUKI, H., and SHINJI, M. (2009). Three dimensional numerical modelling of a natm tunnel. *International Journal of the JCRM*, 5(1):33–38.

Young, W. C. and Budynas, R. G. (2002). *Roark's formulas for stress and strain*, volume 7. McGraw-Hill New York.

Zhang, L., Wu, X., Chen, Q., Skibniewski, M. J., and Hsu, S.-C. (2014). Towards a safety management approach for adjacent buildings in tunneling environments: Case study in china. *Building and Environment*, 75:222–235.

Zhao, Y. (2008). *In situ soil testing for foundation performance prediction*. PhD thesis, University of Cambridge.

Zheng, H., Liu, D., Lee, C. F., and Tham, L. (2005). Displacement-controlled method and its applications to material non-linearity. *International journal for numerical and analytical methods in geomechanics*, 29(3):209–226.

Zhou, B. (2014). *Tunnelling-induced ground displacements in sand*. PhD thesis, University of Nottingham.

Zhou, B., Marshall, A. M., and Yu, H.-S. (2014). Effect of relative density on settlements above tunnels in sands. In *Geo-Shanghai 2014*.

Zymnis, D., Whittle, A., and Chatzigiannelis, I. (2013). Effect of anisotropy in ground movements caused by tunnelling.

Appendix A

Cantilever approach: practical example

In order to show how this method may be used to estimate bending stiffness of the superstructure of a building affected by tunnelling, an example is solved and its results are compared to the numerical prediction of the superstructure bending stiffness. Note that the stiffness contribution of the upper storeys to the floor of the first storey is considered in this example.

Consider a three y-bay, four x-bay, three-storey building made of concrete with an elastic modulus of 30 GPa and Poisson's ratio of 0.15. Column dimensions are 0.3×0.3×3 m (h_{col}, b_{col} and L_{col}, respectively), supporting beam dimensions are 0.3×0.5 m (b_{sb} and h_{sb}, respectively), floor beam dimensions are 0.3×0.5 m (b_{fb} and h_{fb}, respectively), and slab dimensions are 5×6×0.15 m (B_{sl}, $L_{sl}(=L_{fl})$ and t_{sl}, respectively). Three bays in the x-direction are affected by tunnelling. The following steps lead to calculating the bending stiffness of this building.

1. Determine the centroid of the floor cross section

$$\bar{y}_{fl} = \frac{2\times(0.3\times0.5\times0.5/2)+5\times0.15\times(0.5-0.15/2)}{2\times0.3\times0.5+5\times0.15} = 0.375 \text{ m}$$

2. Determine the floor cross sectional moment of inertia and flexural rigidity

$$I_{fl} = \sum\{2\times I_b + 2\times A_b\cdot\left(\bar{y}_{fl}-\bar{y}_b\right)^2 + I_{sl} + A_{sl}\cdot\left(\bar{y}_{fl}-\bar{y}_{sl}\right)^2\}$$
$$= 2\times0.00313+2\times0.00235+0.00141+0.001875 = 0.01424 \text{ m}^4$$
$$EI_{fl} = 30\times10^9\times0.01424 = 42.72\times10^7 \text{ Nm}^2$$

3. Calculate the analytical bending stiffness of the floor from Equation 2.3 using EI_{fl} and $F_K = 3$ for cantilever.

$$K_{b,fl,cant,an,fix} = \frac{3EI_{fl}}{L_{fl}^3} = \frac{3 \times 42.72 \times 10^7}{6^3} = 0.59 \times 10^7 \text{ N/m}$$

4. The ratio of $L_{sl}/B_{sl} = 1.2$ is smaller than 1.25, hence the analytical floor bending stiffness should be divided by coefficient $C_{bf,cant}$ (Equation 5.2) to obtain $K_{b,fl,cant,eq,fix}$ (Equation 5.3).

$$C_{bf,cant} = \left(\frac{6I_{fb}}{I_{sl}}\right)^{\frac{B_{sl}}{20L_{sl}}} = \left(\frac{6 \times 0.00313}{0.00141}\right)^{\frac{5}{20\times 6}} = 1.114$$

$$K_{b,fl,cant,eq,fix} = \frac{K_{b,fl,cant,an,fix}}{C_{bf,cant}} = \frac{0.59 \times 10^7}{1.114} = 0.53 \times 10^7 \text{ N/m}$$

5. Convert the bending stiffness of the fixed floor ($K_{b,fl,cant,eq,fix}$) to that of the actual floor connected to structural parts ($K_{b,fl,cant,eq,1s,1y}$, Equation 5.5) using coefficient $C_{bc,cant}$ (Equation 5.4)

$$G_b = \frac{E_b}{2(1+\nu_b)} = \frac{30 \times 10^9}{2(1+0.15)} = 13.04 \times 10^9 \text{ GPa}$$

$$K_{c,Lfl} = K_{c,Sfl} = \frac{EI_{fl}}{L_{fl}} = \frac{42.72 \times 10^7}{6} = 7.12 \times 10^7 \text{ Nm}$$

$$J_{sb} = \frac{b_{sb}h_{sb}}{12} \times \left(b_{sb}^2 + h_{sb}^2\right) = \frac{0.3 \times 0.5}{12} \times \left(0.3^2 + 0.5^2\right) = 0.00425 \text{ m}^4$$

$$K_{c,sb} = \frac{G_b J_{sb}}{L_{sb}} = \frac{13.04 \times 10^9 \times 0.00425}{5} = 1.11 \times 10^7 \text{ Nm}$$

$$K_{c,col} = \frac{EI_{col}}{L_{col}} = \frac{30 \times 10^9 \times 0.3 \times 0.3^3}{12 \times 3} = 0.675 \times 10^7 \text{ Nm}$$

$$C_{bc,cant} = \frac{K_{c,Sfl} + K_{c,sb} + 2K_{c,col}}{K_{c,Lfl} + K_{c,Sfl} + K_{c,sb} + 2K_{c,col}}$$

$$= \frac{7.12 \times 10^7 + 1.11 \times 10^7 + 2 \times 0.675 \times 10^7}{2 \times 7.12 \times 10^7 + 1.11 \times 10^7 + 2 \times 0.675 \times 10^7} = 0.574$$

$$K_{b,fl,cant,eq,1s,1y} = C_{bc,cant} \times K_{b,fl,cant,eq,fix} = 0.574 \times 0.53 \times 10^7$$

$$= 0.304 \times 10^7 \text{ N/m}$$

6. Compute column stiffening factors ($C_{cf,cant}$) based on Equation 5.6

$$C_{cf,cant,2} = \frac{2K_{c,col}}{2K_{c,col}+K_{c,Lfl}} \times \left(\frac{L_{col,2}}{h_{fl,2}}\right) = \frac{2\times 0.675\times 10^7}{2\times 0.675\times 10^7 + 7.12\times 10^7} \times \frac{3}{3.5} = 0.137$$

$$C_{cf,cant,3} = 0.0683$$

7. Calculate $\alpha_{Kus,cant}$ from Equation 5.8, and then evaluate $C_{Kus,cant,i}$ for each upper storey using Equation 5.7.

$$\frac{L_{x,bldg}}{L_{col}} = \frac{4\times 6+5\times 0.3}{3} = 8.5$$

$$\alpha_{Kus,cant} = 1.9\left(\frac{L_{x,bldg}}{L_{col}}\right)^{0.2} = 1.9\times 8.5^{0.2} = 2.914$$

$$C_{Kus,cant,2} = \log_{10}(C_{cf,cant,2}) + \alpha_{Kus,cant} = \log_{10}(0.137) + 2.914 = 2.05$$

$$C_{Kus,cant,3} = 1.748$$

8. The total bending stiffness of the single y-bay building superstructure with one deflected panel ($K_{b,fl,cant,eq,ms,1y}$) can now be calculated using Equation 5.9. The calculation is summarised in Table A.1.

Table A.1 Calculation of the total Building Stiffness

Floors	$K_{b,fl,cant,eq,i,1y} = K_{b,fl,cant,eq,1s,1y}$ (N/m)	$C_{Kus,cant,i}$	Contribution of each storey (N/m) $\left(C_{Kus,cant,i}\times K_{b,fl,cant,eq,i,1y}\right)$
1^{st}	0.304×10^7	–	0.304×10^7
2^{nd}	0.304×10^7	2.050	0.62×10^7
3^{rd}	0.304×10^7	1.748	0.53×10^7
Total			1.454×10^7

9. There are three bays in the y-direction. The effects of the two extra bays can be added using Equation 5.10.

$$K_{b,fl,cant,eq,ms,my} = (1+0.6(n_y-1))\times K_{b,fl,cant,eq,ms,1y} = (1+0.6\times(3-1))\times 1.454\times 10^7$$
$$= 3.20\times 10^7 \text{ N/m}$$

The numerical stiffness result of the analysed building is 3.17×10^7 N/m. The proposed result is 3.20×10^7 N/m. This leads to an overestimation of about 1%.

10. Calculate coefficient $C_{K,reduct,cant}$ from Equation 5.12, and then compute the final bending stiffness of the building using Equation 5.13.

$L_{xbay} = 6.3$ m (centre to centre)

$L_{inf} = 3 \times 6.3 = 18.9$ m

$C_{K,reduct,cant} = F_{st} \times \frac{L_{xbay}^3}{L_{inf}^3} = 2 \times \frac{6.3^3}{18.9^3} = 0.074$

$K_{b,cant,eq,bldg} = C_{K,reduct,cant} \times K_{b,fl,cant,eq,ms,my} = 0.074 \times 3.20 \times 10^7 = 0.237 \times 10^7$ N/m

It is worth noting that the numerical analysis of the building yielded a value of $C_{K,reduct,cant} = 0.063$.

Appendix B

Fixed–ended approach: practical example

Consider a 2 y-bay, 6 x-bay, seven-storey building made of concrete with an elastic modulus of 30 GPa and Poisson's ratio of 0.15. Column dimensions are 0.35×0.4×3 m (h_{col}, b_{col} and L_{col}, respectively), supporting beam dimensions are 0.35×0.5 m (b_{sb} and h_{sb}, respectively), floor beam dimensions are 0.4×0.5 m (b_{fb} and h_{fb}, respectively), and slab dimensions are 5×6×0.15 m (B_{sl}, L_{sl} and t_{sl}, respectively). 4 bays in the x-direction are affected by tunnelling. The following steps lead to calculating the bending stiffness of this building. Note that the stiffness contribution of the upper storeys to the floor of the first storey is considered in this example.

1. Determine the centroid of the floor cross section

$$\bar{y}_{fl} = \frac{2 \times (0.4 \times 0.5 \times 0.5/2) + 5 \times 0.15 \times (0.5 - 0.15/2)}{2 \times 0.4 \times 0.5 + 5 \times 0.15} = 0.364 \text{ m}$$

2. Determine the floor cross sectional moment of inertia and flexural rigidity

$$I_{fl} = \sum \{2 \times I_b + 2 \times A_b \cdot \left(\bar{y}_{fl} - \bar{y}_b\right)^2 + I_{sl} + A_{sl} \cdot \left(\bar{y}_{fl} - \bar{y}_{sl}\right)^2\}$$
$$= 2 \times 0.00417 + 2 \times 0.0026 + 0.0014 + 0.0028 = 0.0177 \text{ m}^4$$
$$EI_{fl} = 30 \times 10^9 \times 0.0177 = 53.1 \times 10^7 \text{ Nm}^2$$

3. Calculate the analytical bending stiffness of the floor from Equation 2.3 using EI_{fl}, $L_{fl,t} = 2 \times L_{sl} + b_{sb} = 12.35$ m and $F_K = 192$ for a fixed–ended beam.

$$K_{b,fl,fend,an,fix} = \frac{192 EI_{fl}}{L_{fl}^3} = \frac{192 \times 53.1 \times 10^7}{12.35^3} = 5.412 \times 10^7 \text{ N/m}$$

4. Compute $C_{bf,fend}$ (Equation 5.15), then divide the analytical floor bending stiffness by coefficient $C_{bf,fend}$ to obtain $K_{b,fl,fend,eq,fix}$ (Equation 5.16).

$$C_{bf,fend} = \left(\frac{24 I_{fb}}{I_{sl}}\right)^{\left(\frac{B_{sl}}{9 L_{fl,t}} \times (1 - b_{lb}/B_{sl})\right)} = \left(\frac{24 \times 0.00417}{0.0014}\right)^{\left(\frac{5}{9 \times 12.35} \times (1 - 0.35/5)\right)} = 1.196$$

$$K_{b,fl,fend,eq,fix} = \frac{K_{b,fl,fend,an,fix}}{C_{bf,fend}} = \frac{5.412 \times 10^7}{1.196} = 4.525 \times 10^7 \text{ N/m}$$

5. Convert the bending stiffness of the fixed floor ($K_{b,fl,fend,eq,fix}$) to that of the actual floor connected to structural parts ($K_{b,fl,fend,eq,1s,1y}$, Equation 5.18) using coefficient $C_{bc,fend}$ (Equation 5.17)

$$G_b = \frac{E_b}{2(1+\nu_b)} = \frac{30 \times 10^9}{2(1+0.15)} = 13.04 \times 10^9 \text{ GPa}$$

$$K_{c,Lfl} = K_{c,Sfl} = \frac{EI_{fl}}{L_{fl}} = \frac{53.1 \times 10^7}{6} = 8.85 \times 10^7 \text{ Nm}$$

$$J_{sb} = \frac{b_{sb} h_{sb}}{12} \times \left(b_{sb}^2 + h_{sb}^2\right) = \frac{0.35 \times 0.5}{12} \times \left(0.35^2 + 0.5^2\right) = 0.00543 \text{ m}^4$$

$$K_{c,sb} = \frac{G_b J_{sb}}{L_{sb}} = \frac{13.04 \times 10^9 \times 0.00543}{5} = 1.42 \times 10^7 \text{ Nm}$$

$$K_{c,col} = \frac{EI_{col}}{L_{col}} = \frac{30 \times 10^9 \times 0.4 \times 0.35^3}{12 \times 3} = 1.43 \times 10^7 \text{ Nm}$$

$$C_{bc,fend} = \frac{K_{c,Sfl} + K_{c,sb} + 2K_{c,col}}{K_{c,Lfl} + K_{c,Sfl} + K_{c,sb} + 2K_{c,col}} =$$

$$\frac{8.85 \times 10^7 + 1.42 \times 10^7 + 2 \times 1.43 \times 10^7}{2 \times 8.85 \times 10^7 + 1.42 \times 10^7 + 2 \times 1.43 \times 10^7} = 0.597$$

$$K_{b,fl,fend,eq,1s,1y} = C_{bc,fend} \times K_{b,fl,fend,eq,fix} = 0.597 \times 4.525 \times 10^7$$

$$= 2.7 \times 10^7 \text{ N/m}$$

6. Compute column stiffening factors ($C_{cf,fend}$) based on Equation 5.19

$$C_{cf,fend,2} = \frac{2K_{c,col}}{2K_{c,col}+K_{c,Lfl}} \times \left(\frac{L_{col,2}}{h_{fl,2}}\right) = \frac{2\times 1.43\times 10^7}{2\times 1.43\times 10^7 + 8.85\times 10^7} \times \frac{3}{3.5} = 0.12$$

$$C_{cf,fend,3} = 0.06,\ C_{cf,fend,4} = 0.04,\ C_{cf,fend,5} = 0.03,\ C_{cf,fend,6} = 0.024,$$
$$C_{cf,fend,7} = 0.02$$

7. Calculate $\alpha_{Kus,fend}$ from Equation 5.21, and then evaluate $C_{Kus,fend,i}$ for each upper storey using Equation 5.20.

$$K_{c,lb} = \frac{EI_{lb}}{L_{lb}} = \frac{30\times 10^9 \times 0.35 \times 0.5^3/12}{5} = 2.19\times 10^7 \text{Nm}$$

$$\frac{K_{c,lb}}{K_{c,lb}+2K_{c,Lfl}} + \frac{K_{c,col}}{K_{c,col}+K_{c,Lfl}} = \frac{2.19\times 10^7}{2.19\times 10^7 + 2\times 8.85\times 10^7} + \frac{1.43\times 10^7}{1.43\times 10^7 + 8.85\times 10^7}$$
$$= 0.25$$

$$\alpha_{Kus,fend} = -1.65 \times \left(\frac{K_{c,lb}}{K_{c,lb}+2K_{c,Lfl}} + \frac{K_{c,col}}{K_{c,col}+K_{c,Lfl}}\right) + 2.75 = -1.65\times .25 + 2.75$$
$$= 2.34$$

$$C_{Kus,fend,2} = \log_{10}(C_{cf,fend,2}) + \alpha_{Kus,fend} = \log_{10}(0.12) + 2.34 = 1.42$$
$$C_{Kus,fend,3} = 1.11\ C_{Kus,fend,4} = 0.94\ C_{Kus,fend,5} = 0.81\ C_{Kus,fend,6} = 0.72$$
$$C_{Kus,fend,7} = 0.64$$

8. The total bending stiffness of the single y-bay building superstructure with two deflected panels ($K_{b,fl,fend,eq,ms,1y}$) can now be calculated using Equation 5.22. The calculation is summarised in Table B.1.

9. There are two bays in the y-direction. The effects of the extra bay can be added using Equation 5.23.

$$K_{b,fl,fend,eq,ms,my} = (1+0.6(n_y-1)) \times K_{b,fl,fend,eq,ms,1y} = (1+0.6\times(2-1)) \times 17.93\times 10^7$$
$$= 28.7\times 10^7 \text{ N/m}$$

The numerical bending stiffness result of the analysed building is 26.5×10^7 N/m. The proposed result is 28.7×10^7 N/m. This leads to an overestimation of about 8%.

10. Calculate coefficient $C_{K,reduct,fend}$ from Equation 5.24, and then compute the final bending stiffness of the building using Equation 5.25.

$L_{fl,t} = 12.35$ m

Table B.1 Calculation of the total Building Stiffness

Floors	$K_{b,fl,fend,eq,i,1y} = K_{b,fl,fend,eq,1s,1y}$ (N/m)	$C_{Kus,fend,i}$	Contribution of each storey (N/m) $\left(C_{Kus,fend,i} \times K_{b,fl,fend,eq,i,1y}\right)$
1^{st}	2.70×10^7	–	2.70×10^7
2^{nd}	2.70×10^7	1.42	3.83×10^7
3^{rd}	2.70×10^7	1.11	3.00×10^7
4^{th}	2.70×10^7	0.94	2.54×10^7
5^{th}	2.70×10^7	0.81	2.19×10^7
6^{th}	2.70×10^7	0.72	1.94×10^7
7^{th}	2.70×10^7	0.64	1.73×10^7
Total			17.93×10^7

$L_{inf} = 4 \times 6 + 3 \times 0.35 = 25.05$ m

$C_{K,reduct,fend} = F_{st} \times \frac{L_{fl,t}^3}{L_{inf}^3} = 2 \times \frac{12.35^3}{25.05^3} = 0.24$

$K_{b,fend,eq,bldg} = C_{K,reduct,fend} \times K_{b,fl,fend,eq,ms,my} = 0.24 \times 28.7 \times 10^7 = 6.9 \times 10^7$ N/m

It is worth noting that the numerical analysis of the building yielded a value of $C_{K,reduct} = 0.325$.